

DOCTORAL THESIS

Development of Control Methods for Synchronous Reluctance Motors

Hamidreza Heidari

TALLINN UNIVERSITY OF TECHNOLOGY
DOCTORAL THESIS
8/2022

Development of Control Methods for Synchronous Reluctance Motors

HAMIDREZA HEIDARI



TALLINN UNIVERSITY OF TECHNOLOGY
School of Engineering
Department of Electrical Power Engineering and Mechatronics
This dissertation was accepted for the defence of the degree 09/03/2022

Supervisor: Prof. Dr. Anton Rassõlkin
Tallinn University of Technology
Tallinn, Estonia

Co-supervisor: Prof. Dr. Anouar Belahcen
Tallinn University of Technology
Tallinn, Estonia

Opponents: Assoc. Prof. Dr. Tuomo Lindh
Tenure Associate/Assistant Professor at School of Energy Systems
LUT University
Lappeenranta, Finland

Dr. Viktor Beldjajev
Technical Program Manager
ABB Drives
Jüri, Estonia

Defence of the thesis: 07/04/2022, Tallinn

Declaration:

Hereby I declare that this doctoral thesis, my original investigation, and achievement submitted for the doctoral degree at Tallinn University of Technology has not been submitted for a doctoral or equivalent academic degree.

Hamidreza Heidari

signature



European Union
European Regional
Development Fund



Investing
in your future

Copyright: Hamidreza Heidari, 2022
ISSN 2585-6898 (publication)
ISBN 978-9949-83-798-4 (publication)
ISSN 2585-6901 (PDF)
ISBN 978-9949-83-799-1 (PDF)
Printed by Koopia Niini & Rauam

TALLINNA TEHNIKAÜLIKOO
DOKTORITÖÖ
8/2022

Sünkroonreluktantsmootorite juhtimismeetodite edasiarendus

HAMIDREZA HEIDARI



Contents

List of publications	7
Author's contribution to the publications	8
Abbreviations	9
1. Introduction	10
1.1 The motivation of the study.....	10
1.2 The objective of the study.....	10
1.3 The novelties of the study.....	11
2 State of the art of motor technologies and the motor control methods.....	13
2.1 Motor technologies.....	13
2.2 Motor control methods.....	17
2.2.1 Field-oriented control	20
2.2.2 Direct torque control	21
2.2.3 Predictive control.....	22
2.2.4 Novel control theories in motor-drive systems	23
2.2.5 Classification of the motor control methods	23
2.3 Section summary.....	26
3 Efficiency map study of the studied motor-drive systems.....	27
3.1 Section summary.....	31
4 Modelling, parameter identification, and vector control of studied synchronous reluctance machine.....	32
4.1 Synchronous reluctance machine modelling	32
4.2 Parameters identification.....	34
4.2.1 Measurements with LCR meters.....	34
4.2.2 Measurements with DC power supply and current transducer (DC decay test) ...	36
4.2.3 The whole system parameters identification through the controller with the utilization of the inverter	36
4.3 Field-oriented control of synchronous reluctance machine	41
4.4 Maximum torque per ampere control strategy for synchronous reluctance machine .	47
4.5 Field-weakening operation of synchronous reluctance machine	50
4.6 Robust vector control of synchronous reluctance machine employing an adaptive disturbance rejection controller	51
4.7 Torque ripple suppression in the direct torque control of synchronous reluctance machine.....	58
4.7.1 Direct torque control of synchronous reluctance machine	58
4.7.2 The proposed method.....	59
4.8 Section summary.....	61
5 Conclusion	63
6 Future studies	65
References	69
Acknowledgements.....	76
Abstract.....	77

Lühikokkuvõte.....	78
Appendix	79
Curriculum vitae.....	209
Elulookirjeldus.....	210

List of publications

The list of author's publications, on the basis of which the thesis has been prepared:

[Paper I] **Heidari, H.**, Rassölkin, A., Kallaste, A., Vaimann, T., Andriushchenko, E., Belahcen, A., and Lukichev, D. V. (2021). A review of synchronous reluctance motor-drive advancements. *MDPI Sustainability* (Switzerland), 13(2). <https://doi.org/10.3390/su13020729>

[Paper II] **Heidari, H.**, Rassölkin, A., Kallaste, A., Vaimann, T., and Belahcen, A. (2019). Harmonics Distortion in Inverter-Fed Motor-Drive Systems: Case Study. 2019 Electric Power Quality and Supply Reliability Conference (PQ) & 2019 Symposium on Electrical Engineering and Mechatronics (SEEM), 1–4. <https://doi.org/10.1109/PQ.2019.8818230>

[Paper III] **Heidari, H.**, Andriushchenko, E., Rassölkin, A., and Demidova, G. L. (2020). Comparison of Synchronous Reluctance Machine and Permanent Magnet-Assisted Synchronous Reluctance Machine Performance Characteristics, 2020 27th International Workshop on Electric Drives: MPEI Department of Electric Drives 90th Anniversary (IWED), 2020, pp. 1–5, doi: 10.1109/IWED48848.2020.9069583

[Paper IV] **Heidari, H.**, Rassölkin, A., Kallaste, A., Vaimann, T., Andriushchenko, E., A Comparison of the Vector Control of Synchronous Reluctance Motor and Permanent Magnet-Assisted Synchronous Reluctance Motor, 2021 XVIII International Scientific Technical Conference Alternating Current Electric Drives (ACED), 2021, pp. 1–6, doi: 10.1109/ACED50605.2021.9462265

[Paper V] **Heidari, H.**, Rassölkin, A., Kallaste, A., Vaimann, T., Andriushchenko, E., Belahcen, A. Design of a Research Laboratory Drive System for a Synchronous Reluctance Motor for Vector Control and Performance Analysis, *Inventions* 2021, 6(4), 64; <https://doi.org/10.3390/inventions6040064>

[Paper VI] **Heidari H.**, Rassölkin A, Holakooie MH, Vaimann T, Kallaste A, Belahcen A, Lukichev DV. A Parallel Estimation System of Stator Resistance and Rotor Speed for Active Disturbance Rejection Control of Six-Phase Induction Motor. *Energies*. 2020; 13(5):1121. <https://doi.org/10.3390/en13051121>

[Paper VII] **Heidari, H.**, Rassölkin, A., Kallaste, A., Vaimann, T., & Andriushchenko, E. Vector Control of Synchronous Reluctance Motor with Reduced Torque Ripples, 2020 XI International Conference on Electrical Power Drive Systems (ICEPDS), 2020, pp. 1–5, doi: 10.1109/ICEPDS47235.2020.9249309

[Paper VIII] **Heidari H.**, Rassölkin A, Vaimann T, Kallaste A, Taheri A, Holakooie MH, Belahcen A. A Novel Vector Control Strategy for a Six-Phase Induction Motor with Low Torque Ripples and Harmonic Currents. *Energies*. 2019; 12(6):1102. <https://doi.org/10.3390/en12061102>

Author's contribution to the publications

Contribution to the papers in this thesis are:

[Paper I] **Hamidreza Heidari**, as the main author, has surveyed the literature and classified the collected data. The paper was written by him

[Paper II] **Hamidreza Heidari**, as the main author, has devised the methodology for the study and has conducted the tests in the lab. The paper was written by him.

[Paper III] **Hamidreza Heidari**, as the main author, has devised the methodology for the study and has conducted the tests in the lab. The paper was written by him.

[Paper IV] **Hamidreza Heidari**, as the main author, has studied the challenges in the field and has proposed a method to improve the performance of the motor. He has implemented the method and has obtained the results. The paper was written by him.

[Paper V] **Hamidreza Heidari**, as the main author, has implemented the test bench, as well as the simulation of the control methods. The tests were conducted by him, and the results are presented in the paper. The paper was written by him.

[Paper VI] **Hamidreza Heidari**, as the main author, has implemented the test bench, as well as the simulation of the control methods. The tests were conducted by him, and the results were presented in the paper. The paper was written by him.

[Paper VII] **Hamidreza Heidari**, as the main author, has implemented the test bench, as well as the simulation of the control methods. The tests were conducted by him, and the results were presented in the paper. The paper was written by him.

[Paper VIII] **Hamidreza Heidari**, as the main author, has implemented the test bench, as well as the simulation of the control methods. The tests were conducted by him, and the results were presented in the paper. The paper was written by him.

Abbreviations

AC	Alternating current
ADRC	Adaptive disturbance rejection controller
ANN	Adaptive neural network
ARFNN	Adaptive recurrent fuzzy neural network
CCS	Continuous control set
DC	Direct current
DDTC	Dead-beat direct torque control
DevC	Deviation model-based control
DFOC	Direct field-oriented control
DFVC	Direct-flux vector control
DTC	Direct torque control
DTFC	Direct torque flux control
EMF	Electromotive force
EV	Electrical vehicle
FCS	Finite control set
FL	Fuzzy logic
FOC	Field-oriented control
FW	Field-weakening
IE codes	International energy-efficiency codes
IFOC	Indirect field-oriented control
IM	Induction motor
IPM	Interior permanent magnet
MFPC	Model-free predictive current control
MMF	magnetomotive force
MPC	Model-based predictive control
MPCC	Model-based predictive current control
MPDTC	Model-based predictive direct torque control
MTPA	Maximum torque per ampere
Nd-Fe-B	Neodymium-iron-boron
PC	Predictive control
PMSM	Permanent magnet synchronous motor
PMSynRM	Permanent magnet-assisted synchronous reluctance motor
PTC	Predictive torque control
PWM	Pulse with modulation
RFVC	Reference flux vector calculator
SMC	Sliding mode control
Sm-Co	Samarium-cobalt
SVM	Space vector modulation
SVPWM	Space vector pulse modulation-based
SynRMs	Synchronous reluctance motors
VSD	Variable speed drives

1. Introduction

Electrical motor-drive systems are the single largest electrical end-use devices that consume roughly 45% of the global electricity. This attributes to 6040 Mt of CO₂ emission, which is estimated to rise to 8570 Mt per year by 2030 [1]. The mid-size motors with an output of 0.75 kW to 375 kW attribute the largest proportion of the motor electricity consumption. Amongst different technologies, induction motor (IM) has been the most widely implemented technology [1]. However, it is projected to save up to 10% of the global electricity consumption by replacing this motor with cost-effective motor-drive systems [1].

In this work, the efficiencies of the designed synchronous reluctance motors (SynRMs) were studied along with the industrial IM. Since the motor-drive systems are broadly used in variable speed applications, to study the efficiency of a motor-drive system, an efficiency map of the system can solely be a trustworthy option to evaluate the performance of the system. An efficiency map can provide information on the motor-drive system in various speed and load operating conditions.

1.1 The motivation of the study

SynRMs have been around for almost a century, and there has not been a motivation for their development in the industry due to the poor performance of the initial designs of these machines. However, the advent of power electronic devices and the development of variable speed drives have opened new ground for these machines convincing the recent studies to dedicate a considerable portion to the development of these technologies. To realize the importance of studies in different fields of motor-drive systems, a deep study of the life cycle of the machine is required. Although each phase of the life cycle of these machines is of importance and requires study, some phases of the life cycle have a larger share in the source's consumption and the environmental effects. A comprehensive study on the SynRMs in [2] shows the significance of the energy consumption of the SynRMs in the operation phase and presents a huge gap in the study to improve the efficiency and the performance of these machines. In addition, the environmental concerns are more highlighted in the operation phase since the biggest share of the energy consumption as well as energy losses occur in the operation phase. Hence, this thesis was motivated by the efficiency and the performance improvement of the SynRM in the use phase through more sophisticated control algorithms.

1.2 The objective of the study

The study aims to analyze the performance of the SynRM in the experiment and devise several control algorithms to improve the efficiency and the performance of the motors. By improving the performance of the system in the transient state and the steady-state, as well as increasing the efficiency of the SynRM drive, the thesis aims to save resources such as electrical energy and prolong the life expectancy of the system. Moreover, the study sets a goal to improve the performance of the system and increase the robustness against the uncertainties such as load disturbances. To implement the ideas in real-life, the motor and the drive system were simulated for the initial design of the proper control algorithm. Several algorithms were simulated, and the results showed a significant improvement in the motor performance in simulations. Then, an experimental

setup was designed to implement the algorithms in real-time. Finally, the proposed algorithms were applied in real-time, and the results proved the performance of the proposed algorithm in practice.

1.3 The novelties of the study

In this thesis, the motor control algorithms are scrutinized and studied in detail, as well as the basic and novel control methods in the control engineering field. The various features and qualifications of the motor drive systems are studied, and the measures to analyze the qualifications are investigated. Different approaches and techniques to improve certain features are studied in order to provide a tool for comparison. Finally, the thesis presents a novel approach in the classification of the motor control algorithms based on the features that each algorithm possesses. In this classification, the most well-known motor control algorithms in line with the novel control theories are classified in terms of the derivation source and the strongpoint in control.

Several approaches are studied to measure the motor parameters for the sake of control. As an alternative to isolated tests on the motor using DC power supply and multi-meters LCR meters, an identification algorithm is proposed to identify the system parameters through the processor, including not only the studied motor but also the cables and the nonlinearity of the power electronic switches in the inverter. This algorithm is based on a closed-loop system. In this algorithm, a current regulator in a synchronous reference frame on one of the direct or quadrature axis is applied to amplify the command voltage in order to nullify the error signal of the instantaneous value with the reference value. Then the desired current is achieved by the system. Having the information of the regulator and the current reference, the motor parameters such as resistance and the inductances in each axis are identified in standstill conditions.

In this thesis, the conventional vector control algorithm is implemented on SynRM. To maximize the torque in the motor shaft with respect to the phase current, a control algorithm was devised to apply a dynamic current reference in the d-axis, which is obtained from the motor's model. This algorithm not only increases the torque in the motor output but also improves the motor performance in the base speed region due to better exploiting the input current in different axes.

The SynRM's parameters are highly dependent on the conditions such as temperature and the input current. Moreover, the SynRM vector control is highly dependent on the motor parameters. Furthermore, a robust control algorithm is vital to implement to achieve a desirable performance from the motor drive system. Linear control algorithms do not present a robust behavior in case of parameters uncertainties and system disturbance. Hence, in this thesis, a nonlinear control algorithm is proposed and implemented in real-time to improve the robustness of the control against the parameter variation in the motor and the disturbances such as load in the system. This method presents a remarkable improvement in the output torque performance to avoid the speed from sudden changes in the condition of the load injection to the system.

The torque ripples in SynRM associated with the slotting harmonics are extremely high, leading to very poor performance of the motor without current control. Apart from that, direct torque control (DTC) presents high torque ripples because of the instantaneous regulation of the torque and flux in a stationary reference frame without any pulse with modulation (PWM) and current regulation and transformation of the currents in the synchronous reference frame. In this thesis, an algorithm was proposed to apply synchronous reference frame components in the DTC of the SynRM. In this

sense, the direct and quadrature components of the motor current in the synchronous reference frame are applied as the flux and torque correspondents to the switching table. Hence, the algorithm preserves the main structure of the DTC, including the switching table and the flux and torque estimation, and augments the transformation block to the control system to replace inputs to the switching table. Moreover, a duty ratio regulation algorithm is proposed to dedicate a certain time of the switching period for active and then apply a null voltage for the rest of the sampling period. The combination of the proposed algorithms results in a precise current controller, which leads to far lower torque ripples compared to the classical DTC method.

2 State of the art of motor technologies and the motor control methods

This section is based on the publication [Paper I], and [Paper II] where the applications of the SynRMs are investigated in comparison with the conventional motor technologies. Besides, a detailed study of SynRMs is carried out regarding the performance characteristics. Then, the motor control methods are studied regarding their structure. A comprehensive classification of the motor control strategies in terms of the specific features is presented.

2.1 Motor technologies

So far, the motor technologies have lost the market to their IM counterparts in many applications such as pumps and fans. This was mainly due to the line-start capability of IM, which had made it more convenient and affordable to implement in different industries. On the other hand, the production of the aluminum bars in the rotor causes a lot of difficulties and costs in the manufacturing lines. Apart from the cost in the manufacturing stage, the bars cause losses in the rotor in the usage phase, where the efficiency and reliability considerations are of paramount importance. To be more detailed, in the IM, the rotor losses have a share of roughly 20% of all losses in the motor [3]. This can not only lead to low efficiency of the motor but also cause some serious damages to the motor, which makes the motor less reliable. For instance, the high-temperature operation of the rotor leads to the high temperature of the bearings. As a consequence, mechanical damages to the bearings gain more probability, which is listed among the main causes of faults in these motors.

Another motor technology that has dominated traction applications is the permanent magnet synchronous motor (PMSM) [4], [5]. The PMSM benefits from the magnets inside the rotor, which empowers the motor with high efficiency, and high torque density [6]–[8]. However, the back electromotive force (back EMF) issues with this motor concern some applications like electric vehicles (EVs) in high speeds regions. This issue has convinced EV manufacturers like Tesla and Toyota to employ the interior permanent magnet synchronous motor (IPM) in the products [9], [10]. Although the IPM has fairly solved the back EMF issue, the PMs are still the key element of the rotor. Neodymium-iron-boron (Nd-Fe-B) and samarium-cobalt (Sm-Co) are the most popular material among PMSM manufacturers. These materials are mainly rare-earth magnet elements that have recently seen a dramatic rise in price due to the limited resources [11], [12]. The availability of the PMs is an undeniable factor in the manufacturing stage of the PMSMs, which has directed the researchers to study the other alternatives for these applications. Besides, the faults in the PMs in the usage phase of the PMSM are a disputable topic that adds to the drawbacks of these motors.

The SynRM introduces a sophisticated rotor structure that distinguishes it from conventional motor technologies. In this technology, the bars or windings, or PMs are absent in the rotor. This can not only make the manufacturing process more convenient (and consequently less production cost) but also lead to the cold operation of the rotor in the usage phase [13]. Besides, the implementation of this technology is also so convenient, and the motor is service-friendly in the operation phase.

The SynRM was initially attractive to the researchers on account of the high torque density that it produces. However, this technology owes its late popularity to the highly

efficient SynRM drive. Thanks to the cold operation of the motor, higher efficiency is SynRM has become a hot topic among the researchers as well as the industries [14], [3], [15]. The motivation of the efficiency topic for motor technologies comes from the efficiency classes defined by the international energy-efficiency (IE) codes, where the higher the IE code is, the more efficient motor is mandatory in the industry to be employed. The efficiency class in the IEC 60034-30 Part 1,2 defines the efficiency classes to the motors [16], [17]. According to [3], the IE3 efficiency class (Premium class) has been mandatory for industries since 2015. So far, conventional motor technologies can meet the requirements for this standard. However, moving from IE3 to higher efficiency classes such as IE4 or IE5 can severely challenge these technologies. In the meantime, the newly designed SynRM drives can offer IE5 efficiency class, which provides a bigger chance for this technology to dominate the market [14]. The high efficiency of the SynRM decreases the costs for energy consumption of the motor under operation. For instance, the payback time of an IE4 motor against an IE2 is calculated as 1.6 years in the power range of 37 kW and 1500 rpm with 8000 annual running [18]. This can convince the industries to replace their conventional motors with highly efficient SynRM.

SynRM introduces high loadability due to the cold rotor operation, especially at low speeds where it can be loaded up to 2.5 times higher than the nominal torque [19], [20]. The loadability of SynRM where the high breakout torque in a short time is presented in [Paper I]. As discussed in the paper, the motor is capable of operation in a wide speed range by continuous loading without separate cooling. Thanks to the simple rotor structure and high torque density, the motor presents a smaller size in the same power range as a motor with a lower moment of inertia and faster dynamic response [21], [22]. One of the topics that have attracted attention in research works towards SynRM technology is the reliability that this motor offers. SynRM mainly owes its reliability to two factors. Firstly, the low temperature of the rotor (and consequently the bearings) under operation lowers the probability of mechanical damages to the bearing, which have a big share in the faults in electrical motors. Secondly, the lack of cages or PM in the rotor structure results in less vulnerable components in the structure. As a result, having less vulnerable components omits the various types of faults in the structure.

On the other hand, some difficulties still challenge the development of the SynRMs. One of the most important drawbacks of the SynRM is the severely low power factor of this technology [23]. In SynRM, the saliency ratio defines the power factor of the motor. In this sense, by increasing the saliency ratio in the design progress, one can increase the power factor of the motor. In [24], a sophisticated anisotropic design of the rotor laminations has increased the saliency ratio of the motor and improved the power factor of the motor significantly. The idea of the study was to apply some cut-offs in the laminations which control the flux path to obtain a higher saliency ratio. Another obstacle with the SynRM development is the high torque ripple that this motor inherits from the interaction between the spatial harmonics of magnetomotive force (MMF) and the rotor geometry [25]. The high torque ripples of the SynRM result in low performance of the motor and possibly low efficiency of the motor, as well as the high acoustic noise in this motor. To address this issue, many research works were carried out in the design of the motor as well as the control studies [26]–[31]. Recent design solutions have decreased the torque ripples significantly. For instance, it is claimed in [32] that skewing the rotor can halve the torque ripples in SynRMs. Also, it is claimed that the asymmetric rotor flux barriers result in two-thirds torque ripples in the motor shaft. As another example of the

design improvements, the optimization tools for the rotor design are one of the popular approaches to suppress the torque ripples in the motor [33], [34].

As an important factor for the traction application, the SynRM resolves the back EMF issues of PMSM in the higher speeds region and presents a wide constant-power operation [35]. This is mostly due to the pure reluctance torque of the SynRM with no magnetic torque. However, it limits the flux density, which is resulted from the high saturation of the motor. Hence, removing the magnets from the rotor structure sacrifices the high performance of the motor. The permanent magnet-assisted synchronous reluctance motor (PMSynRM) addresses this issue with the introduction of a new version of SynRM with the usage of ferrite PMs in the rotor structure. With the peculiar characteristics of the rotor and benefiting from the magnetic torque, PMSynRM presents a competitive choice [36]. The popularity of these motors has experienced rapid growth among researchers for electrical vehicles (EV) applications [37]–[39]. This is mostly due to the high performance in with speed range and fulfilling the constant power speed range requirement [40], [41]. PMSynRM increases the performance of the SynRM while it avoids the rare-earth PMs in its structure. PMSynRM desirably addresses the power factor issues of the SynRM where it raises by 10% in low currents and 6% for high currents. Moreover, exploiting the magnetic torque in line with the reluctance torque results in a higher maximum torque per ampere (MTPA) of the motor.

On the other hand, adding magnets to the rotor increases the cost for the material as well as the manufacturing process and the assembling in the production phase. Besides, the ferrite PMs show far lower performance in comparison with their rear-earth PM. Also, the possible faults in the magnet can decrease the reliability of the motor under operation. It is worth mentioning that the costs can also fairly increase in the usage phase with harder maintenance.

It is worth mentioning that, lately, the manufacturers provide the control possibility of the drive of IM and SynRM with the identical variable speed drives (VSDs) as in ABB ACS880 [42]. This potentially provides the same cost for the purchasing of the motor drive systems of SynRM and IM, but the lower cost in the operation phase and less maintenance and higher reliability. This possibility presents a viable development base for the SynRMs.

By skimming through the different SynRM design proposals in the literature, it can be concluded that the designs can be divided into high-speed and low-speed categories. In the designs for high-speed applications, the ribs in the rotor design are inevitable for mechanical considerations to increase the robustness of the structure at high speeds. This can severely decrease the power factor and the efficiency of the motor. On the other hand, the ribs can be removed from the rotor in applications where the motor is employed in low-speed ranges. Hence, very high efficiency and the high power factor of the motor can be anticipated.

Generally, the SynRM present a decent alternative for the IM in the applications such as pump and fan on account of its high efficiency, where the PMSynRM can be projected in traction applications to replace the well-developed PMSM. These motor technologies are compared in terms of the structure and applications and regarding the advantages and the disadvantages in Table 2-1. This table aims to investigate the opportunities and the challenges with the SynRMs to replace the conventional motor technologies in different industries.

Table 2-1: A comparison of the SynRMs with conventional motor technologies [Paper 1].

Motor Type	Stator and Rotor Structure Sample	Different Types	Main Applications	Superiorities	Drawback(s)
IM		<ul style="list-style-type: none"> • Copper rotor • Aluminium rotor • Wound rotor • Rotor skewing 	Industrial applications (pump, fan, etc.)	<ul style="list-style-type: none"> + Low cost of material + Line-start capability 	<ul style="list-style-type: none"> - Low power factor - Hard manufacturing - Highly probable bearing fault
PMSM		<ul style="list-style-type: none"> • Interior PM • Surface-mounted PM • Line-start PMSM 	Traction, robotics, aerospace, medical, etc.	<ul style="list-style-type: none"> + Very high performance and efficiency 	<ul style="list-style-type: none"> - Rare-earth material usage - Hard manufacturing and maintenance
SynRM		<ul style="list-style-type: none"> • Line-start SynRM • Skewed rotor • Rotor with asymmetric flux barriers 	Industrial applications (pump, fan, etc.)	<ul style="list-style-type: none"> + Reliable and highly efficient due to cold rotor operation + High dynamic + High overloadability + Very high-speed capability + Simple to manufacture and service-friendly 	<ul style="list-style-type: none"> - High torque ripple - Severe low power factor
PMSynRM		<ul style="list-style-type: none"> • Rotor skewing • Asymmetric rotor structure • Different barrier structure and PM material 	Traction applications	<ul style="list-style-type: none"> + High performance without rare-earth PMs 	<ul style="list-style-type: none"> - Hard manufacturing and maintenance

2.2 Motor control methods

Motor-drive systems play a crucial role in many industries regardless of the grid-fed drive capability of the motors in the variable speed and even constant speed applications. This is mostly on account of high-performance control of the motors through VSDs. One can argue that the frequency converter adds up to the cost of these systems. But, considering the high-efficiency control of the motors that VSDs offer, the initial costs for purchasing the VSDs will be compensated by the less electricity consumption in the operation time [43]. The research and development in motor-drive systems are widespread where the focusses are mainly on three factors [44].

- design on the motors;
- design of the frequency converters;
- design of the control unit.

The conventional motors have been competitively optimized in the industries to nearly the best capability of them where the emergence of the VSDs directs the research works towards the new technologies. The design of the frequency converters is mainly concerned with electronic and power electronic designs and devices where the performance and efficiency of the package along with reliability are of the largest importance. The possibility of the digital control implementation on the motors has provided a vast base for the development of the control unit in the motor-drive systems. The control unit of the motor-drive systems guarantees high-performance energy conversion.

The control unit mainly includes the peripheral modules and the main processor. The peripheral modules include the input and output modules which are employed for data exchanging. The input modules incessantly capture the data from the system via transducers in the form of digital and analog inputs. The output modules provide switching sequences for the inverter's switches or send signals to auxiliary systems such as protection systems. As the second part of the control unit, the processor processes the computations and executes the control algorithms in real-time [45]. Digital control owes its remarkable flexibility to implement various control algorithms to the processor. The research in motor control strategies has leveraged the performance of every part of the motor-drive system in many terms. This section of the chapter surveys the motor control strategies proposed in the literature. A comparative study of the basic motor control methods will be carried out, and a comprehensive study and classification of the different control methods to improve the basic control methods will be presented. The digital motor control methods mainly employ open-loop or closed control on the motor. However, as far as the high-performance control of the motors in different operation conditions is concerned, only a feedback system can guarantee a solid solution to track the commanded reference.

Among the motor control algorithms in the industry, scalar control is broadly implemented in many industries [46]. This algorithm simply maintains the air-gap flux in the motor constant through the control of the stator voltage and frequency simultaneously [47], [48]. The method owes its popularity to the low cost and very simple implementation, especially in open-loop control systems. However, various studies in the closed-loop implementation of scalar control have been carried out in the literature [49]. This method is mainly referred to as the V/f control method with different variations such as V/\sqrt{f} , V/f^2 and $I-f$.

To achieve higher performance of the control, the industries are seeking to apply vector control algorithms in VSDs which work with vector quantities. This method controls the parameters employing the space phasors. Vector control methods are mainly classified as field-oriented control (FOC), direct torque control (DTC), and predictive control (PC). Table 2-2 compares the vector control methods regarding the structure of the control methods. This table investigates the basic control methods in terms of the control principle and the controlled state-space vector as well as the flux angle information or the current controller and modulator requirement, the coordinate transformation, the switching frequency, and the type of the controller. These factors will be studied in detail in this section for each control method.

Table 2-2: Structural comparison of the basic vector control methods [Paper 1]

Items	DTC	FOC	MPDTC	MPCC
Coordinates reference frame	Stationary reference frame	Synchronous reference frame	Stationary reference frame	Synchronous reference frame
Principle	Stationary voltage equations	Rotor reference frame equation	Stationary voltage equations	Rotor reference frame equation
Controlled variables	Torque and stator flux	d, q-axes currents	Torque and stator flux	d, q-axes currents
Rotor position measurement (estimation)	Not required	Required	Required	Required
Current control	Without	With	Without	With
Coordinate transformations	Not required	Required	Not required	Required
Modulator	Not required	Required	Not required	Not required
Switching frequency	Varies widely around the average frequency	Constant	Varies around the average frequency	Varies around the average frequency
Controllers	Hysteresis controller	Proportional integral controller (PI)	Cost function optimization	Cost function optimization

2.2.1 Field-oriented control

FOC is one of the most widely applied vector control methods, which presents a high-performance control of motors [50]. Conceptually, FOC applies two to four error-driven controllers in cascade to controller the currents, speed, or the position of the motor. The method transfers the motor currents from the stationary reference frame to the synchronous reference frame, which empowers the method with a high-resolution control of the motor currents. In the case of three-phase motors, this method decouples the motor currents to flux and torque correspondents, which replicates the DC motor providing a simple and precise control. The method observes the motor currents and transforms them to the synchronous reference frame. In the meanwhile, the optimum references of flux and torque correspondent are generated regarding the speed or position (varies with the control mode). Then the errors between the reference and instant values of the flux and torque correspondent get regulated by a controller to generate the correction voltages. Finally, the method applies the command voltages through the inverter to the motor through a modulator.

Despite the emergence of various control methods, the general trend towards FOC still is dominant. This is mainly true where the high steady-state performance and high efficiency of the motor are preferred to the transient response such as mining and steel industries. Besides, the method offers constant switching frequency, which is critical for safety requirements in some applications such as EV [51]. FOC has gained popularity on account of precise current control, which leads to the low harmonic currents and low torque ripples in the shaft known as high steady-state performance. In addition, the method is simple to implement and scale to a different motor with marginal changes in the algorithm, which has resulted in the wide implementation of the method in different motors' control.

On the other hand, FOC suffers from some drawbacks which have constantly challenged the researchers and industries to improve the method or seek other alternatives. Although the current control in the synchronous reference frame provides a desirable control of motors, some issues such as the low dynamic of the motor in the transient status are risen by this concept. Moreover, the current controllers and the modulation system occupy a considerable portion of the processing, which makes the method fairly complicated from the processor point of view and the execution time [52]. Besides, the method is highly dependent on the motor parameters (especially in the case of IM for flux angle estimation), which significantly decreases the robustness of the control.

Two popular approaches to FOC for decoupling the currents are direct field-oriented control (DFOC) and indirect field-oriented control (IFOC). DFOC estimates the rotor flux to obtain the angle information, whereas IFOC obtains the angle information through the mechanical position information, which is obtained by speed transducer. Many research works have been carried out to address the issue of low dynamics of FOC. Benefiting from DTC, direct-flux vector control (DFVC) offers a hybrid control method that combines FOC and DTC by regulation of the stator flux amplitude directly, instead of the flux correspondent current in the synchronous reference frame. On the other hand, the method regulates the torque correspondent current. This concept offers a desirable control for field-weakening (FW) operation where the flux and torque of the motor require a decouple control [40], [53], [54]. The concern over the low dynamic and complexity of FOC is overcome by rotor flux-oriented switching table-based control (RFSTC) [55], [56]. This method replaces the modulation system with a lookup table and applies two simple hysteresis controllers to provide the error signals for the lookup table.

2.2.2 Direct torque control

As its name suggests, DTC controllers the torque in the motor directly, meaning that there is no coordination transforming. The method estimates the instantaneous torque in the shaft and the flux linkage to compare with the reference values, which are generated by the speed controller and flux reference generator algorithm. This estimation algorithm employs the current feedbacks in the stationary reference frame and avoids the transformation to the synchronous reference frame. Then, the error the instantaneous and the reference values are simply controlled by the hysteresis controller to generate the error signals' sign. The switching table provides the lookup table, which generates the switching sequence to the inverter's gate drives based on the error signs and the sector information where the flux locates.

Thanks to the direct control of the torque, DTC assures a very high dynamic and fast response in control [57]. This inclines the industries with high transient response performance requirements to DTC. Besides, the lack of transformation blocks and complicated controllers, as well as the absences of the complicated modulation system, make the control process so simple and reduces the execution time for the process significantly. This leads to lower cost in the processor, which convinces leading manufacturers to introduce their DTC-based VSDs to the market [58].

On the other hand, the simplifications in the method have led to severe drawbacks that require deep studies in each field. The direct control of the torque and flux (the absence of current control and the application of hysteresis controllers intrinsically results in severely high torque ripples in the shaft [59]. Hysteresis controllers are one of the main reasons for high torque ripples of DTC, meaning that in each control cycle, the method opts for the optimized voltage to apply to the motor regardless of the status of the torque and flux during the sampling period. For this purpose, many research works have studied duty ratio regulation schemes to avoid the torque and flux to pass the hysteresis band significantly. This method that is also known as dead-beat direct torque control (DDTC), estimates the torque which is generated by the application of the selected command voltage to the motor at the end of each control cycle. Considering the estimated torque and flux at the end of each cycle, the method applies zero voltage for a portion of the sampling period. The application of a combination of the active and zero voltage avoids the torque to pass the hysteresis band and fairly settles the torque and flux in the band by the end of the cycle. Therefore, the torque ripples, as well as the flux ripples, decrease significantly. However, the method scarifies the simplicity of DTC by imposing complicated processes in control. Besides, the switching frequency increases due to the application of two or more voltages in each sampling frequency. Another attempt was made in [60] with an overmodulation scheme to amend the shortcoming of high torque ripples in DTC. As an alternative approach, a reference flux vector calculator (RFVC) is applied in [61] to suppress the torque ripples in DTC. The RFVC replaces the hysteresis controllers, which covers the absence of the current controller leading to lower torque ripples.

Although the switching table in DTC proposes a simple approach to opt set of switching sequence for voltage application to the motor, it results in variable switching frequency. In some applications, such as EVs, the manufacturers must provide constant switching frequency for safety requirements. Hence, many studies have modified the classical DTC to achieve constant switching frequency. These studies mainly consider the replacement of the switching table with different modulation methods. In [61], [62], the application of the space vector modulation (SVM) method is considered, which

attains a constant switching frequency. Direct torque flux control with SVM (SVM -DTFC) is studied in [63]. In another attempt towards alternative modulating methods, space vector pulse modulation-based DTC (SVPWM-DTC) is implemented in [52], [64]. The SVM and SVPWM methods are compared in [65]. It should be noted that the alternative approaches for the replacement of the switching table in DTC increase the complexity of the algorithm, which does not seem desirable for many applications with low-cost requirements for the processor.

The robustness of DTC is another topic that has attracted researchers' attention in recent studies [141]–[143]. The external disturbances such as load and the parameter variations of the motor are the main concerns in the motor control studies. Especially in the control of SynRM, the parameter variation is highly likely due to the high flux saturation condition in the rotor and the high temperature of the stator windings resulting in stator resistance and inductances variations. To increase the robustness of the DTC against parameter variations, [57] applies a torque limiting mechanism to modify the flux reference concerning the torque error sign, reducing the torque reference in the failure detection condition to achieve successful torque control.

2.2.3 Predictive control

The predictive control (PC) methods have recently opened new ground in the field of motor control. The concept of this control method is to simply consider different constraints simultaneously and, with the calculation of the cost function in the predicted time, select the optimal switching sequences with regards to the motor status in the instantaneous time.

As this method can consider numerous constraints in the algorithm, high performance of the control can be achieved. However, the complicated processes add up to the computation burden, which requires stronger processors compared to the traditional control concepts [71], [72].

As an alternative for FOC with precise current control, the model-free predictive current control (MFPCC) is studied in [73]–[75]. MFPCC simply controls the currents of the motor by detecting the currents and applying the voltages to the motor based on the deviation from the reference current. Then, in the next sampling period, the variation of the current will be calculated, and the variation of the current will be estimated with regard to the application of a certain voltage. Then, regarding the cost function, the optimal switching status will be chosen. This method proposes the simplest predictive control method avoiding the motor parameters and back-emf estimations.

By the emergence of powerful microprocessors in the industry, more sophisticated model-based predictive control (MPC) algorithms have gained popularity among researchers [76], [77]–[79]. Despite their model-free counterparts, MPC methods take the whole motor drive systems model into account and predict the future status of the system by application of the command voltages. The optimal switching states define the optimal command voltage application in the next sampling period. Model-based predictive current control (MPCC) is an example of this method which controls the currents in the motor with a model-based approach to the predictive control with cost function calculations. Akin to MFPCC, this method proposes current control with high performance control. In another attempt to predictive control of motors, model-based predictive direct torque control (MPDTC) is proposed in [71], [66]. This method is an alternative for DTC where the torque and flux values are the state values and the command voltage is selected to minimize the cost function achieving the desired torque at the end of each cycle [76]. This method is also known as predictive torque control

(PTC). Thanks to the direct control of the torque, this method presents a high dynamic behaviour where it sacrifices the high steady-state performance [80]. As common for all the predictive methods, this method imposes a huge complexity to the control process requiring a powerful microprocessor [81]. The most popular MPDTC is known as finite control set MPDTC (FCS-MPDTC), considering the discrete nature of the system [82]. This method avoids any modulation system in its structure, resulting in a highly dynamic and fairly simpler method. However, the torque ripples issue is a critical concern with this method. On the other hand, continuous control set MPDTC (CCS-MPDTC) employs modulation systems resulting in constant switching frequency and higher performance in steady-state.

2.2.4 Novel control theories in motor-drive systems

The need for high-performance and precise control of motors is increasingly growing in many industries. On the other hand, the traditional control algorithms inherently cannot respond to the call that these industries have for higher performance. Hence, many novel control concepts are increasingly being employed in motor control systems. This section studies the more widely applied methods in motor control.

As an alternative for the traditional motor control concepts, [83] proposes a deviation model-based control (DevC) which simplifies the motor's model obtaining the deviation model through normalization. Then the control algorithm employs the deviation model. Due to the applied normalized model, the method presents a fast dynamic behaviour with considerable robustness [84].

Sliding mode control (SMC) is another novel approach towards robust control purposes [85]. In motor control systems, this method is mainly applied in observers for torque and flux estimation. In [62], a simple observer based on SMC is applied for the online detection of stator resistance variation. The method employs SMC in a variable-structure control-based DTC, resulting in higher robustness of the control. It should be noted that the method increases the computational burden on the processor.

The traditional approach for control systems that usually consider the system's model or define a certain strategy for control has been lately altered by artificial intelligence theory. These methods can work without any information from the analytical model of the system. Adaptive neural network (ANN), fuzzy logic (FL), adaptive recurrent fuzzy neural network (ARFNN) are examples of the artificial intelligence-based control methods that are widely applied in motor control studies [86]–[89]. These methods can work with continuous values, which is compatible with physical components leading to lower cost, higher reliability, and performance in control [90], [91]. The methods provide a possibility to emulate human deductive thinking, but on the other hand, it requires high expertise, as well as big data, which makes it less viable for some applications.

2.2.5 Classification of the motor control methods

In this section, an approach is proposed to classify the motor control methods regarding their type and highlighted features. Figure 2-1 shows the diagram of the classification. The figure categorizes different motor control methods to scalar or vector control methods. Then each method is classified into different categories concerning the specific features that distinguish them from the others. Besides, there are categories of control methods that benefit from two different control methods, which are classified into different groups. The motor control methods are shown in a round shape in the figure. The novel control theories that were discussed in the previous section are presented in the diagram as a separate category. These methods are applied in some of the control

methods to empower them with specific features. These methods are depicted in a rectangular shape in the figure. One factor that distinguishes the classification approach from the other classifications is the features of control methods. In this figure, the highlighted qualities that motor control methods can present are shown in rectangular shapes with different colours. Each colour implies a specific feature. To demonstrate these specific features of the control methods, a round shape block with the colour of that feature is attached to the method. The size of each coloured round shape indicates the merit of the control method from that feature. On the other hand, the lack of one colour or smaller size of the coloured round shape can be interpreted as a weakness for a control method in that feature with the specific colour. For instance, DTC acquires features such as simplicity, high dynamic, high performance in high speed, and robustness, and the colours correspondent for these features are present in the figure. It can be deduced from this that the method lacks features such as low torque ripples and low harmonics and constant switching frequency as the colours of these features are absent in the method. As an example for improving some features of DTC in the derived control methods, SVPWM-DTC proposes a method with the colour correspondent to constant switching frequency. This indicates that the method has modified the DTC method to obtain constant switching frequency. It should be noted that the size of the color for simplicity in this method has decreased compared to DTC. This means that although the method presents constant switching frequency, it imposes some extra computational burden on the method that results in less simplicity of the method.

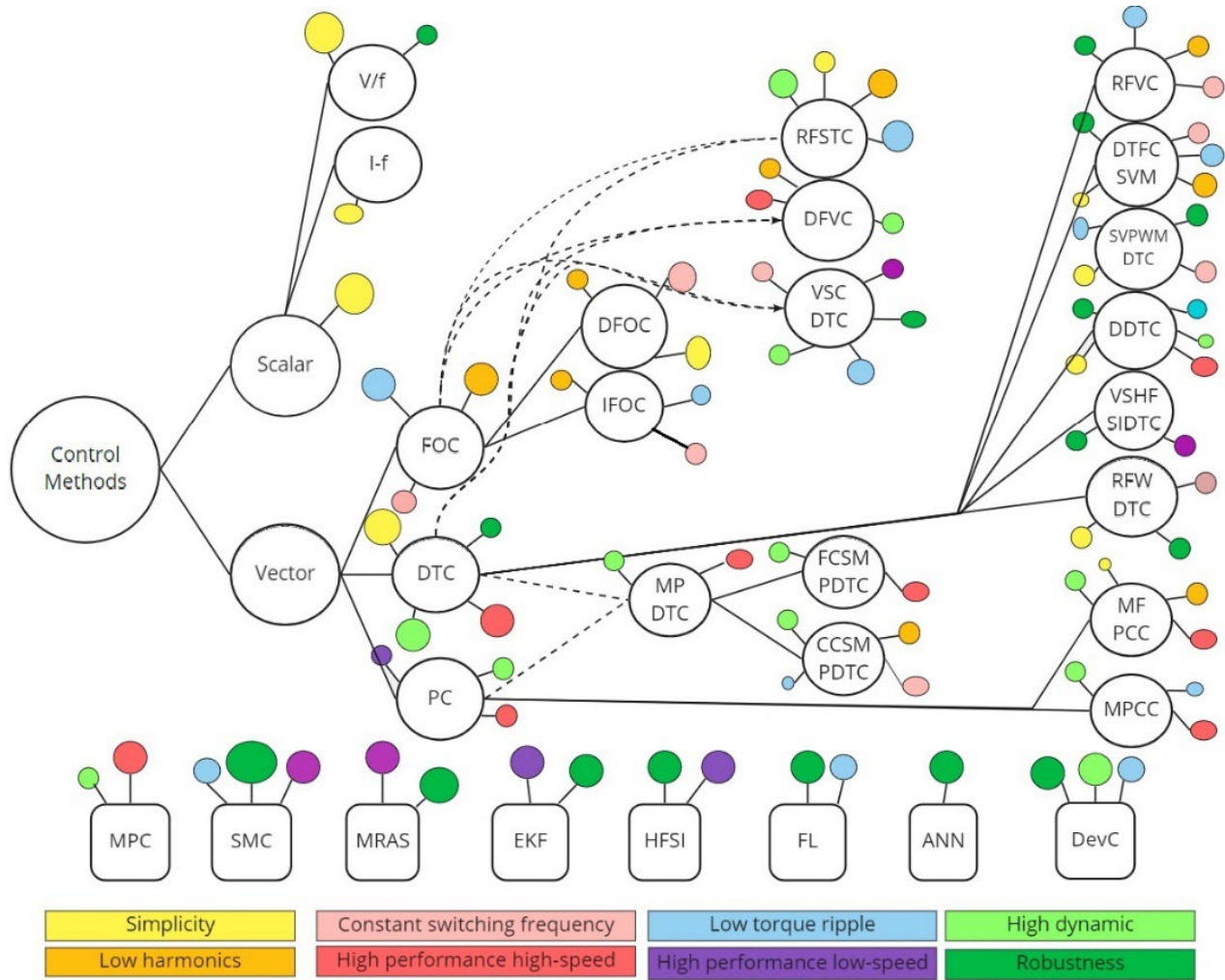


Figure 2-1: Motor control methods classification [Paper 1].

2.3 Section summary

This section shortly surveyed the SynRMs as well as the conventional motors background and the design developments. The study showed a striking development of SynRM and a potential dominancy of these motors against IMs in pump and fan applications. Then, a comprehensive study was carried out to investigate the implemented control algorithms for the sake of motor control. The basic algorithms were deeply studied and described. A comparison of the basic control algorithms concerning their structure was carried out. The study showed a research gap in the robustness increment and the torque ripple suppression in vector control algorithms. The call for high-efficiency SynRM drives was recognized as a critical topic in the field, which requires a deeper study in every stage of the life-cycle, especially in the usage phase. The trends in the motor control studies were studied, and the improvements in the control algorithms were scrutinized. Finally, the section presented a novel approach to the motor control algorithms classification considering the improvements in the conventional control methods and the application of the novel control theories. Moreover, the classification considers the features of each algorithm, which can come in handy for the researchers and the industries to opt for a proper control algorithm based on the requirements that their application demands.

3 Efficiency map study of the studied motor-drive systems

In this section, a SynRM was studied in the lab along with an IM, and a Permanent Magnet (PM) assisted SynRM in the same power range and frame size. For this purpose, a double-layered sinusoidally distributed windings stator with a frame size of 132 M and a power of 10.5 kW was designed in the lab. Figure 3-1 shows the rotors of the studied motors. The sketch of the designed SynRMs is illustrated in Figure 3-2. This figure presents the schematic details about the stator and the rotor structure.



Figure 3-1: Rotors of the tested electrical motor; from the left: industrial IM, the designed SynRM and PMSynRM, respectively.

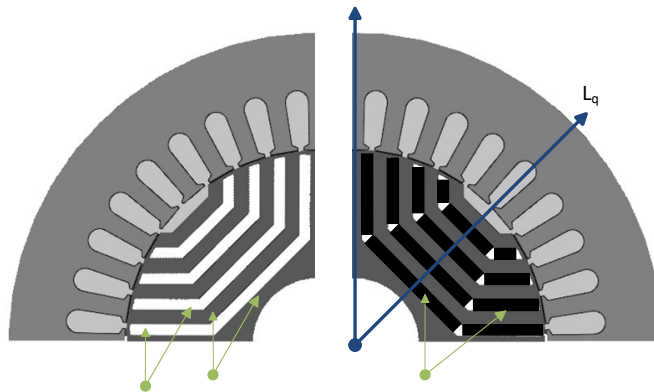


Figure 3-2: The sketch of SynRM (left side) and PMSynRM (right side) stator and rotor structure.

The rotors were assembled to the designed stator and tested under the same condition. By this, a fair test condition was provided to investigate the performance of the motors with the same stator and test condition. The tests were designed in two different categories. Firstly, the motors were tested under no load and constant load conditions with grid-fed and inverter-fed drives. This set of tests was designed to study the harmonic behaviour of the whole motor drive systems in the no-load, loaded, grid-fed, and inverter-fed conditions. Secondly, the motors were tested under ramp load with variable speed conditions. This set of tests was designed to study the efficiency of the whole drive system, including the motors in different speed and torque regions. Figure 3-3 shows the test bench that was designed to study the motor-drive systems. The details of the setup are presented in [Paper II].

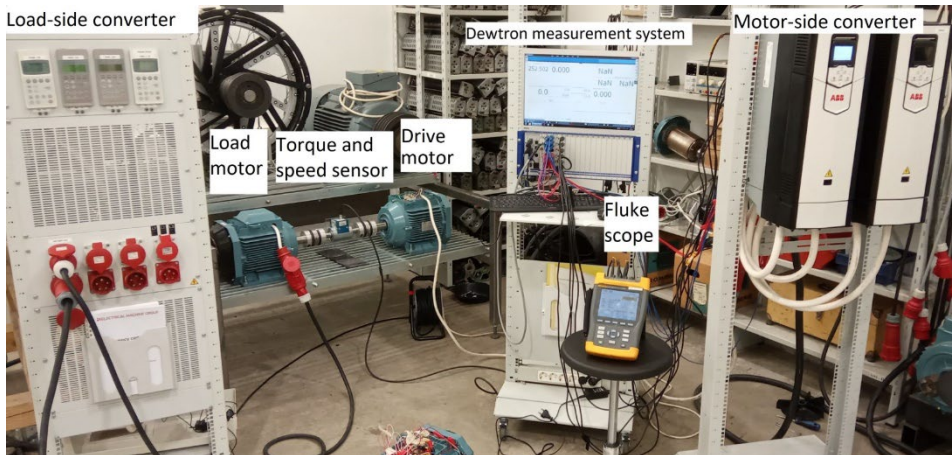


Figure 3-3: The experimental setup for performance analysis of SynRMs.

To investigate the efficiencies of the motor-drive systems in different speed and torque conditions, a set of tests were designed and conducted in the lab. Accordingly, the test motors were driven at a certain constant speed starting from 200 rpm to 1800 rpm with the steps of 200 rpm. Then, at each speed step, a ramp load starting from 0 Nm to 60 Nm was imposed on the motors by the loading motor. In this study, to draw the efficiency maps of the different parts of the system in different speed and torque ranges, an interpolation scheme was used to estimate the efficiency of the non-measured speeds.

The inputs of the frequency converter, including the currents and voltages, were measured by the current transducers and the data acquisition setup, respectively. The results were registered, and the input power of the system was calculated as $P_{VSD_{input}} = 3 * V * I * \cos\theta$, where, $P_{VSD_{input}}$ denotes the input power of the frequency converter, V , and I indicate the phase voltage and currents, and θ represents the angle between the voltage and current or the power factor. It is worth mentioning that the input power of the frequency converter was the grid power output power. The output voltage and current of the frequency converter were also measured and registered. With the same definition of power, the output power of the frequency converter was calculated. It should be noted that the output power of the frequency converter was fed to the motor, meaning that it was equal to motor input power ($P_{motor_{input}}$). Having the input and output powers of the converter, efficiency was calculated.

The mechanical output power of the motor ($P_{motor_{output}}$) was obtained by multiplying the out speed and torque of the motor. By division of the output mechanical power of the motor to the input electrical power of the motor, the efficiency of the motor was also calculated. The output data from the speed and torque of the test motors were obtained by the torque transducer and registered by the data acquisition setup.

To calculate the whole motor-drive systems' efficiency, the output power of the motor was divided into the input power of the frequency converter.

Figure 3-4 shows the Efficiency maps of the motors, VSDs, and the motor drive systems of the IM, SynRM, and PMSynRM.

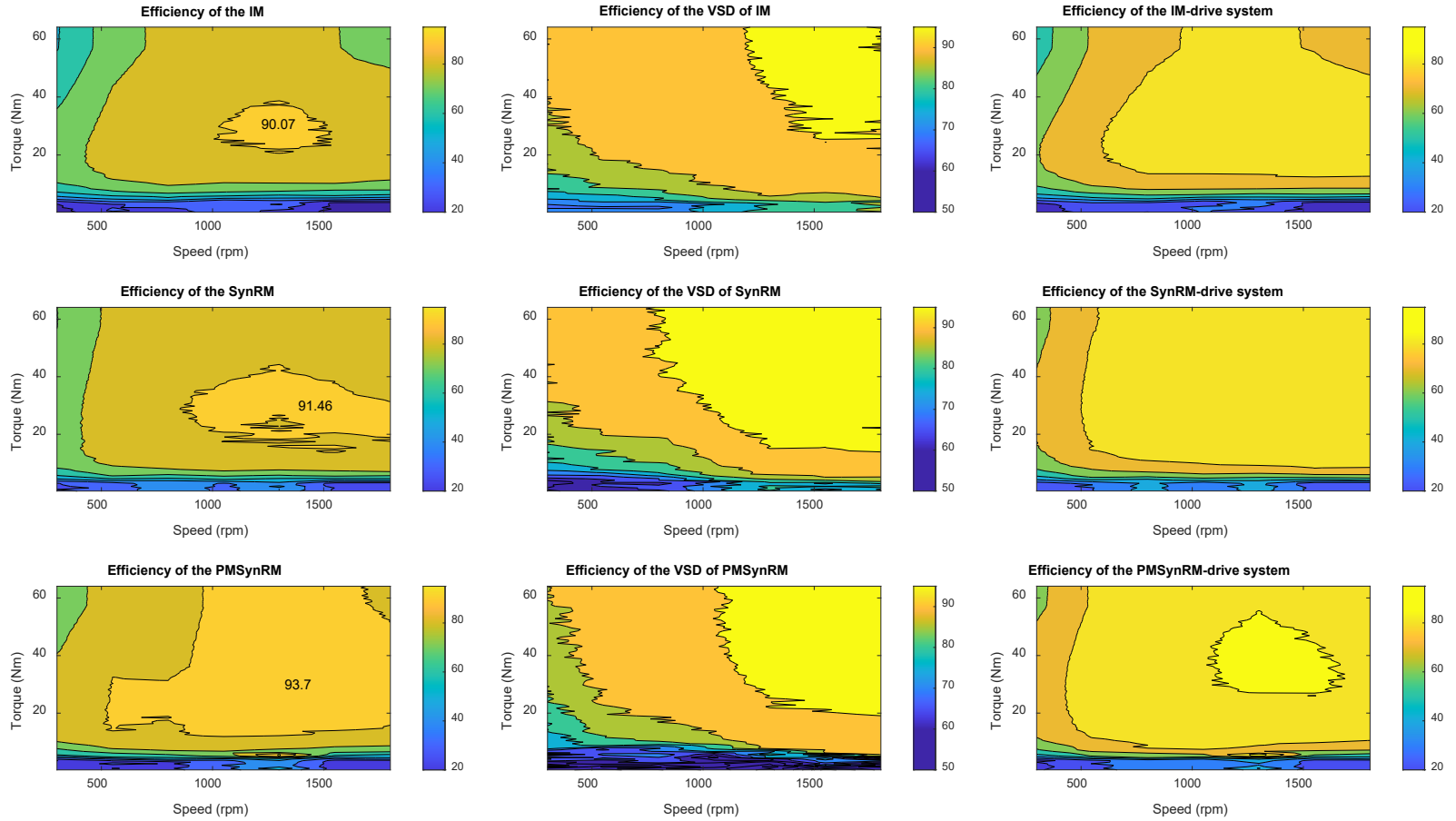


Figure 3-4: Efficiency maps of the motors, VSDs, and the motor drive systems of the IM, SynRM, and PMSynRM.

It can be seen from the figure that the efficiency of the motor at a lower speed is roughly independent of the load, and the motors show fairly low efficiency in this region. Similarly, regardless of the speed, the motors show far lower efficiency in the low torque region. In the nominal speed range and the partial load, the motors present their highest efficiency region. This is an important factor for the industries to consider choosing the motors regarding their highest efficiency region in all the applications. More specifically, in the constant speed regions, the highest efficiency of the motors should be considered to choose the motors.

The figure shows that the designed SynRM presented fairly higher efficiency than the industrial IM in all of the speed-torque regions of the motors. The highest efficiency for SynRM was calculated as 91.46 %, which was 1.39 % higher than IM with 90.07 % efficiency, and this is mostly due to the absence of iron losses in the rotor of the SynRM while the rotor of the IM operates with a higher temperature. It can be seen that the SynRM presented a wider range of very high efficiency in the nominal speed range and the partial load. Thanks to the ferrite PMs, the PMSynRM showed far higher efficiency than the SynRM, with maximum efficiency of 93.7 %. This is on account of the magnetic torque, which increases the torque concerning the input current (consequently the power) of the motor. As a result, for the same input power, the motor showed higher torque (output power), and the efficiency increased significantly. This resulted in higher efficiency in all the speed-torque regions. It is worth mentioning that despite the very high efficiency of the PMSynRM against SynRM (and IM), this motor is not an economical choice for the applications such as pumps and fans. It should be noted that the copper losses and iron losses in the stator, as well as the friction losses, were present in all the motors. On the other hand, the losses in the rotor are absent in SynRMs.

The frequency converters are highly efficient and do not attribute a large proportion of the losses in the system. However, the devices are not ideal, and some losses, including the switching and conducting losses in the switches and the losses in all the devices, lead to heat in the package. This heat should be dissipated by a fan which adds to the energy consumption of the system. With a brief look at the efficiency maps of the VSDs of motors, it can be seen that the frequency converter showed fairly higher efficiency in the operation of the SynRMs comparing the IM. This can be due to the fairly higher current in the IM for the same torque, which adds up to the conducting losses in the power electronic devices as well as the wires and boards in the package. It can be seen that the VSDs showed higher efficiency in the higher output power meaning high speeds and torque. This can be due to the presence of constant losses such as the switching losses and the fan in all the power range and the relatively higher power to loss ratio in the high output power condition. Consequently, the frequency converter showed higher efficiency in the higher power ranges.

The total efficiency maps of the motor-drive systems are presented in the figure. The figures show that the total efficiency maps of the systems resemble the efficiency maps of the motor. This indicates a significant proportion of the power consumption as well as the losses of the motors in the system. Akin to the efficiency maps of the motors, it can be seen that the motor drive systems showed high efficiency in the high output power range. The IM-drive showed a less efficient drive system compared to the designed SynRM, which can be interpreted as less power losses and less costs in the production phase. In a broader view, the SynRM-drive system is more environmentally friendly in the sense of less electricity consumption which can lead to high CO₂ emissions.

The wider high-efficiency region of the SynRM is also a factor that can be attractive for variable speed applications. The PMSynRM-drive system showed the highest efficiency, which was expectable based on the high efficiency of the PMSynRM in all the power ranges.

3.1 Section summary

The SynRM was assembled along with the IM and PMSynRM in an identical stator to study the efficiency of the motors in experiments. The efficiency maps were chosen as a reliable tool for efficiency analysis of the motors in a wide range of speed and torque. The efficiency of the motors in line with the drivers was studied, and the results showed that the total systems efficiency map resembled the motor efficiency indicating the significance of the motor efficiency on the motor drive systems. The PMSynRM showed a higher efficiency compared to the other technologies. However, it should be noted that due to PMs, this motor has a higher cost compared to its SynRM counterpart. The SynRM presented a more efficient motor comparing the IM, proving the claims for a lower temperature in the rotor and less losses.

4 Modelling, parameter identification, and vector control of studied synchronous reluctance machine

This section is based on publication [Paper III], [Paper IV], [Paper V], [Paper VI], [Paper VII], and [Paper VIII]. For control, this chapter presents different approaches for SynRM modelling and studies different approaches for parameter identification of the motor-drive systems. Then, the chapter investigates the classical vector control method and focuses on the improvement of different aspects of control, including efficiency, robustness, and torque ripples.

4.1 Synchronous reluctance machine modelling

As the name indicates, the operation of the SynRM is based on the reluctance torque. In this sense, the changing magnetic reluctance (magnetic resistance) is the source of torque. In this motor, the stator produces magnetic flux, which flows into the lowest magnetic resistance in the rotor. With the assumption of the unalignment of the rotor with the flux, the produced magnetic flux by the stator will tend to flow into the lowest magnetic resistance. This leads to the production of the reluctance torque in the motor. As a result, reluctance torque spins the rotor in a certain direction to achieve the lowest magnetic resistance. This concept of variable reluctance is also known as saliency, which generates the MMF in the SynRM and rotates the rotor. The alignment of the magnetic flux with the lowest magnetic reluctance in the rotor is also known as synchronization, where the synchronous term in the name suggests. In this section, different models of the SynRMs which are applied for control are discussed.

For the sake of control, the SynRMs are commonly modeled in the rotor reference frame. The dynamic equations of the motor known as Park's equations in the rotor reference frame are presented in this section. The Park's equations for direct and quadrature (d, q)-axes fluxes are as below

$$\phi_d = L_d i_d + \phi_m, \phi_q = L_q i_q, \quad 4.1$$

$$\phi_s = \phi_d + \phi_q, \quad 4.2$$

where $\phi_{d,q}$ denote the fluxes in d and q-axes, respectively and ϕ_s is the total stator flux. $L_{d,q}$ imply the inductances in d and q-axes, which are different in value due to the anisotropic design. $i_{d,q}$ denote the currents in d and q-axes in synchronous reference frame resulting from the transformation of the three-phase currents by Park's transform. ϕ_m denotes the magnetic flux, which is resulted from the PMs in the rotor for PMSynRM. It should be noted that the magnetic flux in the d-axis distinguishes the PMSynRM from its reluctance counterpart, where the equations for SynRM solely contain the fluxes coming from the saliency of the motor. Hence, the magnetic flux is indicated by different colours, meaning that it is absent in SynRM equations. Since the laminations of the rotors were identical, the fluxes only differ from each other in the presence of magnetic flux in their flux equations.

The voltage equations in the synchronous reference frame are obtained as:

$$V_d = R_s i_d + \frac{d\phi_d}{dt} - \omega_e L_q i_q, \quad 4.3$$

$$V_q = R_s i_q + \frac{d\phi_q}{dt} + \omega_e L_d i_d + \omega_e \phi_m, \quad 4.4$$

where $V_{d,q}$ demote the voltages in the d and q-axes, respectively. R_s implies to the stator resistance and ω_e is the electrical speed of the motors in rad/s where $\omega_e = \frac{p}{2} \omega_m$ and ω_m is the mechanical speed and p is the number of pole pairs. It is worth mentioning that the d-axis voltage in PMSynRM is independent of magnetic flux, where the magnetic flux is present in the q-axis voltage equation. Besides, the magnetic flux has no effect on the voltage in the standstill condition. At a standstill, the voltages in the d-axis for the motors are independent of the q-axis current. This is true for the voltage in the q-axis, where it is only dependent on the q-axis current.

The reluctance torque, as well as the power factor, are functions of the saliency ratio. The saliency ratio can be developed from the equation below

$$\zeta = \frac{L_d}{L_q}, \quad 4.5$$

where ζ is the saliency ratio.

The power factor equation is defined as below

$$\cos(\varphi) = \sin(\delta), \varphi = 90 - \delta, \quad 4.6$$

$$PF = \frac{\zeta-1}{\zeta+1}, \quad 4.7$$

where φ is the angle between voltage and current vectors in the synchronous reference frame. This phase lag results in less power factor in the motor, which is desired to be minimized. δ represents the flux and current angle which is known as torque angle. This factor is desired to be maximized to increase the torque and the power factor

$$T = \frac{3}{2} p |\overline{\phi_{dq}}| |\overline{i_{dq}}| \sin(\delta), \quad 4.8$$

$$T = \frac{3}{2} p (L_d - L_q) i_d i_q + \phi_m i_q. \quad 4.9$$

Both of the motors benefit from the reluctance torque coming from the saliency of the rotor. It should be noted the magnetic torque is only present in the torque equation for PMSynRM, which comes from the multiplication of the magnetic flux to the q-axis current.

The vector diagram of the motors is presented in Figure 4-1. It can be seen that adding ferrite magnets to the rotor resulted in a bigger torque angle and, as a result, the improvement of the power factor.

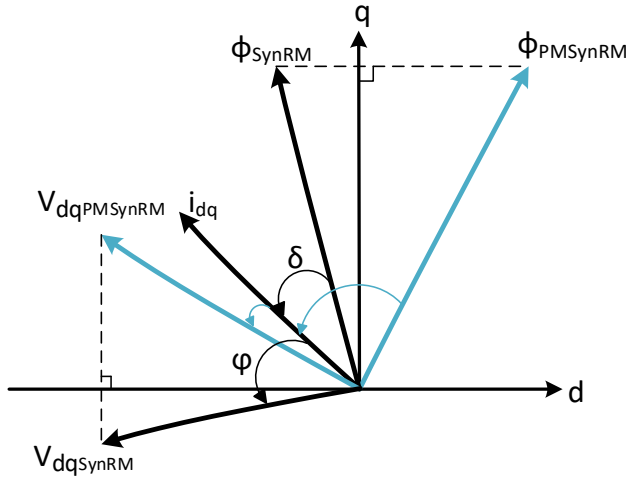


Figure 4-1: The SynRMs vector diagram.

Figure 4-2 presents the d-q equivalent circuit of the motors where the fluxes in the d-axis are different, resulting in different voltages in the q-axis.

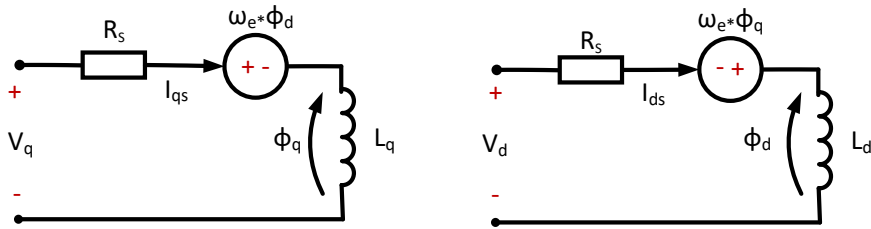


Figure 4-2: The d-q equivalent circuit of SynRMs.

4.2 Parameters identification

The parameters of the motors are of critical importance for acquiring a more precise model of the motors. Moreover, the parameters of the motors are widely employed to define different control parameters not only in model-based control methods but also in the error-driven control approaches. In this study, two main approaches are presented to obtain the motor parameters. Firstly, the motor parameters were measured by the measurement devices in two isolated tests. Then, an approach is proposed using a microprocessor in a closed-loop to identify the motor parameters along with the inverter and cables.

4.2.1 Measurements with LCR meters

The first method that was employed in this study was to simply use an LCR meter to measure the resistance of the phases. This method was initially used to measure the motor parameters for the motor simulation. In this test, the line-to-line resistances were measured, as shown in Figure 4-3. The relation of the measured resistance and the phase resistance was as follows

$$R_s = R_{ABavg}/2 . \quad 4.10$$

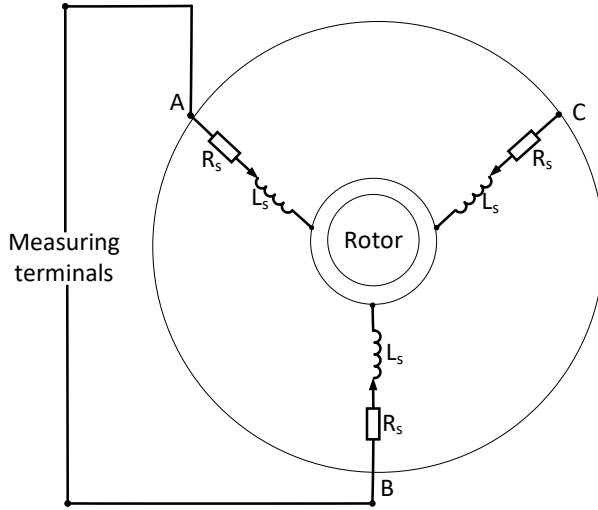


Figure 4-3: Measurement circuit for parameters measurements using LCR meters.

The next step was to measure the motor inductances in the d- and q-axes, which were employed in the simulation of the motor, as well as the control algorithm. To measure the inductances with this setup, the LCR meter was set to inductance measurement, and the measurements were carried out. The inductances in the SynRM are dependent on the rotor angle as follows

$$L(\theta) = \begin{bmatrix} L_s & L_{ms} & L_{ms} \\ L_{ms} & L_s & L_{ms} \\ L_{ms} & L_{ms} & L_s \end{bmatrix} + L_m \begin{bmatrix} \cos(2P\theta) & \cos(2P\theta - 2\pi/3) & \cos(2P\theta + 2\pi/3) \\ \cos(2P\theta - 2\pi/3) & \cos(2P\theta + 2\pi/3) & \cos(2P\theta) \\ \cos(2P\theta + 2\pi/3) & \cos(2P\theta) & \cos(2P\theta - 2\pi/3) \end{bmatrix}, \quad 4.11$$

where, L_s is the self-inductance of the stator, and L_{ms} is the mutual inductance of the stator. These inductances are independent of the position of the rotor. Apart from these constant inductances, the saliency of the motor results in variable inductance, which is a function of L_m (stator inductance) and P (number of pole pairs).

With the transformation of the SynRM parameters to the synchronous reference frame using Park transform, the inductances in this axis can be obtained from

$$L_d = L_s - L_{ms} + 1.5L_m, \quad 4.12$$

$$L_q = L_s - L_{ms} - 1.5L_m. \quad 4.13$$

Measuring the inductances according to the circuit demonstrated in Figure 4-4, the line to line inductance can be expressed as:

$$L_{AB} = 2L_s - 2L_{ms} - 3L_m \cos(2P\theta - 2\pi/3). \quad 4.14$$

The inductance of the motor in the synchronous reference frame can be derived by applying 4.14 to 4.12 and 4.13 as

$$L_d = L_{AB \max} / 2, \quad 4.15$$

$$L_q = L_{AB\ min}/2, \quad 4.16$$

where $L_{AB\ max}$ and $L_{AB\ min}$ are the maximum and minimum inductances of the AB terminals of the motor, measured by the LCR meter, respectively. According to equations 2.15 and 2.16, the inductances in the synchronous reference frame were acquired by measuring the maximum and minimum line to line inductances while rotating the rotor.

4.2.2 Measurements with DC power supply and current transducer (DC decay test)

In this test, a more sophisticated test design was proposed to measure the motor inductances in different axes in the synchronous reference frame. The motor terminals were connected according to Figure 4-4. The test required a precise determination of phase a. For this purpose, a DC voltage was applied to the terminals to align the motor to phase A. Then, the motor was locked in this position. With the assumption of the locked rotor, referring to equation 4.3, the effect of the flux linkage in the voltage was eliminated. Simplifying this equation, with the application of a step voltage to the terminals of the test circuit and profile of the current, the d-axis current was obtained as follows

$$i = \frac{V}{R_s} (1 - e^{-\frac{t}{\tau}}), \quad 4.17$$

where, $\tau = L/R_s$ is the time constant of the circuit. In this test, the q-axis inductance was measured with the same method considering the voltage equation for in the q-axis and locking the rotor in this axis. It should be noted that this method could heat and damage the motor, which was resulted from a long-term DC test and exposure to the high temperature. This term is more valid when obtaining a wide range of inductance values that were objected in the current higher than the nominal current.

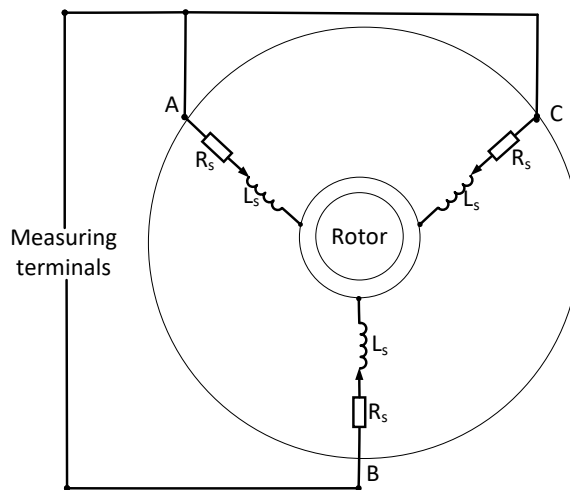


Figure 4-4: Measurement circuit for DC decay test.

4.2.3 The whole system parameters identification through the controller with the utilization of the inverter

The proposed methods for the parameters' identification were limited to the motor parameters. Apart from the isolated test without considerations of the inverter and the cables, the proposed methods could not accurately obtain the parameters due to the

wide uncertainties in the measurement devices and the approximations in the measurement. Moreover, the motor parameters severely change in different current ranges. Hence, a comprehensive method is required to calculate the system parameters with the processor, which considers the nonlinearities of the switches in the inverter and the cables as well as the variable parameters of the motor in different currents.

This study implements a closed-loop method through a processor to obtain the system parameters with the utilization of a three-phase inverter. Hence, the parameters of all the systems in the loop, including the motor, inverter, and wires, were identified.

By converting the real-time variables to the complex variable, equations 4.3, and 4.4 can be simplified. Also, by testing the motor at a standstill, the SynRM voltage equations can be rewritten in Laplace transform domain as

$$V_d(s) = (R_s + sL_d)i_d(s), \quad 4.18$$

$$V_q(s) = (R_s + sL_q)i_q(s). \quad 4.19$$

These equations provide a relation between the voltages and currents of SynRM in the synchronous reference frame. To benefit from these equations for parameters' identification purposes, the motor current equations were transformed to the synchronous reference frame using Park's transform. Then, a proper set of references in d, and q-axes were applied to the system to remain the motor in standstill status. The current errors were regulated by particular PI controllers to generate the command voltages in the synchronous reference frame. The generated voltages were transformed to the stationary reference frame using inverse Park's transform and applied to the motor through the inverter. Figure 4-5 shows the block diagram of the implemented algorithm to measure the motor parameters through the microprocessor.

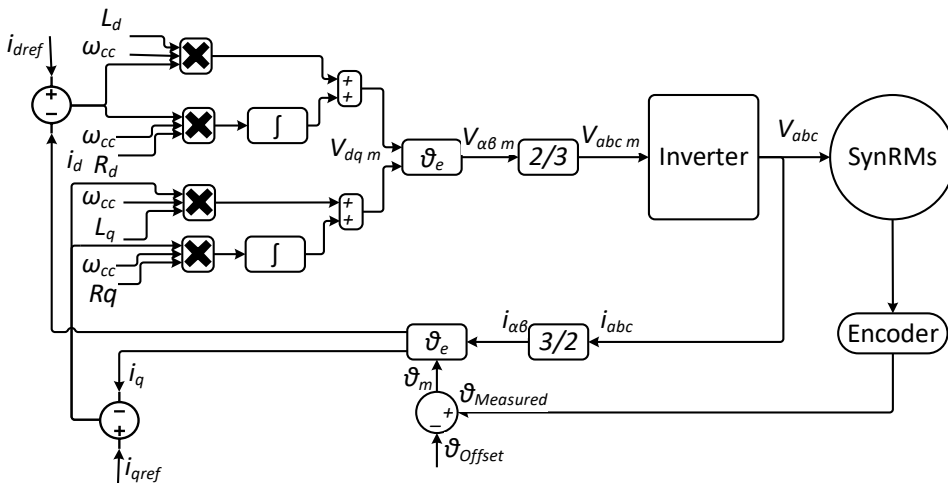


Figure 4-5: Parameter identification algorithm.

The reference voltages, which were generated by the algorithm as the output of the controller, were applied to the motor terminal with the application of the inverter and through wires. Hence, there was a voltage drop on the reference voltages resulting from the switches in the inverter and the connecting wires. The relation between the reference voltages and the terminal voltages on the motor can be represented as

$$V_{dm}(s) = V_d(s) + R_{ds}i_d(s), \quad 4.20$$

$$V_{qm}(s) = V_q(s) + R_{qs}i_q(s), \quad 4.21$$

where the R_{ds} and R_{qs} are the resulting resistances of the wires and the switches in the d, and q-axes, respectively. $V_{d,qm}$ are the terminal voltages of the motor and the $V_{d,q}$ are the command voltages in the synchronous reference frame. $i_{d,q}$ are the measured current in the d, and q-axes, respectively.

The reference voltages in the synchronous reference frame can be calculated according to Figure 4-6 as follows

$$V_{dm}(s) = \frac{1}{s} (i_{dref}(s) - i_d(s)) * (R_d\omega_{cc} + sL_d\omega_{cc}), \quad 4.22$$

$$V_{qm}(s) = \frac{1}{s} (i_{qref}(s) - i_q(s)) * (R_q\omega_{cc} + sL_q\omega_{cc}), \quad 4.23$$

where the ω_{cc} is the bandwidth of the current controller. $R_{d,q}$ are the resistance and $L_{d,q}$ of the whole system in the d, and q-axes, respectively. For simplification, the constants can be defined as $K_{pd} = R_d\omega_{cc}$, $K_{pq} = R_q\omega_{cc}$, $K_{id} = L_d\omega_{cc}$, $K_{iq} = L_q\omega_{cc}$. These constants will be used in the control of SynRM in the next section.

By combining 4.20, and 4.21 with 4.22, and 4.23, the current equations can be obtained independently from voltage equations. Hence, the constant parameters can be easily obtained. The current equations can be written as

$$\frac{1}{s} (i_{dref}(s) - i_d(s)) * (K_{id} + sK_{pd}) = (R_s + sL_d)i_d(s) + R_{ds}i_d(s), \quad 4.24$$

$$\frac{1}{s} (i_{qref}(s) - i_q(s)) * (K_{iq} + sK_{pq}) = (R_s + sL_q)i_q(s) + R_{qs}i_q(s), \quad 4.25$$

hence,

$$i_{dref}(s) - i_d(s) = \frac{R_d + sL_d}{K_{id} + sK_{pd}} s i_d(s), \quad 4.26$$

$$i_{qref}(s) - i_q(s) = \frac{R_q + sL_q}{K_{iq} + sK_{pq}} s i_q(s), \quad 4.27$$

where $R_{d,q}$ and $L_{d,q}$ are the resistances and the inductances of the loop including all components, respectively.

To calculate the resultant resistance of the whole system by the proposed algorithm, a constant value was applied to the current reference in one of the axes, and a zero value was applied to the other axis. Employing (the last equation d) and applying $K_{id} = 0$, the relation between the reference current in the d-axis and the measured current can be rewritten as

$$\frac{i_d(s)}{i_{dref}(s)} = \frac{K_{pd}}{sL_d + R_d + K_{pd}}. \quad 4.28$$

A step function was applied to the d-axis current, and a zero value was applied to the q-axis current. Using (the top equation), one can calculate the d-axis current in the time domain as

$$i_d(t) = \frac{i_{dref}(t)K_{pd}}{R_d + K_{pd}} \left(1 - e^{-\frac{R_d + K_{pd}}{L_d}t}\right). \quad 4.29$$

By the assumption of the too small inductance of the motor compared to the summation of the resistance and the proportional constant, the steady-state current in the d-axis can be derived as

$$i_d(t) = \frac{K_{pd}}{R_d + K_{pd}} i_{dref}(t). \quad 4.30$$

Finally, by simplifying the (top equation), the d-axis resistance of the whole system can be obtained as,

$$R_d = \frac{i_{dref}(t)}{i_d(t)} K_{pd} - K_{pd}. \quad 4.31$$

Similarly, the equation for the q-axis resistance can be obtained as

$$R_q = \frac{i_{qref}(t)}{i_q(t)} K_{pq} - K_{pq}. \quad 4.32$$

By exploiting equation 4.32 and measuring the current from the motor, and transforming it to the synchronous reference frame, the resistances in both axes were measured. It is to note that the K_{pd} was chosen an arbitrary value as large as the measured current was close to reference current in the steady-state.

To measure the inductance of the whole system in different current ranges, the equations (deviation equation) can be rewritten by expanding the constant value as follows

$$\frac{i_d(s)}{i_{dref}(s)} = \frac{\omega_{cc}(R_d + sL_d)}{L_d s^2 + (\omega_{cc}L_d + R_d)s + R_d\omega_{cc}}. \quad 4.33$$

Equation 4.33 is a second-degree function of the reference and measured currents in the Laplace transformed domain. By applying a step function in d-axis reference and zero value in q-axis and by applying $K_{id} = R_d\omega_{cc}$ for integral constant, the transient state current equation in the d-axis can be obtained as

$$i_d(t) = i_{dref}(t) + k_1 e^{-\delta t} i_{dref}(t) + k_2 e^{-\gamma t} i_{dref}(t), \quad 4.34$$

where

$$\begin{aligned} k_1 &= \frac{\omega_{cc}}{L_d} \frac{1}{\gamma - \delta} \left(L_d - \frac{R_d}{\delta} \right), \\ k_2 &= \frac{\omega_{cc}}{L_d} \frac{1}{\gamma - \delta} \left(\frac{R_d}{\gamma} - L_d \right), \\ \delta &= \frac{(\omega_{cc}L_d + R_d) - \sqrt{(\omega_{cc}L_d + R_d)^2 - 4L_d\omega_{cc}R_d}}{2L_d}, \\ \gamma &= \frac{(\omega_{cc}L_d + R_d) + \sqrt{(\omega_{cc}L_d + R_d)^2 - 4L_d\omega_{cc}R_d}}{2L_d}. \end{aligned} \quad 4.35$$

An experimental setup was designed to measure the parameter of the systems in experiments. Figure 4-6 shows the block diagram of this setup, and Figure 4-7 shows the test bench. The design and implementation of this setup were presented in [Paper VI].

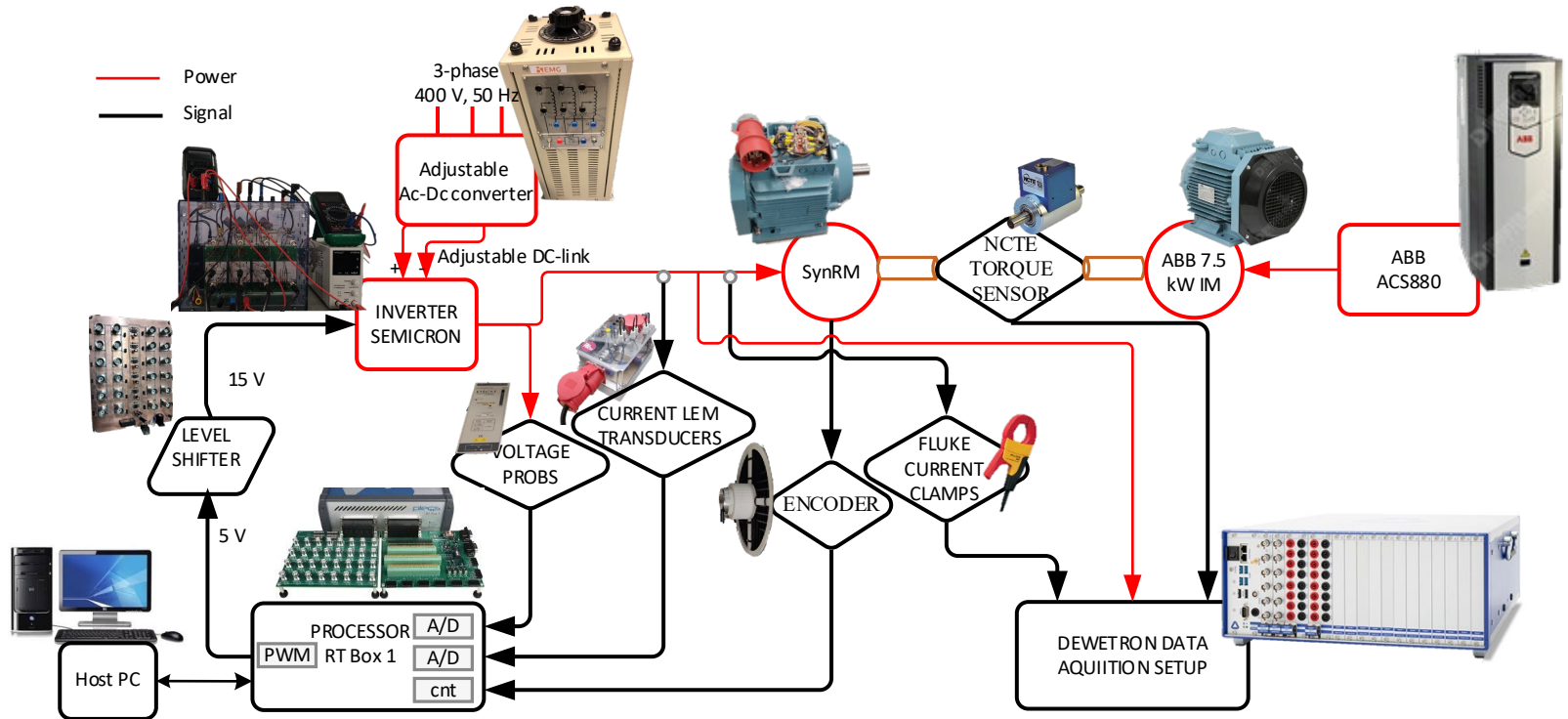


Figure 4-6: The block diagram of the experimental setup [Paper V].

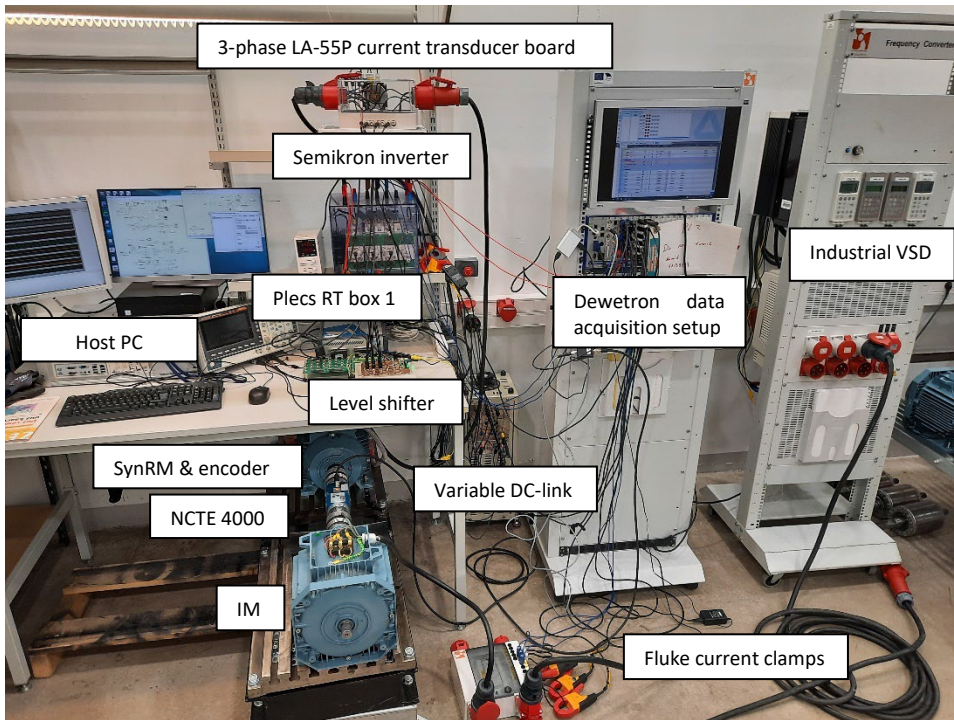


Figure 4-7: The experimental setup for the control of SynRM.

4.3 Field-oriented control of synchronous reluctance machine

This section aims to provide a base for the control of the SynRM. As discussed in [Paper I], SynRMs suffer from high torque ripples mainly coming from the slotting harmonics. This requires precise control of the currents of the motor. Apart from that, the recent attention on the SynRM is on account of the high efficiency of the motor, which makes the FOC a promising candidate for the sake of control. To implement FOC on the SynRM, firstly, the model of the motor was simulated in the Plecs platform. Then, the d-q model of the motor was controlled by conventional FOC in the simulation. For this purpose, the motor currents were transformed to the synchronous reference frame. Then, two PI current controllers were employed to control the currents in the synchronous reference frame. The regulated signals were transformed to the stationary reference frame to apply to the motor's model through the model of the inverter. To generate the q-axis current reference, an outer speed controller was employed, and for d-axis current, a constant value was used. Figure 4-8 shows the block diagram of the implemented FOC algorithm.

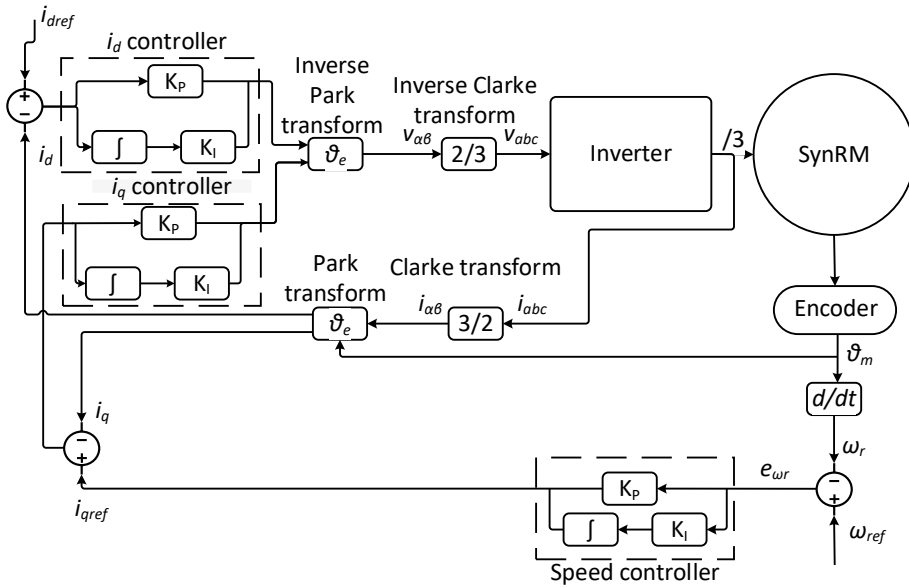


Figure 4-8: FOC of SynRM.

The results of the simulation are presented in Figure 4-9. This figure shows that by applying a ramp speed reference, the control algorithm applies increasing voltage in the q-axis. Hence, the q-axis current tends to increase to a certain value. According to 4.9, and considering a non-zero value of the d-axis current, the torque in the motor shaft raises to a non-zero value. Therefore, the rotor starts spinning, and the speed of the motor follows the reference speed. The results showed that the model of the motor was simulated properly, and the model was functioning. Besides, the performance of the control algorithm was proved in simulation. Hence, the ground was founded to apply new algorithms and methods in simulation, leading to faster and less cost in the test phase for the implementation of the new algorithm.

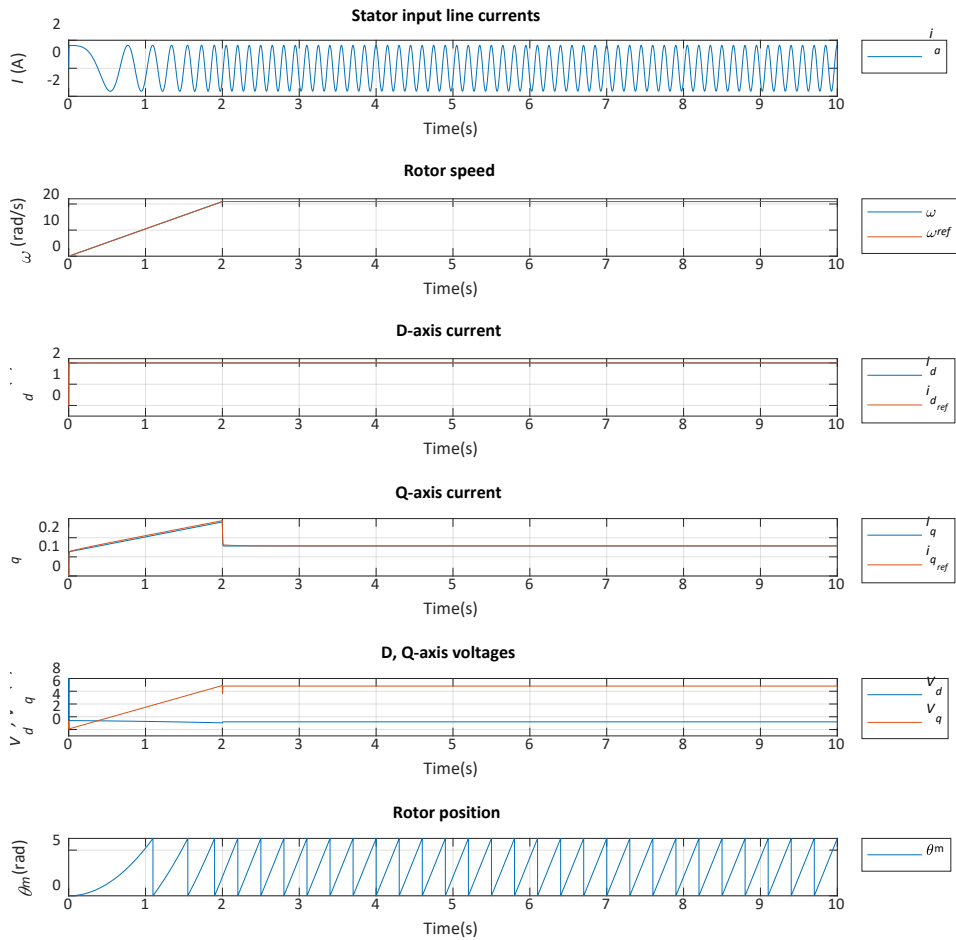


Figure 4-9: The simulation results of FOC of SynRM.

In this section, the results of the tests are organized in an identical sequence. In this sense, in the presented results, i_a shows the measured phase a current; ω is the measured speed, and the reference speed is presented by ω_{ref} ; i_d represents the direct axis current and the direct axis current reference is shown by i_{dref} ; the quadrature axis current is presented as i_q , and the quadrature axis current reference is shown by i_{qref} ; V_{dq} show the direct and quadrature axis voltages, respectively; θ_m is the mechanical angle of the rotor. The simulated algorithm was implemented in real-time in the experimental tests. For this purpose, rapid control prototyping was applied using Plecs RT Box 1. The design of the experimental test bench was described in detail in [Paper VI]. Figure 4-10 shows the experimental results of the FOC of the SynRM. The results show that the experimental results match the simulation results meaning that the simulation results are reliable. Hence, the base was founded for implementing the algorithms in simulations rather than real-time implementation. This resulted in less cost and time and more safe tests for the control algorithms implementations. Since the results were in good agreement, the simulation results for the rest of the tests were neglected, and only the experimental results will be presented.

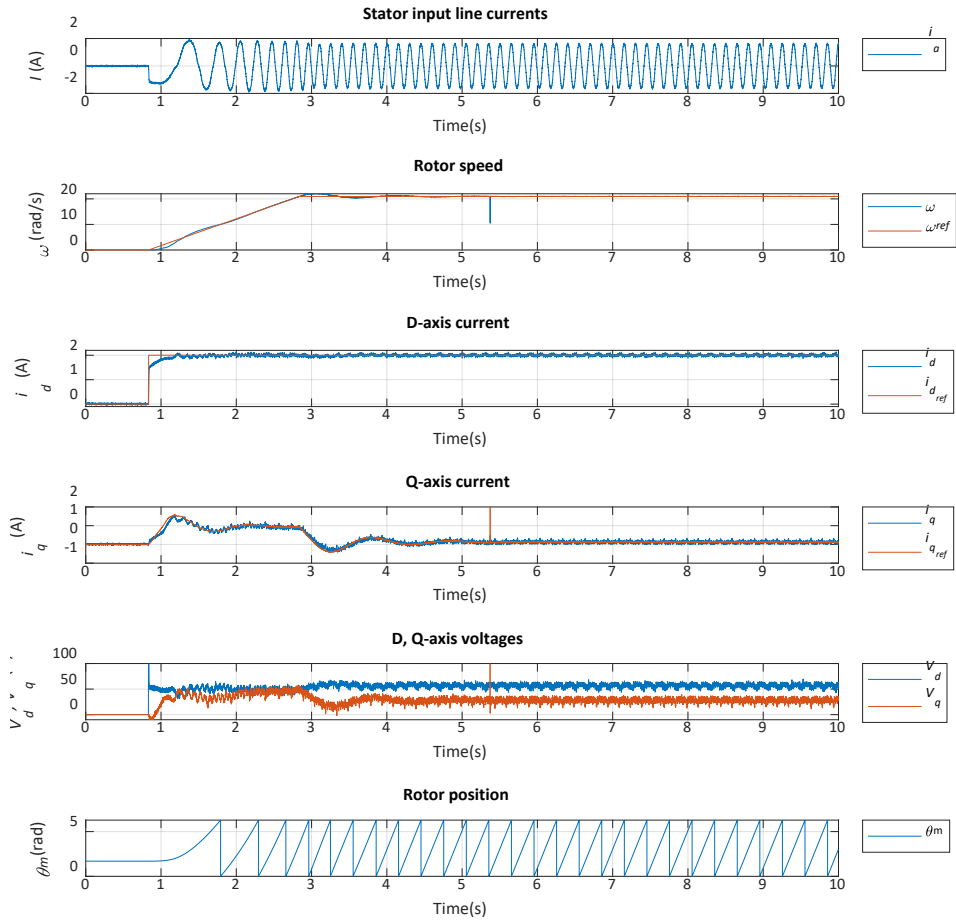


Figure 4-10: The experimental results of FOC of SynRM.

It should be noted that there were marginal differences between simulation and experimental results. One of the most important factors was the flux angle calculation. Since the FOC algorithm highly relies on the flux position information, this value is of paramount importance. The flux angle was calculated through the model's equations resulting in very precise information of the flux position. On the other hand, the flux position was obtained using the incremental encode. Section 4.2.3 described the adjustment of the encoder output to acquire precise information from the encoder. It should be noted from Figure 4-11 that there was a spike in the speed output resulting in a spike in the other parameter. This resulted from the noise in the encoder output. To address this issue, the differential output of the encoder channels was measured to remove the noise from the encoder output, and in the rest of the tests, the noise encoder output was avoided.

To analyse the performance of the implemented algorithm, a step load was applied and removed in steady-state to the motor. Figure 4-11 shows the experimental results for loading and unloading the motor in steady-state. The figure shows that by applying load in the time of 1.5 s, the algorithms increased the q-axis voltage and decreased the q-axis voltage. By this, the current in the q-axis saw a rapid change and the current in

d-axis roughly remained constant. According to equation 4.9, the increment in the q-axis current along with the constant parameters and d-axis current resulted in higher torque in the motor. Hence, initially, the motor speed dropped to a lower value than the reference speed. Then, with a good dynamic, the motor produced more torque and dominated the injected load resulting in the compensation of the higher load in the shaft. Therefore, the motor speed followed the reference speed, and the motor ran in the steady-state with the same speed but higher torque, meaning higher current in the motor windings. In the second phase of the test, after reaching the steady-state, the injected load was removed from the shaft in the time 6.7 s. Since the motor was under load, the produced torque was high, and by removing the load from the shaft, the motor started to speed up, resulting in higher speeds than the reference speed. Then, the control algorithm increased the d-axis voltage and decreased the q-axis voltage leading to a decrement in the q-axis current. Consequently, the torque in the motor dropped, and a good dynamic motor speed followed the reference speed. It should be noted that the current in the winding was smooth, meaning that the slotting harmonics in the phase current were removed by properly regulating the current in the motor.

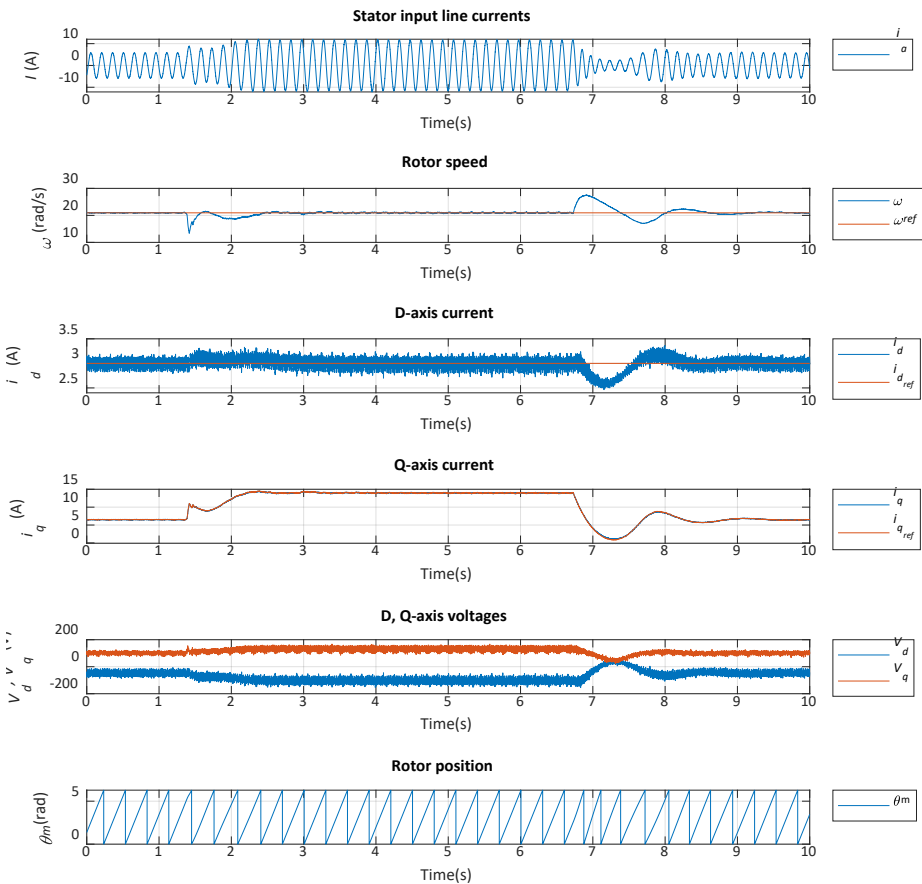


Figure 4-11: Loading test of FOC in the experimental setup.

One of the extreme conditions for the motor drive systems is the step response of the motor. When the motor speed reference sees a sudden change, the derivation of the speed tends to increase to an infinite value. According to the mechanical equation of the motor, the torque in the motor tends to be infinite, which is an extreme condition for the motor. This control algorithm should be designed in a very precise way to avoid this condition and control the motor speed. This test was conducted in the experiments, and the performance of the control was analysed. Figure 4-12 shows the step response of the control at different speeds. The figure shows that by applying step reference to the motor, the current in the q-axis saw a rapid raised as a result of a sudden increment in the q-axis voltage. Then, the motor speeded up to a speed higher than the reference speed. Then, the motor followed the reference speed, and the current in q-axis dropped to a lower value near zero due to the no-load condition of the test. The motor showed similar behaviour in the downward step speed change where the motor showed an undershoot in the q-axis voltage and current. Consequently, the motor speed saw an undershoot and recovered to the reference speed after a short period. It is worth mentioning that at the beginning of the control, the flux position was not recognized since the correct information of the flux depending on the index pulse position from the encoder. It can be seen from the rotor position graph that in the time 1 s, the index pulse was received, and the flux position was corrected. Then, the control was properly carried out with correct flux position information.

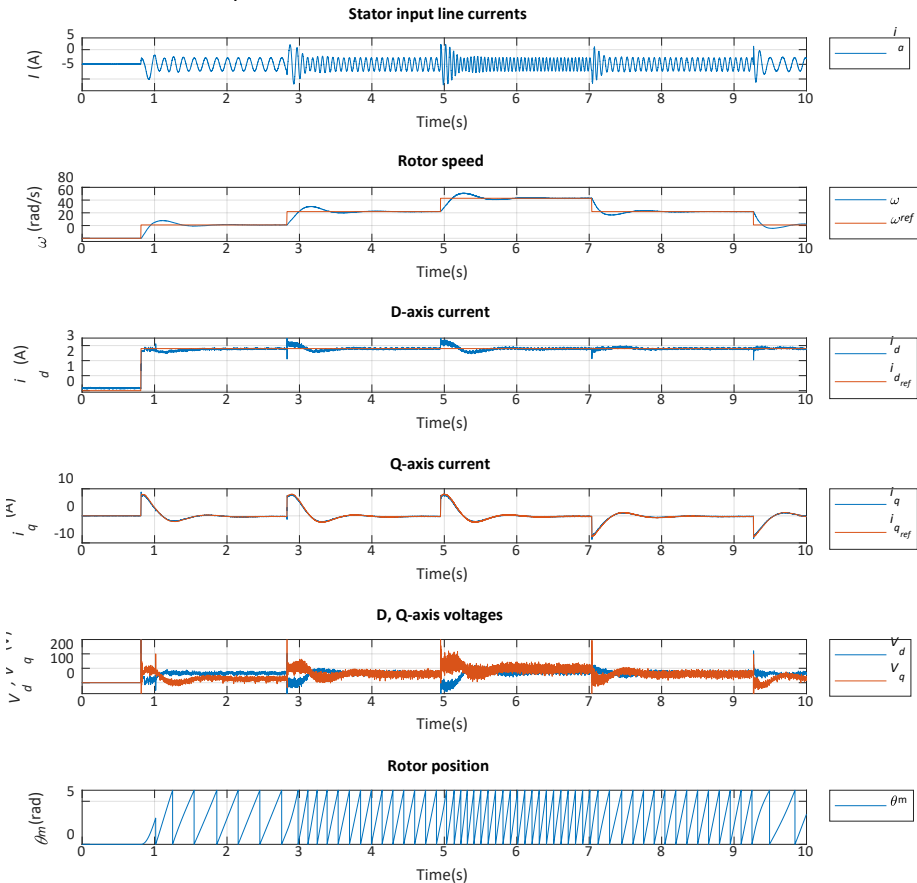


Figure 4-12: Speed step response of FOC in different speeds in the experimental setup.

4.4 Maximum torque per ampere control strategy for synchronous reluctance machine

One of the key specifications of the SynRM, especially in the speeds below base speed, is the high efficiency of the motor. One of the approaches to improve the efficiency of the motor in the base speed region is to reduce copper losses. For this purpose, it is essential to maximize the torque concerning the phase current of the motor. This algorithm is commonly known as the MTPA algorithm. The MTPA operation is essential for the efficient operation of the SynRM in the base speed region. Besides, the desirable performance of the motor can only be obtained by the MTPA operation of the motor.

To obtain the MTPA operation of SynRM, the torque equation of the motor is considered. The current of the motor should be controlled to achieve the optimum torque angle. As the FOC provides a decoupled control on the currents in the synchronous reference frame, it is convenient to generate the desired current references in this frame. For this purpose, the current angle in the d,q reference frame is defined as γ . The maximum of the torque equation can be obtained by calculating the derivative of equation 4.9. The torque equation 4.8 as a function of the current angle can be rewritten as follows.

$$i_d = I_s \sin\gamma \quad 4.36$$

$$i_q = I_s \cos\gamma \quad 4.37$$

$$T_e = \frac{3}{2}p(L_d - L_q)I_s^2 \sin\gamma \cos\gamma \quad 4.38$$

The derivative of the torque equation is as calculated as follows

$$\frac{dT_e}{d\gamma} = \frac{\frac{3}{2}p(L_d - L_q)}{2} \cdot 2 \cdot I_s^2 \cos 2\gamma \quad 4.39$$

In the maximum torque, the derivative of torque should be equal to zero. Hence, to achieve the optimum current angle in which the torque is maximum, the derivative is considered as zero.

$$\frac{dT_e}{d\gamma} = 0 \Rightarrow \cos 2\gamma = 0 \Rightarrow \cos 2\gamma = \cos 90^\circ \Rightarrow \gamma_{MTPA} = 45^\circ \quad 4.40$$

This current angle governs the optimum control of the current in the synchronous reference frame. To implement this algorithm in the FOC, the q-axis current reference should be obtained by the speed regulator, and then the angle between the d and q-axis current should be governed using equation 4.40.

It is to be said that this MTPA algorithm can provide the optimal performance of the motor under certain circumstances. For instance, in the condition of iron saturation, the rotor will show different behaviour where the inductances will vary from their initial values. In that case, different inductances should be considered in control. Apart from that, by increasing the current angle more than the MTPA value, the power factor will increase according to equation 4.6. Moreover, a big portion of the losses in the motor results from iron loss which needs a deeper study on MTPA operation, and a trade-off between copper loss (which is minimized by the MTPA algorithm) and iron loss should be carried out.

To evaluate the performance of the proposed method, the motor was driven by conventional FOC, and the control algorithm was switched on the MTPA algorithm.

Figure 4-13 the results of the test. The results show that by applying the MTPA algorithm, the currents in the d-q axes decreased significantly. The peak-to-peak current in classic FOC was 5.9 A which dropped by 2.8 A to 3.1 A with applying MTPA to the algorithm. As a consequence, for the same loading condition, the controller injects far less current in the stator winding resulting in less copper losses in the motor. It should be noted that by optimized control on the motor, better performance in terms of the currents, voltages, and speed was achieved when it comes to less ripples and distortions.

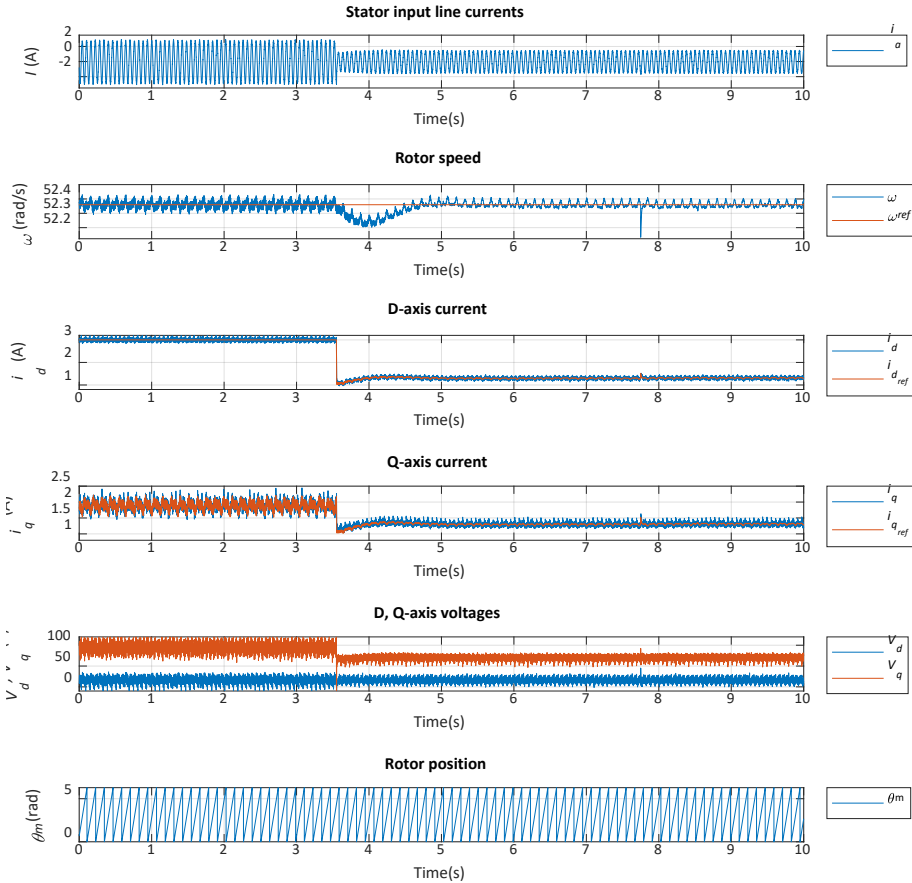


Figure 4-13: Applying the MTPA algorithm in the experimental setup.

To analyse the performance of the control in different scenarios, firstly, the speed direction change was tested in experiments. For this, the motor was driven in the opposite direction in a steady state. The reference speed was changed to a positive value employing a ramp reference. Figure 4-14 shows the results of this test. By changing the motor rotation direction, the voltage and current in the d-axis recovered to the initial steady-state value after a short transient period when the motor was changing the direction and speeding up to the constant reference speed. On the other hand, the control algorithm applied positive voltage and current values replacing them with negative values resulting in positive torque instead of the negative torque to the motor shaft. Consequently, the control algorithm could change the direction of the rotation of the motor and follow the reference speed. It is to note that the current frequency

dropped to zero for a period when the speed dropped to zero. This can be seen from the position of the motor where the encoder showed a constant speed value in the output of the shaft.

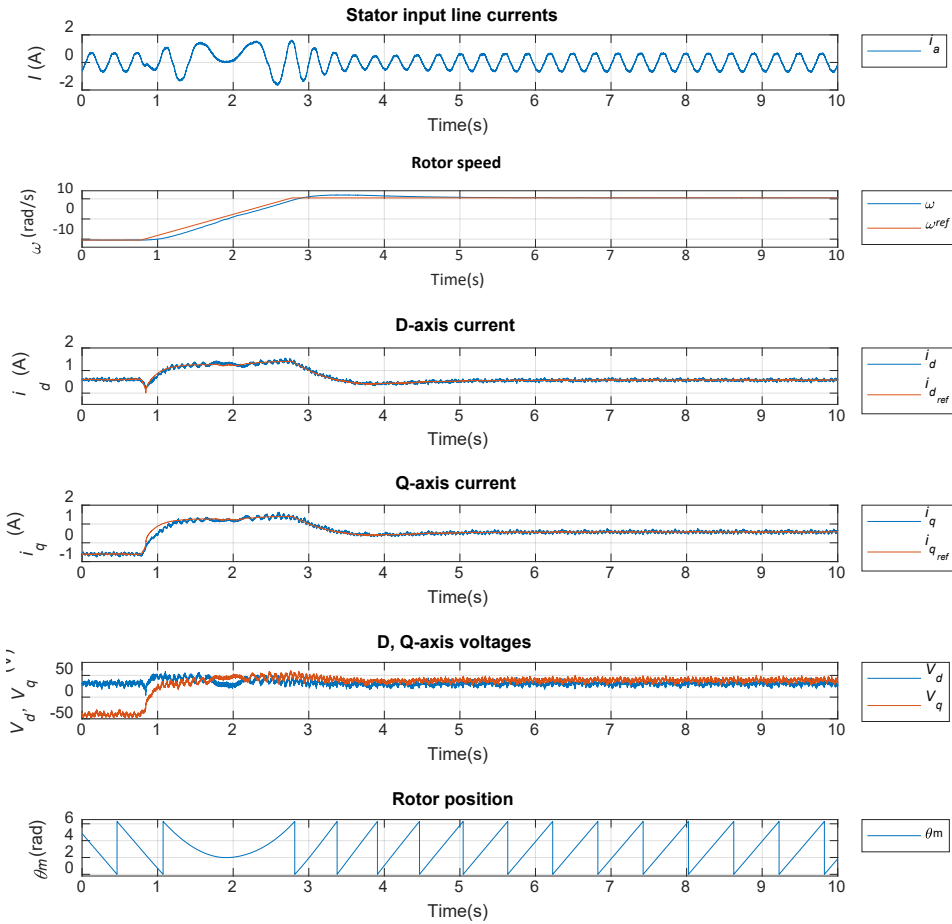


Figure 4-14: Speed direction change experimental results.

To analyse the performance of the implemented algorithm in step response condition, a set of step references to the speed reference in different speeds in upward and downward directions. Figure 4-15 shows the results of this test. The results show that the algorithm presents a desirable performance with a good dynamic following the reference speed in a short period with a marginal overshoot and undershoots. It is worth mentioning that the motor speed followed reference speed and all the applied speeds, including zero speed where a DC current was injected to keep the speed zero. Regarding the currents, it can be seen that the motor saw a sudden change in currents in the step time, and after the transient time, the motor speed followed the reference speed, and a steady-state was achieved. The stator current was smooth sinusoidal, and the slotting harmonic current was properly regulated.

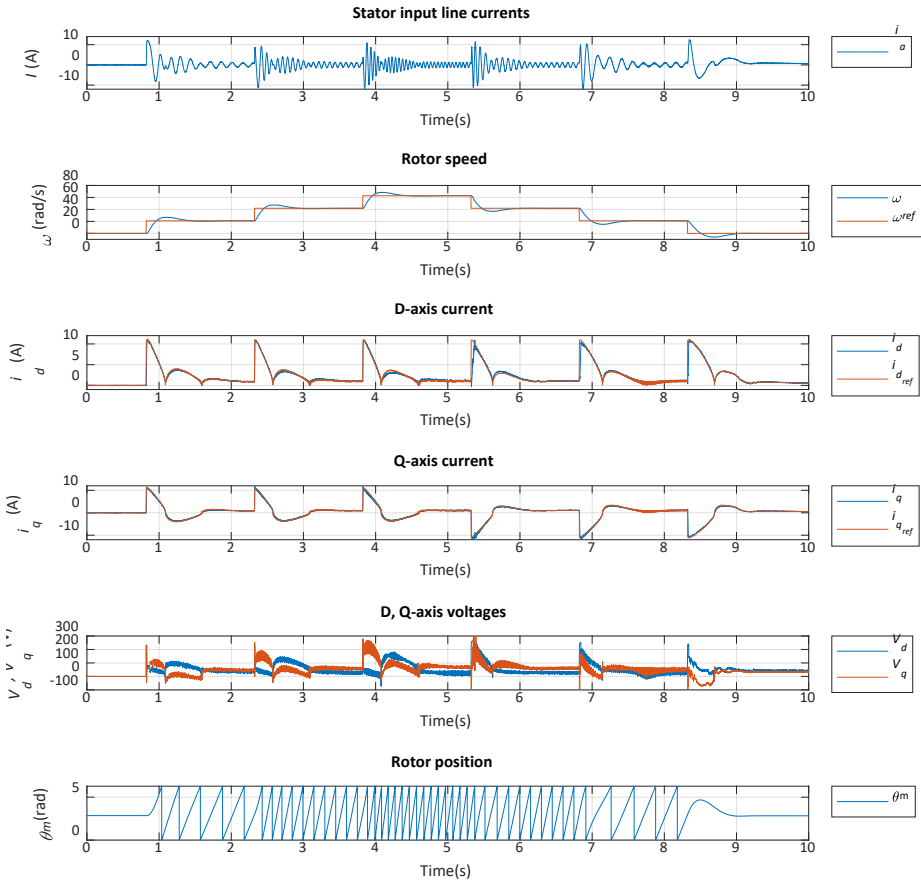


Figure 4-15: The speed step response of the experimental implemented MTPA algorithm of SynRM in different speeds, including zero speed .

4.5 Field-weakening operation of synchronous reluctance machine

As discussed in [Paper 1], in speeds higher than base speed, the speed induced voltage (back EMF) will dominate the motor input voltage. This disables the controller to inject current to the motor through the inverter, which avoids higher speed achievement in the motor shaft. Besides, the back EMF grows higher than the DC link, which can result in severe damages to the inverter resulting in lower reliability of the system. To address this issue, the controller drops the flux in the motor leading to less back EMF, and the speed can rise to even higher values.

In the control of the SynRM, there are limits for currents and voltages in d, q-axes, which should be considered. The limits are as follows

$$V_s^2_{max} = V_d^2 + V_q^2, \quad 4.41$$

$$I_s^2_{max} = i_d^2 + i_q^2, \quad 4.42$$

where V_s_{max} and I_s_{max} are the maximum phase current and voltage, respectively. $V_s_{max} = \frac{V_{dc}}{2}$ where V_{dc} is the DC-link voltage of the inverter.

Field-weakening operation point can be obtained by the voltage limit consideration of the motor at higher speeds than base speed. In this way, an optimum angle of the d and q-axes current should be governed in control to meet the voltage limits leading to lowering the flux in the motor to dominate the speed induced voltage by the input voltage of the motor. With the assumption of high speed, the resistance voltage drop can be neglected with a comparison with the speed induced voltage. Besides, the derivative term can be omitted, assuming the steady-state operation of the motor. Hence the voltage limit equations can be rewritten by a combination of 4.3 and 4.4

$$V_{s\max}^2 = (\omega_e L_q i_q)^2 + (\omega_e L_d i_d)^2. \quad 4.43$$

Considering the equation 2.37

$$V_{s\max}^2 = \omega^2 I_s^2 (L_q^2 \cos^2 \gamma + L_d^2 \sin^2 \gamma), \quad 4.44$$

$$V_{s\max}^2 = \omega^2 I_s^2 (L_q^2 (1 - \sin^2 \gamma) + L_d^2 \sin^2 \gamma), \quad 4.45$$

$$\sin^2 \gamma = \frac{V_{s\max}^2 - \omega_e^2 L_q^2 I_s^2}{\omega_e^2 I_s^2 (L_d^2 - L_q^2)}, \quad 4.46$$

$$\gamma = \sin^{-1} \sqrt{\frac{V_{s\max}^2 - \omega_e^2 L_q^2 I_s^2}{\omega_e^2 I_s^2 (L_d^2 - L_q^2)}}. \quad 4.47$$

Equation 4.47 provides the optimum angle of the currents in d, q-axes at speeds higher than base speed. Using this equation, the reference currents for d and q-axes will be generated. It should be noted that the algorithm for reference current generation differs from each other in different speed regions.

4.6 Robust vector control of synchronous reluctance machine employing an adaptive disturbance rejection controller

Novel digital control methods for electrical motors can be categorized into error-driven and model-based technologies. Although the modern-based motor control methods have proved high-performance methods, the trend towards vector control (which is an error-driven technology) has not yet been dominated by the model-based methods. The concept of transformation to the synchronous reference frame and simple application of the voltage vector to the motor through modulation blocks and, more importantly, the control on the current have increasingly raised high demand for this popular method in the industry. The vector control provides the possibility of the control of a three-phase AC motor with a DC motor control concept having a comparable performance of the motor.

On the other hand, FOC utilizes classical PI controllers leading to lower performance, especially in the transient state compared to the model-based methods. The PI controllers have been around for almost a century and have dominantly developed in various industries. These controllers proposed a simple control concept in the analog control era that later was widely employed in digital control systems. Despite the analog control systems, the newly designed microprocessors have enriched the digital control systems of opportunities that convince the industries to investigate more sophisticated controllers for their feedback control systems. The PI controller is inherently inadequate

for the raised demand for high efficiency, high dynamic, smooth transient profile, and robustness in the feedback control systems. The existing PI controllers mainly suffer from four general drawbacks. Firstly, they lack any control on the input setpoint resulting in a poor dynamic of the control, especially in step function inputs that result in a sudden jump. Secondly, the linear combination of the proportional and integration does not produce the optimal control law. Thirdly, the integral term in the controller can cause saturation resulting in reduced stability in the system. Finally, the controller does not facilitate the system with any noise tolerance tracking differentiator. In motor control systems, the main drawbacks of the PI controllers come from the lack of adaptability to the parameter mismatch or variation due to temperature change in the operation. Additionally, the recovery period of the PI controller is long, which degrades the performance of the control system in the presence of the load disturbance. There are numerous studies around online parameters identification methods in motor control methods to compensate for the variations of the parameters in the motor [92]. Nonetheless, the slow dynamic and low accuracy of PI controllers remain severe challenges. Besides, the parameters in the motor highly depend on each other, which requires complicated systems for online parameters estimation leading to a high computation burden on the control. Hence, many alternatives have been advised in the literature to replace the traditional PI controller, mainly to improve the robustness, rapidity, and accuracy of the control systems.

Among the modern error-driven controllers, adaptive disturbance rejection controller (ADRC) has proved an accurate and high dynamic controller that offers a high tolerance to uncertainties and disturbances in the system [93]. This sophisticated yet simple to use controller provides a nonlinear feedback control resulting in a precise control law generation. The other superiority of the ADRC against other controllers is the applied nonlinear differentiator on the setpoint, which generates a transient profile to avoid sudden jumps, especially in the step references. Last but not least, the ADRC estimates and then rejects the disturbances in the system using an extended system observer, leading to higher robustness of the systems.

In this study, the outer speed controller in the cascade control of the SynRM was substituted by a nonlinear controller based on a first-order ADRC. The controller was mainly designed to enrich the control with robustness against the load disturbances. To do so, the states of the controller were extended in one order through an observer to estimate not only the system state but also the disturbances. Hence, by imposing a load on the system, the observer estimates the disturbance, and an appropriate control law generation recovers the system state in a short time avoiding high overshoots and undershoots in the speed output of the system. Moreover, a non-linear differentiator was employed on the reference value resulting in a smooth speed output of the system, especially for the step reference values. Figure 4-16 shows the block diagram of the implemented non-linear controller for the speed control of the motor. In the rest of this chapter, the control method will be described in detail. Firstly, the transient profile generator will be discussed. Then, the extended state observer will be investigated to estimate the states, as well as the disturbances. And finally, the nonlinear system error feedback controller will be determined to generate the control law.

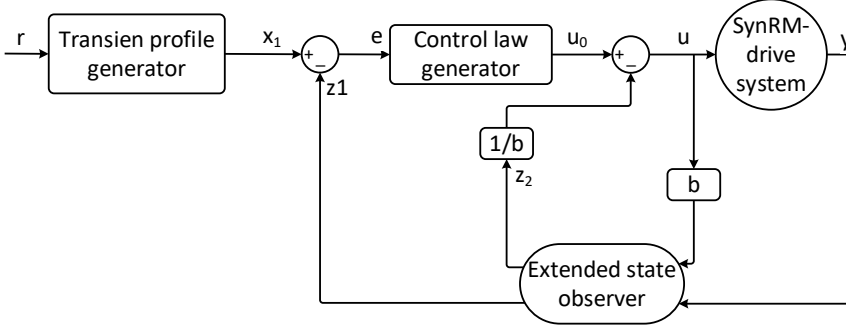


Figure 4-16: The block diagram of the ADRC of speed.

One of the main drawbacks of the PI controller as a speed controller is the lack of a nonlinear control on the reference value, meaning that the error signal is directly generated by comparing the reference and the instantaneous speed value. This issue causes a severe problem in the output speed of the motor. Especially, a step reference can severely cause sudden changes in the output with a dramatically high overshoot. Apart from the sudden changes in the reference speed, PI has no control over the noise of the system. To smoothen the output speed of the motor with change in the reference speed and filter the noise in the system, a nonlinear algorithm was employed as follows

$$x_1(n+1) = x_1(n) + s \cdot x_2(n), \quad 4.48$$

$$x_2(n+1) = x_2(n) + s \cdot NF(x_1(n) - r(n), x_2(n), g, f), \quad 4.49$$

where $r(k)$ is the reference speed. $x_1(k)$ is the output of the nonlinear differentiator on the reference speed and $x_2(n)$ is the derivative of $x_1(n)$. s is the step size of the speed controller. g is the growing rate coefficient of reference speed which directly defines the speed of convergence of the $x_1(n)$ to the $r(n)$. f are the filtering factor in reducing the noise in the system. NF is a nonlinear function of the error between the reference speed and the output of the nonlinear differentiator as well as the differentiator of the output, the nonlinear differentiator, and the constant parameters. This function is given as

$$NF(m_1(n), x_2(n), n, f) = - \begin{cases} \frac{g \cdot a(n)}{g \cdot f}, & |a(n)| \leq g \cdot f \\ g \cdot \text{sgn}(a(n)), & |a(n)| > g \cdot f \end{cases}, \quad 4.50$$

where, $m_1(n) = x_1(n) - r(n)$, and

$$a(n) = \begin{cases} x_2(n) + \frac{a_0(n) - g \cdot f}{2}, & |y(n)| > g \cdot f^2 \\ x_2(n) + \frac{y(n)}{f}, & |y(n)| \leq g \cdot f^2 \end{cases}, \quad 4.51$$

and

$$a_0(n) = (g^2 \cdot f^2 + 8g |y(n)|)^{\frac{1}{2}}, \quad 4.52$$

$$y(n) = x_1(n) + f x_2(n).$$

The robustness increment was the main motivation for the implementation of this control algorithm. Thanks to the extended state observer, the implemented nonlinear

algorithm was capable of estimating the disturbances in the system. This empowered the control algorithm to remain the performance of the control despite the uncertainties and disturbances. To introduce the extended state observer, firstly, the motor's mechanical equations will be presented. Then, the observer will be defined to extend the states in one order.

Based on the mechanical equation of the SynRM, the torque-speed relation can be written as

$$T_e - T_l = j \frac{d\omega}{dt}, \quad 4.53$$

$$\omega = (T_e - T_l)/j. \quad 4.54$$

Considering the torque equation in the motor, by combining the equations of 4.54 with equation 4.9, the derivative of the mechanical speed can be obtained as follows

$$\omega = \frac{\frac{3}{2}p(L_d - L_q)i_d i_q - T_L}{j}. \quad 4.55$$

where T_L is the load on the motor, and j denotes the rotor's moment of inertia.

The disturbances and the motor parameter constants can be defined as follows

$$D(t) = -\frac{T_L * p}{j}, \quad 4.56$$

$$C = \frac{3}{2}p(L_d - L_q), \quad 4.57$$

where $D(t)$ can be considered as the disturbance in the system with direct relation to the imposed load by the coupled motor. C is the constant that directly relates to the motor's parameter, which can vary under certain circumstances. Hence, the speed equation can be written as follows

$$\omega = C * i_d i_q + D(t). \quad 4.58$$

To compensate for the load disturbances or the uncertainties in the parameters of the system, an observer can be defined as

$$\begin{cases} e(n) = z_1(n) - y(n) \\ z_1(n + 1) = z_1(n) + s \cdot (z_2(n) - \beta_1 \cdot NEF(e(n), \alpha, \delta) + bu(n)), \\ z_2(n + 1) = z_2(n) - s \cdot \beta_2 NEF(e(n), \alpha, \delta) \end{cases} \quad 4.59$$

where $z_1(n)$ are the system state estimation and the extended state $z_2(n)$ is the disturbance estimation. $y(n)$ is the motor speed which is considered as system output. $e(n)$ represents the error between the systems state estimation and the output of the system. The constant parameters of α , δ , β_1 , and β_2 are adjustable and can be tuned to optimize the performance of the control. In this system, the nonlinear function NEF is represented by

$$NEF(e(k), \alpha, \delta) = \begin{cases} |e(k)|^\delta \text{sgn}(e(k)), & |e(n)| > \delta \\ \frac{e(k)}{\delta^{1-\alpha}}, & |e(n)| \leq \delta \end{cases}. \quad 4.60$$

The nature of nonlinearity of the implemented ADRC provides the opportunity for the proper control on the control states, as well as the reference input and the disturbances. Hereafter, a nonlinear function will be defined to produce the control law to the systems.

In other words, exploiting the output of the nonlinear differentiator for the transient profile generator and the output of the extended state observer, a nonlinear system error feedback is employed to give control to the system. The control function is represented by

$$\begin{cases} e_1(n) = x_1(n) - z_1(n) \\ u_0(n) = \beta_3 NEF(e_1(n), \alpha_1, \delta_2), \\ u(n) = u_0(n) - z_2(n)/b \end{cases} \quad 4.61$$

where $u(n)$ is the generated control law for the systems and α_1 , β_3 , b , and δ_2 are adjustable constant values in the system that are tuned to have the optimal solution for the control. It is to be noted that the NEF function governs the control similar to the nonlinear function in the extended system observer. The constant of α_1 is in the range between 0 to 1 and β_3 defines the dynamic performance of the system. Since the output control law in this controller is the current in the q-axis, increasing β_3 leads to faster convergence of the speed to the reference speed by increasing the q-axis current. It should be noted that the MTPA algorithm was employed in this system resulting in a higher d-axis current application in case of disturbances in the system. It is worth mentioning that too large β_3 can lead to high overshoot and divergence of the control function.

In this study, the constant parameters were adjusted intuitively by hit and trial. α could be defined in the range between 0 to 1, where the smaller value for this parameter would lead to the higher capability of the disturbance estimation. δ defines the width of the linearity area. β_1 and β_2 directly relates to the dynamic of the method where β_1 defines the dynamic performance of the system state estimation and β_2 defines the dynamic performance of the disturbances. However, opting for too large values can lead to the divergence of the estimated values and the states. These parameters can be further optimized by using optimization methods such as particle swarm optimization or the Taguchi method.

The proposed algorithm was initially simulated and applied to the model of the motor in simulation. Then, the real-time implementation of the algorithm was carried out in the experimental setup. Figure 4-17 shows the results of the implemented non-linear algorithm on SynRM. A ramp function was applied as a reference speed to observe the behavior of the motor with the implemented algorithm. The results show that the motor current increased concurrently to impose a positive torque on the shaft resulting in the rotation of the motor in the positive direction. This resulted from the d,q-axes voltage application by the inverter to the motor. The speed profile shows that the motor speeded up to the reference speed where the constant speed was commanded to the motor. Then in the steady-state, the motor followed the reference speed and the currents and voltages in both axes fairly remained constant with negligible ripples. It can be seen that the phase current was nearly sinusoidal, indicating a proper control on the current and high performance of the control.

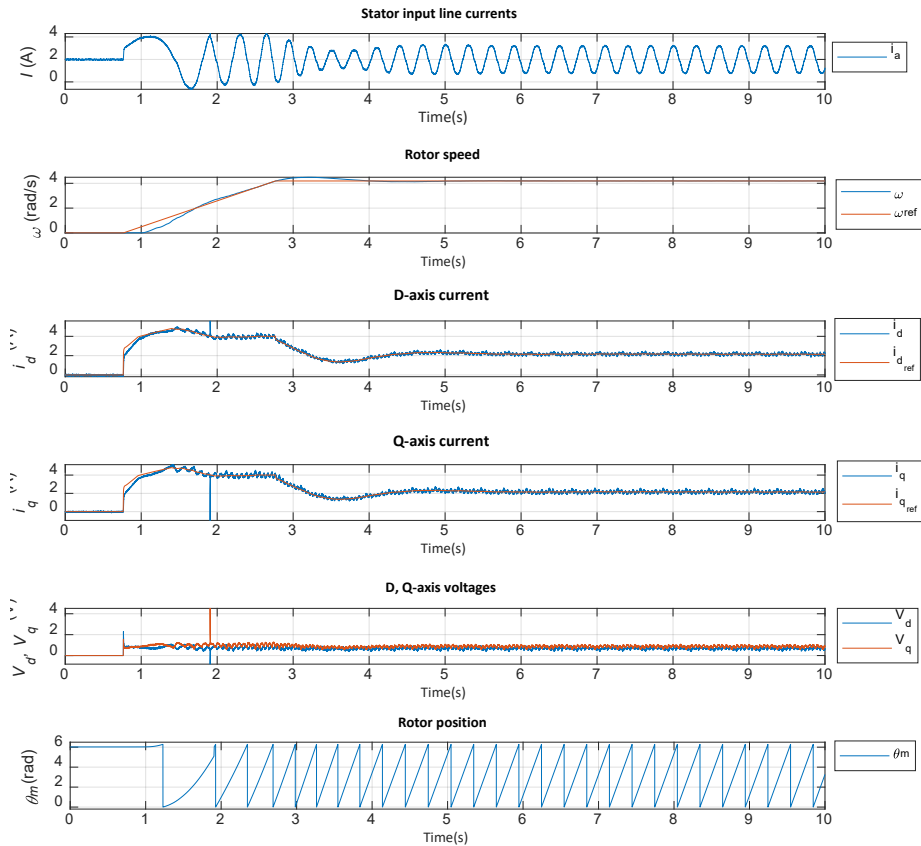


Figure 4-17: The experimental results of ADRC of SynRM.

The nonlinear algorithm was mainly proposed to increase the robustness of the control against the load disturbances. To evaluate the performance of the motor in the loading condition, a set of tests were designed to compare the method with the classical PI controller. In this sense, a step load was injected into the motor in the same condition for both of the methods, and the speed output of the motor was profiled in the tests. Figure 4-18 shows the experimental results of the loading for both the PI and ADRC methods with constant speed reference. The figure shows that the ADRC algorithm showed far more robustness against the load disturbance in comparison with the PI controller. To be more detailed, by applying a step load to the motor in both algorithms, the motor speed in the PI algorithm dropped to 48.5 rad/s from 52.3 rad/s, where the speed roughly dropped to 51.9 rad/s in the ADRC algorithm. This can be interpreted as a 7 % speed drop in the speed in the PI algorithm compared to only a 0.8 % drop in the speed response of the motor. Apart from the undershoot in the speed output, the recovery time was by far less in the ADRC algorithm compared to the PI algorithm. In the ADRC algorithm, the speed reached the steady-state in 0.6 s where the recovery time for the PI algorithm was roughly 2.5 s meaning that in this particular test, its recovery period was more than four times bigger for PI in comparison to the ADRC algorithm.

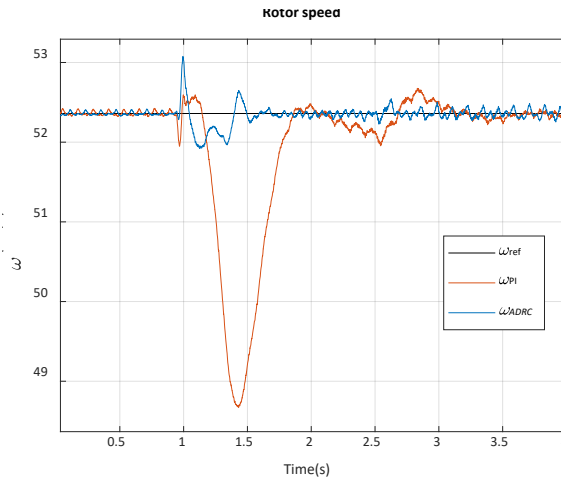


Figure 4-18: Loading test of PI controller and the ADRC method in the experimental setup.

A similar test was designed to assess the robustness of the implemented algorithm against the disturbance load. To do so, the motor was under load, and at a certain time, the load was removed from the motor leading to a sudden increment in the motor speed output. Figure 4-19 shows the results of the unloading test under the same conditions for PI and ADRC control. It can be seen that the speed in the motor with PI controller raised from 52.3 rad/s to 56.7 rad/s, meaning 8 % of the reference speed. However, the motor raised only to 54.2 rad/s, meaning 3 % of the reference speed.

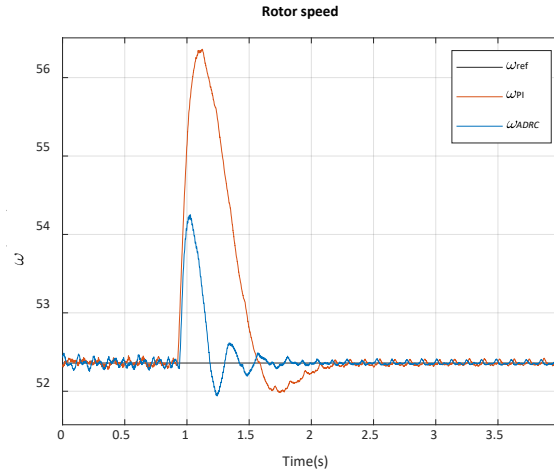


Figure 4-19: Unloading test of PI controller and the ADRC method in the experimental setup.

It can be concluded that the proposed algorithm showed a desirable performance in control. More specifically, the algorithm showed by far more robust against the load disturbances resulting in higher performance of the motor in comparison with the PI controller.

4.7 Torque ripple suppression in the direct torque control of synchronous reluctance machine

As discussed, SynRM severely suffers from high torque ripples. Similarly, the DTC-based drive systems face a severe challenge when the high torque ripples are concerned. Having said that, the DTC-based SynRM drive systems require a deep study to suppress the torque ripples in the shaft. A detailed study was carried out in the second section on the torque ripple reduction techniques. This section proposes a method to reduce the torque ripples in the DTC of SynRM using the FOC concept and duty ratio regulation concept.

4.7.1 Direct torque control of synchronous reluctance machine

As its name suggests, DTC directly controls the flux and torque generating voltage vectors by switching table. Figure 4-20 shows the block diagram of the DTC of SynRM. In this method, simple hysteresis controllers provide the flux and torque error sign for the switching table. Along with the error signs, the estimated flux sector information is also utilized in this lookup table to simply generate the voltage vectors with no need for modulations. Figure 4-21 shows the voltage vector of the switching table using a three-phase inverter. It can be seen that the lookup table generates six active voltages and three null voltages. Table 4-1 presents the switching table in the DTC of SynRM. The switching table generates the voltages considering the flux position sector and two-level flux error sign and three-level torque error sign.

On the other hand, the hysteresis controller and switching table-based control lead to high torque ripples in the motor shaft. Moreover, the lack of control on the current deteriorates the performance of the control, especially in SynRM, due to the presence of the severe slotting harmonics.

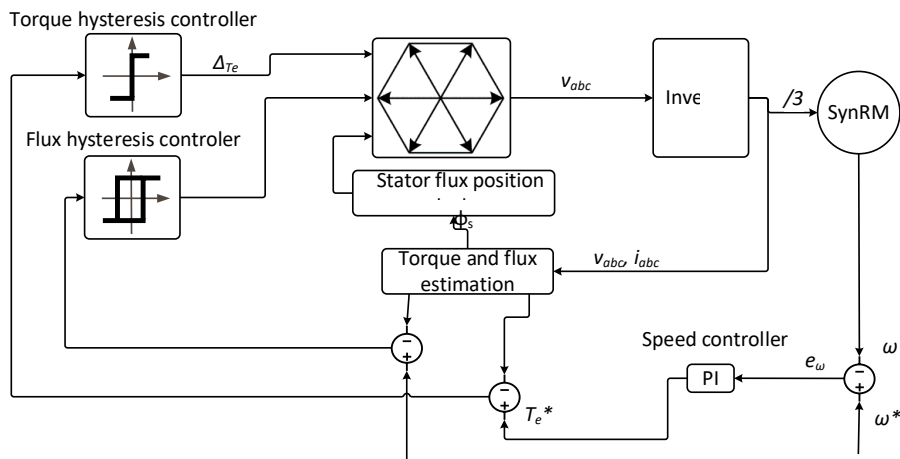


Figure 4-20: DTC of SynRM.

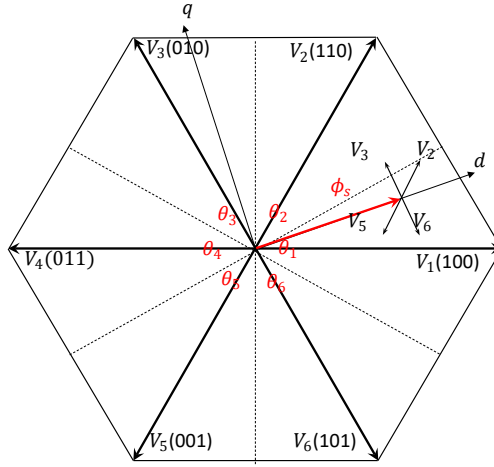


Figure 4-21: The voltage vectors- active voltages ($V_{1..6}$) and the zero voltages ($V_7(000)$, $V_8(111)$).

Table 4-1: The switching table of conventional DTC.

e_λ, e_T, θ	θ_1	θ_2	θ_3	θ_4	θ_5	θ_6	
$e_\lambda = 1$	$e_T = 1$	V_2	V_3	V_4	V_5	V_6	V_1
	$e_T = 0$	V_7	V_8	V_7	V_8	V_7	V_8
	$e_T = -1$	V_6	V_1	V_2	V_3	V_4	V_5
$e_\lambda = 0$	$e_T = 1$	V_3	V_4	V_5	V_6	V_1	V_2
	$e_T = 0$	V_8	V_7	V_8	V_7	V_8	V_7
	$e_T = -1$	V_5	V_6	V_1	V_2	V_3	V_4

4.7.2 The proposed method

As discussed earlier, in the literature, the research works focus on the modification or replacement of the switching table with different modulation techniques for torque ripples reduction. Another popular approach is to replace hysteresis controllers with other controllers in DTC to amend the shortcoming of high torque ripples.

This study aims to reduce the torque ripples in the DTC of the SynRM by changing the input voltages rather than modification or replacement of the controllers or the switching table. For this purpose, the FOC concept was borrowed to transform the flux and torque of the motor to their d- and q-axes in the synchronous reference frame. By this, more precise inputs were utilized in the switching table to generate the voltage vector for the control purpose. The correspondent currents for torque and flux are described as

$$\begin{cases} T_e \propto i_q \\ \lambda_s \propto i_d \end{cases} \quad 4.62$$

Moreover, a duty ratio regulator technique was employed to suppress the torque ripples further in the shaft. Figure 4-22 shows the block diagram of the proposed method that reduces the torque ripples in the motor shaft, and it can be seen the method preserves the structure of the method by changing the inputs of the hysteresis controllers.

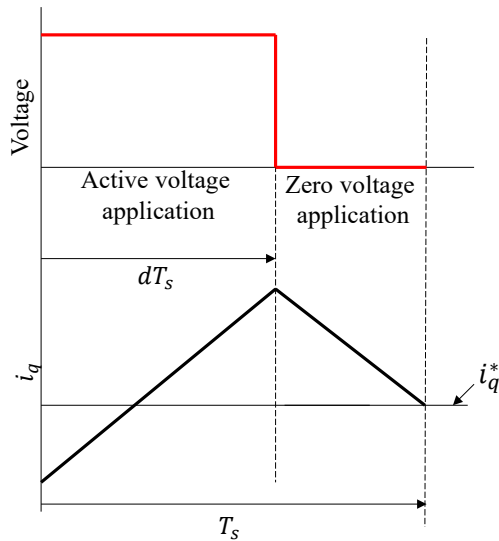


Figure 4-23: The demonstration of the duty ratio regulation of the q-axis current.

Figure 4-24 presents the torque output results of the DTC and the proposed method for no-load and loading conditions. It can be seen that the proposed method shows a similar dynamic with far less torque ripples, especially in the loading condition.

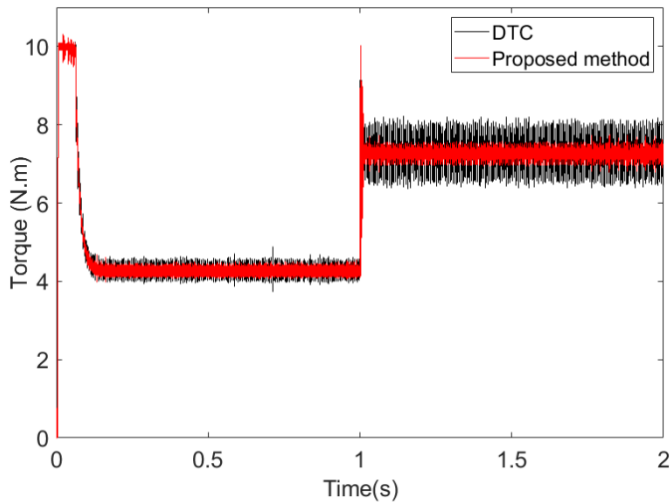


Figure 4-24: The torque response of the SynRM for DTC and the proposed method for applied load.

4.8 Section summary

This section studied and simulated the model of SynRM. The parameters of the motor were identified using lab equipment with two tests. A method was proposed using the microprocessor to identify the parameters of not only the motor but also the cables and the inverter. The FOC of the motor was simulated in the Plecs platform. The control was carried out in real-time. The experimental and simulation results were in good agreement, assuring that the simulation could be utilized for the initial implementation of the proposed algorithms. An MTPA algorithm was implemented in practice to improve

the efficiency of the motor. A nonlinear algorithm was proposed to improve the robustness of the control. A control method was proposed to suppress the torque ripples in the DTC of SynRM. The results proved the performance of the proposed methods and validated the simulated algorithms.

5 Conclusion

This study surveyed the SynRMs developments along with the drive systems. The study investigated the potential development fields for SynRM drives by scrutinizing the strength points of these systems and highlighting the challenges that they encounter. The study focused on the control field in motor-drive systems. To do so, different control algorithms were studied with regard to their structure, the drawbacks, and the benefits that they offer to the different industries. A novel classification method was proposed to summarise the control algorithms regarding their derivation source and the features they obtain. In this classification, modern control theories which were applied in motor control systems were studied and classified based on their highlighted specifications. As a field study in the experimental setup to found a base for the thesis, three motors of IM, SynRM, and PMSynRM were mounted in a rig and driven by an industrial frequency converter, and loaded by an industrial IM-drive. A comprehensive study was carried out on the efficiency maps of the motors to prove the superiority of the SynRMs to the IM technology. In this study, the SynRM presented 1.39 % higher maximum efficiency than IM, which can be desirable for fixed-speed applications. This was extended to the whole speed-torque region where the SynRM had not only higher efficiency but also a wider high-efficiency region which is attractive for variable speed applications. The PMSynRM showed 3.63 % higher maximum efficiency than IM and, similar to SynRM, a very wide range of high efficiency in various speed-torque operations. It can be concluded from the study that the motors define the efficiency of the whole motor-drive systems, while the figures for VSD resemble the motors' figures. Hence, the PMSynRM and SynRM drive systems had higher efficiency than the IM drive system.

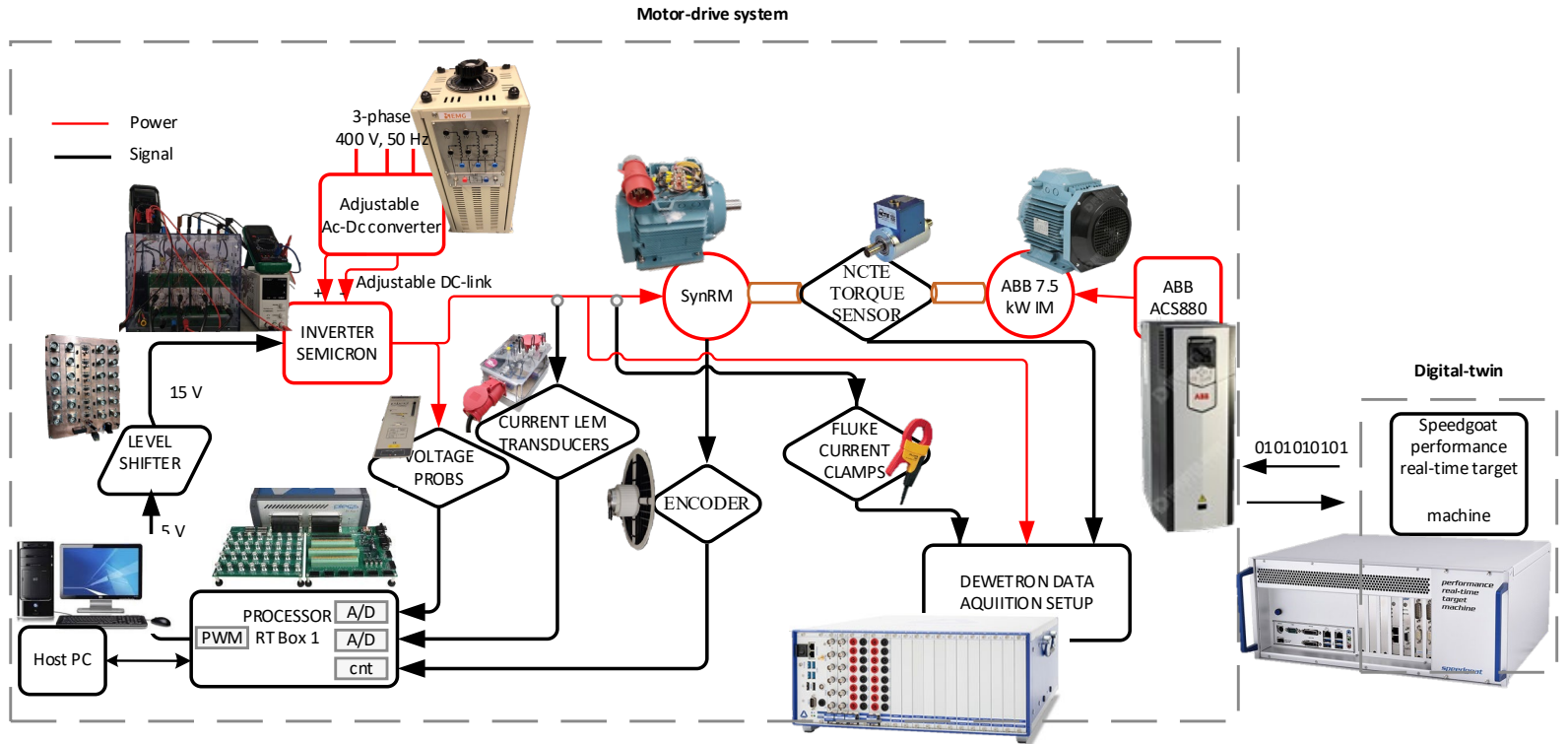
In this study, firstly, the d-q model of the SynRM was simulated as a faster and safer tool for control algorithms implementation. Then, the parameters of the motor were initially measured in isolated test using a power supply and measuring devices in DC-decay test. Then, the FOC and the DTC algorithms were simulated on the simulated model as a base for the control. To verify the simulation results and the performance of the simulated algorithms, a test-bench was designed based on Plecs RT box1 to implement the algorithms in simulation. In this setup, an incremental encoder was used for the position and speed information from the motor, and a board based on the Hall effect sensor was designed to measure the phase current from the system. Then, the FOC algorithm was implemented in real-time in the experimental setup. The experimental results matched the simulation results with acceptable precession, which proved the performance of the implemented control algorithms. Therefore, the simulated model was employed for control algorithms prototyping. As a first step to improve the control algorithms, a closed-loop algorithm based on the microprocessor was designed at a standstill to identify the system parameters. This algorithm identified not only the motor but also the inverter and the wires in the loop in different conditions, especially in high currents. The algorithm measured the system parameters in a wide current range and considered the nonlinearity of the switches in the loop. By applying the values of the updated parameters in the control parameters, a more precise control was achieved in the experimental setup. The next study to improve the performance of the FOC algorithm was to implement a MTPA algorithm to apply a dynamic direct axis current that tunes the current demand based on the output speed and torque of the motor. In this algorithm, the MTPA of the motor was achieved by proposing an analytical algorithm. The algorithm was implemented in the simulation as well as the experimental

setup. To profile the performance of the algorithm, a test was designed to monitor the behavior of the motor under both classical and the proposed algorithm. By applying the MTPA algorithm, the current dropped by roughly 50 % in the motor phase. In another attempt to improve the performance of the system, a nonlinear algorithm was proposed, designed, simulated, and implemented in real-time to increase the robustness of the control algorithm against the parameters variations and the load disturbances. A step load was injected into the system under both the FOC algorithm and the ADRC to compare the behavior of the algorithms in the identical test condition. The robustness of the nonlinear control algorithm against load disturbances was increased by 6.2 % compared to the classical FOC. Additionally, by applying the proposed method, the recovery time for the speed control loop to settle down on the reference speed was shortened by four times which proved the effectiveness of the implemented algorithm. In another study, a novel approach was proposed to decrease the torque ripples in the DTC-driven motor. In this approach, the direct and quadrature components of the motor current in the synchronous reference frame were employed to replace the torque and flux components in the algorithm. This resulted in more precise inputs of the switching table, which could decrease the torque ripples in the motor shaft. Additionally, a duty ratio regulation method was devised to modify the switching table where it applied an active voltage for a portion of a sampling period, and for the rest of the sampling period, a null voltage vector was applied to the motor. The results proved the performance of the proposed methods where the torque with the proposed algorithm was far less than the classical DTC, especially where the loaded condition of the motor was concerned.

6 Future studies

To benefit the highest performance of the SynRMs, it is crucial to analyze the electromagnetic behavior of the motor in different conditions. For this purpose, the FEA model of the motor offers a substantial tool that provides a comprehensive understanding of the electromagnetic behavior of the motor. In this study work, the FEA model of the motor was designed in Magnet Simcenter (by Siemens) software to estimate the inductances of the motor for the sake of initial control. It is projected in the study as a future plan to design a lookup table based on the outputs of the FEA model. This lookup table will provide information about inductances based on the current in the motor as well as the flux in the motor and the voltages with respect to the motor position and speed, and torque. Initially, the control of the FEA model (lookup table) will be carried out and compared with the analytical model and the experimental results. This model is projected to behave more similarly than the analytical model to the experimental setup since it considers the material saturations and crosses saturations in the motor, as well. Therefore, the FEA model will be utilized in future works for simulation instead of the d-q model. Moreover, a lookup will be designed based on the relationship between currents and the inductances in the motor from the FEA model. This lookup table will monitor the currents and regulate the control parameters in the real-time control based on the relationship between current and inductances. Due to the high precision of the FEA model, it is predicted to increase the performance of the control with the updated control parameters.

In this study, a motor drive system as an isolated intelligent system was designed based on the Plecs RT box 1 real-time target machine. The next step for a more sophisticated design of the system is to implement a supervisor for the system based on the AI algorithms. For this, initially, Speedgoat real-time performance target machine was used to register the data from the parameters such as input voltages and current as well as the output speed and torque of the motor. Then, various empirical models of the SynRMs were designed based on the experimental results from the setup utilizing various AI algorithms and with a different number of samples as well as a different number of layers. It is projected to compare different models of the system and opt for the optimal model for the sake of implementation of the digital twin of the system. After selecting the optimal model, a digital twin of the system will be designed. The digital twin can be used for the predictive maintenance of the system, which not only reduces the risk of any type of damages in the system but also prolongs the lifetime of the system and reduces the cost for the maintenance. Apart from the predictive maintenance purpose, the digital twin can be utilized to improve the performance of the control by providing information about the most efficient control scenarios. Figure 6-1 shows the block diagram of the motor drive systems along with the digital twin.



*The scale of the devices is different

Figure 6-1: The block diagram of the motor drive system and the digital twin.

This PhD thesis studied the MTPA operation of the SynRM to improve the efficiency of the motor. It is projected as future work to investigate the effect of the MTPA algorithm on the losses in the motor, including copper losses and core losses. Then, the efficiency map of the motor with the proposed algorithms will be studied. Finally, an in-depth study of the efficiency of the motor at different speeds and current situations will be carried out to obtain the optimum operation of the motor.

Another topic regarding the MTPA operation of the motor is the selection of the optimum torque angle of the motor. In this study, the optimal angle was chosen by analytical calculation with neglecting the cross-saturation effect. In practice, this assumption results in deviated optimal angles, particularly in high currents. Due to the cross saturation, the MTPA point differs from the analytical estimation. Hence, as a future study, the MTPA operation point will be achieved from the FEM model of the motor. The results will be used to design a lookup table. The lookup table will be employed to govern the optimum angle of the d and a-axes currents angle.

For the more realistic calculation of the MTPA working point, a test will be designed to measure the MTPA points of the motor in the experimental setup. To do so, the motor will be coupled to a torque transducer, and the shaft of the torque transducer will be locked from the other side. Then, current will be injected into the motor with different amplitude and different angles. By monitoring the output torque of the motor from the torque transducer, the optimal current angle in different current amplitudes will be obtained with very high precision. Then, a lookup table will be designed based on the results. The lookup table will be utilized in the control algorithm to implement the MTPA based on the numerical experimental results of the current magnitude and angle with respect to the torque.

In this study, a duty ratio algorithm was applied to reduce the torque ripple in the motor shaft. By the application of two voltage vectors instead of one voltage vector to the motor, the switching frequency will be increased. However, the increment in the switching will be approximately 1.5 times higher than the classical switching table-based DTC. This is due to the same status of some of the switches for active voltages and the null voltage. This topic requires a deep study on the effect of the proposed algorithm on power electronic devices. Hence, the switching losses will be analytically calculated based on the measured gate drivers signals to investigate the effect of higher switching frequency on the switches. On the other hand, a higher switching frequency might result in less ripple current on the DC-link, which can positively affect the lifetime of the capacitors. This topic will be studied in practice.

The proposed algorithms can bring complexity and, as a result, higher execution time for the microprocessor, which might not be applicable for some applications. The execution time of the proposed algorithms will be studied in an experimental setup to compare with the conventional method in terms of the computation burden.

In this PhD thesis, the loading tests on the motor for different algorithms were conducted by coupling an industrial IM driven by an industrial VSD. Using this loading setup, the load was injected into the motor in the opposite direction. The applied load was assumed to be a step load since the applied torque reference in the VSD was chosen to be a step torque reference. In practice, there is no ideal VSD that can generate step torque by application of the step torque command. Moreover, the applied load was coupled to the motor, and the reaction between two motors requires a deep study to analyze the behavior of the motor under the load. To do so, it is crucial to study the behavior of the loading motor independently and along with the motor. In the future,

the outputs of the loading motor will be measured, and the behavior of the loading motor will be investigated to scrutinize the interaction of the two motors to specify the effect of the coupled motor on the system. Moreover, the replication of different scenarios in real applications will be studied. Finally, the performance of the motor will be studied regarding the behavior of the applied torque in transient status as well as the steady-state.

In this study, the control parameters were defined by analytical calculation. As discussed, the analytical calculations were carried out by some assumptions such as neglecting the cross saturation, which can result in a not optimal selection of the control parameters such as PI regulator coefficients of the ADRC method constants. It is projected in future works to implement an approach to optimize the control parameters with the objectives of better steady-state performance such as low torque ripples. The control parameters will be optimized in both classic PI controllers and the ADRC method. Firstly, the Taguchi method will be utilized as an optimization algorithm. Then, the other AI methods will be applied, such as a neural network. The results will be compared regarding the better performance of the motor and the complexity of the method. The best approach will be defined and chosen for control parameter optimization.

As discussed in the first chapter, SynRM sacrifices the high torque output and efficiency and the power factor of PMSM to avoid rare-earth magnets in the rotor. On the other hand, PMSynRM utilizes ferrite magnets which can be manufactured in the mass production range, and it is environmental-friendly. Therefore, PMSynRM can be a suitable candidate for traction application as an alternative for PMSMs. Since the manufactured PMSynRM in the lab owns the identical stator and the rotor lamination with the studied SynRM, it is convenient to extend the studied approaches on the PMSynRM. The simulations were carried out, and the classical FOC of the PMSynRM was implemented in experiments. As an extensive study in the future, the proposed algorithms for SynRM will be implemented in simulation and experiments on the PMSynRM.

References

- [1] International Energy Agency, P. Waide, and C. U. Brunner, "Energy-Efficiency Policy Opportunities for Electric Motor-Driven Systems," *Int. energy agency*, vol. na, no. na, p. 132, 2011, doi: 10.1787/5kkg52gb9gjd-en.
- [2] A. Rassölkin *et al.*, "Life cycle analysis of electrical motor-drive system based on electrical machine type," *Proc. Est. Acad. Sci.*, vol. 69, no. 2, p. 162, 2020, doi: 10.3176/proc.2020.2.07.
- [3] A. T. De Almeida, F. J. T. E. Ferreira, and G. Baoming, "Beyond induction motors - Technology trends to move up efficiency," *IEEE Trans. Ind. Appl.*, vol. 50, no. 3, pp. 2103–2114, 2014, doi: 10.1109/TIA.2013.2288425.
- [4] Q. Zhang, H. Liu, Z. Zhang, and T. Song, "A Cast Copper Rotor Induction Motor for Small Commercial EV Traction: Electromagnetic Design, Analysis, and Experimental Tests," *China Electrotech. Soc. Trans. Electr. Mach. Syst.*, vol. 2, no. 4, pp. 417–424, 2019, doi: 10.30941/cestems.2018.00053.
- [5] G. Wu, S. Huang, Q. Wu, F. Rong, C. Zhang, and W. Liao, "Robust Predictive Torque Control of N*3-Phase PMSM for High-Power Traction Application," *IEEE Trans. Power Electron.*, vol. 35, no. 10, pp. 10799–10809, Oct. 2020, doi: 10.1109/TPEL.2020.2981914.
- [6] S. Fang, H. Liu, H. Wang, H. Yang, and H. Lin, "High power density PMSM with lightweight structure and high-performance soft magnetic alloy core," *IEEE Trans. Appl. Supercond.*, vol. 29, no. 2, Mar. 2019, doi: 10.1109/TASC.2019.2891630.
- [7] J. Xu, B. Zhang, X. Kuang, H. Guo, and S. Guo, "Influence analysis of slot parameters and high torque density optimisation for dual redundant permanent magnet motor in aerospace application," *IET Electr. Power Appl.*, vol. 14, no. 7, pp. 1263–1273, Jul. 2020, doi: 10.1049/iet-epa.2019.0724.
- [8] Y. Kong, M. Lin, and L. Jia, "A novel high power density permanent-magnet synchronous machine with wide speed range," *IEEE Trans. Magn.*, vol. 56, no. 2, Feb. 2020, doi: 10.1109/TMAG.2019.2947611.
- [9] "Tesla Model 3's IPM-SynRM electric motor." <https://www.lesics.com/tesla-model-3's-ipm-synrm-electric-motor.html> (accessed Sep. 17, 2021).
- [10] J. R. Hendershot and T. J. E. (Timothy J. E. Miller, "Design of brushless permanent-magnet motors," 1994.
- [11] G. Pellegrino, T. M. Jahns, N. Bianchi, W. Soong, and F. Cupertino, *The Rediscovery of Synchronous Reluctance and Ferrite Permanent Magnet Motors*. Cham: Springer International Publishing, 2016.
- [12] I. Boldea *et al.*, "Automotive Electric Propulsion Systems With Reduced or No Permanent Magnets: An Overview," *IEEE Trans. Ind. Electron.*, vol. 61, no. 10, pp. 5696–5711, 2014, doi: 10.1109/TIE.2014.2301754.
- [13] R. R. Moghaddam and F. Gyllensten, "Novel High-Performance SynRM Design Method : An Easy Approach for A Complicated Rotor Topology," *IEEE Trans. Ind. Electron.*, vol. 61, no. 9, pp. 5058–5065, 2014, doi: 10.1109/TIE.2013.2271601.
- [14] "ABB IE5 SynRM motors deliver ultra-premium energy efficiency." <https://new.abb.com/news/detail/58874/abb-ie5-synrm-motors-deliver-ultra-premium-energy-efficiency> (accessed May 27, 2020).
- [15] S. Taghavi, S. Member, and P. Pillay, "A Sizing Methodology of the Synchronous Reluctance Motor for Traction Applications," *IEEE J. Emerg. Sel. Top. Power Electron.*, vol. 2, no. 2, pp. 329–340, 2014, doi: 10.1109/JESTPE.2014.2299235.

- [16] "IEC 60034-30-1:2014 | IEC Webstore | pump, motor, water management, smart city, energy efficiency." <https://webstore.iec.ch/publication/136> (accessed Feb. 15, 2019).
- [17] "IEC TS 60034-30-2:2016 | IEC Webstore | energy efficiency, efficiency rating." <https://webstore.iec.ch/publication/30830> (accessed Feb. 15, 2019).
- [18] ABB, "Synchronous reluctance motor-drive package for industrial use - Optimized cost of ownership."
- [19] ABB, "Synchronous reluctance motor-drive package for machine builders. High performance for ultimate machine design," [Online]. Available: <http://search-ext.abb.com/library/Download.aspx?DocumentID=3AUA0000120962&LanguageCode=en&DocumentPartId=1&Action=Launch>.
- [20] M. N. F. Ibrahim, A. S. Abdel-Khalik, E. M. Rashad, and P. Sergeant, "An Improved Torque Density Synchronous Reluctance Machine With a Combined Star-Delta Winding Layout," *IEEE Trans. Energy Convers.*, 2018, doi: 10.1109/TEC.2017.2782777.
- [21] S. S. R. Bonthu, A. Arafat, and S. Choi, "Comparisons of Rare-Earth and Rare-Earth-Free External Rotor Permanent Magnet Assisted Synchronous Reluctance Motors," *IEEE Trans. Ind. Electron.*, vol. 64, no. 12, pp. 9729–9738, 2017, doi: 10.1109/TIE.2017.2711580.
- [22] R. R. Moghaddam, F. Magnussen, and C. Sadarangani, "Theoretical and Experimental Reevaluation of Synchronous Reluctance Machine," *IEEE Trans. Ind. Electron.*, vol. 57, no. 1, pp. 6–13, 2010, doi: 10.1109/TIE.2009.2025286.
- [23] Y. Wang, D. Ionel, D. G. Dorrell, and S. Stretz, "Establishing the Power Factor Limitations for Synchronous Reluctance Machines," *IEEE Trans. Magn.*, vol. 51, no. 11, pp. 1–4, 2015, doi: 10.1109/TMAG.2015.2443713.
- [24] A. Vagati, A. Canova, M. Chiampi, M. Pastorelli, and M. Repetto, "Design refinement of synchronous reluctance motors through finite-element analysis," *IEEE Trans. Ind. Appl.*, vol. 36, no. 4, pp. 1094–1102, Jul. 2000, doi: 10.1109/28.855965.
- [25] Jung-Min Park, Seong-June Park, Min-Myung Lee, Jang-Sung Chun, and Jung-Ho Lee, "Rotor Design on Torque Ripple Reduction for a Synchronous Reluctance Motor with Concentrated Winding using Response Surface Methodology," in *2006 12th Biennial IEEE Conference on Electromagnetic Field Computation*, pp. 424–424, doi: 10.1109/CEFC-06.2006.1633214.
- [26] X. Diao, H. Zhu, Y. Qin, and Y. Hua, "Torque Ripple Minimization for Bearingless," *IEEE Trans. Appl. Supercond.*, vol. 28, no. 3, pp. 1–5, 2018, doi: 10.1109/TASC.2018.2798632.
- [27] M. N. F. Ibrahim, P. Sergeant, and E. Rashad, "Simple design approach for low torque ripple and high output torque synchronous reluctance motors," *Energies*, vol. 9, no. 11, 2016, doi: 10.3390/en9110942.
- [28] M. N. Uddin, S. Member, and M. Rahman, "Online Torque-Flux Estimation-Based Nonlinear Torque and Flux Control Scheme of IPMSM Drive for Reduced Torque Ripples," *IEEE Trans. Power Electron.*, vol. 34, no. 1, pp. 636–645, 2019, doi: 10.1109/TPEL.2018.2827332.
- [29] T. A. Lipo, "Synchronous reluctance machines-a viable alternative for ac drives?," *Electr. Mach. Power Syst.*, vol. 19, no. 6, pp. 659–671, 1991, doi: 10.1080/07313569108909556.

- [30] S. Taghavi, S. Member, and P. Pillay, "A Novel Grain-Oriented Lamination Rotor Core Assembly for a Synchronous Reluctance Traction Motor With a Reduced Torque Ripple Algorithm," *IEEE Trans. Ind. Appl.*, vol. 52, no. 5, pp. 3729–3738, 2016, doi: 10.1109/TIA.2016.2558162.
- [31] S. Sudheer, R. Bonthu, T. Bin Tarek, and S. Choi, "Optimal Torque Ripple Reduction Technique for Outer Rotor Permanent Magnet Synchronous Reluctance," *IEEE Trans. Energy Convers.*, vol. 33, no. 3, pp. 1184–1192, 2018, doi: 10.1109/TEC.2017.2781259.
- [32] N. Bianchi, S. Bolognani, E. Carraro, M. Castiello, and E. Fornasiero, "Electric Vehicle Traction Based on Synchronous Reluctance Motors," *IEEE Trans. Ind. Appl.*, vol. 52, no. 6, pp. 4762–4769, 2016, doi: 10.1109/TIA.2016.2599850.
- [33] N. Bianchi, S. Bolognani, D. Bon, and M. D. Pr, "Torque Harmonic Compensation in a Synchronous Reluctance Motor," vol. 23, no. 2, pp. 466–473, 2008.
- [34] N. Bianchi, S. Bolognani, D. Bon, and M. D. Pré, "Rotor flux-barrier design for torque ripple reduction in synchronous reluctance and PM-assisted synchronous reluctance motors," *IEEE Trans. Ind. Appl.*, 2009, doi: 10.1109/TIA.2009.2018960.
- [35] G. Lo Calzo and M. Galea, "Design Optimization of a High-Speed Synchronous," *IEEE Trans. Ind. Appl.*, vol. 54, no. 1, pp. 233–243, 2018, doi: 10.1109/TIA.2017.2758759.
- [36] A. Rassölkin, H. Heidari, A. Kallaste, J. P. Acedo, and E. Romero-cadaval, "Efficiency Map Comparison of Induction and Synchronous Reluctance Motors," in *26th International Workshop on Electric Drives: Improvement in Efficiency of Electric Drives (IWED)*, 2019, pp. 4–7.
- [37] T. A. Huynh and M. F. Hsieh, "Comparative Study of PM-Assisted SynRM and IPMSM on Constant Power Speed Range for EV Applications," *IEEE Trans. Magn.*, vol. 53, no. 11, Nov. 2017, doi: 10.1109/TMAG.2017.2707125.
- [38] G. V. Kumar, C. H. Chuang, M. Z. Lu, and C. M. Liaw, "Development of an Electric Vehicle Synchronous Reluctance Motor Drive," *IEEE Trans. Veh. Technol.*, vol. 69, no. 5, pp. 5012–5024, May 2020, doi: 10.1109/TVT.2020.2983546.
- [39] D. Herrera, J. Villegas, E. Galván, and J. M. Carrasco, "Powertrain EV synchronous reluctance motor design with redundant topology with novel control," *IET Electr. Power Appl.*, vol. 13, no. 11, pp. 1647–1659, Nov. 2019, doi: 10.1049/iet-epa.2018.5891.
- [40] G. Pellegrino, E. Armando, and P. Guglielmi, "Direct-Flux Vector Control of IPM Motor Drives in the Maximum Torque Per Voltage Speed Range," *IEEE Trans. Ind. Electron.*, vol. 59, no. 10, pp. 3780–3788, 2012, doi: 10.1109/TIE.2011.2178212.
- [41] M. Barcaro, N. Bianchi, and F. Magnussen, "Permanent-magnet optimization in permanent-magnet-assisted synchronous reluctance motor for a wide constant-power speed range," *IEEE Trans. Ind. Electron.*, 2012, doi: 10.1109/TIE.2011.2167731.
- [42] "All-compatible ACS880 single drives - Industrial drives - unlimited possibilities for your business (Low voltage AC) | ABB." <https://new.abb.com/drives/low-voltage-ac/industrial-drives/acs880-single-drives> (accessed Aug. 24, 2020).
- [43] S. Piriienko *et al.*, "Influence of the control strategy on the efficiency of synrm based small-scale wind generators," in *Proceedings of the IEEE International Conference on Industrial Technology*, Feb. 2019, vol. 2019-February, pp. 280–285, doi: 10.1109/ICIT.2019.8755122.
- [44] Danfoss, "Facts Worth Knowing about Frequency Converters," p. 180, 2014.

- [45] HEC-HMS, "Technical Reference Manual," *US Army Corps Eng.*, no. March, p. 155, 2000, [Online]. Available: [http://www.hec.usace.army.mil/software/hec-hms/documentation/HEC-HMS_Technical Reference Manual_\(CPD-74B\).pdf](http://www.hec.usace.army.mil/software/hec-hms/documentation/HEC-HMS_Technical Reference Manual_(CPD-74B).pdf).
- [46] K. Lee, H. Kim, and S. M. Lukic, "A Rotating Restart Method for Scalar (v/f) Controlled Synchronous Reluctance Machine Drives Using a Single DC-Link Current Sensor," *IEEE Access*, vol. 8, pp. 106629–106638, 2020, doi: 10.1109/ACCESS.2020.3000220.
- [47] G. Roy and G. E. April, "Cycloconverter operation under a new scalar control algorithm," in *PESC Record - IEEE Annual Power Electronics Specialists Conference*, 1989, vol. 1, pp. 368–375, doi: 10.1109/pesc.1989.48511.
- [48] A. Consoli, G. Scelba, G. Scarcella, and M. Cacciato, "An effective energy-saving scalar control for industrial IPMSM drives," *IEEE Trans. Ind. Electron.*, vol. 60, no. 9, pp. 3658–3669, 2013, doi: 10.1109/TIE.2012.2207651.
- [49] "Scalar V/f and I-f Control of AC Motor Drives: An Overview." <https://ieeexplore.ieee.org/stamp/stamp.jsp?tp=&arnumber=7426739&tag=1> (accessed Dec. 08, 2020).
- [50] T. Imen, K. Amor, S. Oussamal, C. Abdelkader, and B. Mohamed, "Performance analysis of FOC and DTC for Synchronous Reluctance Motor," in *2016 17th International Conference on Sciences and Techniques of Automatic Control and Computer Engineering, STA 2016 - Proceedings*, Jun. 2017, pp. 260–264, doi: 10.1109/STA.2016.7952109.
- [51] L. Yen-Shin and C. Jian-Ho, "A new approach to direct torque control of induction motor drives for constant inverter switching frequency and torque ripple reduction," *IEEE Trans. Energy Convers.*, vol. 16, no. 3, pp. 220–227, 2001, doi: 10.1109/60.937200.
- [52] A. Kumar, B. G. Fernandes, and K. Chatterjee, "Simplified SVPWM-DTC of 3-phase induction motor using the concept of imaginary switching times," in *IECON Proceedings (Industrial Electronics Conference)*, 2004, vol. 1, pp. 341–346, doi: 10.1109/iecon.2004.1433334.
- [53] G. Pellegrino, R. I. Bojoi, S. Member, and P. Guglielmi, "Unified Direct-Flux Vector Control for AC Motor Drives," *IEEE Trans. Ind. Appl.*, vol. 47, no. 5, pp. 2093–2102, 2011, doi: 10.1109/TIA.2011.2161532.
- [54] A. Yousefi-Talouki, P. Pescetto, G. Pellegrino, I. Boldea, and S. Member, "Combined Active Flux and High-Frequency Injection Methods for Sensorless Direct-Flux Vector Control of Synchronous Reluctance Machines," *IEEE Trans. Power Electron.*, vol. 33, no. 3, pp. 2447–2457, 2018, doi: 10.1109/TPEL.2017.2697209.
- [55] H. Heidari *et al.*, "A Novel Vector Control Strategy for a Six-Phase Induction Motor with Low Torque Ripples and Harmonic Currents," *Energies*, vol. 12, no. 6, p. 1102, 2019, doi: 10.3390/en12061102.
- [56] H. Heidari, A. Rassötkin, A. Kallaste, T. Vaimann, and E. Andriushchenko, "Vector Control Of Synchronous Reluctance Motor With Reduced Torque Ripples," 2020.
- [57] X. Zhang, G. H. Foo, D. M. Vilathgamuwa, S. Member, D. L. Maskell, and S. Member, "An Improved Robust Field-Weakening Algorithm for Direct-Torque-Controlled Synchronous-Reluctance-Motor Drives," *IEEE Trans. Ind. Electron.*, vol. 62, no. 5, pp. 3255–3264, 2015, doi: 10.1109/TIE.2014.2386798.
- [58] ABB, "DTC: A motor control technique for all seasons." <https://new.abb.com/drives/dtc> (accessed Jan. 23, 2020).

- [59] Z. Zhang and X. Liu, "A Duty Ratio Control Strategy to Reduce Both Torque and Flux Ripples of DTC for Permanent Magnet Synchronous Machines," *IEEE Access*, vol. 7, pp. 11820–11828, 2019, doi: 10.1109/ACCESS.2019.2892121.
- [60] X. Zhang, "Overmodulation of Constant-Switching-Frequency-Based DTC for Reluctance Synchronous Motors Incorporating," *IEEE Trans. Ind. Electron.*, vol. 66, no. 1, pp. 37–47, 2019, doi: 10.1109/TIE.2018.2826478.
- [61] L. Tang, L. Zhong, M. F. Rahman, and Y. Hu, "A novel direct torque controlled interior permanent magnet synchronous machine drive with low ripple in flux and torque and fixed switching frequency," *Power*, vol. 19, no. 2, pp. 346–354, 2004, doi: 10.1109/TPEL.2003.823170.
- [62] J. Soltani, H. Abootorabi Zarchi, and G. R. Arab Markadeh, "Stator-flux-oriented based encoderless direct torque control for synchronous reluctance machines using sliding mode approach," *World Acad. Sci. Eng. Technol.*, vol. 58, no. 10, pp. 883–889, 2009.
- [63] L. Tutelea *et al.*, "DTFC-SVM motion-sensorless control of a PM-assisted reluctance synchronous machine as starter-alternator for hybrid electric vehicles," *IEEE Trans. Power Electron.*, vol. 21, no. 3, pp. 711–719, 2006, doi: 10.1109/tpel.2006.872369.
- [64] C. Che and Y. Qu, "Research on drive technology and control strategy of Electric Vehicle based on SVPWM-DTC," in *Proceedings 2011 International Conference on Mechatronic Science, Electric Engineering and Computer, MEC 2011*, 2011, pp. 44–49, doi: 10.1109/MEC.2011.6025397.
- [65] B. Arunkumar, C. S. A. Sekhar, V. Raghavendra Rajan, N. Tejesvi, and M. Sasikumar, "Comparison of SVPWM and SVM controlled smart VSI fed PMSG for wind power generation system," *Proc. - NCET NRES EM 2014 2nd IEEE Natl. Conf. Emerg. Trends New Renew. Energy Sources Energy Manag.*, pp. 221–226, Apr. 2015, doi: 10.1109/NCETNRESEM.2014.7088771.
- [66] H. Hadla and S. Cruz, "Predictive Stator Flux and Load Angle Control of Synchronous Reluctance Motor Drives Operating in a Wide Speed Range," *IEEE Trans. Ind. Electron.*, vol. 64, no. 9, pp. 6950–6959, 2017, doi: 10.1109/TIE.2017.2688971.
- [67] Y. Ren and Z. Q. Zhu, "Enhancement of steady-state performance in direct-torque-controlled dual three-phase permanent-magnet synchronous machine drives with modified switching table," *IEEE Trans. Ind. Electron.*, vol. 62, no. 6, pp. 3338–3350, 2015, doi: 10.1109/TIE.2014.2376881.
- [68] P. Niazi, H. A. Toliyat, S. Member, A. Goodarzi, S. Member, and A. Recently, "Robust Maximum Torque per Ampere (MTPA) Control of PM-Assisted SynRM for Traction Applications," vol. 56, no. 4, pp. 1538–1545, 2007.
- [69] G. H. B. Foo and X. Zhang, "Robust Direct Torque Control of Synchronous Reluctance Motor Drives in the Field-Weakening Region," *IEEE Trans. Power Electron.*, vol. 32, no. 2, pp. 1289–1298, 2017, doi: 10.1109/TPEL.2016.2542241.
- [70] E. Trancho *et al.*, "PM-Assisted Synchronous Reluctance Machine Flux Weakening Control for EV and HEV Applications," *IEEE Trans. Ind. Electron.*, 2018, doi: 10.1109/TIE.2017.2748047.
- [71] R. Morales-Caporal and M. Pacas, "A Predictive Torque Control for the Synchronous Reluctance Machine Taking Into Account the Magnetic Cross Saturation," *IEEE Trans. Ind. Electron.*, vol. 54, no. 2, pp. 1161–1167, Apr. 2007, doi: 10.1109/TIE.2007.891783.

- [72] R. Antonello, M. Carraro, L. Peretti, and M. Zigliotto, "Hierarchical Scaled-States Direct Predictive Control of Synchronous Reluctance Motor Drives," *IEEE Trans. Ind. Electron.*, vol. 63, no. 8, pp. 5176–5185, Aug. 2016, doi: 10.1109/TIE.2016.2536581.
- [73] X. Yuan, C. Zhang, S. Zhang, R. Wang, and X. Zhang, "Predictive current control for SynRM drives under low dc link voltage," May 2019, doi: 10.1109/PRECEDE.2019.8753201.
- [74] I. Jlassi and A. J. M. Cardoso, "Model predictive current control of synchronous reluctance motors, including saturation and iron losses," in *Proceedings - 2018 23rd International Conference on Electrical Machines, ICEM 2018*, Oct. 2018, pp. 1598–1603, doi: 10.1109/ICELMACH.2018.8506944.
- [75] C. Lin, J. Yu, H. Yu, and Y. Lo, "Simplified model-free predictive current control for synchronous reluctance motor drive systems," Jul. 2015, doi: 10.1109/INTMAG.2015.7157237.
- [76] A. Veysinejad, S. Rahmati, and S. Shamlou, "Predictive Direct Torque Control with Reduced Number of Considered States in Synchronous Reluctance Motor Drive," in *2019 10th International Power Electronics, Drive Systems and Technologies Conference, PEDSTC 2019*, Apr. 2019, pp. 90–95, doi: 10.1109/PEDSTC.2019.8697735.
- [77] N. Aros, V. Mora, and C. Alarcón, "Model predictive control for synchronous reluctance motor drive," in *2017 CHILEAN Conference on Electrical, Electronics Engineering, Information and Communication Technologies, CHILECON 2017 - Proceedings*, Dec. 2017, vol. 2017-January, pp. 1–6, doi: 10.1109/CHILECON.2017.8229704.
- [78] H. Hadla and S. Cruz, "Active flux based finite control set model predictive control of synchronous reluctance motor drives," Oct. 2016, doi: 10.1109/EPE.2016.7695377.
- [79] A. Kiselev, G. R. Catuogno, A. Kuznietsov, and R. Leidhold, "Finite Control Set MPC for Open-Phase Fault Tolerant Control of Synchronous Reluctance Motor," in *Proceedings of the IEEE International Conference on Industrial Technology*, Feb. 2020, vol. 2020-February, pp. 1077–1082, doi: 10.1109/ICIT45562.2020.9067220.
- [80] C. S. Lim, E. Levi, M. Jones, N. A. Rahim, and W. P. Hew, "FCS-MPC-based current control of a five-phase induction motor and its comparison with PI-PWM control," *IEEE Trans. Ind. Electron.*, vol. 61, no. 1, pp. 149–163, 2014, doi: 10.1109/TIE.2013.2248334.
- [81] J. A. Riveros, F. Barrero, E. Levi, M. J. Duran, S. Toral, and M. Jones, "Variable-speed five-phase induction motor drive based on predictive torque control," *IEEE Trans. Ind. Electron.*, vol. 60, no. 8, pp. 2957–2968, 2013, doi: 10.1109/TIE.2012.2198034.
- [82] J. Rodríguez *et al.*, "High-Performance Control Strategies for Electrical Drives : An Experimental Assessment," vol. 59, no. 2, pp. 812–820, 2012, doi: 10.1109/TIE.2011.2158778.
- [83] E. Daryabeigi, A. Mirzaei, H. Abootorabi Zarchi, and S. Vaez-Zadeh, "Deviation Model-Based Control of Synchronous Reluctance Motor Drives with Reduced Parameter Dependency," *IEEE Trans. Power Electron.*, vol. 34, no. 7, pp. 6697–6705, Jul. 2019, doi: 10.1109/TPEL.2018.2876660.

- [84] E. Daryabeigi, A. Mirzaei, H. A. Zarchi, and S. Vaez-Zadeh, "Deviation Control in Comparison with DTC and FOC for SynRM Drives," in *2019 10th International Power Electronics, Drive Systems and Technologies Conference, PEDSTC 2019*, Apr. 2019, pp. 713–717, doi: 10.1109/PEDSTC.2019.8697756.
- [85] W.-L. Mao, C.-T. Chu, and C.-W. Hung, "Synchronous Reluctance Motor Speed Tracking Using a Modified Second-Order Sliding Mode Control Method," *Neural Process. Lett.* 2019 511, vol. 51, no. 1, pp. 251–270, Jul. 2019, doi: 10.1007/S11063-019-10085-X.
- [86] S. G. Chen, F. J. Lin, C. H. Liang, and C. H. Liao, "Intelligent Maximum Power Factor Searching Control Using Recurrent Chebyshev Fuzzy Neural Network Current Angle Controller for SynRM Drive System," *IEEE Trans. Power Electron.*, vol. 36, no. 3, pp. 3496–3511, Mar. 2021, doi: 10.1109/TPEL.2020.3016709.
- [87] F. J. Lin, S. G. Chen, and C. W. Hsu, "Intelligent backstepping control using recurrent feature selection fuzzy neural network for synchronous reluctance motor position servo drive system," *IEEE Trans. Fuzzy Syst.*, vol. 27, no. 3, pp. 413–427, 2019, doi: 10.1109/TFUZZ.2018.2858749.
- [88] J. C. Ting and D. F. Chen, "Nonlinear backstepping control of SynRM drive systems using reformed recurrent Hermite polynomial neural networks with adaptive law and error estimated law," *J. Power Electron.*, vol. 18, no. 5, pp. 1380–1397, 2018, doi: 10.6113/JPE.2018.18.5.1380.
- [89] H.-K. Chiang and C.-T. Chu, "Reference Model with an Adaptive Hermite Fuzzy Neural Network Controller for Tracking a Synchronous Reluctance Motor," *Electr. Power Components Syst.*, vol. 43, no. 7, pp. 770–780, Apr. 2015, doi: 10.1080/15325008.2014.1003157.
- [90] R. Strzelecki, G. L. Demidova, D. V. Lukichev, N. A. Polyakov, A. A. Abdullin, and S. Y. Lovlin, "Survey on fuzzy logic methods in control systems of electromechanical plants," *Sci. Tech. J. Inf. Technol. Mech. Opt.*, vol. 19, no. 1, pp. 1–14, Feb. 2019, doi: 10.17586/2226-1494-2019-19-1-1-14.
- [91] D. V. Lukichev, G. L. Demidova, A. Y. Kuzin, and A. V. Saushev, "Application of adaptive Neuro Fuzzy Inference System (ANFIS) controller in servodrive with multi-mass object," in *2018 25th International Workshop on Electric Drives: Optimization in Control of Electric Drives, IWED 2018 - Proceedings*, Mar. 2018, vol. 2018-Janua, pp. 1–6, doi: 10.1109/IWED.2018.8321388.
- [92] A. Glac, V. Šmídl, Z. Peroutka, and C. M. Hackl, "Dependence of IPMSM Motor Efficiency on Parameter Estimates," *Sustain.* 2021, Vol. 13, Page 9299, vol. 13, no. 16, p. 9299, Aug. 2021, doi: 10.3390/SU13169299.
- [93] J. Han, "From PID to active disturbance rejection control," *IEEE Trans. Ind. Electron.*, vol. 56, no. 3, pp. 900–906, 2009, doi: 10.1109/TIE.2008.2011621.

Acknowledgements

My sincere gratitude to my supervisors for their continuous support and guidance through their immense knowledge, experience, and motivation. Also, I am thankful for the help and support that I received from my colleagues and fellow students. This work would not have been possible without their encouragement, patience, and support.

Abstract

Development of control methods for synchronous reluctance motors

This Ph.D. dissertation presents motor technologies and motor control methods. The study focused on the improvement of the control methods for synchronous reluctance motor (SynRM).

The motor technologies were scrutinized and the superiorities and the drawbacks of the SynRMs were recognized. Different motor control methods were studied and compared concerning the structure. A holistic approach was employed to classify the motor control strategies which included the different control theories considering the features of each control strategy.

A test bench was designed based on industrial frequency converters to study the designed SynRMs in experiments along with an industrial induction motor. The efficiency maps of the motors were studied in a comparative approach.

The SynRM was modeled in the PLECS platform and the field-oriented control (FOC) and the direct torque control (DTC) were implemented in the simulation. A test bench was designed to implement the algorithms in real-time. Using the designed motor drive system, the parameters of the motor and the inverter, and the cables were measured with high precision. The FOC of SynRM was implemented in real-time and the experimental results matched the simulation results. An algorithm was implemented to apply the maximum torque per ampere (MTPA) in the control to improve the efficiency of the motor in base speed range operation. The results showed far less current injection to the motor for the same loading condition. For higher speeds, a current angle was defined to be governed to meet the voltage limits of the motor. A nonlinear algorithm was proposed to improve the robustness of the control using the adaptive disturbance rejection control (ADRC) concept. The results showed far higher robustness of the proposed algorithm against the load disturbances compared to the conventional proportional-integral (PI) controller. An algorithm was proposed to suppress the torque ripples in the DTC of SynRM by employing torque and flux correspondent in the synchronous reference frame to the switching table. The results showed a significant decrease in the torque ripples.

Lühikokkuvõte

Sünkroonreluktantsmootorite juhtimismeetodite edasiarendus

Käesolev doktoritöö käsitleb mootorite tehnoloogiat ja nende juhtimismeetodeid. Uurimus on keskendunud sünkroonreluktantsmootorite juhtimismeetodite edasiarendusele.

Mootorite tehnoloogiat uuriti süvendatult ning sünkroonreluktantsmootorite eelised ja puudused tuvastati. Uuriti erinevaid mootorite juhtimismeetodeid ja neid võrreldi omavahel, keskendudes nende struktuurile. Mootorite juhtimisstrateegiad uuriti terviklikult, mille hulgas vaadeldi erinevaid juhtimisteooriaid, arvestades nende spetsiifilisi omadusi.

Rajati tööstuslikel sagedusmuunduritel põhinev katsepink, et katsetada projekteeritud sünkroonreluktantsmootoreid koos tööstusliku asünkroonmootoriga. Koostati ja omavahel võrreldi ka mõlema mootori efektiivsuskaarte.

Sünkroonreluktantsmootor mudeldati kasutades Plecs tarkvara, mille simulatsioonides kasutati vektorjuhtimist (ingl.k. *field-oriented control*, ehk FOC) ja momendi otsejuhtimist (ingl.k. *direct torque control*, ehk DTC). Algoritme katsetati katsepingil reaajas. Projekteeritud mootor-ajami süsteemis mõõdeti suure täpsusega mootori, muunduri ja kaablite parameetreid. Sünkroonreluktantsmootori vektorjuhtimist katsetati reaajas ning katsetulemused kattusid modelleerimistulemustega. Loodi algoritm, et rakendada juhtimisstrateegias elektrivoolu kohta maksimaalset momenti, tõstes seeläbi mootori efektiivsust nimikiiruse talitluses. Tulemused näitasid, et sama koormuse korral võimaldas antud strateegia oluliselt madalamat voolusisestust. Kõrgematel kiirustel talitlemiseks defineeriti voolujuhtimisnurk, mida juhtides on võimalik jõuda mootori pinge piirideni. Pakuti välja mittelineaarne algoritm, mille abil on võimalik tõsta juhtimise stabiilsust kasutades kohanduvat häiringu tõkestamise juhtimise (ingl.k. *adaptive disturbance rejection control*, ehk ADRC) kontseptsiooni. Tulemused näitasid välja pakutud algoritmi puhul oluliselt suuremat stabiilsust koormuse häiringute suhtes võrreldes tavapärase PI kontrolleri kasutamisega. Lisaks pakuti välja algoritm, mille abil saab vähendada momendi värelust sünkroonreluktantsmootori momendi otsejuhtimise korral (DTC), kasutades momenti ja voogu, mis vastab lülitustabeli sünkroonsele taustsüsteemile. Tulemused näitasid olulist momendi väreluse langust.

Appendix

Paper I

Heidari, H., Rassölkin, A., Kallaste, A., Vaimann, T., Andriushchenko, E., Belahcen, A., and Lukichev, D. V. (2021). A review of synchronous reluctance motor-drive advancements. *MDPI Sustainability (Switzerland)*, 13(2). <https://doi.org/10.3390/su13020729>

Review

A Review of Synchronous Reluctance Motor-Drive Advancements

Hamidreza Heidari ^{1,*}, Anton Rassõlkin ^{1,2}, Ants Kallaste ¹, Toomas Vaimann ^{1,2}, Ekaterina Andriushchenko ¹, Anouar Belahcen ^{1,3} and Dmitry V. Lukichev ²

¹ Department of Electrical Power Engineering and Mechatronics, Tallinn University of Technology, Ehitajate tee 5, 19086 Tallinn, Estonia; anton.rassolkin@taltech.ee (A.R.); ants.kallaste@taltech.ee (A.K.); toomas.vaimann@taltech.ee (T.V.); ekandr@taltech.ee (E.A.); anouar.belahcen@taltech.ee (A.B.)

² Faculty of Control Systems and Robotics, ITMO University, 197101 Saint Petersburg, Russia; lukichev@itmo.ru

³ Department of Electrical Engineering and Automation, Aalto University, P.O. Box 15500 Aalto, Finland

* Correspondence: haheid@taltech.ee; Tel.: +372-56139797

Abstract: Recent studies show that synchronous reluctance motors (SynRMs) present promising technologies. As a result, research on trending SynRMs drive systems has expanded. This work disseminates the recent developments of design, modeling, and more specifically, control of these motors. Firstly, a brief study of the dominant motor technologies compared to SynRMs is carried out. Secondly, the most prominent motor control methods are studied and classified, which can come in handy for researchers and industries to opt for a proper control method for motor drive systems. Finally, the control strategies for different speed regions of SynRM are studied and the transitions between trajectories are analyzed.

Keywords: synchronous reluctance motor; efficiency map analysis; efficient motor technology; efficient control strategy; direct torque control; field-oriented control; predictive torque control; sensorless control; maximum torque per ampere; field-weakening



Citation: Heidari, H.; Rassõlkin, A.; Kallaste, A.; Vaimann, T.; Andriushchenko, E.; Belahcen, A.; Lukichev, D.V. A Review of Synchronous Reluctance Motor-Drive Advancements. *Sustainability* **2021**, *13*, 729. <https://doi.org/10.3390/su13020729>

Received: 11 December 2020

Accepted: 8 January 2021

Published: 13 January 2021

Publisher's Note: MDPI stays neutral with regard to jurisdictional claims in published maps and institutional affiliations.



Copyright: © 2021 by the authors. Licensee MDPI, Basel, Switzerland. This article is an open access article distributed under the terms and conditions of the Creative Commons Attribution (CC BY) license (<https://creativecommons.org/licenses/by/4.0/>).

1. Introduction

Industrial development has a significant impact on global warming and climate change. Considering the human impact on the environment from the aspect of resources, there are high demands for effective systems. This fact leads to the investigation of alternative developments in the field of electrical machines, as well. Energy efficiency requirements have led to the research and development of alternative technologies to produce electrical motors. The recent advances in the motor design area have provided manufacturers with some opportunities to save energy, use less rare-earth materials, and decrease the cost in terms of material and manufacturing processes. A life cycle analysis of electrical motor-drive systems by Rassõlkin et al. provides a comprehensive study on synchronous reluctance motors (SynRM) [1]. This study shows that starting from the acquisition of the materials, through manufacturing, transporting, and marketing, SynRMs are competitive at the usage stage, and efficient at the recycling phase. Lack of rare-earth materials, low cost, comparable constant-power speed range, maximum torque per ampere, and efficiency of SynRMs, in particular, permanent magnet (PM)-assisted ones (PMSynRM), have made these motors an interesting choice in traction [2,3] and more-electrical aircraft applications [4–6]. Besides, the need for highly efficient motors in centrifugal machines, conveyor systems, fans and pumps, cranes, compressors, elevators, crushers, and general machine building (winders, extruders, and servo pumps) can be met by SynRM [7–10].

Although almost a century has passed since the first invention of SynRMs, they have recently gained a lot of attention resulted from the emergence of the power-electronic device. In the last decade, the leading manufacturers such as SIEMENS and ABB have

released their newly designed SynRM drive systems [11,12]. While the line-start capability of SynRMs is provided by new designs, an additional shorted winding in the rotor can decrease the efficiency up to 10% resulting from the damping effect of the shorted rotor winding [13]. On the other hand, variable-speed drives (VSDs) provide highly efficient motor drives, especially for operating at partial-load conditions and high-speed operation [14,15]. Therefore, SynRMs are mostly applied in the industry with their drive package. From the control point of view, the research into motor control methods has experienced a boom to reach higher performance and efficiency of electric motors. This fact convinced the authors to survey the advancements in the whole SynRM drive system.

In this literature review, we collected the most prominent research works in the area from MDPI, SCOPUS, and IEEE XPLORÉ databases. The paper qualitatively summarizes the evidence on the topic of SynRM drive systems and is organized as follows: Section 2 reviews the dominant motor technologies and potential alternatives. Moreover, it investigates the applications and the opportunities and compares the performance of the motors regarding the cost and environmental considerations. Section 3 discusses the modeling strategies of SynRMs and investigates the applications, advantages, and shortcomings of each model. Then, the paper is more focused on the control aspect of the drive systems, where Section 4 classifies different motor control strategies regarding different features and deeply analyzes the latest development in the motor control methods to enhance the performance of the motor-drive systems. The wide speed range control of SynRM, which demonstrates their potent potential for traction application, is studied in Section 5 and the developments of the control strategies in each speed region are addressed, as well as the transition between each speed region. A comprehensive discussion and a conclusion of the study are provided in Section 6.

2. The Need for SynRMs

The mature three-phase induction motor (IM) is recognized as a well-established and widely available structure on account of its rigid mechanical construction and low cost and maintenance requirements. However, the implementation of the bars on the rotor leads to many drawbacks in this motor. The inherent warm rotor operation due to the currents in the bars can lead to rotor losses, which consist of around 20% of all losses in IM [13]. As a consequence of high substantial losses, the high temperature of the rotor can lead to more probable faults in bearings, which have the biggest share in IMs' faults according to Reference [16]. Moreover, the losses lead to lower efficiency of the motor. Besides, the mechanical faults in the bars are also likely in IM, which decreases the reliability of this motor [17–20]. The high-frequency slotting harmonics can be a problematic drawback of the IMs, which can be rarely attenuated by employing skewing [21]. Using an aluminum die-cast rotor cage for small- and medium-size IMs decreases the material cost and weight, which is the most common structure for these motors. However, the tendency to increase power density and efficiency has directed some manufacturers to produce a copper cage rotor for some applications [22,23].

Today, permanent magnet (PM) synchronous motors (PMSMs) are the dominant technologies for many applications, including traction [24,25]. High efficiency, high torque density, and desirable wide speed range performance of these motors have made the technology popular among manufacturers [26–28]. PM materials are the most important elements of PMSMs. Two common applicable PM materials for PMSMs are neodymium-iron-boron (Nd-Fe-B) and samarium-cobalt (Sm-Co), both of which contain the rare-earth elements [29,30]. The dramatic rise and fall of the price of the rare-earth magnets, especially Nd-Fe-B magnets, have directed the research towards rare-earth-free machines to replace high-performance PMSMs [31,32]. The reliability issues in PMSM due to possible faults of the magnets are also disputable.

The rotor design of SynRM distinguishes it from its IM and PMSM counterparts. In comparison with those conventional motors, SynRM attains higher reliability and easier maintenance (due to the very low winding and bearing temperature, and they also lack

cage or PMs in rotor structure) [33,34], lower cost (due to the lack of PMs in comparison with PMSM), faster dynamic response (due to smaller size in the same power range and lower moment of inertia), higher speed range (due to the wide constant-power operation in comparison with IM) [35] and higher efficiency in the same power range with the same frame size (due to the cold rotor operation in comparison with IM) [13,36], and higher power density and higher torque per ampere (in comparison with IM) [4,37]. In this sense, SynRM offers the high performance of PMSM, while it can be as cheap, simple, and service-friendly as IM. Therefore, the attention paid for these motors in high-speed applications has experienced continuous growth in the literature, which has convinced the electric vehicles (EVs) and hybrid electric vehicles (HEVs) manufacturers to apply SynRMs as an alternative for PMSM [38–40]. Having said this, the possibility of the drive with the same VSDs for IM and PMSM in various recently designed VSDs has provided a viable development base for SynRM [41]. All in all, the high efficiency of SynRMs against IM has attracted attention for applications such as pumps and fans. Also, the high performance and especially wide speed operation capability with the consideration of lack of rare-earth PMs compared to the PMSM has attracted the researchers to study these motors for traction application.

Table 1 summarizes the highlighted features of the dominant motors and SynRMs. The main goal of this comparison is to investigate the superiorities and discuss the drawbacks of the motors to provide an overview of the possible replacement of the dominant technologies with the cutting-edge SynRM technologies. It is worth mentioning that in some applications such as pump, fan, and conveyors, IMs are the dominant motors, which can be projected to be replaced by SynRM. Due to this fact, the SynRM should maintain the low cost, and provide higher efficiency to convince the industries to replace the IM drives with new technologies. Likewise, while the PMSynRM benefits from ferrite-magnet, the technology should maintain the performance competitive to PMSM to attract the manufacturers' attention.

Table 1. A comparison of motor technologies in highlighted features.

Motor Type	Stator and Rotor Structure Sample	Different Types	Main Applications	Superiorities	Drawback(s)
IM		<ul style="list-style-type: none"> • copper rotor • aluminum rotor • wound rotor • rotor skewing 	Industrial applications (pump, fan, traction, etc.)	<ul style="list-style-type: none"> + low cost of material and manufacturing process + line-start capability 	<ul style="list-style-type: none"> – low power factor – highly probable bearing fault
PMSM		<ul style="list-style-type: none"> • interior PM [42] • surface-mounted PM [43] • line-start PMSM 	precise control and high-speed performance (traction, robotics, aerospace, medical, etc.)	<ul style="list-style-type: none"> + high performance in wide speed range operation 	<ul style="list-style-type: none"> – rare-earth material usage
SynRM		<ul style="list-style-type: none"> • line-start SynRM • skewed rotor • rotor with asymmetric flux barriers 	Industrial applications (pump, fan, traction, etc.)	<ul style="list-style-type: none"> + reliable and highly efficient due to cold rotor operation + high dynamic + high overloadability + very high-speed capability 	<ul style="list-style-type: none"> – high torque ripple – severe low power factor
PMSynRM		<ul style="list-style-type: none"> • rotor skewing • asymmetric rotor structure • different barrier structure and PM material 	Traction applications	<ul style="list-style-type: none"> + very high performance without rare-earth PMs 	<ul style="list-style-type: none"> – hard manufacturing and installment process

In the rest of this section, the advancement of SynRMs is investigated and the prospect of their development in the industry is projected in different applications.

2.1. SynRM

As its name suggests, SynRM produces reluctance torque resulting from changing the magnetic reluctance, which is also called magnetic resistance. The magnetic flux flows into the lowest magnetic resistance. Therefore, the produced flux by the stator flows into the lowest magnetic resistance in the rotor. Hence, if the rotor is not aligned with the flux, the reluctance torque will rotate the rotor in the direction with minimum magnetic resistance. In this sense, the saliency ratio causes magnetomotive force (MMF) and the reluctance torque spins the rotor.

The rotor design of SynRM lacking bars and magnets leads to cold rotor operation. As a result, SynRM has praiseworthy loadability, particularly at lower speeds [44]. This motor can be loaded up to 2.5 times higher than the nominal torque [45]. This breakout torque is accessible for a short period on account of a cold start. Figure 1 presents the loading capability of an industrial SynRM versus speed [45]. As can be seen, there is a wide speed operation range for the motor with continuous loading capability with no need for separate cooling. To increase the torque density, a combined star-delta winding layout can lead to 5.2% higher torque density over the conventional star case in rated conditions [46].

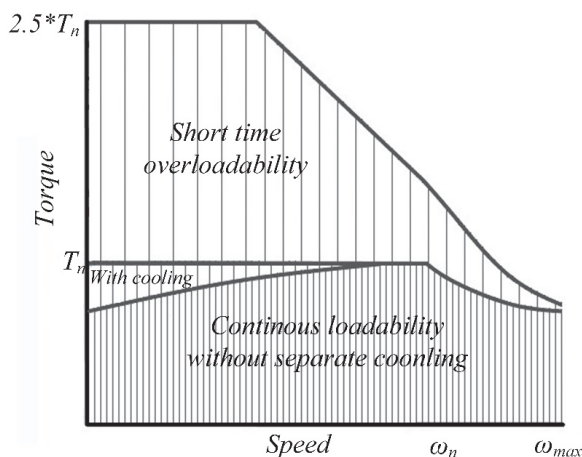


Figure 1. The loadability of synchronous reluctance motors (SynRM).

In the past, the focus on SynRMs was based on torque density, while recently, these motors are recognized as a highly efficient choice for the industry [12]. Owing to the lack of bars in the rotor, the iron loss is roughly omitted, leading to efficient motor operation [47]. Because of this superiority, the payback time of the SynRM drive is so short that it makes it quite reasonable to replace IM. The example payback time of the IE4 SynRM drive in comparison with the IE2 drive is projected for 1.6 years for 37 kW, 1500 rpm SynRM, with 8000 annual running hours [48]. The efficiency class in the IEC 60034-30 Part 1,2 [49,50] is defined by International Energy-Efficiency (IE) codes, where the higher the IE code is, the higher the efficiency of the electric motor is required. While the IE3 efficiency class (Premium class) has been mandatory in the European Union countries since 2015 [13], the SynRM offers the IE5 efficiency class (Super-Premium class) [12]. Moving from IEC 60034-30-2, IE3 to IE4, or even IE5 class [50] can make the SynRM a more probable dominant technology, especially for low power range applications.

On the other hand, SynRM suffers from some severe drawbacks. In this technology, the power factor is quite low [51]. The maximum power factor of SynRM depends on the saliency ratio. The definition of the saliency ratio and power factor can be found in

Reference [52]. Figure 2 gives information about the power factor improvement in terms of saliency ratio change in a typical SynRM. In this sense, the higher the saliency ratio the SynRM has, the higher the power factor the motor can provide. A sophisticated design of a laminated anisotropic rotor is proposed in Reference [53], which can increase the saliency ratio and as a result, improve the power factor and torque density. In this study, to control flux paths, some cut-offs are applied in the laminations, which influences the direct and quadrature axis inductances. This proposal leads to power factor improvements. This strategy preserves all the benefits of the motor. However, the recent improvements by these approaches are negligible. The interaction between the spatial harmonics of MMF and the rotor geometry causes considerable torque ripples in SynRMs [54]. High torque ripples and as a consequence, the acoustic noise of these motors, have become a challenge, which persuaded considerable effort to cover this drawback in both design and control aspects [5,55–59]. Some research works address the reduction of the torque ripples through optimization of the rotor structure [60,61]. Among proposed design solutions, rotor skewing can halve the torque ripples of SynRM, and asymmetric rotor flux barriers decrease the torque ripples to two-thirds, in both SynRM and PMSynRM [62].

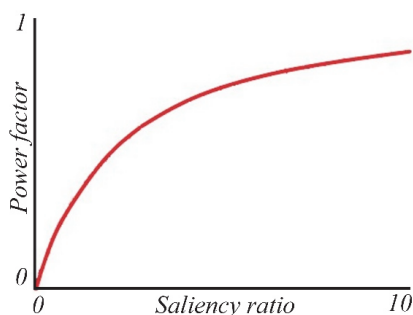


Figure 2. The relation between saliency ratio and power factor in SynRM [58].

2.2. PMSynRM

Although the SynRM avoids PMs in its structures, it sacrifices the efficiency, power factor, and torque density of the PM motors. The torque produced by SynRM is purely reluctance torque due to saliency and rotor anisotropy. This contributes to the high saturation of this motor, which limits the flux density. Adding ferrite PMs to the rotor, PMSynRM exploits the peculiar rotor characteristic of SynRM and the high performance of PMSM at the same time, as shown in Reference [63]. These motors have a desirable performance at higher speeds than base speed, fulfilling the constant-power speed range requirements [64,65]. The currents for the same torque are decreased in PMSynRM. Consequently, the losses also decline, especially for the partial load. The power factor sees a significant change of about 10% for low currents and 6% for high currents. Figure 3 shows that the voltage vectors of the SynRM and PMSynRM have different q -axis values and the same d -axis values. This leads to different values for the machines' voltage and current angle (φ). Fluxes have the same value on the q -axis and different values on the d -axis. This can be presented as an effect of the magnets, which affects the torque angle (δ).

On the other hand, in terms of maintenance, manufacturing, and assembling, SynRM and IM are superior to PMSynRM. Besides, similar to SynRM, PMSynRM suffers from high torque ripples [66], which has directed many research efforts on the design [43] and also the control aspects [67,68]. In Reference [43], the torque ripples of a direct-drive PMSynRM are decreased by material-efficient axial pole pairing. Multiphase PMSynRM also presents fewer torque pulsations and higher torque density with fault-tolerant operation capability [4,69–72]. Besides, these motors are applied where there is a need for less power in each phase to increase reliability. A comparison of a typical SynRM and a PMSynRM performance based on the literature review is provided in Figure 4.

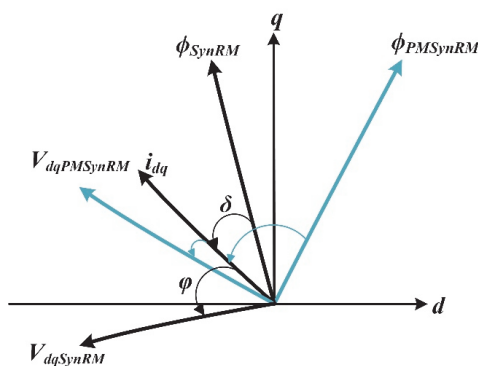


Figure 3. The vector diagram of SynRM/PMSynRM.

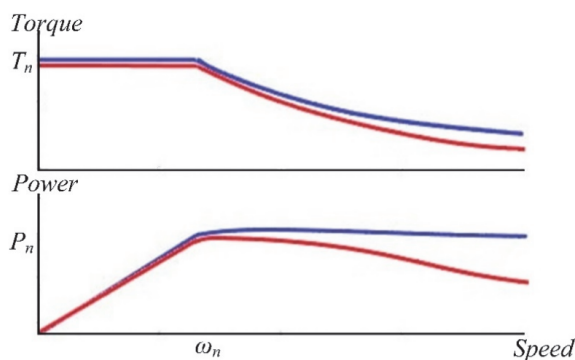
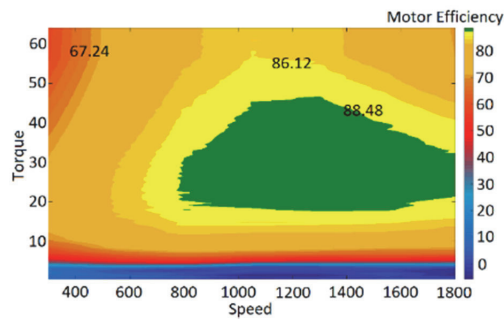


Figure 4. Torque and power versus speed diagram for SynRM (red) and PMSynRM (blue).

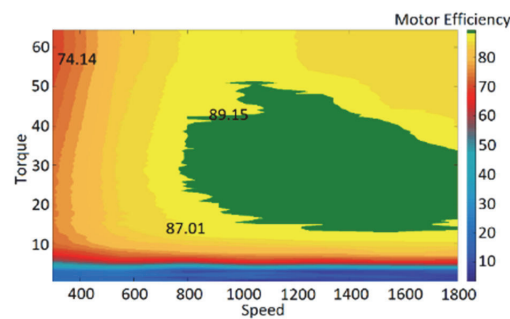
Where, T_n , P_n , and ω_n denote the rated torque, rated power, and rated speed of the motors, respectively. In this figure, the torque and power output versus the speed of a typical SynRM and a PMSynRM in the same power and speed range is depicted. The figure demonstrates the enhancement of the torque and power of the motor due to the inserted ferrite PMs, particularly in the high-speed operation of the motor.

2.3. Comparative Analysis of Motor Technologies Efficiency

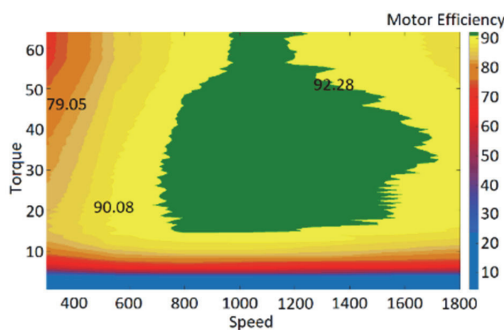
Studied electrical motors present different efficiency behavior under different circumstances. To compare the efficiency of the motors in variable-speed applications, only the efficiency map can provide trustworthy information. Figure 5 illustrates the efficiency map for IM, SynRM, and PMSynRM. The motors were run in the same power range and the same test environments. The tests and the setup's specifications are described in Reference [63]. In general, PMSynRM had the highest efficiency in the whole speed, torque area. SynRM was the second most efficient motor in the whole region. More importantly, in the partial load, IM provided lower efficiency than the other two motors, causing a high energy cost for the operation in the lower load and speed range. This specification is a notable reason to consider SynRM as a cost-efficient alternative for IMs.



(a)



(b)



(c)

Figure 5. Efficiency map of 10 kW (a) IM, (b) SynRM, and (c) PMSynRM prototype.

3. Qualities of SynRM Modeling

For the sake of different purposes, such as design [26], control [73], fault diagnosing [74,75], thermal analysis [76], loss determination [77], motor parameter calculation [52], stability analysis [78], and efficiency improvements [79], modeling is an inseparable part of many studies in motor drive areas. In the modeling of SynRM, parameters' estimation preciseness, the computation time of the parameter determination, and some factors for different motor operation areas, linearity and nonlinearity of the model have been crucial criteria to consider. The most critical topic in different modeling methods of SynRM for different purposes is the parameter identification of SynRM. Especially, for more accurate control of SynRM, the inductances and the stator resistance are of paramount importance to be identified in a self-commissioning process. This is mostly due to parameter variation

under the different thermal conditions and cross saturation of the rotor. More specifically, the inductances are considered as constant values, while these parameters are functions of currents in different axes. We categorized the parameter identification into three different groups as follows:

1. Numerical and analytical models of SynRM
2. Offline parameter identification
3. Online parameter identification through an inverter

As a numerical approach, the finite element analysis (FEA)-based model is a precise and confinable model for motors. Commonly, new modeling methods are compared to FEA to validate their results. However, the high computation burden imposed by FEA leads to a tedious and time-consuming process, which severely limits the applications for online purposes, such as control applications. This characteristic makes the FEA more applicable to design and optimization purposes for all types of electrical machines, including transformers [80,81]. However, using FEA, the parameter values could be obtained and utilized as a lookup table for simulation purposes, as in Reference [82]. Correspondingly, the authors believe that the parameters obtained by FEA could be utilized in the control loop as a lookup table in different operation points. An FEA-based model of SynRMs has been determined in References [83–85]. In Reference [86], a novel rotor structure is proposed based on two-dimensional (2D) FEA analysis for PMSynRM. This structure proposes adding bypass ribs on the flux barriers which reduces the irreversible demagnetization of PM and torque ripple. The size and the location of the bypass ribs are investigated and improved based on FEA. Figure 6 shows the rotor structure of the proposed method and the field distribution of the rotor. The figure illustrates that at the rated operation point, the flux density in the bypass ribs is very low and a small portion of the flux passes through them. It can be concluded that the bypass ribs can pass a part of demagnetization flux and protect the PMs.

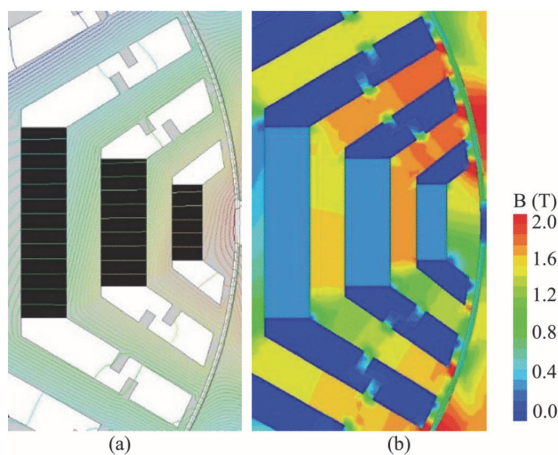


Figure 6. (a) The novel rotor structure and (b) field distribution at rated operation point [86].

The experimental results show that the motor with the proposed structure performs roughly the same output torque ability. Besides, regarding the higher anti-demagnetization ability of the PMs, the proposed motor structure presents 35% less torque ripple in comparison with the motor with the conventional structure. The output torque of the proposed motor and the conventional motor is presented in Figure 7. The figure shows almost the same average torque and less torque ripple for the proposed structure.

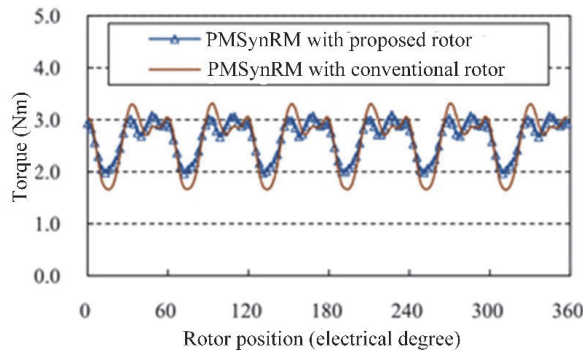


Figure 7. Torque response of the novel structure and the conventional motor [86].

As an alternative to FEA, analytical models are mostly applied in the literature for various purposes. The winding function model is one of the models of SynRM, which is studied in References [87,88]. In these studies, the obtained inductance values are compared to the FEA model. The d, q model of SynRM is also one of the analytical models, which is studied in many research works. In Reference [52], the offline parameters' identification is carried out through the Dc decay test applying the d, q model. A similar study with a more detailed description for parameter identification is carried out for both SynRM and PMSM in Reference [89]. An accurate analytical model of PMSynRM is also defined by Armando et al. in Reference [90]. In this research work, the impact of cross-saturation on rotor position estimation is investigated and a simple model is proposed and validated, disregarding cross-saturation. With a different approach, radial basis function neural networks are applied in Reference [91] to obtain currents and flux linkages in SynRM and interior permanent magnet synchronous motor (IPM). The relation between these values has been reported to develop magnetic models.

Apart from standstill tests, inverters provide more precise identification possibilities for the SynRMs. In SynRM, due to the lack of PMs, injecting currents for parameter identification in both d - and q -axes is viable, with no need to lock the rotor. The flexibility of the voltage applied to the motor through the inverter has encouraged the researchers to study the parameter identification of SynRM with various self-commissioning methods. Online parameter identifications are inevitable for precise control of SynRM due to the severe cross-coupling and the rotor saturation of this motor. In Reference [92], a sensorless self-commissioning method of SynRM at standstill is presented to identify the magnetic model of the motor by injection of the test voltages. Since the test voltages are high frequency as compared to the motor rated voltage, the model is robust against stator resistance errors and inverter voltages.

Considering all the available models for SynRM, the d, q model of SynRM is addressed in many research works. For control purposes, the d, q model presents the most simple and practical model of the motor. A comprehensive model of SynRM and PMSynRM can be found in Reference [52]. A short description of the d, q model of SynRM from this paper is presented as follows.

$$\begin{aligned}
 \bar{I}_s &= i_d + ji_q; \bar{V}_s = V_d + jV_q; \Psi_d = L_{sl}i_d + \Psi_{dm}, \Psi_q = L_{sl}i_q + \Psi_{qm} \\
 \bar{V}_s &= \frac{2}{3} \left(V_a + e^{\frac{j2\pi}{3}} V_b + e^{-\frac{j2\pi}{3}} V_c \right) e^{-j\theta_{er}}; i_m = \sqrt{i_d^2 + i_q^2} \\
 \bar{\Psi}_s &= L_d i_d + jL_q i_q = \Psi_d + j\Psi_q \\
 \bar{V}_s &= R_s \bar{I}_s + \frac{d\Psi_s}{dt} + j\omega_r \bar{\Psi}_s \\
 T_e &= \frac{3}{2} p (\Psi_d i_d - \Psi_q i_q) = \frac{3}{2} p (L_d - L_q) i_d i_q \\
 \frac{1}{dt} \frac{d\omega_r}{dt} &= T_e - T_{load}; \frac{d\theta_{er}}{dt} = \frac{\omega_r}{p}; \Psi_{dm} = L_{dm} i_d, \Psi_{qm} = L_{qm} i_q
 \end{aligned} \tag{1}$$

In this model, the cross-coupling magnetic saturation effects are neglected for simplification purposes. However, for the precise control of SynRM, the cross-coupling magnetic saturations should be considered in the control.

4. Latest Developments of SynRM Control Strategies

Nowadays, VSDs have been applied in many industries for efficient, high-performance, robust, and precise control of electrical motors. Although implementing VSDs adds up to the cost, it is inevitable for both variable-speed and fixed-speed operation to reach high efficiency for any motor technology. Besides, the differences between the prices of the drive systems in the same rated power can be compensated by the lower energy cost. Recent studies, innovations, and also the need for higher efficiency and better performance support the prospect of more future widespread development of motor drive systems in the industry [12,93,94]. These parameters require more study in different areas that can be categorized as follows:

- Optimal design of motors,
- Optimal design of converters,
- Optimal design of controllers.

The control unit of the electric drive system plays a crucial role in system performance. A control system technology with high performance ensures an efficient and reliable energy conversion. In general, a control unit contains the following [95]:

- Input modules, e.g., analog to digital converters, which continuously capture input variables from electrical and mechanical sensors and/or transducers.
- Output modules, i.e., pulse-width modulation (PWM) module, which continuously provides switching sequences.
- Peripherals modules for programming and data exchanging.
- Main processor for executing and processing control algorithms.

The control algorithms characterize the behavior of the electric drive systems. Hence, to provide a high-performance drive system for motors, firstly, a proper control strategy should be devised. Usage of frequency converters, controlled by microprocessors, provides researchers with a high potential of using flexible methods to reach a better performance. On the other hand, VSDs inject some high-frequency currents into the system [96]. Consequently, some unexpected losses occur, which requires to have a more precise control algorithm on the drive side. As the SynRMs in industries are dominantly driven by frequency converters, the researchers are convinced to study more in this field. Efforts of the researchers in SynRM drive systems are mainly targeted to increase robustness [97–99], suppress torque and current ripples [67,100–103], decrease losses, and improve efficiency [104–106], improve the performance of the speed and position estimation [107,108], and amend the dynamic torque response with smooth transition between different speed regions [98,101]. Despite the existing efforts, investigating improved control strategies for SynRMs remains a challenging task.

In practice, control strategies for motors are classified as scalar and vector control methods. Scalar control methods are mainly known as V/f control methods. These methods are the simplest and the most applied control methods in industrial VSDs [109]. The method can be applied in open-loop or closed-loop control systems with current and speed sensors or with the sensorless control approach [110]. V/f , V/f^2 , and V/\sqrt{f} or $I-f$ are the main scalar control methods studied in the literature. The V/f control method generates voltages regarding the amplitude and frequency to keep the ratio of the values constant. This simple concept makes the method applicable for many low-cost-demanding purposes [111,112]. However, the tracking of the commanded speed is not guaranteed in this method. As the second group of motor control methods, field-oriented control (FOC), direct torque control (DTC), and predictive control (PC) methods including model-based predictive DTC (MPDTC) and model-based predictive current control (MPCC) are recognized as vector control methods addressed in many papers and implemented in many industrial VSDs.

An overview of the main vector control methods regarding the control method structure is presented in Table 2.

Table 2. Structural comparison of the basic motor control methods.

Items	DTC	FOC	MPDTC	MPCC
Coordinates reference frame	α, β	d, q	α, β	d, q
Principle	Stationary voltage equations	Rotor reference frame equation	Stationary voltage equations	Rotor reference frame equation
Controlled variables	Torque and stator flux	d -, q -axes currents	Torque and stator flux	d -, q -axes currents
Rotor position measurement	Not required	required	required	required
Current control	without	with	without	with
Coordinate transformations	Not required	required	Not required	required
Modulator	Not required	required	Not required	Not required
Switching frequency	Varies widely around the average frequency	constant	Varies around the average frequency	Varies around the average frequency
Controllers	hysteresis	Proportional integral controller (PI)	Cost function optimization	Cost function optimization

Traditionally, all the conventional control methods are based on machines' models or some predefined strategies. To alter this classic view on the control system, lately, artificial intelligence-based controllers have been implemented in the power electronics and drive systems. To name a few, fuzzy logic (FL), adaptive neuro-fuzzy artificial neural network (ANN), and adaptive recurrent fuzzy neural network (ARFNN) are the methods that have been studied for SynRM drives [113–116]. FL helps the researchers to analyze continuous values—in contrast with discrete values in traditional methods—and control the system in a continuous mathematical system [117,118]. This provides a control system with characteristics compatible with the physical components. Lower cost in comparison with the traditional systems, higher efficiency, more robust system, more reliable, more customizable, and the possibility to emulate human deductive thinking are some advantages of FL control. The drawback of fuzzy control can be the need for high human expertise and regular updating of rules, not applicable for much smaller or larger data than historical data, and the requirement for massive data. An ARFNN control for SynRM servo drive is studied in Reference [119]. In this paper, FOC is implemented to formulate the dynamic equations. Then, the ARFNN control system tracks the reference and drives the motor. Additionally, the Lyapunov stability theorem and the backpropagation method is applied for online parameter training.

Apart from the artificial intelligent method, deviation model-based control (DevC) is also an alternative to the traditional control method [120]. As its name suggests, this method benefits from a deviation model of the motor for control. With this approach, the model of the motor is simplified through normalization to obtain the deviation model of the motor. Then, the deviation model of the motor is utilized to control the motor. Since the motor drive systems deal with the dynamic behavior of the motors, the DevC proposes a fast dynamic control method. In Reference [121], the DevC of SynRM is proposed in comparison with FOC and DTC. Due to the normalized model, the method proposes simpler and more robust control against parameters' variation compared to the FOC.

Besides, DevC presents less torque ripple, higher dynamic, and better flux regulation at startup when compared with DTC.

In this section, the control methods are classified based on their highlighted strength. We categorized the motor control methods into scalar and vector control methods. Then, some improvements in the main control algorithms were investigated. These methods change some parts of the main algorithm by adding or removing some extra computation for some specific purposes. Moreover, some combinations of the main methods have also been studied to benefit from some advantages of the two methods, simultaneously. Finally, the general control theories are studied. These methods are either singly applied to drive the motors or they are utilized in the main motor control algorithms to enhance their performances.

Figure 8 demonstrates the classification of motor control methods. In this diagram, all the methods, which are more specifically applied for motor control systems, are depicted in round shapes. The general control theories are demonstrated in square shapes below the motor control methods. Finally, at the bottom of the diagram, different features of the control method are demonstrated in rectangular shapes with different colors. Each color represents a specific feature showing the strength of each method in different terms. The highlighted features of each control method are demonstrated as bubbles in specific colors. The size of each bubble implies the significance of the feature in the method. The bigger the bubble of each color, the more significant feature the method has in that area. With the concept in this figure, the drawbacks of the methods can also be interpreted. For instance, the most significant advantages of FOC are its low torque ripples in the motor shaft and low harmonics in phase currents. These two advantages of the FOC method are shown in its block as bubbles. Also, FOC has a constant switching frequency, which is shown in its block, as well. On the other hand, as compared to other control methods, FOC has a high computation burden for the microprocessor, which is known as a shortcoming for this method. Therefore, there is no bubble in the same color as the block for simplicity. The abbreviations are presented in the text.

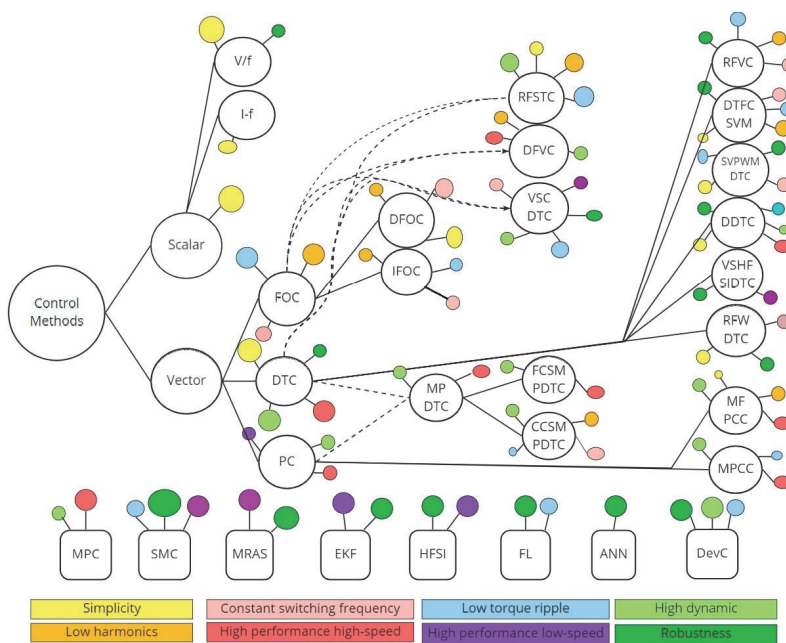


Figure 8. Motor control methods classification.

For a more detailed description of the block diagram, the features are to be discussed. As the first feature of the control methods, the simplicity of a control method denotes less computational burden on the microprocessor. Normally, complicated mathematic calculations such as proportional-integral (PI) regulations lead to high execution time. Consequently, the cost for the microprocessor becomes high, which can make the control algorithm less desirable. For instance, scalar control is considered as a simple control algorithm due to simple calculation in the control loop. Therefore, if a simple control algorithm is looked for, scalar control can be a desirable choice. Low current harmonics is the next feature to discuss, which is considered as a strong point for a control method. In the motor-drive systems, harmonic currents can be deduced from many different sources, including motors, drive systems, and the control algorithm, as well. In the literature, many research works are carried out to decrease harmonic currents. Some control methods have variable switching frequency, which is considered a weak point in many applications such as EV due to safety concerns. Variable switching frequency makes the fault diagnostic of these systems difficult using switching frequency monitoring. High performance of the method at high speeds is one of the popular topics, especially in traction applications. Proper control of the method on flux and torque is crucial at high speed. The next feature to discuss is the low torque ripple, which can lead to less acoustic noise and higher efficiency of the system. The operation of the control methods in low-speed regions of motors is also an important factor to consider. For instance, classic control methods do not consider variable references for flux, which leads to inefficient control of the motor. Besides, rotor position tracking is a challenge that motor control methods face at very low speeds. The performance of the control methods in transient mode is also crucial to pay attention to. One of the key features of control methods in transient mode is the high dynamic. The high dynamic of a method denotes the fast response of the method to the changes in references. Robustness is the next feature that has attracted researchers' attention in motor control systems. This feature in control algorithms denotes the robustness of the method against parameter variation (e.g., stator resistance) and external disturbances (e.g., load) in drive systems.

The rest of this section describes the main control methods and the improvements in this area that have been recently studied in the literature.

4.1. FOC of SynRM

Thanks to the high steady-state performance of FOC, the general trend toward other methods has not yet been dominated. The precise control method, low torque ripples, and the constant switching frequency of FOC still draw the researchers' attention [122]. FOC is more popular in the area, such as the mining and steel industry, where the need for efficiency and better steady-state response is preferred to transient response. This method controls the motor in the d, q reference frame, modeling the motor as a DC motor to achieve a convenient control. Direct field-oriented control (DFOC) and indirect field-oriented control (IFOC) are the main approaches to control the decoupled currents in the synchronous reference frame. If the rotor flux angle is obtained through the estimated flux, the method is referred to as DFOC. On the other hand, the IFOC method obtains the flux angle through the detected rotor position using a mounted shaft encoder. Briefly, the advantages of FOC are as follows:

1. High steady-state performance,
2. Precise current control,
3. Simple implementation of the method,
4. Simple compatibility with many AC motors,
5. Simple modulation system implementation,
6. Constant switching frequency.

The dominant trend in the studies on FOC is towards decreasing the position estimation error [122,123] and increasing the efficiency of the motor under control [124,125].

compares the most prominent control methods in terms of torque ripples. As discussed, FOC presents the lowest torque ripples, while DTC presents the worst performance when it comes to torque ripple in the motor’s shaft.

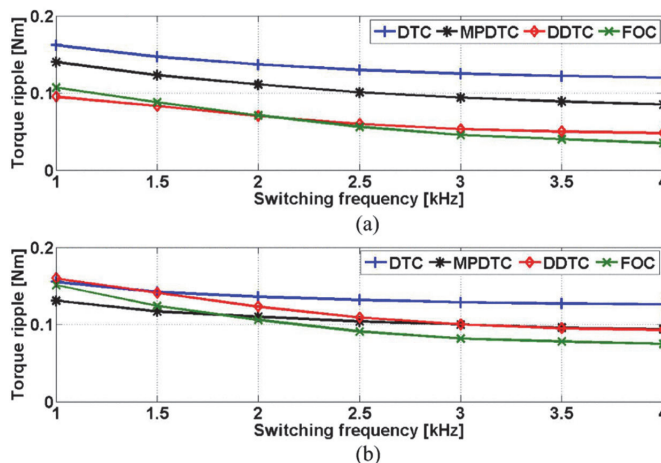


Figure 10. A comparison of torque ripples of different control methods in different switching frequencies under zero load and (a) 500 r/min, (b) 1000 r/min [129].

4.2. DTC of SynRM

The first attempt to implement DTC on SynRM was carried out by Boldea et al. in 1991 [130]. DTC of SynRM-drives is now attracting market interest [131]. According to the literature, this is attributed to the intrinsic features, as follows:

1. Simplicity due to the lack of PWM signal generator module and current control.
2. Fast response and high dynamic due to the direct control of torque.
3. Robust control due to low dependence on motor parameters.

In the DTC method, the instantaneous torque of the motor, as well as stator flux linkage, are directly controlled, and the transformation of the coordinates is avoided. The switching table is a lookup-table, which opts for a defined combination of switching sequences with regards to the inputs. The inputs of the switching table are the stator flux and torque error signs along with the sector of the stator flux. To obtain these inputs, stator flux and torque estimators are required in DTC. Similarly, the stator flux position sector with respect to the phase a of SynRM is calculated. However, compared to FOC, the online estimation has smaller issues, since the observers are not in the control loop and require lower speed. The estimation of flux and torque in DTC is carried out through observers by applying the following equations.

$$\overline{\Psi}_s = \int \overline{V}_s - R_s \overline{I}_s \tag{2}$$

$$T_e = \frac{3}{2} p (\lambda_\alpha i_\beta - \lambda_\beta i_\alpha) \tag{3}$$

The active voltages (\overline{V}_s) are defined in DTC through Equation (1). It should be noted that, since the rotor position is synchronized with the flux, in the encoder-based DTC, the sector of the rotor flux with respect to phase a is obtained through the encoder. A more detailed description of the DTC of SynRMs is reported in Reference [128]. Figure 11 shows the block diagram of the conventional DTC of SynRM.

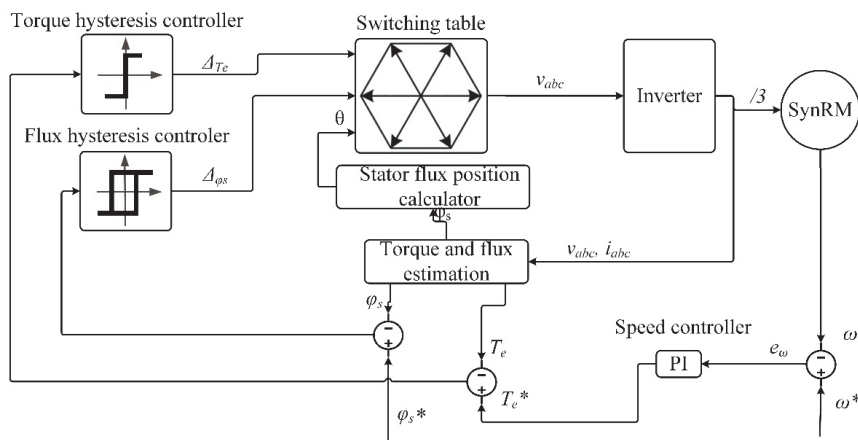


Figure 11. DTC of SynRM.

Direct control of torque assures a high dynamic control, which makes DTC superior over other methods [132]. As this method does not apply the current regulator, it significantly attains higher transient torque control performance. DTC also uses only the stator resistance for motor control, which causes relatively robust control of the motor. This method is mostly implemented in servo applications due to the fast dynamic. In general, the customers who are seeking a better transient response, rather than a steady-state response, are inclined to DTC.

However, the DTC method suffers from high torque ripples [133]. To take SynRMs' high torque ripples into account, the conventional DTC of these motors cause severe torque ripples in the motor. The disadvantages of DTC are listed below:

1. High torque and flux ripples,
2. Variable switching frequency,
3. Relatively high harmonic currents,
4. Bad performance at low speed, which may include high noise, bad torque and flux control, and bad speed tracking.

Lack of current controller in DTC's block diagram leads to high torque ripples. Multi-level inverters have proven a proper solution for torque ripples, which are applied with DTC in Reference [134]. Another solution that amends this shortcoming of DTC is the overmodulation scheme for DTC of SynRM, presented in Reference [101]. This method keeps the simplicity of DTC, decreases the torque ripples, and provides constant switching frequency. Another viable approach is DDTC. Basically, by this method, an attempt is made to apply the active voltages for some period of sampling time and apply zero voltages for the rest of the sampling time. Therefore, the motors' torque and similarly the flux does not considerably pass the hysteresis limits. This results in a notable reduction in torque ripples at the cost of complexity imposed on the method. Besides, a notably higher switching frequency occurs in switches. A more sophisticated and more robust version of this method is applied for the control of PMSM in Reference [135] and also exploited in Reference [98] for the DTC of SynRM. This method is also applied in Reference [128] in RFSTC for more torque ripple suppression. The usage of a reference flux-vector calculator (RFVC) is another solution for high torque ripples suppression of DTC. RFVC has been proposed for DTC in Reference [136] to decrease torque ripples in IPM. This method replaces the two hysteresis controllers and the torque PI controllers with the RFVC block. Moreover, RFVC achieves a constant switching frequency with the replacement of the switching table with space vector modulation (SVM) and covers the drawback of variable switching frequency, as well. The method retains the robustness of DTC and the lack of a current control loop. On the other hand, the Space vector modulation (SVM) block and the usage of flux angle impose some

complexities to the system. A direct torque flux control (DTFC) with SVM is also proposed in Reference [137] for PMSynRM in hybrid-EV applications. Space vector pulse width modulation-based DTC (SVPWM-DTC) is another approach to overcome the high torque ripples and the variable switching frequency of DTC, which is studied for EV applications in References [138,139]. This method significantly decreases the switching losses in the switches. By this approach, some computation burden will be augmented to DTC.

Some strength points of DTC can also be improved to achieve better performance. Among these features, robustness has gained growing popularity for DTC of SynRMs [140–142]. These motors operate under high flux saturation conditions. Thus, high parameter variations are likely in SynRM, not only in stator resistance under thermal conditions but also in inductances due to saturated rotor. In Reference [132], a mechanism is applied to limit the torque in the DTC of SynRM. The method is robust against parameter variation. In this method, to obtain stable operation of the motor, the torque-limiting mechanism modifies the flux reference with respect to the torque error sign. In line with the robustness of the method, this method leads to a smooth transition between the maximum torque per ampere (MTPA) and FW regions. In this article, to demonstrate the robustness of the method, the authors have implemented the acceleration of the motor with the normal condition of the control along with the acceleration in the same condition with a 35% increase of inductance in the d -axis (L_d). With this experiment, the parameter mismatch and erroneous torque reference are modeled, and the performance of the method is tested. It is worth mentioning that without compensation, the operation of the motor can be unstable under this condition. Nevertheless, with this torque-limiting mechanism, the torque reference will be reduced in the failure detection condition until successful torque control is detected. This is shown in Figure 12. In this figure, in the second subplot, the torque response of the method is illustrated, in which the red line indicates the motor's torque, and the blue line shows the reference torque. This figure shows that the torque limit ($T_{e-limit}$) surges due to the consecutive torque control failure, which indicates the parameter mismatch. Then, the torque reference drops to a lower limit, which leads to successful torque control of the motor. Consequently, a stable acceleration of the motor is achieved.

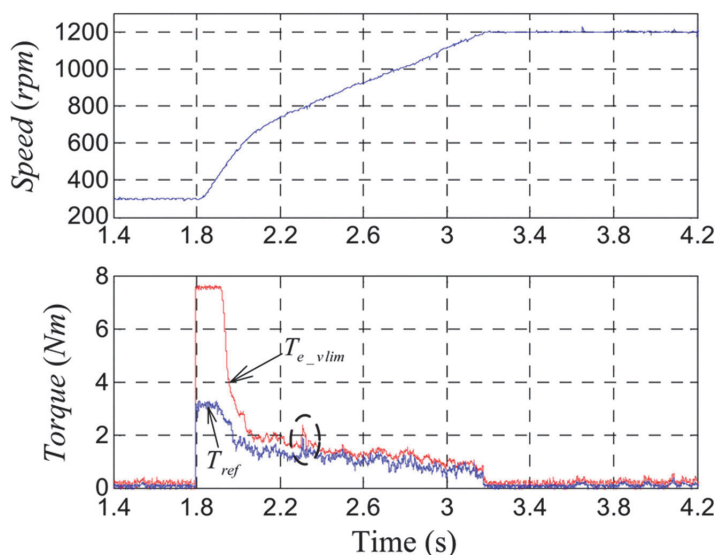


Figure 12. SynRM speed (first subplot) and torque (second subplot) response to the 35% increase of L_d with a torque-limiting robust DTC control algorithm [132].

Sliding mode control (SMC) is also one of the main approaches to increase the robustness of DTC. This method is mainly applied for torque and flux estimations in DTC. SMC is applied for DTC of SynRM in Reference [143]. In this paper, the robustness against stator resistance variation is achieved through an online detection with a simple observer. This observer exploits SMC in the variable structure control-based DTC (VSC-DTC) for the objective of robustness. In this method, the constant switching frequency is also achieved through the SVM block and the torque ripples are also decreased because of stator-flux field-oriented referenced PI controllers. The simplicity of the DTC has been deteriorated instead, although the high dynamic of the method is guaranteed. From another angle of view, it is alleged in Reference [120] that less parameter dependency can be achieved by replacing the commonly used PI controller with a normalized deviation model of SynRM. The results for this claim validate the performance of the method and the proposed approach can increase the VSD’s robustness.

Limited performance of DTC at low speed, such as reduced torque and flux controllability, and consequently, high noise due to the high torque ripples, are concerned in many research works [144,145]. Sensorless DTC is one of the solutions, estimating the rotor position and speed with different strategies. The high-frequency (HF) signal injection (HFSI) is one of the most popular methods. These methods are reliable and have a desirable performance at low speed, particularly at the standstill. Even though, the resonance and extra losses are notable drawbacks of this method, which limits their utilization, especially at medium and high speeds. Sayeef et al. have addressed the HFSI in References [146,147] at low speed, including standstill, to obtain the rotor position and speed. Reference [146] discusses the variable structure control, using HFSI (VSHFSI-DTC) at very low speed, which offers a highly robust control against parameter variation. The method exploits HFSI in low speed and sliding mode observers at high speeds to obtain rotor position and speed. In Reference [148], the authors have investigated a sensorless DTC for low speed, based on extended Kalman filter (EKF). In this paper, the estimations of rotor position and speed are achieved without HFSI.

4.3. PC of SynRM

Modern PC methods are becoming popular among researchers. These methods open a new avenue for control solutions with simple and high-performance control. In principle, PC can consider several constraints at the same time and calculates the optimal switching states based on the status of the motor in the current sampling period. Despite the simple concept of the method, PC methods cause a high computational burden, as well as high sampling and switching frequency. However, with the emergence of powerful microprocessors, many research works have been recently conducted on the PC of SynRM [100,149]. The predictive control methods can be categorized as in Table 3.

Table 3. PC methods.

Model-Free		Model-Free Predictive Current Control (MFPC)	
		MPCC	
		Finite control set MPDTC (FCS-MPDTC)	Duty ratio modulation MPDTC (DRM-MPDTC)
Model-based	Model-based predictive direct torque control (MPDTC)	Continuous control set MPDTC	Based on PWM
		(CCS-MPDTC)	Based on SVM

One of the predictive approaches to control SynRM is MFPC, which is studied in References [102,150,151]. Regardless of the motor’s model, this method simply controls the motor current, which leads to low switching frequency and low computational burden. The method detects the current of the motor and generates the voltage vector to directly apply to the motor. In the next sampling period, based on the new current measurement,

the old current variation will be calculated. Then, the current variation in the next period will be estimated. Then, the current prediction will be executed, and the cost function will be calculated to choose the optimal switching state. This strategy will execute constantly to control the motor current, predictively. With this simple strategy, MFPC avoids the motor parameters or back-electromotive force (emf) estimation. However, the method requires two current measurements in each sampling period. This can cause the detection of the spikes in current, which are due to instantaneous switching inside the inverter. Additionally, stagnant current-variation updates can degrade the performance of the method. These drawbacks of MFPC are fairly eliminated in Reference [103] through the sampling of the current once, instead of measuring the current twice per sampling period.

Apart from model-free predictive motor control methods, model-based control (MPC) methods are gaining more attention in SynRM drive systems [152–155]. MPC considers the model of all of the system, including the inverter and the motor. Based on the system's model and the feedback from the system, MPC predicts the future states of the system in the next step regarding the command switches in the current sampling period time. These states have a constant number, which is referred to as the prediction horizon. Based on the prediction horizon, the cost function will be calculated and the optimal switching state will be opted to control the motor. Numerous objectives can be considered in cost function with various coefficients. Considering the weight of each objective, the value of the weight coefficients can vary. One example of a cost function to obtain voltage vectors to apply to the motor is addressed in Reference [141] as follows:

$$g = |u_{ds}^*(k+1) - u_{dsn}|^2 + |u_{qs}^*(k+1) - u_{qsn}|^2; n = 0, 1, \dots, 6 \quad (4)$$

where g represents the cost function and $u_{ds}^*(k+1)$ and $u_{qs}^*(k+1)$ indicate the predicted reference voltage vectors at $k+1$ instant in d - and q -axes and u_{dsn} and u_{qsn} are the instant values of the voltages with seven different states. The predicted voltages are obtained using the model of the motor, as presented in (1). As a more descriptive approach, a flowchart of a sample PC is illustrated in Figure 13 that shows the predictive algorithm.

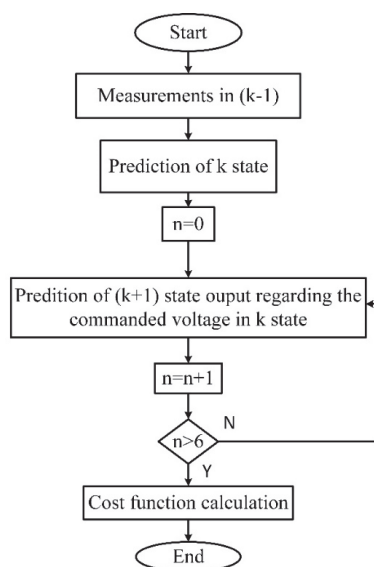


Figure 13. Flowchart of a PC algorithm.

The most popular model-based approach is the integration of MPC with DTC, which is generally known as MPDTC in the literature [152]. Figure 14 shows the diagram of an example of MPDTC. As can be seen, the method is like DTC and can be implemented on a setup with a DTC drive system with no other hardware required [100]. The state values in this method are motor torque and stator flux, which can be changed, as in Reference [140]. Theoretically, MPDTC is a new approach to DTC which directly controls the mean torque value. Akin to DTC, the switching states are calculated to achieve the desired torque at the end of each control cycle. Apart from its simple programming, this control method produces the optimized voltage vector in each sampling time, leading to a heavy computational burden. This results in 2.5 times higher execution time than DTC [156]. MPDTC offers a viable alternative for DTC, which works with high dynamic performance, fast speed response, and lower torque ripple. Considering the high flexibility in the structure, this method can protect the power electronic elements from overcurrent and guarantee a lower average switching frequency. In comparison with FOC, MPDTC has higher performance in the transient state, while FOC offers better steady-state performance [157]. The authors of Reference [158] present an encoderless MPDTC for SynRM, which covers the low performance of DTC at very low and zero speed operation.

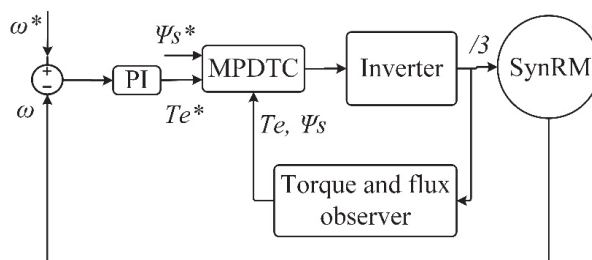


Figure 14. Block diagram of MPDTC of SynRM.

MPDTC is generally categorized into two categories. First, FCS-MPC, which takes the discrete nature of the system into account, is recognized as the most popular MPC method [159]. Akin to DTC, FCS-MPDTC does not involve modulation in its voltage application to the motor and generates the voltages through the inverter directly. This method provides a high-performance control method with high dynamic. However, the high computational burden of the method requires high processing power. Besides, due to the direct control of torque, high torque ripples in the motor shaft are inevitable. The second category of the MPDTC methods is CCS-MPDTC. This method applies modulation methods such as PWM or SVM to apply voltages to the motor.

5. Control Strategies for Different Speed Regions of SynRM Drives

At different motor speeds, some constraints limit the performance of the control methods. The problem of tracking the speed and positioning by an encoder and low current requirement to drive in low speed and the voltage requisites at high speed are just some of the issues. At very low speeds, sensorless controls have gained attention [160,161]. In speeds up to nominal speeds, researchers mostly focus on maximum torque per ampere (MTPA) operation [162,163], while in speeds higher than nominal speed, FW is considered as a dominant approach for control [97,164] and MTPV has been implemented in speeds higher than crossover speed [165,166]. Generally, in SynRMs, the copper losses are dominant [51]. Thus, in terms of control, a dynamic flux reference should be determined, instead of a constant reference, to reach the lowest current magnitude to minimize the copper losses. This strategy allows the motor to deliver maximum electromagnetic torque with lower copper losses, leading to the higher overall efficiency of the drive. However, exploiting different approaches for each trajectory requires a smooth transition in between.

The control strategies in different speed regions are discussed in the rest of this section. Section 5.1 investigates the research works at standstill and very low-speed control of SynRM and analyzes the challenges and the advancements to cover them. A review of the speed range of up to base speed and a review of high-speed and critical speed control of SynRM is addressed in Sections 5.2 and 5.3, respectively. Section 5.4 surveys the studies on wide speed range control and the transition between the ranges.

5.1. Standstill and Very Low-Speed Control

Due to the difficulties to measure the speed and the position of the flux in SynRM at very low speed, the sensorless control is currently preferable for VSDs [158,161,167]. Sensorless control applies current and/or voltage sensors and it is called sensorless control since the speed sensor is absent. The sensorless control methods are not only used for low-speed control but also the motors can be controlled in the entire speed range with these methods. Lack of speed sensor downsizes the system and saves space, costs less, eases the implementation of the drive, provides a more reliable system, and gives more flexibility to the system design for environmental compatibility, while it imposes complexity to the control [122,168–171].

We categorized the sensorless control methods into two classes, where the model-based sensorless control methods are mainly considered for middle- and high-speed range and the saliency-based methods are studied for low-speed range.

Model-based sensorless control techniques are reported to be carried out either with physical modeling [172] or mathematical modeling [173] of the machine. Physical modeling employs rotor slot tracking, saturation by main flux, and customized rotor slots. On the other hand, mathematic-based modeling provides more flexible control techniques. The mathematical model-based sensorless methods include extended electromagnetic force (EEMF)-based methods and direct flux observer (DFO)-based methods. In the EEMF-based methods, the rotor position is obtained as:

$$\theta_e = tg^{-1}\left(\frac{e_\beta}{e_\alpha}\right), \left(\frac{e_\beta}{e_\alpha}\right) = \left(\frac{u_\alpha - R_s i_\alpha - L_d p i_\alpha + \omega_\theta (L_d - L_q) i_\beta}{u_\beta - R_s i_\beta - L_q p i_\beta + \omega_e (L_d - L_q) i_\alpha}\right) \tag{5}$$

where $e_\alpha, e_\beta, u_\alpha, u_\beta, i_\alpha,$ and i_β are the EEMF voltages and the stator voltages and currents in the stationary reference frame, respectively. The method requires the model of the motor. This fact deteriorates the method’s performance in conditions of system mismatch or measurement error. To improve the robustness of the method, some research work proposes adaptive speed observers without a voltage transducer [169].

The second model-based method is DFO, which calculates the rotor position with the estimation of flux linkage, as follows:

$$\theta_e = tg^{-1}\left(\frac{\Psi_\beta}{\Psi_\alpha}\right), \left(\frac{\Psi_\beta}{\Psi_\alpha}\right) = \left(\frac{\int (u_\beta - R_s i_\beta) dt}{\int (u_\alpha - R_s i_\alpha) dt}\right) \tag{6}$$

DFO presents a less accurate method in comparison with the EEMF method. Akin to EEMF, the parameter variation can degrade the estimation process in DFO.

As another common approach for sensorless techniques, open-loop estimators and observers have been implemented in many studies [174]. In the sensorless control method, to obtain information such as rotor position and speed, stator flux vector position, back-electromotive force (back-emf), and extended back-emf, estimators are applied in the literature [142]. This information is extracted from the motor state using arc-tangent calculation or phase-locked loops (PLL) tracking estimators [147]. A drawback for estimators can lead to the accumulated numerical error and the integrator drift from DC offsets in measured values [175]. Bearing all these approaches in mind, firstly, machine model application to sensorless control can cause high voltage distortion. Secondly, motor parameter

variation due to the high temperature and saturation of SynRM is likely, which degrades the method's robustness, leading to instability and less accurate control.

Figure 15 presents a classification of the different sensorless control methods.

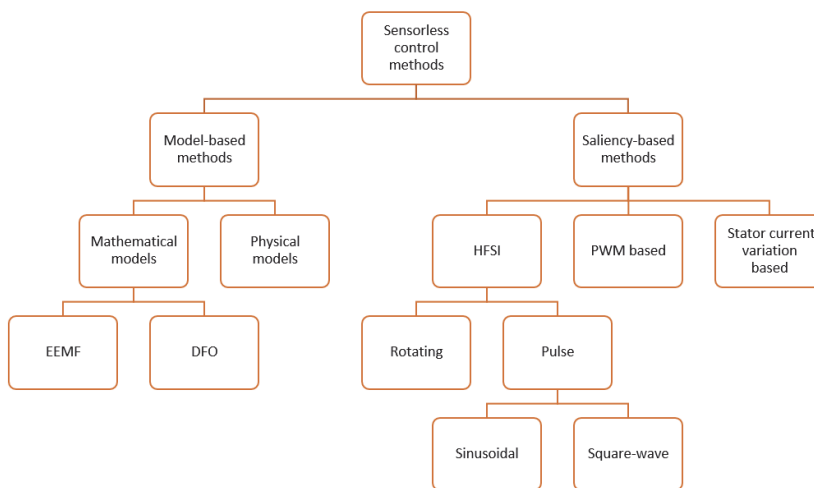


Figure 15. Sensorless control methods' classification.

The model-based sensorless methods are not reliable for low-speed range due to the low signal to ratio and the inaccuracy of the parameters, as well as the nonlinearity of the inverters. In contrast to the model-based sensorless control methods, the saliency-based methods are quite reliable for SynRM in the low-speed range, including zero speed. Saliency-based methods generally benefit from the inherent salient structure of the SynRM and are applied using test signals and filters [158]. PWM-based methods [176], signal injection-based [122,145], and stator current variation-based methods [177] are the main concepts for saliency-based control methods. Using test signals, either pulses or high-frequency signals with saliency consideration provides a sensorless control, which avoids the machine's model exploitation. The independence of this method from machine parameters increases the method's robustness against parameter variations and external disturbances in low and even zero speed control. It is worth mentioning that for high-frequency signals, an additional sensor is required. Also, multiple saliencies, non-sinusoidal distribution of saliency, and the non-linearity of the methods are challenging.

The signal injection can be carried out either in the d -, q -axis or in the α -, β -axis. The concept of high-frequency injection is described as follows:

$$\begin{bmatrix} V_{d_{HF}} \\ V_{q_{HF}} \end{bmatrix} = \begin{bmatrix} L_{d_{HF}} & 0 \\ 0 & L_{q_{HF}} \end{bmatrix} * \begin{bmatrix} \frac{di_{d_{HF}}}{dt} \\ \frac{di_{q_{HF}}}{dt} \end{bmatrix} \quad (7)$$

$$\begin{bmatrix} V_{\alpha_{HF}} \\ V_{\beta_{HF}} \end{bmatrix} = \begin{bmatrix} L_1 + L_2 \cos(2\theta_e) & L_2 \sin(2\theta_e) \\ L_2 \sin(2\theta_e) & L_1 - L_2 \cos(2\theta_e) \end{bmatrix} * \begin{bmatrix} \frac{di_{\alpha_{HF}}}{dt} \\ \frac{di_{\beta_{HF}}}{dt} \end{bmatrix} \quad (8)$$

In the literature, the high-frequency pulsation signals are injected into the d - and q -axes to obtain the rotor position information. Equation (7) denotes the high-frequency voltage and current relations in a synchronous reference frame. Equation (8) can also be applied to estimate the rotor position. This equation is defined in a stationary reference frame and high-frequency rotating signals are normally applied to determine the rotor position. These concepts are illustrated for HFSI of sensorless FOC of SynRM in Figure 16.

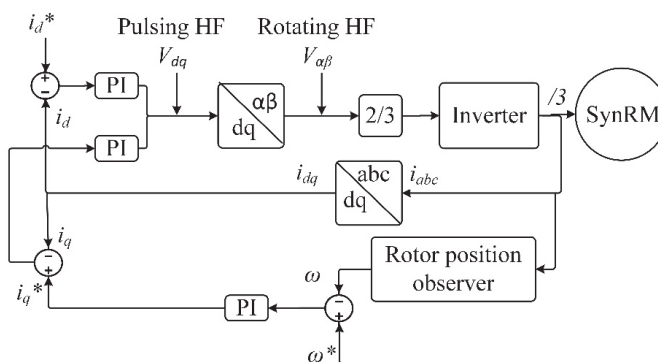


Figure 16. HF injection-based sensorless FOC of SynRM.

Some control theories are applied for sensorless control methods in drive systems. Model reference adaptive system (MRAS) [178–180] open-loop speed estimation [181], EKF [106,182], sliding mode control (SMC) [178], and artificial neural networks (ANN) [114] are the most well-known strategies presented in the literature. With these methods, still, the measurements' integrated drift and highly noisy voltage remain a challenge and very low and zero speed control are controversial issues due to the lack of back-emf.

5.2. Up to Base Speed

SynRM owes its popularity to the high efficiency and can be projected as a dominant motor in industries with the development of VSDs [13]. In particular, in the base speed range, the efficiency issues are attracting more attention in the industries to save energy [12]. Hence, MTPA is becoming inevitable in the recent, more energy aware VSDs, as this method is a smart answer to the call for VSD's efficiency demands.

MTPA is a general strategy for all advanced control techniques, with some considerations for each control method. Regardless of the motor and control algorithm, MTPA has decent flexibility to increase each drive system's efficiency. This method is applied to DTC [98,101,183,184], FOC [142,185,186], DFVC [187], and MPDTC [187,188] for different motors, including SynRMs.

As a brief description, MTPA is an approach to maximize the motor torque towards the current, as follows:

$$\frac{\partial T_e}{\partial i_d} = 0; \quad (9)$$

According to Equation (1):

$$T_e = \frac{3}{2}p(L_d - L_q)i_d\sqrt{i_s^2 - i_d^2} \Rightarrow T_{eMTPA} = \frac{3}{2}p\frac{(L_d - L_q)i_s^{*2}}{2} \quad (10)$$

It should be noted that Equation (10) is derived from the simplified model of the motor, where the cross-coupling magnetic saturation is neglected. Thus, the current reference of $i_d^* = \frac{i_{sm}}{\sqrt{2}}$ is applied to low loads where the saturation of the rotor is less likely. As mentioned in the previous section, the cross-coupling magnet saturation is severe in SynRM, and to improve the performance of the control in higher loads, it is inevitable to consider the variable inductances regarding the currents, as well as the saturation effects.

The first efforts directed to MTPA of SynRM have focused on the minimization of input power with different algorithms. The perturbed d -axis current and low convergence [189], the instability of the response due to a slow current chattering around the minimum loss operating point, and noisy input power signal effect [190] were some challenges with MTPA strategies. The other issue that the MTPA strategies are faced with is machine parameter dependence. MTPA is an online procedure and it needs the machine parameters

knowledge [125]. As a consequence, the nonlinearity of parameters such as inductances will affect the effectiveness of the method [191–193]. Thus, in line with the efficiency improvements of systems through MTPA strategies, the robustness of the drive systems with MTPA strategies is to be taken into consideration. In particular, SynRMs' parameter variations such as inductances to the air-gap flux, PM flux density (in case of PMSynRM) and saturation effects, and stator resistance dependency to the motor's temperature are inevitable [194,195]. Niazi and Toliyat have proposed a robust MTPA for PMSynRM in Reference [142], which calculates the MTPA point, provisionally. Since the saturation effect and high ambient temperature of the motor are inevitable, the method avoids the offline model. Using an online estimator, the practical MTPA point is introduced by method, which proposes a highly efficient and robust method. However, it is likely to fail with this strategy in the initial working point if it is far away from MTPA.

The zero flux situations remain challenging in MTPA control methods. As the position estimators in many research works are applied using machine back-emf, minimum excitation flux should be fulfilled to suitably track the back-emf. For this purpose, in the very low torques, the MTPA approach should be avoided or modified. In Reference [186], an online procedure is proposed for MTPA of SynRM. The algorithm exploits the HFSI strategy in DTC with a random-based perturbation pattern. The method shows a desirable performance in the base speed range. Besides, the method only requires motor resistance for an automatic procedure. However, these strategies can inject perturbation signal waveform, which can cause resonance if the waveform frequency is close to the loads' mechanical resonance. Figure 17 shows the concept of the search for MTPA in this paper. The detector is supposed to generate the flux reference for the DTC algorithm to compare with the estimated flux in the SynRM and generate the error signal for the flux hysteresis controller.

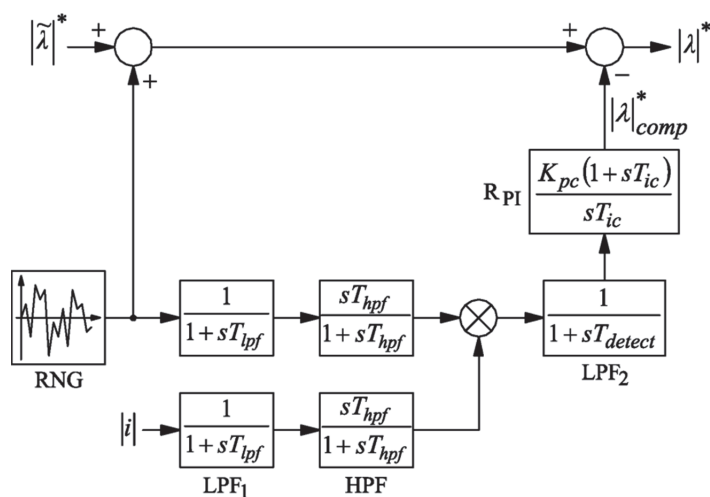


Figure 17. MTPA detector schematic [188].

As can be seen, a random number generator (RNG) block produces a pseudorandom signal with uniform distribution, which distributes the injected signal on a wider harmonic frequency range. This can result in smoother torque rather than that of pure sinusoidal signal injection. The same filters are applied for the current and RNG inputs to maintain the same phase relationship between the signals. Then, the product of the signals is filtered through a low-pass filter with the time constant of the detection procedure (T_{detect}). The output of the low-pass filter is magnified employing a PI regulator to generate a compensation signal. The compensation signal is subtracted from the reference flux to generate the desired flux for the opted MTPA operation point. The flux, current, and speed

response of SynRM to the search algorithm are illustrated in Figure 18, respectively. The time steps are presented as vertical dashed lines in each plot. To verify the performance of the algorithm, the flux of the motor is abruptly decreased by 10% from the MTPA operation point at time 1.5 s. Then, after 0.3 s, the perturbation is started. Then, the PI controller starts to regulate its input at 2 s. The algorithm finds the optimal operation point at 3.3 s and is manually deactivated. The results clearly show that the current magnitude rapidly increases to find the optimized operation point. The speed of the motor is not considerably affected in the transient mode. The process successfully finds the MTPA point, where the optimal current settles down in the initial current value.

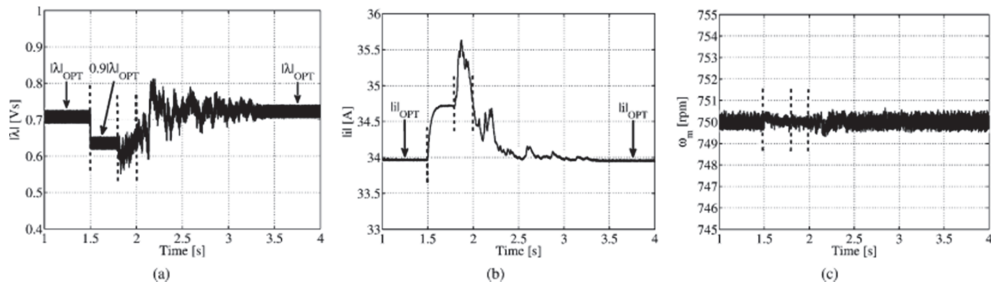


Figure 18. Automatic MTPA search algorithm response, (a) flux, (b) current, (c) speed [188].

In the base speed range, alternatively, the maximum power factor (MPF) guarantees the proper control of the power of the motor. With this concept in the rated speed range, the MPF is delivered with zero losses. The power factor is described as:

$$\cos\Phi = \frac{(L_d - L_q)i_d i_q}{L_d \frac{i_d^2}{2} + L_q \frac{i_q^2}{2}} \quad (11)$$

Therefore, the tangent of the power factor is described as:

$$\tan\Phi = \frac{Q}{P} = \frac{L_d \frac{i_d^2}{2} + L_q \frac{i_q^2}{2}}{(L_d - L_q)i_d i_q} \quad (12)$$

To obtain the MPF for the motor, the minimum tangent should be obtained, where $\left(\frac{i_d}{i_q}\right) = \sqrt{\frac{L_q}{L_d}}$. Therefore, the MPF is obtained as follows:

$$MPF = \frac{1 - \frac{L_q}{L_d}}{1 + \frac{L_q}{L_d}} \quad (13)$$

It should be noted that these equations are defined with the assumption of the neglected cross-coupling magnetic saturation and constant inductances situation. Under these conditions, the maximum torque delivered with the motor is higher than the torque under the MTPA condition.

Apart from MTPA and MPF, at the base speed range, the maximum torque is produced by SynRM applying the maximum torque per flux (MTPF) approach. In this strategy, the given stator flux reference is described as:

$$\Psi_s^{*2} = (L_d i_d)^2 + (L_q i_q)^2 \quad (14)$$

$$\left(\frac{i_d}{i_q}\right) = \frac{L_d}{L_q} \quad (15)$$

Consequently, the obtained torque is:

$$T_e = \frac{3}{2}p(L_d - L_q)i_d^2 \frac{L_d}{L_q} \quad (16)$$

The resulted torque by MTPF is the highest torque obtained to the given flux reference at very high speed. Regarding the control considerations, the MPF and MTPF approaches can be applied in the control stage.

5.3. Beyond Base Speed

SynRMs possess an inherent unlimited speed range with only mechanical constraints [165]. Owing to the anisotropic rotor design, the saliency of the rotor leads to the reluctance torque. This specific characteristic of the rotor saliency promotes a more convenient FW operation for control purposes. In general, for motors in traction applications and spindle drives, the MTPV in the FW region is vital. While many studies in FW operation are utilizing FOC algorithms, the control methods of MTPV operation in the research works are mostly based on DTC [96,132,196].

For the sake of high-speed operation of SynRM, the increase of back-emf is inevitable. Consequently, a reduction of the stator flux is required to reach higher speeds. The stator flux produces the electromagnetic torque, which will be reduced by the reduction in stator flux at high speed. Furthermore, for the given current level, the high speed of the motor requires an imminent regulation of stator flux and electromagnetic torque, concurrently, so that the current and voltage limits will not be exceeded. Regarding direct torque and flux control of DTC, this method can serve as the best choice for FW operation. However, FOC- and MPC-based MTPV operation algorithms of SynRM in the FW region can be found in the literature [140,165,197,198]. Due to the sensitivity of current vector control to the orientation errors in the MTPV region, such as encoder offset, any angle error can result in undesired torque reversal. This is the result of the closeness of the current vector to the negative d -axis. Moreover, the current vector control imposes some complexities, particularly in the FW region [199]. As MPC requires a precise model of motor, the control method's performance under FW operation can be extremely deteriorated by parameter variations.

The SynRM's parameters, and in particular inductances, are more likely to change under the iron saturation situation. Therefore, among FW operation concerns, the robustness of the controller against parameter variations of SynRMs as well as external disturbances are vital considerations [170,200]. In Reference [132], a robust FW algorithm for the DTC algorithm has been presented for the DTC of SynRM. This algorithm modifies the flux reference concerning the torque error and provides a smooth transition between MTPA to the FW speed region. DFVC can be another simple solution for FW of SynRM, which is proposed in References [107,187]. Although this method provides a desirable base for simple and high-performance control of SynRM, in the FW area, the machine is always along the intersection between the limits of current and voltage. This drawback of DFVC avoids the motor to reach MTPV operation. In Reference [64], Gianmario et al. have worked on the DFVC in the FW region in case of MTPV limitations. This method provides an optimal maximum flux vector phase angle, so the MTPV limits are satisfied. A model-based FW strategy is proposed for synchronous machines in Reference [201] to leverage the presence of digital non-linear models. The superiority of this method is the operation without the need of FW regulators that ensures a seamless transition between the operating regions of the machine.

5.4. Transition Between Different Speed Ranges

The wide speed range control of SynRM has attracted a lot of attention in the literature, and the low-speed and high-speed control of SynRM have been studied, concurrently. The attempt to implement the control strategies in the whole speed ranges requires a more scrutinized study on the transition of the motor speed between different trajectories. For

this purpose, firstly, it is crucial to opt for a proper control strategy for each speed region. Secondly, the integration of the strategies should be considered in the method and a comprehensive mechanism should be devised to provide a proper control algorithm with high performance in each speed region and a smooth transition between control regimes. As discussed previously, control trajectories are mainly divided into three regions. In this category, the standstill and very low-speed and MTPA and FW regimes are generally considered. It should be noted that the torque and flux of SynRM must always be limited by MTPA or MPTF limits, as well as voltage and current limits. As an example, Zhang et al. have studied two regimes of MTPA and FW in Reference [132]. In this research work, the MTPA trajectory is described as:

$$|\lambda_s| = \sqrt{\frac{2}{3p} \frac{L_d^2 + L_q^2}{L_d - L_q} |T_e|} \quad (17)$$

In this trajectory, the control algorithm produces the minimum current concerning the torque, which decreases the copper losses. These flux and torque demands are required with the method when the motor speeds up to the rated speed. This trajectory is referred to as region I in this method. If the speed passes the base speed, the FW strategy is applied. In this scenario, the maximum inverter voltage is applied to the motor. The FW trajectory is divided into two regions of region II and region III. In region II, the flux reference and the torque reference of the motor are obtained as:

$$|\lambda_s| = \sqrt{\left((L_d^2 - L_q^2) i_d^2 + (L_q I_{max})^2 \right)} \quad (18)$$

$$T_e = \frac{3p}{2} (L_d - L_q) i_d \sqrt{I_{max}^2 - i_d^2} \quad (19)$$

where, I_{max} is the machine's maximum current. In this region, the machine's current limit is satisfied. In this study, region III is referred to as the MTPF trajectory. In this region, the relation between the flux and the torque is defined as:

$$T_e = \frac{3p}{4} \frac{L_d - L_q}{L_d L_q} |\lambda_s|^2 \quad (20)$$

In the MTPF trajectory, the motor can spin at a very high speed and only mechanical constraints limit the speed of the SynRM. In Figure 19, the defined regions are mapped onto the torque-flux plane.

A comprehensive study of sensorless DFVC control of SynRM in a wide speed range is presented by Yousefi et al. [107,187]. Figure 20 demonstrates the block diagram of this method, which implements MTPA, FW, and active flux and position observer for speed sensorless drive objectives in one comprehensive drive control approach. Using a combination of HFSI and active flux and position observer makes the method capable of operation in even zero-speed condition, which avoids position estimation error resulted from cross-saturation. Covering the MTPA law and FW approach, the method is capable of a very broad speed operation range from standstill to the very high speed, with highly efficient and high-performance control. This technique seems a desirable choice for the applications that require a wide speed range such as home appliances, or automotive and aerospace actuators and generators. This work provides constant switching frequency with the application of the PWM block. Operating in stator-flux-oriented coordinates, the algorithm requires the flux vector precise position causing a complex and less robust control method.

Motor control methods may not guarantee the acceptable level of all control aspects, for example, good robustness, fast dynamic, low torque ripple, and accurate tracking, when singly used in drive systems. For this reason, research and development in the field of electric drives are incrementally updated to develop the technical knowledge and provide a modified version of the drive system, as much as possible. We studied the more popular control strategies and investigated the advantages and disadvantages of each method. Regarding the highlighted feature of each method, we classified the methods, which can provide a reliable reference for the researchers to overview the motor control methods.

A high-performance controller for VSD-fed SynRMs was evaluated by different factors. Three more important factors are the robustness of the controller against parameter variation and external disturbances, the level of torque ripples imposed on the average torque, and the more efficient drive in a wide speed range. Both electrical parameter variability and torque ripple are chiefly generated from the anisotropic rotor structure of SynRMs. The undesirable parameter variation can lead to degraded performance of the drive system. Furthermore, disregarding the system mismatch is in contradiction to efficiency, productivity, and environmental and energy issues. To tackle parameter variation problems, a robust control algorithm should be developed because the parameter variation has a direct impact on machine controllability. The robustness of the controller against external disturbances, such as tough load torques, can be investigated and modified. The study shows that one of the biggest concerns in the SynRMs drive systems is the high torque ripples compared to other technologies. A high level of torque ripple causes pulsation and vibration, which can not only lead to the low efficiency of the systems but also the noise in the environment. We reviewed the techniques and proposals for both the design and control aspects that are addressed to decrease the torque ripples.

Designing a control method to cover the whole speed range of the motors with desired efficiency and performance seems an overwhelming task due to the imposed theoretical and practical constraints. Considering the vast potential uses of SynRMs with VSDs, more intelligent control techniques are projected to be developed to preserve the striking efficiency of these motors in a wide speed range with desirable performance in both transient moods and steady-state. This expanded review paper covered the control methods that are proposed to enhance the performance and controllability and efficiency of the SynRM from standstill to very high speeds. We gathered some approaches for other motor technologies that can be applied to SynRM with some modifications and advised for future research works. The findings and outcomes of the paper may be interesting and usable for researchers, industrial companies, and manufacturers of SynRM drive systems.

Author Contributions: Conceptualization, methodology, validation, formal analysis, writing—original draft preparation, H.H.; writing—review and editing, resources, funding acquisition, A.R.; project administration, T.V.; investigation, A.K., E.A. and D.V.L.; supervision, A.B. The literature review was carried out by H.H. towards Ph.D. study under the supervision of A.R. and A.B. The study was managed by A.K. and T.V. and D.V.L. and E.A. collaborated in the survey for revision and collecting the database. All authors have read and agreed to the published version of the manuscript.

Funding: The research has been supported by the Estonian Research Council under grant PSG453 “Digital twin for propulsion drive of an autonomous electric vehicle”.

Institutional Review Board Statement: Not applicable.

Informed Consent Statement: Not applicable.

Data Availability Statement: Data is contained within the article or supplementary material.

Conflicts of Interest: The authors declare no conflict of interest.

References

1. Rassölkin, A.; Belahcen, A.; Kallaste, A.; Vaimann, T.; Lukichev, D.V.; Orlova, S.; Heidari, H.; Asad, B.; Acedo, J.P. Life cycle analysis of electrical motor-drive system based on electrical machine type. *Proc. Estonian Acad. Sci.* **2020**, *69*, 162. [CrossRef]
2. Carraro, E.; Morandin, M.; Bianchi, N. Traction PMASR motor optimization according to a given driving cycle. *IEEE Trans. Ind. Appl.* **2016**, *52*, 209–216. [CrossRef]
3. Taghavi, S.M.; Pillay, P. A mechanically robust rotor with transverse laminations for a wide-speed-range synchronous reluctance traction motor. *IEEE Trans. Ind. Appl.* **2015**, *51*, 4404–4414. [CrossRef]
4. Bonthu, S.S.R.; Arafat, A.; Choi, S. Comparisons of rare-earth and rare-earth-free external rotor permanent magnet assisted synchronous reluctance motors. *IEEE Trans. Ind. Electron.* **2017**, *64*, 9729–9738. [CrossRef]
5. Bonthu, S.S.R.; Bin Tarek, T.; Choi, S. Optimal torque ripple reduction technique for outer rotor permanent magnet synchronous reluctance motors. *IEEE Trans. Energy Convers.* **2018**, *33*, 1184–1192. [CrossRef]
6. Bonthu, S.S.R.; Choi, S.; Baek, J. Design optimization with multiphysics analysis on external rotor permanent magnet-assisted synchronous reluctance motors. *IEEE Trans. Energy Convers.* **2017**, *33*, 290–298. [CrossRef]
7. Park, J.; Kalev, C.; Hofmann, H.F. Control of high-speed solid-rotor synchronous reluctance motor/generator for flywheel-based uninterruptible power supplies. *IEEE Trans. Ind. Electron.* **2008**, *55*, 3038–3046. [CrossRef]
8. Ibrahim, M.N.; Rashad, E.; Sergeant, P. Performance comparison of conventional synchronous reluctance machines and PM-assisted types with combined star—Delta winding. *Energies* **2017**, *10*, 1500. [CrossRef]
9. Subtitle, P. *High Output Synchronous Reluctance Motor and Drive Package—Optimized Cost of Ownership for Pump and Fan Applications*; ABB: Zurich, Switzerland, 2012.
10. Moghaddam, R.-R. Synchronous Reluctance Machine (SynRM) in Variable Speed Drives (VSD) Applications. Ph.D. Thesis, KTH School of Electrical Engineering, Stockholm, Sweden, 2011.
11. SIEMENS. Highest Efficiency Synchronous-Reluctance Drive System with IES2 Efficiency—Topics—Siemens. Available online: <https://www.industry.siemens.com/topics/global/en/integrated-drive-systems/drive-system-offerings/synchronous-reluctance-drive-system/Pages/Default.aspx> (accessed on 20 August 2019).
12. ABB. IE5 SynRM Motors Deliver Ultra-Premium Energy Efficiency. Available online: <https://new.abb.com/news/detail/58874/abb-ie5-synrm-motors-deliver-ultra-premium-energy-efficiency> (accessed on 27 May 2020).
13. De Almeida, A.T.; Ferreira, F.J.T.E.; Baoming, G. Beyond induction motors—Technology trends to move up efficiency. *IEEE Trans. Ind. Appl.* **2014**, *50*, 2103–2114. [CrossRef]
14. Boldea, I. Control issues in adjustable speed drives. *IEEE Ind. Electron. Mag.* **2008**, *2*, 32–50. [CrossRef]
15. Betin, F.; Capolino, G.-A.; Casadei, D.; Kawkabani, B.; Bojoi, R.I.; Harnefors, L.; Levi, E.; Parsa, L.; Fahimi, B. Trends in electrical machines control: Samples for classical, sensorless, and fault-tolerant techniques. *IEEE Ind. Electron. Mag.* **2014**, *8*, 43–55. [CrossRef]
16. Asad, B.; Vaimann, T.; Rassölkin, A.; Kallaste, A.; Belahcen, A. A survey of broken rotor bar fault diagnostic methods of induction motor. *Electr. Control Commun. Eng.* **2018**, *14*, 117–124. [CrossRef]
17. Ojaghi, M.; Sabouri, M.; Faiz, J. Performance analysis of squirrel-cage induction motors under broken rotor bar and stator inter-turn fault conditions using analytical modeling. *IEEE Trans. Magn.* **2018**, *54*, 1–5. [CrossRef]
18. Trujillo-Guajardo, L.A.; Rodriguez-Maldonado, J.; Moonem, M.A.; Platas-Garza, M.A. A Multiresolution Taylor–Kalman approach for broken rotor bar detection in cage induction motors. *IEEE Trans. Instrum. Meas.* **2018**, *67*, 1317–1328. [CrossRef]
19. Morales-Perez, C.; Rangel-Magdaleno, J.D.J.; Peregrina-Barreto, H.; Amezcua-Sanchez, J.P.; Valtierra-Rodriguez, M. Incipient broken rotor bar detection in induction motors using vibration signals and the orthogonal matching pursuit algorithm. *IEEE Trans. Instrum. Meas.* **2018**, *67*, 2058–2068. [CrossRef]
20. Asad, B.; Vaimann, T.; Belahcen, A.; Kallaste, A.; Iqbal, M.N. Broken rotor bar fault detection of the grid and inverter-fed induction motor by effective attenuation of the fundamental component. *IET Electr. Power Appl.* **2019**, *13*, 2005–2014. [CrossRef]
21. Fan, Z.-N.; Han, L.; Liao, Y.; Xie, L.-D.; Wen, K.; Wang, J.; Dong, X.-C.; Yao, B. Effect of damper winding and stator slot skewing structure on no-load voltage waveform distortion and damper bar heat in large tubular hydro generator. *IEEE Access* **2018**, *6*, 22281–22291. [CrossRef]
22. Mallard, V.; Parent, G.; Demian, C.; Brudny, J.-F.; Delamotte, A. Increasing the energy efficiency of induction machines by the use of grain-oriented magnetic materials and die casting copper squirrel cage in the rotor. *IEEE Trans. Ind. Appl.* **2018**, *55*, 1280–1289. [CrossRef]
23. Zhang, Q.; Liu, H.; Zhang, Z.; Song, T. A cast copper rotor induction motor for small commercial EV traction: Electromagnetic design, analysis, and experimental tests. *China Electrotech. Soc. Trans. Electr. Mach. Syst.* **2018**, *2*, 417–424. [CrossRef]
24. Wu, G.; Huang, S.; Wu, Q.; Rong, F.; Zhang, C.; Liao, W. Robust predictive torque control of N*3-phase PMSM for high-power traction application. *IEEE Trans. Power Electron.* **2020**, *35*, 10799–10809. [CrossRef]
25. Reddy, P.N.; Amarnath, J.; Linga Reddy, P. Hybrid random PWM algorithm for direct torque-controlled induction motor drive for reduced harmonic distortion. In Proceedings of the 2011 Annual IEEE India Conference, Hyderabad, India, 16–18 December 2011; pp. 1–5.
26. Fang, S.; Liu, H.; Wang, H.; Yang, H.; Lin, H. High power density PMSM with lightweight structure and high-performance soft magnetic alloy core. *IEEE Trans. Appl. Supercond.* **2019**, *29*, 1–5. [CrossRef]

27. Xu, J.; Zhang, B.; Kuang, X.; Guo, H.; Guo, S. Influence analysis of slot parameters and high torque density optimisation for dual redundant permanent magnet motor in aerospace application. *IET Electr. Power Appl.* **2020**, *14*, 1263–1273. [[CrossRef](#)]
28. Kong, Y.; Lin, M.; Jia, L. A novel high-power density permanent-magnet synchronous machine with wide speed range. *IEEE Trans. Magn.* **2020**, *56*, 1–6. [[CrossRef](#)]
29. Chau, K.T. *Electric Vehicle Machines and Drives: Design, Analysis and Application*; John Wiley and Sons: Chichester, UK, 2015.
30. Korn, N.; Vaimann, T.; Kallaste, A.; Belahcen, A. Comparative study of slow speed slotless synchronous generator using SmCo and NdFeB permanent magnets. In Proceedings of the 2014 Electric Power Quality and Supply Reliability Conference (PQ), Rakvere, Estonia, 11–13 June 2014; pp. 247–250.
31. Pellegrino, G.; Jahns, T.M.; Bianchi, N.; Soong, W.; Cupertino, F. *The Rediscovery of Synchronous Reluctance and Ferrite Permanent Magnet Motors*; Springer: Cham, Switzerland, 2016.
32. Boldea, I.; Tutelea, L.N.; Parsa, L.; Dorrell, D. Automotive electric propulsion systems with reduced or no permanent magnets: An overview. *IEEE Trans. Ind. Electron.* **2014**, *61*, 5696–5711. [[CrossRef](#)]
33. Moghaddam, R.-R.; Gyllensten, F. Novel high-performance SynRM design method: An easy approach for a complicated rotor topology. *IEEE Trans. Ind. Electron.* **2014**, *61*, 5058–5065. [[CrossRef](#)]
34. Bianchi, N.; Fornasiero, E.; Soong, W. Selection of PM flux linkage for maximum low-speed torque rating in a PM-assisted synchronous reluctance machine. *IEEE Trans. Ind. Appl.* **2015**, *51*, 3600–3608. [[CrossRef](#)]
35. Di Nardo, M.; Calzo, G.L.; Galea, M.; Gerada, C. Design optimization of a high-speed synchronous reluctance machine. *IEEE Trans. Ind. Appl.* **2018**, *54*, 233–243. [[CrossRef](#)]
36. Taghavi, S.; Pillay, P. A sizing methodology of the synchronous reluctance motor for traction applications. *IEEE J. Emerg. Sel. Top. Power Electron.* **2014**, *2*, 329–340. [[CrossRef](#)]
37. Moghaddam, R.R.; Magnussen, F.; Sadarangani, C. Theoretical and experimental reevaluation of synchronous reluctance machine. *IEEE Trans. Ind. Electron.* **2010**, *57*, 6–13. [[CrossRef](#)]
38. Huynh, T.A.; Hsieh, M.-F. Comparative study of PM-Assisted SynRM and IPMSM on constant power speed range for EV applications. *IEEE Trans. Magn.* **2017**, *53*, 1–6. [[CrossRef](#)]
39. Kumar, G.V.; Chuang, C.-H.; Lu, M.-Z.; Liaw, C.-M. Development of an electric vehicle synchronous reluctance motor drive. *IEEE Trans. Veh. Technol.* **2020**, *69*, 5012–5024. [[CrossRef](#)]
40. Herrera, D.; Villegas, J.; Galván, E.; Carrasco, J.M. Powertrain EV synchronous reluctance motor design with redundant topology with novel control. *IET Electr. Power Appl.* **2019**, *13*, 1647–1659. [[CrossRef](#)]
41. ABB. All-Compatible ACS880 Single Drives—Industrial Drives—Unlimited Possibilities for Your Business (Low Voltage AC). Available online: <https://new.abb.com/drives/low-voltage-ac/industrial-drives/acs880-single-drives> (accessed on 24 August 2020).
42. Foo, G.; Rahman, M.F. Sensorless direct torque and flux controlled IPM synchronous motor drive at very low speed without signal injection. *IEEE Trans. Ind. Electron.* **2009**, *57*, 395–403. [[CrossRef](#)]
43. Fei, W.-Z.; Luk, P.C.-K. Torque ripple reduction of a direct-drive permanent-magnet synchronous machine by material-efficient axial pole pairing. *IEEE Trans. Ind. Electron.* **2011**, *59*, 2601–2611. [[CrossRef](#)]
44. Bedetti, N.; Calligaro, S.; Petrella, R. Stand-still self-identification of flux characteristics for synchronous reluctance machines using novel saturation approximating function and multiple linear regression. *IEEE Trans. Ind. Appl.* **2016**, *52*, 3083–3092. [[CrossRef](#)]
45. ABB. Synchronous Reluctance Motor-Drive Package for Machine Builders. High Performance for Ultimate Machine Design. Available online: <http://search-ext.abb.com/library/Download.aspx?DocumentID=3AUA0000120962&LanguageCode=en&DocumentPartId=1&Action=Launch> (accessed on 24 August 2020).
46. Ibrahim, M.N.; Abdel-Khalik, A.S.; Rashad, E.E.M.; Sergeant, P. An improved torque density synchronous reluctance machine with a combined star–delta winding layout. *IEEE Trans. Energy Convers.* **2018**, *33*, 1015–1024. [[CrossRef](#)]
47. Betz, R.; Lagerquist, R.; Jovanovic, M.; Miller, T.; Middleton, R. Control of synchronous reluctance machines. *IEEE Trans. Ind. Appl.* **1993**, *29*, 1110–1122. [[CrossRef](#)]
48. ABB. Synchronous Reluctance Motor-Drive Package for Industrial Use—Optimized Cost of Ownership. Available online: <https://www.baldor.com/mvc/DownloadCenter/Files/3AUA0000132610> (accessed on 24 August 2020).
49. IEC Webstore. IEC 60034-30-1:2014—Pump, Motor, Water Management, Smart City, Energy Efficiency. Available online: <https://webstore.iec.ch/publication/136> (accessed on 15 February 2019).
50. IEC Webstore. IEC TS 60034-30-2:2016—Energy Efficiency, Efficiency Rating. Available online: <https://webstore.iec.ch/publication/30830> (accessed on 15 February 2019).
51. Wang, Y.; Ionel, D.M.; Dorrell, D.G.; Stretz, S. Establishing the power factor limitations for synchronous reluctance machines. *IEEE Trans. Magn.* **2015**, *51*, 1–4. [[CrossRef](#)]
52. Heidari, H.; Andriushchenko, E.; Rassölkina, A.; Demidova, G.L. Comparison of synchronous reluctance machine and permanent magnet-assisted synchronous reluctance machine performance characteristics. In Proceedings of the 2020 27th International Workshop on Electric Drives: MPEI Department of Electric Drives 90th Anniversary (IWED), Moscow, Russia, 27–30 January 2020; pp. 9–13.
53. Vagati, A.; Canova, A.; Chiampi, M.; Pastorelli, M.; Repetto, M. Design refinement of synchronous reluctance motors through finite-element analysis. *IEEE Trans. Ind. Appl.* **2000**, *36*, 1094–1102. [[CrossRef](#)]

54. Park, J.-M.; Park, S.-J.; Lee, M.-M.; Chun, J.-S.; Lee, J.-H. Rotor design on torque ripple reduction for a synchronous reluctance motor with concentrated winding using response surface methodology. *IEEE Trans. Magn.* **2006**, *42*, 3479–3481. [[CrossRef](#)]
55. Diao, X.; Zhu, H.; Qin, Y.; Hua, Y. Torque ripple minimization for bearingless synchronous reluctance motor. *IEEE Trans. Appl. Supercond.* **2018**, *28*, 1–5. [[CrossRef](#)]
56. Ibrahim, M.N.; Sergeant, P.; Rashad, E. Simple design approach for low torque ripple and high output torque synchronous reluctance motors. *Energies* **2016**, *9*, 942. [[CrossRef](#)]
57. Uddin, M.N.; Rahman, M.M. Online torque-flux estimation-based nonlinear torque and flux control scheme of IPMSM drive for reduced torque ripples. *IEEE Trans. Power Electron.* **2018**, *34*, 636–645. [[CrossRef](#)]
58. Lipo, T.A. Synchronous reluctance machines—A viable alternative for AC drives? *Electr. Mach. Power Syst.* **1991**, *19*, 659–671. [[CrossRef](#)]
59. Taghavi, S.; Pillay, P. A novel grain-oriented lamination rotor core assembly for a synchronous reluctance traction motor with a reduced torque ripple algorithm. *IEEE Trans. Ind. Appl.* **2016**, *52*, 3729–3738. [[CrossRef](#)]
60. Bianchi, N.; Bolognani, S.; Bon, D.; Pr, M.D. Torque harmonic compensation in a synchronous reluctance motor. *IEEE Trans. Energy Convers.* **2008**, *23*, 466–473. [[CrossRef](#)]
61. Bianchi, N.; Bolognani, S.; Bon, D.; Pre, M.D. Rotor flux-barrier design for torque ripple reduction in synchronous reluctance and PM-assisted synchronous reluctance motors. *IEEE Trans. Ind. Appl.* **2009**, *45*, 921–928. [[CrossRef](#)]
62. Bianchi, N.; Bolognani, S.; Carraro, E.; Castiello, M.; Fornasiero, E. Electric vehicle traction based on synchronous reluctance motors. *IEEE Trans. Ind. Appl.* **2016**, *52*, 4762–4769. [[CrossRef](#)]
63. Rassölkin, A.; Heidari, H.; Kallaste, A.; Acedo, J.P.; Romero-Cadaval, E. Efficiency map comparison of induction and synchronous reluctance motors. In Proceedings of the 2019 26th International Workshop on Electric Drives: Improvement in Efficiency of Electric Drives (IWED), Moscow, Russia, 30 January–2 February 2019; pp. 4–7.
64. Pellegrino, G.-M.L.; Armando, E.; Guglielmi, P. Direct-flux vector control of IPM motor drives in the maximum torque per voltage speed range. *IEEE Trans. Ind. Electron.* **2012**, *59*, 3780–3788. [[CrossRef](#)]
65. Barcaro, M.; Bianchi, N.; Magnussen, F. Permanent-magnet optimization in permanent-magnet-assisted synchronous reluctance motor for a wide constant-power speed range. *IEEE Trans. Ind. Electron.* **2012**, *59*, 2495–2502. [[CrossRef](#)]
66. Liu, H.-C.; Kim, I.-G.; Oh, Y.J.; Lee, J.; Go, S.-C. Design of permanent magnet-assisted synchronous reluctance motor for maximized Back-EMF and torque ripple reduction. *IEEE Trans. Magn.* **2017**, *53*, 1–4. [[CrossRef](#)]
67. Flieller, D.; Nguyen, N.K.; Wira, P.; Sturtzer, G.; Abdeslam, D.O.; Mercklé, J. A self-learning solution for torque ripple reduction for nonsinusoidal permanent-magnet motor drives based on artificial neural networks. *IEEE Trans. Ind. Electron.* **2014**, *61*, 655–666. [[CrossRef](#)]
68. Zhu, H.; Xiao, X.; Li, Y. Torque ripple reduction of the torque predictive control scheme for permanent-magnet synchronous motors. *IEEE Trans. Ind. Electron.* **2011**, *59*, 871–877. [[CrossRef](#)]
69. Wang, B.; Wang, J.; Griffo, A.; Sun, Z.; Chong, E. A fault tolerant machine drive based on permanent magnet assisted synchronous reluctance machine. In Proceedings of the 2016 IEEE Energy Conversion Congress and Exposition (ECCE), Milwaukee, WI, USA, 18–22 September 2016; pp. 1–8.
70. Arafat, A.; Choi, S.; Baek, J. Open-phase fault detection of a five-phase permanent magnet assisted synchronous reluctance motor based on symmetrical components theory. *IEEE Trans. Ind. Electron.* **2017**, *64*, 6465–6474. [[CrossRef](#)]
71. Ilamparithi, T.C.; Nandi, S. Detection of eccentricity faults in three-phase reluctance synchronous motor. *IEEE Trans. Ind. Appl.* **2012**, *48*, 1307–1317. [[CrossRef](#)]
72. Wang, B.; Wang, J.; Griffo, A.; Sen, B. Experimental assessments of a triple redundant nine-phase fault-tolerant PMA SynRM drive. *IEEE Trans. Ind. Electron.* **2019**, *66*, 772–783. [[CrossRef](#)]
73. Heidari, H.; Rassölkin, A.; Holakooie, M.H.; Vaimann, T.; Kallaste, A.; Belahcen, A.; Lukichev, D.V. A Parallel estimation system of stator resistance and rotor speed for active disturbance rejection control of six-phase induction motor. *Energies* **2020**, *13*, 1121. [[CrossRef](#)]
74. Asad, B.; Vaimann, T.; Belahcen, A.; Kallaste, A.; Rassolkin, A.; Heidari, H. The Low Voltage Start-up Test of Induction Motor for the Detection of Broken Bars. In Proceedings of the 2020 International Conference on Electrical Machines (ICEM), Gothenburg, Sweden, 23–26 August 2020; Volume 1.
75. Asad, B.; Vaimann, T.; Rassölkin, A.; Kallaste, A.; Belahcen, A. Review of electrical machine diagnostic methods applicability in the perspective of industry 4.0. *Electr. Control Commun. Eng.* **2018**, *14*, 1–9. [[CrossRef](#)]
76. Boglietti, A.; Cavagnino, A.; Pastorelli, M.; Staton, D.; Vagati, A. Thermal analysis of induction and synchronous reluctance motors. *IEEE Trans. Ind. Appl.* **2006**, *42*, 675–680. [[CrossRef](#)]
77. Ghahfarokhi, P.S.; Belahcen, A.; Kallaste, A.; Vaimann, T.; Gerokov, L.; Rassolkin, A. Thermal analysis of a SynRM using a thermal network and a hybrid model. In Proceedings of the 2018 XIII International Conference on Electrical Machines (ICEM), Alexandroupoli, Greece, 3–6 September 2018; pp. 2682–2688.
78. Wang, D.; Zhang, B.; Qiu, D.; Xie, F.; Wei, D. Stability analysis of the coupled synchronous reluctance motor drives. *IEEE Trans. Circuits Syst. II* **2017**, *64*, 196–200. [[CrossRef](#)]
79. Holakooie, M.H.; Taheri, A.; Sharifian, M.B.B. MRAS based speed estimator for sensorless vector control of a linear induction motor with improved adaptation mechanisms. *J. Power Electron.* **2015**, *15*, 1274–1285. [[CrossRef](#)]

80. Orosz, T.; Pánek, D.; Karban, P. FEM based preliminary design optimization in case of large power transformers. *Appl. Sci.* **2020**, *10*, 1361. [[CrossRef](#)]
81. Karban, P.; Pánek, D.; Orosz, T.; Petrášová, I.; Doležel, I. FEM based robust design optimization with Agros and Ārtap. *Comput. Math. Appl.* **2021**, *81*, 618–633. [[CrossRef](#)]
82. Pando-Acedo, J.; Rassolkin, A.; Lehikoinen, A.; Vaimann, T.; Kallaste, A.; Romero-Cadaval, E.; Belahcen, A. Hybrid FEA-simulink modelling of permanent magnet assisted synchronous reluctance motor with unbalanced magnet flux. In Proceedings of the 2019 IEEE 12th International Symposium on Diagnostics for Electrical Machines, Power Electronics and Drives (SDEMPED), Toulouse, France, 27–30 August 2019; pp. 174–180.
83. Kamper, M.; Van Der Merwe, F.; Williamson, S. Direct finite element design optimisation of the cageless reluctance synchronous machine. *IEEE Trans. Energy Convers.* **1996**, *11*, 547–555. [[CrossRef](#)]
84. Lee, J.H.; Lee, I.K.; Cho, Y.H.; Yun, T.W. Characteristics analysis and optimum design of anisotropy rotor synchronous reluctance motor using coupled finite element method and response surface methodology. *IEEE Trans. Magn.* **2009**, *45*, 4696–4699. [[CrossRef](#)]
85. Lopez-Torres, C.; Espinosa, A.G.; Riba, J.-R.; Romeral, L. Design and optimization for vehicle driving cycle of rare-earth-free SynRM based on coupled lumped thermal and magnetic networks. *IEEE Trans. Veh. Technol.* **2017**, *67*, 196–205. [[CrossRef](#)]
86. Kong, Y.; Lin, M.; Yin, M.; Hao, L. Rotor structure on reducing demagnetization of magnet and torque ripple in a PMA-synRM with ferrite permanent magnet. *IEEE Trans. Magn.* **2018**, *54*, 1–5. [[CrossRef](#)]
87. Obe, E. Direct computation of ac machine inductances based on winding function theory. *Energy Convers. Manag.* **2009**, *50*, 539–542. [[CrossRef](#)]
88. Obe, E. Calculation of inductances and torque of an axially laminated synchronous reluctance motor. *IET Electr. Power Appl.* **2010**, *4*, 783. [[CrossRef](#)]
89. Rahman, K.M.; Hiti, S. Identification of machine parameters of a synchronous motor. *IEEE Trans. Ind. Appl.* **2005**, *41*, 557–565. [[CrossRef](#)]
90. Armando, E.; Guglielmi, P.; Pellegrino, G.-M.L.; Pastorelli, M.A.; Vagati, A. Accurate modeling and performance analysis of IPM-PMASR motors. *IEEE Trans. Ind. Appl.* **2009**, *45*, 123–130. [[CrossRef](#)]
91. Ortombina, L.; Tinazzi, F.; Zigliotto, M. Magnetic modeling of synchronous reluctance and internal permanent magnet motors using radial basis function networks. *IEEE Trans. Ind. Electron.* **2017**, *65*, 1140–1148. [[CrossRef](#)]
92. Hinkkanen, M.; Pescetto, P.; Molsa, E.; Saarakkala, S.E.; Pellegrino, G.; Bojoi, R. Sensorless self-commissioning of synchronous reluctance motors at standstill without rotor locking. *IEEE Trans. Ind. Appl.* **2017**, *53*, 2120–2129. [[CrossRef](#)]
93. Aarniovuori, L.; Kolehmäinen, J.; Kosonen, A.; Niemela, M.; Chen, H.; Cao, W.; Pyrhönen, J.J. Application of calorimetric method for loss measurement of a SynRM drive system. *IEEE Trans. Ind. Electron.* **2016**, *63*, 2005–2015. [[CrossRef](#)]
94. ABB. *A Century of ABB Review*; ABB Process Automation, Turbocharging; Baden, Switzerland, 2012; pp. 1–80.
95. Toliyat, H.A.; Campbell, S.G. *DSP-Based Electromechanical Motion Control*; CRC Press: Boca Raton, FL, USA, 2003.
96. Heidari, H.; Rassolkin, A.; Kallaste, A.; Vaimann, T.; Belahcen, A. Harmonics distortion in inverter-fed motor-drive systems: Case study. In Proceedings of the 2019 Electric Power Quality and Supply Reliability Conference (PQ) and 2019 Symposium on Electrical Engineering and Mechatronics (SEEM), Kärdla, Estonia, 12–15 June 2019; pp. 1–4.
97. Trancho, E.; Ibarra, E.; Arias, A.; Kortabarria, I.; Jurgens, J.; Marengo, L.; Fricasse, A.; Gragger, J.V. PM-Assisted synchronous reluctance machine flux weakening control for EV and HEV applications. *IEEE Trans.* **2018**, *65*, 2986–2995. [[CrossRef](#)]
98. Foo, G.H.B.; Zhang, X. Robust direct torque control of synchronous reluctance motor drives in the field-weakening region. *IEEE Trans. Power Electron.* **2016**, *32*, 1289–1298. [[CrossRef](#)]
99. Stumper, J.-F.; Hagenmeyer, V.; Kuehl, S.; Kennel, R. Deadbeat control for electrical drives: A robust and performant design based on differential flatness. *IEEE Trans. Power Electron.* **2014**, *30*, 4585–4596. [[CrossRef](#)]
100. Caporal, R.M.; Pacas, M. A Predictive torque control for the synchronous reluctance machine taking into account the magnetic cross saturation. *IEEE Trans. Ind. Electron.* **2007**, *54*, 1161–1167. [[CrossRef](#)]
101. Zhang, X.; Foo, G. Overmodulation of constant-switching-frequency-based dtc for reluctance synchronous motors incorporating field-weakening operation. *IEEE Trans. Ind. Electron.* **2019**, *66*, 37–47. [[CrossRef](#)]
102. Antonello, R.; Carraro, M.; Peretti, L.; Zigliotto, M. Hierarchical scaled-states direct predictive control of synchronous reluctance motor drives. *IEEE Trans. Ind. Electron.* **2016**, *63*, 1. [[CrossRef](#)]
103. Lin, C.-K.; Yu, J.-T.; Lai, Y.-S.; Yu, H.-C. Improved model-free predictive current control for synchronous reluctance motor drives. *IEEE Trans. Ind. Electron.* **2016**, *63*, 3942–3953. [[CrossRef](#)]
104. Yamamoto, S.; Hirahara, H.; Adawey, J.B.; Ara, T.; Matsuse, K. Maximum efficiency drives of synchronous reluctance motors by a novel loss minimization controller with inductance estimator. *IEEE Trans. Ind. Appl.* **2013**, *49*, 2543–2551. [[CrossRef](#)]
105. Hofmann, H.F.; Sanders, S.R.; El-Antably, A. Stator-flux-oriented vector control of synchronous reluctance machines with maximized efficiency. *IEEE Trans. Ind. Electron.* **2004**, *51*, 1066–1072. [[CrossRef](#)]
106. Senjyu, T.; Omoda, A.; Uezato, K. High efficiency control of synchronous reluctance motors using extended kalman filter. *IEEE Trans. Ind. Electron.* **2003**, *50*, 726–732. [[CrossRef](#)]
107. Yousefi-Talouki, A.; Pescetto, P.; Pellegrino, G.; Boldea, I. Combined active flux and high-frequency injection methods for sensorless direct-flux vector control of synchronous reluctance machines. *IEEE Trans. Power Electron.* **2018**, *33*, 2447–2457. [[CrossRef](#)]

108. Antonello, R.; Ortombina, L.; Tinazzi, F.; Zigliotto, M. Enhanced low-speed operations for sensorless anisotropic PM synchronous motor drives by a modified back-EMF observer. *IEEE Trans. Ind. Electron.* **2018**, *65*, 3069–3076. [CrossRef]
109. Lee, K.; Kim, H.; Lukic, S.M. A Rotating restart method for scalar (v/f) controlled synchronous reluctance machine drives using a single DC-Link current sensor. *IEEE Access* **2020**, *8*, 106629–106638. [CrossRef]
110. Scalar V/f and I-f Control of AC Motor Drives: An Overview. Available online: <https://ieeexplore.ieee.org/stamp/stamp.jsp?tp=&number=7426739&tag=1> (accessed on 8 December 2020).
111. Roy, G.; April, G.-E. Cycloconverter operation under a new scalar control algorithm. In Proceedings of the 20th Annual IEEE Power Electronics Specialists Conference, Milwaukee, WI, USA, 26–29 June 1989; Volume 1, pp. 368–375.
112. Consoli, A.; Scelba, G.; Scarcella, G.; Cacciato, M. An effective energy-saving scalar control for industrial IPMSM drives. *IEEE Trans. Ind. Electron.* **2012**, *60*, 3658–3669. [CrossRef]
113. Chen, S.-G.; Lin, F.-J.; Liang, C.-H.; Liao, C.-H. Intelligent maximum power factor searching control using recurrent chebyshev fuzzy neural network current angle controller for SynRM drive system. *IEEE Trans. Power Electron.* **2021**, *36*, 3496–3511. [CrossRef]
114. Lin, F.-J.; Chen, S.-G.; Hsu, C.-W. Intelligent backstepping control using recurrent feature selection fuzzy neural network for synchronous reluctance motor position servo drive system. *IEEE Trans. Fuzzy Syst.* **2018**, *27*, 413–427. [CrossRef]
115. Ting, J.C.; Chen, D.F. Nonlinear backstepping control of SynRM drive systems using reformed recurrent Hermite polynomial neural networks with adaptive law and error estimated law. *J. Power Electron.* **2018**, *18*, 1380–1397. [CrossRef]
116. Chiang, H.-K.; Chu, C.-T. Reference model with an adaptive hermite fuzzy neural network controller for tracking a synchronous reluctance motor. *Electr. Power Compon. Syst.* **2015**, *43*, 770–780. [CrossRef]
117. Strzelecki, R.; Demidova, G.; Lukichev, D.; Polyakov, N.; Abdullin, A.; Lovlin, S. Survey on fuzzy logic methods in control systems of electromechanical plants. *Sci. Tech. J. Inf. Technol. Mech. Opt.* **2019**, *19*, 1–14. [CrossRef]
118. Lukichev, D.V.; Demidova, G.L.; Kuzin, A.Y.; Saushev, A. Application of adaptive Neuro Fuzzy Inference System (ANFIS) controller in servodrive with multi-mass object. In Proceedings of the 2018 25th International Workshop on Electric Drives: Optimization in Control of Electric Drives (IWED), Moscow, Russia, 31 January–2 February 2018; pp. 1–6.
119. Lin, C. Adaptive recurrent fuzzy neural network control for synchronous reluctance motor servo drive. *IEE Proc. Electr. Power Appl.* **2004**, *151*, 711–724. [CrossRef]
120. Daryabeigi, E.; Mirzaei, A.; Zarchi, H.A.; Vaez-Zadeh, S. Deviation model-based control of synchronous reluctance motor drives with reduced parameter dependency. *IEEE Trans. Power Electron.* **2019**, *34*, 6697–6705. [CrossRef]
121. Daryabeigi, E.; Mirzaei, A.; Zarchi, H.A.; Vaez-Zadeh, S. Deviation control in comparison with DTC and FOC for SynRM drives. In Proceedings of the 2019 10th International Power Electronics, Drive Systems and Technologies Conference (PEDSTC), Shiraz, Iran, 12–14 February 2019; pp. 713–717.
122. Li, C.; Wang, G.; Zhang, G.; Xu, D.G.; Xiao, D. Saliency-based sensorless control for SynRM drives with suppression of position estimation error. *IEEE Trans. Ind. Electron.* **2019**, *66*, 5839–5849. [CrossRef]
123. Li, C.; Wang, G.; Zhang, G.; Xu, D.G. Eliminating position estimation error caused by cross-coupling effect in saliency-based sensorless control of SynRMs. In Proceedings of the 2018 21st International Conference on Electrical Machines and Systems (ICEMS), Jeju, Korea, 7–10 October 2018; pp. 1600–1605.
124. Piriienko, S.; Ammann, U.; Neuberger, M.; Bertele, F.; Roser, T.; Balakhontsev, A.; Neuberger, N.; Cheng, P.-W. Influence of the control strategy on the efficiency of SynRM based small-scale wind generators. In Proceedings of the 2019 IEEE International Conference on Industrial Technology (ICIT), Melbourne, Australia, 13–15 February 2019; pp. 280–285.
125. Daryabeigi, E.; Zarchi, H.A.; Markadeh, G.R.A.; Soltani, J.; Blaabjerg, F. Online MTPA control approach for synchronous reluctance motor drives based on emotional controller. *IEEE Trans. Power Electron.* **2015**, *30*, 2157–2166. [CrossRef]
126. Pellegrino, G.; Bojoi, R.I.; Guglielmi, P. Unified direct-flux vector control for AC motor drives. *IEEE Trans. Ind. Appl.* **2011**, *47*, 2093–2102. [CrossRef]
127. Heidari, H.; Rassolkin, A.; Vaimann, T.; Kallaste, A.; Taheri, A.; Holakooie, M.H.; Belahcen, A. A Novel vector control strategy for a six-phase induction motor with low torque ripples and harmonic currents. *Energies* **2019**, *12*, 1102. [CrossRef]
128. Heidari, H.; Rassolkin, A.; Kallaste, A.; Vaimann, T.; Andriushchenko, E. Vector control of synchronous reluctance motor with reduced torque ripples. In Proceedings of the 2020 XI International Conference on Electrical Power Drive Systems (ICEPDS), Saint Petersburg, Russia, 4–7 October 2020; pp. 1–5.
129. Niu, F.; Wang, B.; Babel, A.S.; Li, K.; Strangas, E.G. Comparative evaluation of direct torque control strategies for permanent magnet synchronous machines. *IEEE Trans. Power Electron.* **2016**, *31*, 1408–1424. [CrossRef]
130. Boldea, I.; Fu, Z.X.; Nasar, S.A. Torque Vector Control (TVC) OF Axially-Laminated Anisotropic (ALA) rotor reluctance synchronous motors. *Electr. Mach. Power Syst.* **1991**, *19*, 381–398. [CrossRef]
131. ABB. DTC: A Motor Control Technique for all Seasons. Available online: <https://new.abb.com/drives/dtc> (accessed on 23 January 2020).
132. Zhang, X.; Foo, G.H.B.; Vilathgamuwa, D.M.; Maskell, D.L. An improved robust field-weakening algorithm for direct-torque-controlled synchronous-reluctance-motor drives. *IEEE Trans. Ind. Electron.* **2015**, *62*, 3255–3264. [CrossRef]
133. Zhang, Z.; Liu, X. A duty ratio control strategy to reduce both torque and flux ripples of DTC for permanent magnet synchronous machines. *IEEE Access* **2019**, *7*, 11820–11828. [CrossRef]
134. Mohan, D.; Zhang, X.; Foo, G.H.B. Generalized DTC strategy for multilevel inverter fed IPMSMs with constant inverter switching frequency and reduced torque ripples. *IEEE Trans. Energy Convers.* **2017**, *32*, 1031–1041. [CrossRef]

135. Ren, Y.; Zhu, Z.Q.; Liu, J. Direct torque control of permanent-magnet synchronous machine drives with a simple duty ratio regulator. *IEEE Trans. Ind. Electron.* **2014**, *61*, 5249–5258. [[CrossRef](#)]
136. Tang, L.; Zhong, L.; Rahman, M.; Hu, Y. A novel direct torque controlled interior permanent magnet synchronous machine drive with low ripple in flux and torque and fixed switching frequency. *IEEE Trans. Power Electron.* **2004**, *19*, 346–354. [[CrossRef](#)]
137. Boldea, I.; Pitic, C.; Lascu, C.V.; Andreescu, G.D.; Tutelea, L.; Blaabjerg, F.; Sandholdt, P. DTFC-SVM motion-sensorless control of a PM-assisted reluctance synchronous machine as starter-alternator for hybrid electric vehicles. *IEEE Trans. Power Electron.* **2006**, *21*, 711–719. [[CrossRef](#)]
138. Kumar, A.; Fernandes, B.; Chatterjee, K. Simplified SVPWM-DTC of 3-phase induction motor using the concept of imaginary switching times. In Proceedings of the 30th Annual Conference of IEEE Industrial Electronics Society (IECON 2004), Busan, Korea, 2–6 November 2004; Volume 1, pp. 341–346.
139. Changjin, C.; Yongyin, Q. Research on drive technology and control strategy of electric vehicle based on SVPWM-DTC. In Proceedings of the 2011 International Conference on Mechatronic Science, Electric Engineering and Computer (MEC), Jilin, China, 19–22 August 2011; pp. 44–49.
140. Hadla, H.; Cruz, S. Predictive stator flux and load angle control of synchronous reluctance motor drives operating in a wide speed range. *IEEE Trans. Ind. Electron.* **2017**, *64*, 6950–6959. [[CrossRef](#)]
141. Ren, Y.; Zhu, Z.Q. Enhancement of steady-state performance in direct torque controlled dual-three phase permanent magnet synchronous machine drives with modified switching table. *IEEE Trans. Ind. Electron.* **2014**, *62*, 1. [[CrossRef](#)]
142. Niazi, P.; Toliyat, H.A.; Goodarzi, A. Recently, robust Maximum Torque per Ampere (MTPA) control of PM-Assisted SynRM for traction applications. *IEEE Trans. Veh. Technol.* **2007**, *56*, 1538–1545. [[CrossRef](#)]
143. Soltani, J.; Abootorabi Zarchi, H.; Arab Markadeh, G.R. Stator-flux-oriented based encoderless direct torque control for synchronous reluctance machines using sliding mode approach. *World Acad. Sci. Eng. Technol.* **2009**, *58*, 883–889.
144. Saleh, S.A.; Rubaai, A. The performance of the frame-angle-based direct torque controller for PMSM drives at low and very low speeds. In Proceedings of the 2018 IEEE Industry Applications Society Annual Meeting (IAS), Portland, OR, USA, 23–27 September 2018.
145. Saleh, S.A.; Rubaai, A. Extending the frame-angle-based direct torque control of pmsm drives to low-speed operation. *IEEE Trans. Ind. Appl.* **2018**, *55*, 3138–3150. [[CrossRef](#)]
146. Sayeef, S.; Foo, G.; Rahman, M.F. Rotor position and speed estimation of a variable structure direct-torque-controlled IPM synchronous motor drive at very low speeds including standstill. *IEEE Trans. Ind. Electron.* **2010**, *57*, 3715–3723. [[CrossRef](#)]
147. Foo, G.; Sayeef, S.; Rahman, M.F. Low-speed and standstill operation of a sensorless direct torque and flux controlled IPM synchronous motor drive. *IEEE Trans. Energy Convers.* **2010**, *25*, 25–33. [[CrossRef](#)]
148. Guven, S.; Usta, M.A.; Okumus, H.I. An improved sensorless DTC-SVM for three-level inverter-fed permanent magnet synchronous motor drive. *Electr. Eng.* **2018**, *100*, 2553–2567. [[CrossRef](#)]
149. Yuan, X.; Zhang, C.; Zhang, S.; Wang, R.; Zhang, X. Predictive current control for SynRM drives under low dc link voltage. In Proceedings of the 2019 IEEE International Symposium on Predictive Control of Electrical Drives and Power Electronics (PRECEDE), Quanzhou, China, 31 May–2 June 2019; pp. 1–4.
150. Jlassi, I.; Cardoso, A.J.M. Model predictive current control of synchronous reluctance motors, including saturation and iron losses. In Proceedings of the 2018 XIII International Conference on Electrical Machines (ICEM), Alexandroupoli, Greece, 3–6 September 2018; pp. 1598–1603.
151. Lin, C.; Yu, J.; Yu, H.; Yu, H.-C.; Lo, Y.-T. Simplified model-free predictive current control for synchronous reluctance motor drive systems. In Proceedings of the 2015 IEEE International Magnetism Conference (INTERMAG), Beijing, China, 11–15 May 2015.
152. Veysinejad, A.; Rahmati, S.; Shamlou, S. Predictive direct torque control with reduced number of considered states in synchronous reluctance motor drive. In Proceedings of the 2019 10th International Power Electronics, Drive Systems and Technologies Conference (PEDSTC), Shiraz, Iran, 12–14 February 2019; pp. 90–95.
153. Aros, N.; Mora, V.; Alarcón, C. Model predictive control for synchronous reluctance motor drive. In Proceedings of the 2017 CHILEAN Conference on Electrical, Electronics Engineering, Information and Communication Technologies (CHILECON), Pucon, Chile, 18–20 October 2017; pp. 1–6.
154. Hadla, S.C.H. Active flux based finite control set model predictive control of synchronous reluctance motor drives. In Proceedings of the 2016 18th European Conference on Power Electronics and Applications (EPE'16 ECCE Europe), Karlsruhe, Germany, 5–9 September 2016; pp. 1–10.
155. Kiselev, A.; Catuogno, G.R.; Kuznietsov, A.; Leidhold, R. Finite control set MPC for open-phase fault tolerant control of synchronous reluctance motor. In Proceedings of the 2020 IEEE International Conference on Industrial Technology (ICIT), Buenos Aires, Argentina, 26–28 February 2020; pp. 1077–1082.
156. Riveros, J.A.; Barrero, F.; Levi, E.; Duran, M.J.; Toral, S.; Jones, M. Variable-speed five-phase induction motor drive based on predictive torque control. *IEEE Trans. Ind. Electron.* **2013**, *60*, 2957–2968. [[CrossRef](#)]
157. Lim, C.S.; Levi, E.; Jones, M.; Rahim, N.A.; Hew, W.P. FCS-MPC-based current control of a five-phase induction motor and its comparison with PI-PWM control. *IEEE Trans. Ind. Electron.* **2014**, *61*, 149–163. [[CrossRef](#)]
158. Morales-Caporal, R.; Pacas, M. Encoderless predictive direct torque control for synchronous reluctance machines at very low and zero speed. *IEEE Trans. Ind. Electron.* **2008**, *55*, 4408–4416. [[CrossRef](#)]

159. Rodriguez, J.; Kennel, R.; Espinoza, J.R.; Trincado, M.; Silva, C.A.; Rojas, C.A. High-performance control strategies for electrical drives: An experimental assessment. *IEEE Trans. Ind. Electron.* **2012**, *59*, 812–820. [CrossRef]
160. Li, C.; Wang, G.; Zhang, G.; Zhao, N.; Gao, Y.; Xu, D. Torque ripples minimization of sensorless synrm drives for low-speed operation using Bi-HFSI scheme. *IEEE Trans. Ind. Electron.* **2020**, *1*. [CrossRef]
161. Bugsch, M.; Piepenbreier, B. High-bandwidth sensorless control of synchronous reluctance machines in the low- and zero-speed range. *IEEE Trans. Ind. Appl.* **2020**, *56*, 2663–2672. [CrossRef]
162. Lin, F.-J.; Huang, M.-S.; Chen, S.-G.; Hsu, C.-W. Intelligent maximum torque per ampere tracking control of synchronous reluctance motor using recurrent legendre fuzzy neural network. *IEEE Trans. Power Electron.* **2019**, *34*, 12080–12094. [CrossRef]
163. Lin, F.-J.; Huang, M.-S.; Chen, S.-G.; Hsu, C.-W.; Liang, C.-H. Adaptive backstepping control for synchronous reluctance motor based on intelligent current angle control. *IEEE Trans. Power Electron.* **2020**, *35*, 7465–7479. [CrossRef]
164. Energy Efficient Control of Synchronous Machines in Deep Field-Weakening Operation Including Saturation Effects—IEEE Conference Publication. Available online: <https://ieeexplore.ieee.org/document/9065519> (accessed on 16 June 2020).
165. Manzolini, V.; Da Rù, D.; Bolognani, S. An effective flux weakening control of a SyRM drive including MTPV operation. *IEEE Trans. Ind. Appl.* **2018**, *55*, 2700–2709. [CrossRef]
166. Mahmoud, H.; Bacco, G.; Degano, M.; Bianchi, N.; Gerada, C. Synchronous reluctance motor iron losses: Considering machine nonlinearity at MTPA, FW, and MTPV operating conditions. *IEEE Trans. Energy Convers.* **2018**, *33*, 1402–1410. [CrossRef]
167. Ha, J.-I.; Kang, S.-J.; Sul, S.-K. Position-controlled synchronous reluctance motor without rotational transducer. *IEEE Trans. Ind. Appl.* **1999**, *35*, 1393–1398. [CrossRef]
168. Xu, D.; Wang, B.; Zhang, G.; Wang, G.; Yu, Y. A review of sensorless control methods for AC motor drives. *China Electrotech. Soc. Trans. Electr. Mach. Syst.* **2018**, *2*, 104–115. [CrossRef]
169. Amin, M.M.; Aziz, G.A.A.; Durkin, J.; Mohammed, O.A. A Hardware-in-the-loop realization of speed sensorless control of PMA-SynRM with steady-state and transient performances enhancement. *IEEE Trans. Ind. Appl.* **2019**, *55*, 5331–5342. [CrossRef]
170. Joo, K.-J.; Kim, I.-G.; Lee, J.; Go, S.-C. Robust speed sensorless control to estimated error for PMA-SynRM. *IEEE Trans. Magn.* **2017**, *53*, 1–4. [CrossRef]
171. Caporal, R.M.; Pacas, M. Suppression of saturation effects in a sensorless predictive controlled synchronous reluctance machine based on voltage space phasor injections. *IEEE Trans. Ind. Electron.* **2010**, *58*, 2809–2817. [CrossRef]
172. The Sensorless Vector Control Characteristics Analysis of Synchronous Reluctance Motor Using a Coupled FEM and Preisach Model—IEEE Conference Publication. Available online: <https://ieeexplore.ieee.org/document/4411981> (accessed on 16 June 2020).
173. Jung, S.-H.; Kobayashi, H.; Doki, S.; Okuma, S. An improvement of sensorless control performance by a mathematical modelling method of spatial harmonics for a SynRM. In Proceedings of the 2010 International Power Electronics Conference (ECCE ASIA), Sapporo, Japan, 21–24 June 2010; pp. 2010–2015.
174. Zbede, Y.B.; Gadoue, S.M.; Atkinson, D.J. Model predictive MRAS estimator for sensorless induction motor drives. *IEEE Trans. Ind. Electron.* **2016**, *63*, 3511–3521. [CrossRef]
175. Wang, D.; Lu, K.; Rasmussen, P.O. Improved closed-loop flux observer based sensorless control against system oscillation for synchronous reluctance machine drives. *IEEE Trans. Power Electron.* **2018**, *34*, 4593–4602. [CrossRef]
176. Schroedl, M.; Weinmeier, P. Sensorless control of reluctance machines at arbitrary operating conditions including standstill. *IEEE Trans. Power Electron.* **1994**, *9*, 225–231. [CrossRef]
177. Wei, M.-Y.; Liu, T.-H. A high-performance sensorless position control system of a synchronous reluctance motor using dual current-slope estimating technique. *IEEE Trans. Ind. Electron.* **2011**, *59*, 3411–3426. [CrossRef]
178. Sensorless Indirect Field Oriented Control of Single-sided Linear Induction Motor with a Novel Sliding Mode MRAS Speed Estimator. Available online: http://www.ije.ir/article_72544.html (accessed on 16 December 2019).
179. Reddy, C.U.; Prabhakar, K.K.; Singh, A.K.; Kumar, P. Speed estimation technique using modified stator current error-based MRAS for direct torque controlled induction motor drives. *IEEE J. Emerg. Sel. Top. Power Electron.* **2019**, *8*, 1223–1235. [CrossRef]
180. Holakooie, M.H.; Ojaghi, M.; Taheri, A. Direct torque control of six-phase induction motor with a novel MRAS-based stator resistance estimator. *IEEE Trans. Ind. Electron.* **2018**, *65*, 7685–7696. [CrossRef]
181. Kumar, R.; Das, S.; Syam, P.; Chattopadhyay, A.K. Review on model reference adaptive system for sensorless vector control of induction motor drives. *IET Electr. Power Appl.* **2015**, *9*, 496–511. [CrossRef]
182. Taheri, A.; Ren, H.-P.; Holakooie, M.H. Sensorless loss model control of the six-phase induction motor in all speed range by extended kalman filter. *IEEE Access* **2020**, *8*, 118741–118750. [CrossRef]
183. Lascu, C.V.; Jafarzadeh, S.; Fadali, M.S.; Blaabjerg, F. Direct torque control with feedback linearization for induction motor drives. *IEEE Trans. Power Electron.* **2017**, *32*, 2072–2080. [CrossRef]
184. Bolognani, L.; Peretti, L.; Zigliotto, M. Online MTPA control strategy for DTC synchronous-reluctance-motor drives. *IEEE Trans. Power Electron.* **2011**, *26*, 20–28. [CrossRef]
185. Matsuo, T.; El-Antably, A.; Lipo, T. A new control strategy for optimum-efficiency operation of a synchronous reluctance motor. *IEEE Trans. Ind. Appl.* **1997**, *33*, 1146–1153. [CrossRef]
186. Sun, T.; Wang, J.; Koc, M.; Chen, X. Self-learning MTPA control of interior permanent-magnet synchronous machine drives based on virtual signal injection. *IEEE Trans. Ind. Appl.* **2016**, *52*, 3062–3070. [CrossRef]

187. Yousefi-Talouki, A.; Pescetto, P.; Pellegrino, G. Sensorless direct flux vector control of synchronous reluctance motors including standstill, MTPA, and flux weakening. *IEEE Trans. Ind. Appl.* **2017**, *53*, 3598–3608. [[CrossRef](#)]
188. Varatharajan, A.; Cruz, S.; Hadla, H.; Briz, F. Predictive torque control of SynRM drives with online MTPA trajectory tracking and inductances estimation. In Proceedings of the 2017 IEEE International Electric Machines and Drives Conference (IEMDC), Miami, FL, USA, 21–24 May 2017.
189. Oliveira, A.; Cavaleiro, D.; Branco, R.; Hadla, S.C.H.; Cruz, S.M. An encoderless high-performance synchronous reluctance motor drive. In Proceedings of the 2015 IEEE International Conference on Industrial Technology (ICIT), Seville, Spain, 17–19 March 2015; pp. 2048–2055.
190. Vaez, S. An on-line loss minimization controller for interior permanent magnet motor drives. *IEEE Trans. Energy Convers.* **1999**, *14*, 1435–1440. [[CrossRef](#)]
191. Mademlis, C.; Member, A. Compensation of magnetic saturation in maximum torque to current vector controlled synchronous. *IEEE Trans. Energy Convers.* **2003**, *18*, 379–385. [[CrossRef](#)]
192. Mademlis, C.; Kioskeridis, I.; Margaritis, N. Optimal efficiency control strategy for interior permanent-magnet synchronous motor drives. *IEEE Trans. Energy Convers.* **2004**, *19*, 715–723. [[CrossRef](#)]
193. Rashad, E.; Radwan, T.; Rahman, M. A maximum torque per ampere vector control strategy for synchronous reluctance motors considering saturation and iron losses. In Proceedings of the Conference Record of the 2004 IEEE Industry Applications Conference, 2004. 39th IAS Annual Meeting, Seattle, WA, USA, 3–7 October 2004.
194. Sneyers, B.; Novotny, D.W.; Lipo, T.A. Field weakening in buried permanent magnet AC motor drives. *IEEE Trans. Ind. Appl.* **1985**, *21*, 398–407. [[CrossRef](#)]
195. Sebastian, T. Temperature effects on torque production and efficiency of PM motors using NdFeB magnets. *IEEE Trans. Ind. Appl.* **1995**, *31*, 353–357. [[CrossRef](#)]
196. Inoue, Y.; Morimoto, S.; Sanada, M. A novel control scheme for maximum power operation of synchronous reluctance motors including maximum torque per flux control. *IEEE Trans. Ind. Appl.* **2011**, *47*, 115–121. [[CrossRef](#)]
197. Da Rù, D.; Morandin, M.; Bolognani, S.; Castiello, M. Model predictive hysteresis current control for wide speed operation of a synchronous reluctance machine drive. In Proceedings of the IECON 2016—42nd Annual Conference of the IEEE Industrial Electronics Society, Florence, Italy, 23–26 October 2016; pp. 2845–2850.
198. Ahn, J.; Lim, S.-B.; Kim, K.-C.; Lee, J.; Choi, J.-H.; Kim, S.; Hong, J.P. Field weakening control of synchronous reluctance motor for electric power steering. *IET Electr. Power Appl.* **2007**, *1*, 565–570. [[CrossRef](#)]
199. Xu, L.; Xu, X.; A Lipo, T.; Novotny, D. Vector control of a synchronous reluctance motor including saturation and iron loss. *IEEE Trans. Ind. Appl.* **1991**, *27*, 977–985. [[CrossRef](#)]
200. Zhang, X.; Foo, G.H. A Robust field-weakening algorithm based on duty ratio regulation for direct torque controlled synchronous reluctance motor. *IEEE/ASME Trans. Mechatron.* **2015**, *21*, 765–773. [[CrossRef](#)]
201. Zanuso, G.; Peretti, L.; Sandulescu, P. Model-based flux weakening strategy for synchronous machines without additional regulators. *IET Electr. Power Appl.* **2018**, *12*, 1283–1290. [[CrossRef](#)]

Paper II

Heidari, H., Rassõlkin, A., Kallaste, A., Vaimann, T., and Belahcen, A. (2019). Harmonics Distortion in Inverter-Fed Motor-Drive Systems: Case Study. 2019 Electric Power Quality and Supply Reliability Conference (PQ) & 2019 Symposium on Electrical Engineering and Mechatronics (SEEM), 1–4. <https://doi.org/10.1109/PQ.2019.8818230>

Harmonics Distortion in Inverter-Fed Motor-Drive Systems: Case Study

Hamidreza Heidari, Anton Rassõlkin,
Ants Kallaste, Toomas Vaimann,
Department of Electrical Power
Engineering and Mechatronics
Tallinn University of Technology
Tallinn, Estonia
haheid@taltech.ee

Anouar Belahcen
Department of Electrical
Engineering and Automation
Aalto University
Espoo, Finland
anouar.belahcen@aalto.fi

Abstract— Current and voltage harmonics lead to iron losses in motors. As the iron losses have the largest portion of total losses in many motors, harmonic analysis of motors is of paramount importance. In this study, we compared the new designed permanent magnet assisted synchronous reluctance motor (PMSynRM) and synchronous reluctance motor (SynRM) with an industrial induction motor (IM) in terms of harmonic currents and harmonic voltages. To investigate the performance of the motors in terms of harmonic distortion, an industrial frequency converter based on direct torque control (DTC) strategy is adopted. The study shows the high harmonic injection of frequency converter to the system.

Keywords— permanent magnet synchronous reluctance motor, synchronous reluctance motor, induction motor, power quality

I. INTRODUCTION

Nowadays, Variable Speed Drives (VSDs) have become so popular in the industry, even for some fixed-speed applications. To save energy, extend motors' operation life and performance optimization, VSDs are the best choice in the industry. On the other hand, in the power quality point of view, VSDs as any power electronic devices integrated into grid produce distortions since they have non-linear loads into electric power systems that has become a serious issue in recent years [1], [2]. Power quality requirements of loads that have over 100% current total harmonic distortions (THD) may not be precisely regulated [3]. Moreover, harmonics affect power factor as shown in [4]. Considering this critical issue, it is needed to study VSD-fed drives in terms of harmonics and their effects on the power quality of systems. As an extensive solution for AC drives' harmonics distortion, some harmonics were eliminated by using passive [5], [6] or active [7] filters. Using passive filters on the grid-side before the frequency converter decreases the currents harmonics notably. Moreover, the structure for this method is quite simple and affordable to implement. However, it causes further disadvantages, which in some cases will cause irreparable damages to the system. Since the passive filters are configured based on the system design and limitations, the changes and modifications in the system can cause even higher distortions [8]. Besides, the size and cost of passive filters are also high which makes the active filter application more reasonable. Lack of inductors makes active filters size quite small and decreases the cost. The disadvantage of these filters can be a more power supply requirement [9].

VSD-fed IMs are widely used nowadays. However, SynRMs are gaining popularity in some applications such as pumps, fans, compressors, extruders, conveyors, and mixers [10]. Rotor anisotropy in SynRM results in high flux density

fluctuations in the iron. As a result, the harmonic currents in SynRM are striking. As the rotor anisotropy is the same with PMSynRM, the harmonic currents in PMSynRM are high. Due to the fairly high iron losses in these motors, the study in this area seems necessary. Determination of iron losses requires a precise study for design purposes. In terms of computation time of total loss calculation, it is crucial to choose an economical method. A nonlinear analytical model of SynRM has been proposed in [11] to calculate iron losses considering the magnetic iron saturation and slotting effect. Using coupled finite element method and response surface methodology the characteristic analyses of SynRM is done in [12].

DTC is a well-established and interesting control technique for different electric motor drive systems. In industrial frequency converters. The switching table-based DTC strategy benefits from fast dynamics response and simple control method, compared to the PWM-based techniques such as field oriented control (FOC) strategy. Because of the nonlinear characteristics of DTC, its DC-side harmonics spectrum is much different from that of PWM, as it does not have a deterministic model for its harmonics patterns [13]. A probabilistic AC-side voltage harmonics model was proposed in [2]. Also, DTC suffers from high harmonic currents which degrades its performance and affects the power quality of the system [14].

This paper focuses on the analysis of the grid-side and motor-side harmonics produced by industrial frequency converter running IM, SynRM and PMSynRM. For this purpose, a comparative study is obtained in terms of the current and voltage harmonics, when the aforementioned motors are driven using DTC strategy.

II. TEST SETUP

The test bench was designed in Electrical Machine Group Lab of Tallinn Technology University. Fig. 1 shows the implemented setup which the three motors were changed in three separate tests.

In this setup, we have coupled an industrial IM as a load to all three motors to test them under the same load condition. All the motors were driven by an industrial frequency converter, which is based on DTC strategy.

For control objectives, DTC method was chosen for all tests that is defined in the industrial frequency converter's setup. For measuring the currents, the Fluke 1400s AC current clamps with bandwidth of 5 kHz were used. The harmonic currents up to 100 times of the fundamental frequency were measured. NCTE 4000 Series 50Nm non-contact rotary torque sensor with 360 CPR angle sensor was implemented to measure the motors torque and speed. The NCTE 4000 series

The present research has been supported by the Estonian Research Council under grant PUT1260.

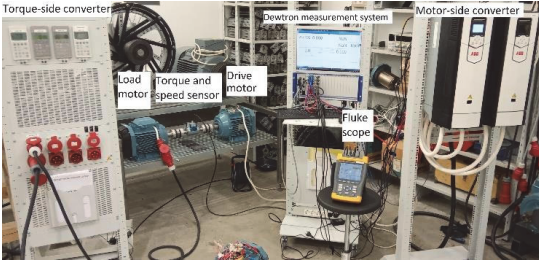


Fig. 1. Experimental setup.

is coupled to the load and motor mechanically. To measure voltages of lines, the DEWETRON data acquisition system was implemented. Displaying and registering all the measured data from torque and speed transducer and current clamps were done by the DEWETRON system, providing a universal measurement system for the tests. Using the Oxygen platform in the DEWETRON system, the harmonics were measured online and all power analysis and data acquisitions were done, simultaneously.

III. HARMONIC CURRENT ANALYSIS

The harmonic currents and voltages due to the frequency converter-fed electric motors highly affect the performance indices of the systems such as power quality. The voltage and current harmonic contents also lead to the torque variations. Windings, slotting, magnetic saturation and other geometrical configuration such as air gap length inequalities lead to flux spatial harmonics. Induced voltage of these harmonics results in harmonic currents in rotor windings in the IM. Moreover, VSDs distort the voltage and current shape and cause harmonics in grid and the motors, as well. DTC has attracted increasing attention in recent decades as it has quicker dynamic response comparing to the other control methods such as field oriented control (FOC) due to the usage of look-up table instead of modulators. Lack of direct current controller has also led to more simplicity of this method. However, direct control of the torque and flux contributes to low frequency current harmonics, especially the fifth and seventh harmonics. The $6n \pm 1; n = \text{odd}$ order harmonics. These harmonics causes harmonics loss and will affect electromagnetic interference. In addition, DTC has variable switching frequency as well as nonlinear elements in the control loop which complicate the analytical studies, including harmonic analysis, in this method. To cover this complexity, probabilistic analysis has been performed in [13].

In DTC method for IM, the flux vector is calculated from the voltage and current vectors as follows:

$$V_i = V_{dc} e^{\frac{j(i-1)\pi}{3}} \quad \text{for } i = 1 \text{ to } 3 \quad (1)$$

$$\Phi_s = \int (U_s - R_s I_s) dt \quad (2)$$

where, j is the square root of -1 , Φ_s is stator flux, U_s, I_s are the stator voltage and current, respectively, and R_s is the stator resistance.

The harmonic currents in the rotor interact with harmonic fluxes in the stator and cause harmonic torques, vibrations and noises in the motor. Stator windings carry sinusoidal currents with some harmonics. This is also true for the SnyRM and the PMSynRM, considering less effect on the rotor side due to

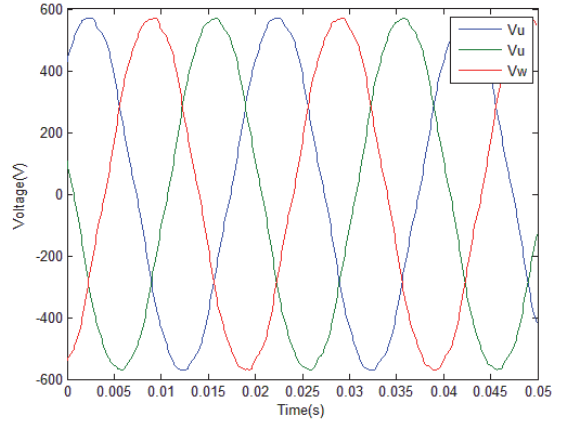


Fig. 2. Grid Input voltages of grid connected IM drive.

cold rotor of these motors. Since the flux wave shape is half-way symmetry and it is odd, the even harmonics are absent in Fourier series. Consequently, the currents have only the odd harmonics. Among these harmonics, third harmonics of each phases decrease each other's magnitude and this harmonic always has a negligible value. As a result, third harmonic of air gap flux is so small as the phase currents. On the other hand, fifth harmonic and seventh harmonics have striking magnitudes. In case of the torque, the fifth harmonic is called braking torque since its rotation direction is just apposite of the fundamental frequency. Besides, the seventh harmonic flux has the same rotational direction with fundamental flux. This results in the same torque production of the fundamental torque frequency and the seventh frequency. On the motor side, the current's harmonics are negligible leading to low losses. Motors, as a low pass filter avoid the high frequency harmonics. The low order of harmonics are measured by the order of 20 times higher than fundamental frequency.

IV. TEST RESULTS

To compare the harmonics of voltage and currents, all the drive systems were tested under 59 Nm load condition. In these tests, the result values are exported from oxygen platform and analyzed by MATLAB 2018b. This analysis enabled us to compare the harmonics of the drive systems in terms of voltages and currents. Fig. 2 shows the input voltages of the three phases of IM, which was connected to the grid without frequency converter. Basically, the voltages were supposed to be constant during all the tests as the grid is considered as an infinite bus bar. As a result, comparing Fig. 2 and Fig. 3, the same results are measured from the inverter-fed IM and grid connected IM. The figures show the low effect of the drive systems on the grid. In this test, the IM has been connected in delta connection and the measured voltages were the line voltages, which could be different with the phase voltages in terms of harmonic voltages. SynRM and PMSynRM were connected in star connection as well. It should be mentioned that the neutral point for the motors and the grid were not connected and the results for third harmonics were not precisely confidable.

To analyze the voltage harmonics of the both grid connected and inverter-fed IM, the Fast Fourier Transform of the voltages were calculated. Fig. 4 gives information about the low order harmonics of line 1st grid input voltage. The harmonics were supposed to be the same for all three phases

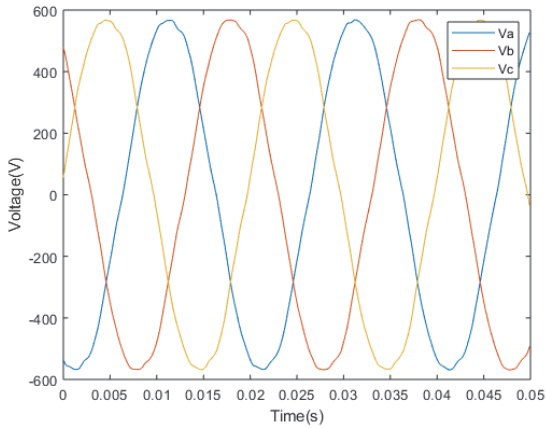


Fig. 3. Grid input voltages of inverter-fed IM drive.

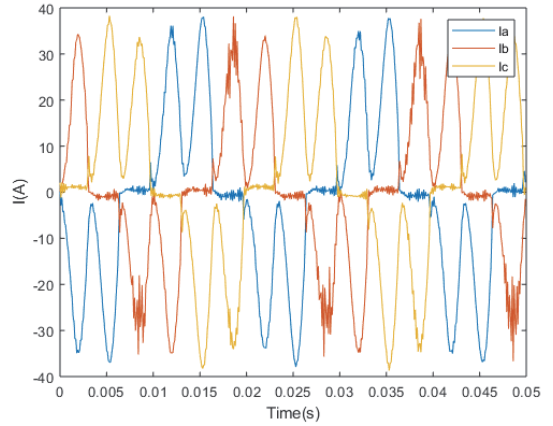


Fig. 5. Grid input currents of inverter-fed IM drive.

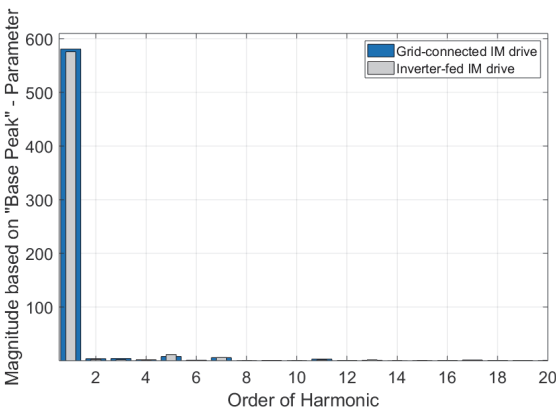


Fig. 4. Grid input voltage harmonics of IM drives.

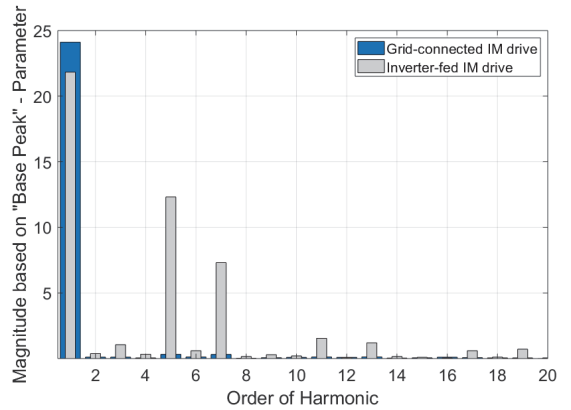


Fig. 6. Grid current harmonics of IM drive systems.

and only one phase was investigated. It was found out that the frequency converter has almost no effect on the grid voltage and injects no extra harmonics to the grid due to infinite bus.

On the other hand, the frequency converter made the input currents to the grid completely distorted. The three phase currents are shown in Fig. 5. The shape of currents were quite distorted and they were almost in the same shapes. To investigate the harmonics distortion injected by frequency converter, the harmonics of the IM were studied in both grid connected and inverter-fed drive. Fig. 6 shows that the results the fifth and seventh harmonics of the grid current was a big deal in inverter-fed drive, comparing to the grid connected drive. This result conforms the low amount of third harmonic produced by the frequency converter. The harmonics higher than 20th were not considerable and were neglected in this study.

To compare the effect of the three motor drive systems on the grid current, the harmonics were calculated for all the test and showed in Fig. 7. Taking the fundamental frequency magnitude into account, the PMSynRM produces higher fifth and seventh harmonics which are generally the most striking differences between the motor drive systems. Comparing SynRM and IM, almost the same fifth harmonic were calculated. The seventh harmonics of the two drive systems have the same magnitude which considering the fundamental frequency, it was found out that the IM has higher seventh

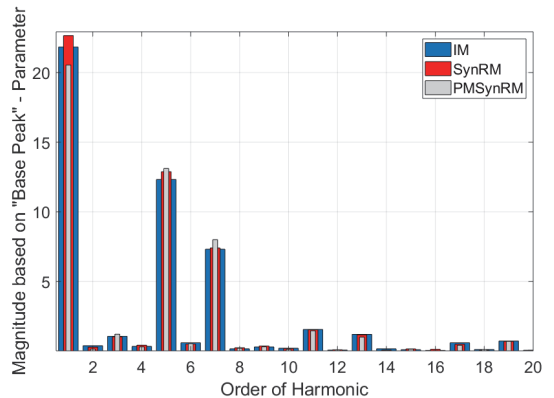


Fig. 7. Grid current harmonics of inverter-fed drives.

harmonics than SynRM. The higher order harmonics had negligible magnitudes.

On the motor side, the motors have different harmonic voltages which is shown in Fig. 8. Generally, the motors' voltages have no significant harmonics and driving the motors by the same industrial frequency converter, almost the same results has been achieved. Besides, the industrial frequency

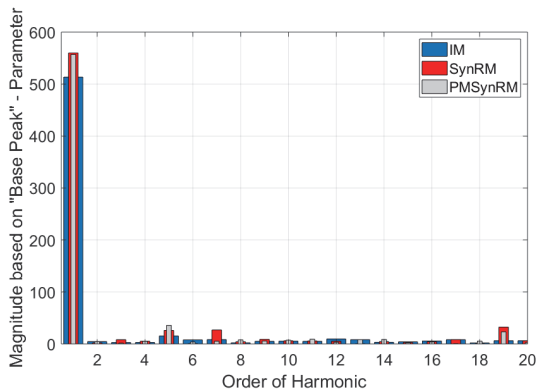


Fig. 8. Motor voltage harmonics of inverter-fed drives.

converter has a filter which avoids some harmonics to be injected to the motor. In case of fifth harmonics, PMSynRM has the biggest harmonic. Having look on the seventh harmonics, SynRM produced the biggest seventh harmonics.

As the motors are low pass filter, the harmonic currents have very small magnitudes which is negligible. Fig. 9 demonstrates the motors' current harmonics. It can be clearly seen that no harmonic has been produced in motors' current. The motors' current shaped are supposed to be almost pure sinusoidal.

V. CONCLUSIONS AND DISCUSSION

To investigate the motor drive systems in terms of power quality, it is inevitable to study voltage and current harmonics. In this study three different motors are driven in the same loading and driving status. The IM is driven in both grid connected and inverter-fed mode to analyse the effect of frequency converter to the system behaviour. In terms of harmonic voltages, the two systems have the same harmonics. In inverter-fed drive system, currents are distorted and the shape of input currents are not sinusoidal. The most significant harmonics are the fifth and seventh harmonics, which are injected to the grid. The even harmonics have negligible magnitude. Comparing motor voltage harmonics in inverter-fed drives, all the three motors have almost the same behaviour which is mostly because of the same stator structure. SynRM and PMSynRM have higher motor current harmonics, which are caused by rotor anisotropy in these motors.

REFERENCES

[1] M. Farbis, A. H. Hoevenaars, and J. L. Greenwald, "Oil field retrofit of ESPs to meet harmonic compliance," *IEEE Trans. Ind. Appl.*, vol. 52, no. 1, pp. 718–728, Jan. 2016.

[2] H. Liu, J. Liang, and L. Qi, "Harmonics mitigation and stability analysis of DTC motor drives in MVDC systems," in 2015 IEEE Energy Conversion Congress and Exposition (ECCE), 2015, pp. 3172–3178.

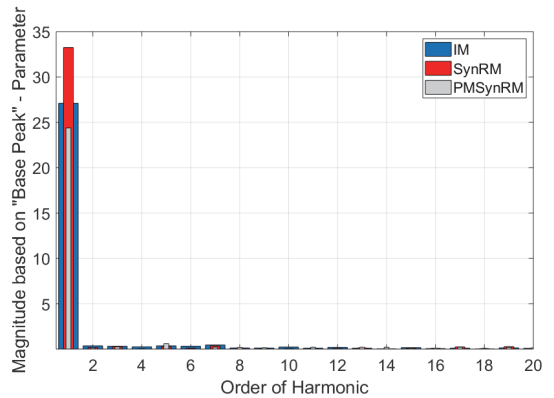


Fig. 9. Motor current harmonics of inverter-fed drives.

[3] J. Niitsoo, I. Palu, J. Kilter, P. Taklaja, and T. Vaimann, "Residential load harmonics in distribution grid," in 2013 3rd International Conference on Electric Power and Energy Conversion Systems, 2013, pp. 1–6.

[4] W. Mack Grady and R. J. Gilleskie, "Harmonics and how they relate to power factor," *Proc. EPRI Power Qual. Issues Oppor. Conf. (PQA'93)*, San Diego, CA, Nov. 1993., no. November, pp. 1–8, 1993.

[5] T. Hruby and S. Kocman, "Using broadband passive harmonic filters for harmonic mitigation in AC drives," *Proc. Int. Conf. Harmon. Qual. Power, ICHQP*, vol. 1, no. 3, pp. 172–176, 2014.

[6] N. A. Azeez, S. Pramanick, K. Gopakumar, and C. Cecati, "A 5th and 7th order harmonic suppression scheme using capacitive filtering for 2-level VSI fed IM drive," in 2014 International Symposium on Power Electronics, Electrical Drives, Automation and Motion, 2014, pp. 780–783.

[7] W.-H. Ko and J.-C. Gu, "Impact of shunt active harmonic filter on harmonic current distortion of voltage source inverter-fed drives," *IEEE Trans. Ind. Appl.*, vol. 52, no. 4, pp. 2816–2825, Jul. 2016.

[8] J. C. Das, "Passive filters – potentialities and limitations," *IEEE Trans. Ind. Appl.*, vol. 40, no. 1, pp. 232–241, 2004.

[9] "Basic Introduction to Filters – Active, Passive, and Switched-Cap (Rev. A) Analog and Mixed-Signal SNOA224A - TI.com."

[10] A. Rassölkin, H. Heidari, A. Kallaste, J. P. Acedo, and E. Romero-Cadaval, "Efficiency map comparison of induction and synchronous reluctance motors," in 26th International Workshop on Electric Drives: Improvement in Efficiency of Electric Drives (IWED), 2019, pp. 4–7.

[11] H. Mahmoud et al., "Synchronous reluctance motor iron losses: considering machine nonlinearity at MTPA, FW, and MTPV operating conditions," *IEEE Trans. Energy Convers.*, vol. 33, no. 3, pp. 1402–1410, 2018.

[12] Jung Ho Lee, Il Kyo Lee, Yong Hyun Cho, and Tae Won Yun, "Characteristics analysis and optimum design of anisotropy rotor synchronous reluctance motor using coupled finite element method and response surface methodology," *IEEE Trans. Magn.*, vol. 45, no. 10, pp. 4696–4699, 2009.

[13] S. Kaboli, E. Vahdati-Khajeh, and M. R. Zolghadri, "Probabilistic voltage harmonic analysis of direct torque controlled induction motor drives," *IEEE Trans. Power Electron.*, vol. 21, no. 4, pp. 1041–1052, 2006.

[14] H. Heidari et al., "A novel vector control strategy for a six-phase induction motor with low torque ripples and harmonic currents," *Energies*, vol. 12, no. 6, p. 1102, 2019.

Paper III

Heidari, H., Andriushchenko, E., Rassölkin, A., and Demidova, G. L. (2020). Comparison of Synchronous Reluctance Machine and Permanent Magnet-Assisted Synchronous Reluctance Machine Performance Characteristics, 2020 27th International Workshop on Electric Drives: MPEI Department of Electric Drives 90th Anniversary (IWED), 2020, pp. 1–5, doi: 10.1109/IWED48848.2020.9069583

Comparison of Synchronous Reluctance Machine and Permanent Magnet-Assisted Synchronous Reluctance Machine Performance Characteristics

Hamidreza Heidari, Ekaterina Andriushchenko, Anton Rassõlkin,
Ants Kallaste, Toomas Vaimann,
*Department of Electrical Power Engineering and Mechatronics
Tallinn University of Technology*
Tallinn, Estonia
haheid@taltech.ee

Galina L. Demidova
*Faculty of Control Systems and Robotics
ITMO University*
St. Petersburg, Russia

Abstract—Since the dominant induction machines and permanent magnet synchronous machines are well-established in the industry, the reluctance machines require more research work and investigation to substitute the conventional technologies. This paper analyzes the synchronous reluctance machines and permanent magnet-assisted synchronous reluctance machines in terms of the effect of permanent magnets in the model and the performance characteristic of the machines. The machines are designed and the parameters are measured. The vector diagrams of the machines and the equivalent circuits of the machines are analyzed. A comparison of the machines in terms of power factor, efficiency, and torque of the machines is provided based on the measurements. The study presents a notable improvement in power factor and efficiency in the case of inserting permanent magnets in the synchronous reluctance machine's rotor.

Keywords—*ac machines, permanent magnet machines, rotors.*

I. INTRODUCTION

Recently, much attention is paid to the synchronous reluctance machine (SynRM) in the pump, fan, and traction applications [1], [2]. On the account of the variable-speed drives development and their efficient drive possibilities, SynRM has the potential to replace the conventional machine technologies in the future [3]–[6]. Based on the literature review [7]–[9], some highlighted features of SynRM can be listed as:

- High efficiency
- Low-cost
- Easy maintenance
- Robust rotor structure
- High power to inertia ratio
- High power density
- High dynamic
- Wide-speed range

The operation of SynRM is based on the salient poles with no need for permanent magnets (PM) or any field-windings on the rotor side. Owing to the lack of bars or field-windings on the rotor and possible low-temperature operation, higher efficiency than induction machine (IM) is projected for SynRM [10]. Moreover, the bearing faults that can be caused also by rotor overheating, in the IM make the biggest portion

of machine faults [11]. Similar faults can be decreased in SynRM due to the possible low-temperature operation. Additionally, the elimination of the rotor bars or field-windings results in fewer elements in the rotor and consequently more reliable machine technology. This can offer an economical technology not only in the manufacturing stage [12] but also in maintenance. This rotor structure of SynRM leads to low inertia of the machine and the power to the inertia ratio can be higher as compared with IM. In addition, the higher power density of this machine provides the possibility of producing a smaller frame size in the same power range [13]. Moreover, because of the low moment of inertia, SynRMs can present higher dynamic performance and short acceleration time in comparison with IM. However, bearing in mind all the design improvements in the literature, SynRM presents a very low power factor, which is considered as a severe limitation for this machine [14].

Adding ferrite PMs to SynRM leads to a novel class of permanent magnet synchronous machine (PMSM) that can notably improve the performance of SynRM. In this sense, permanent magnet-assisted synchronous reluctance machine (PMSynRM) is a type of interior PMSM with comparable performance. This machine exploits the peculiar rotor characteristics of SynRM and the PMs, concurrently, which can lead to a considerable improvement in SynRM performance. On account of the growing price of rare-earth magnets [15], the interest in PMSM is decreasing. Among the competitive machines, PMSynRM offers a cost-effective and high-performance alternative for PMSM.

In recent decades, many research works on PMSynRM are carried out in traction applications [3]. This machine has a desirable performance at high speeds, fulfilling the constant-power speed range requirements [16]. In addition, the usage of ferrite PMs has provided a reliable and low-cost choice for manufacturers. One significant superiority of the PMSynRM against SynRM is its high power factor, which can provide a more efficient machine technology [17]. Having said this, the manufacturing and maintenance of PMSynRM can be more difficult than SynRM due to the usage of PMs and the difficulties with the assembling and disassembling. In addition, the additive mass due to the ferrite PMs can result in a higher moment of inertia of the rotor. Also, the possible faults [18] in PMs can be a drawback for this type of machine.

In the rest of this paper, the SynRM and PMSynRM are analyzed in terms of the $d - q$ equivalent circuit and vector diagram and the equations in section II. The comparison of the designed machines in terms of performance

The present research has been supported by the Estonian Research Council under grant PUT1260

characteristics is carried out in section III, based on the section II analysis. A conclusion of the study and the future plan of the study is presented in section IV.

II. SYNRM AND PMSYNRM ANALYSIS

SynRM produces reluctance torque, resulting from changing the magnetic reluctance. The flux produced by the stator flows into the lowest reluctance. Therefore, if the rotor is not aligned with the flux, the reluctance torque will spin the rotor in the direction with minimum magnetic reluctance. On the other hand, the operation of the PMSynRM is based on not only the reluctance torque but also the magnetic torque. Augmenting the magnetic torque due to the PMs, PMSynRM can produce higher torque than SynRM.

Fig. 1 shows the structure of the machines in one sketch. It can be seen from this figure that the machines can have the same stator. The difference between the machines is in the utilization of the ferrite magnets. In SynRM, the flux paths provide a low magnetic reluctance in the d -axis. The flux barriers are implemented to avoid the flux to flow into the q -axis. This leads to a higher reluctance in the q -axis. Therefore, the inductance in the d -axis (L_d) is bigger than the inductance in q -axis (L_q). The ratio between d, q -axis inductances is known as the saliency ratio. This ratio is defined as:

$$\zeta = \frac{L_d}{L_q} \quad (1)$$

The saliency ratio defines the reluctance torque and the power factor of the machines. This ratio can be increased by means of ferrite PMs.

From the power factor point of view, adding PMs to the SynRM's rotor can lead to an improved power factor in PMSynRM. The power factor equation is also defined as:

$$\cos(\varphi) = \sin(\delta), \quad \varphi = 90 - \delta \quad (2)$$

where φ is the phase angle between the voltage and current vectors of the machines. The less phase lag between the voltage and current vectors of the machine, the bigger power factor the machine can have. In this equation, δ denotes the phase lag between the flux and current in the $d-q$ reference frame. This angle is also called torque angle, which is described in this section.

In reluctance machines, the power factor can also be defined as follows.

$$PF = \frac{\zeta-1}{\zeta+1} \quad (3)$$

This equation shows that a higher saliency ratio leads to a higher power factor in the machine. It is predicted to have a higher power factor in PMSynRM than SynRM, considering a possible higher saliency ratio in PMSynRM.

The torque can be described for the machines as the following:

$$T = \frac{3}{2} p |\overline{\Phi_{dq}}| |i_{dq}| \sin(\delta) \quad (4)$$

where p denotes the pole pairs of the machines, i_{dq} , Φ_{dq} represent the d , and q -axis currents, and fluxes of the machines, respectively. The torque angle can be improved by means of the PMs, where the angle is bigger for the PMSynRM. This can lead to higher maximum torque per ampere for the PMSynRM, as in equation (4).

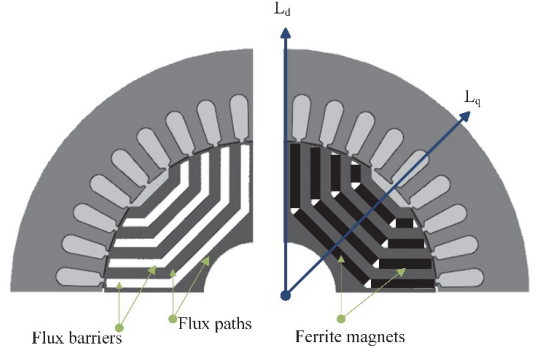


Fig. 1. The sketch of SynRM (left side) and PMSynRM (right side) stator and rotor structure.

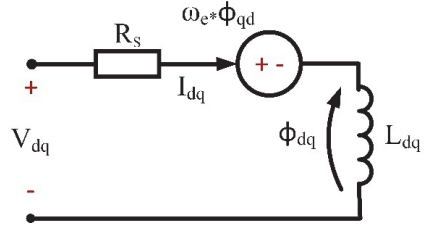


Fig. 2. The d - q equivalent circuit of SynRM and PMSynRM.

The derived torque equation in the synchronous reference frame for the SynRM, and PMSynRM, which is independent of the rotor angle is simplified as below.

$$T = \frac{3}{2} p (L_d - L_q) i_d i_q + \phi_m i_q \quad (5)$$

Where ϕ_m denotes the flux linkage of the PMs in PMSynRM. Due to the lack of magnets in SynRM, the flux linkage is zero in this machine, which shows that the torque equation for the SynRM is purely reluctance and is only produced due to the saliency of the rotor.

In order to analyze the parameters of the machines for performance characteristic comparison, the machines' equivalent circuit in the $d-q$ reference frame is illustrated in Fig. 2. The equivalent circuit in $d-q$ reference frame provides the voltage equations of the $d-q$ reference frame. These voltages are as follows.

$$V_d = R_s i_d + \frac{d\Phi_d}{dt} - \omega_e L_q i_q \quad (6)$$

$$V_q = R_s i_q + \frac{d\Phi_q}{dt} + \omega_e L_d i_d + \omega_e \Phi_m \quad (7)$$

Where V_{dq} denote the d , and q -axis voltages, respectively. R_s is the stator resistance of the machines, which is the same for the machines on account of the same stator application for both of the machines. The voltage vectors of the SynRM and PMSynRM have different q -axis values and the same d -axis values. This leads to different values for the machines' voltage and current angle (φ). The decrement in φ and increment in power factor is projected as a result of ferrite PMs inserting.

The flux equations are defined for the machines as:

$$\phi_d = L_d i_d + \phi_m \quad (8)$$

$$\phi_q = L_q i_q \quad (9)$$

The fluxes have the same value in the q -axis and different values in the d -axis. This can be presented as the effect of the magnets, which affects the torque angle (δ).

It is worth mentioning that the inserted PMs can only affect the PMSynRM's voltage equations in the d -axis in the situation of running the machine, while in zero-speed control or locked situation the voltage equation is the same with SynRM.

The displacement of flux and voltage vectors of SynRM due to the magnets is also presented in Fig 3. The discussed topics can be concluded from this figure, as well.

III. COMPARISON OF THE STUDIED SYNRM AND PMSYNRM

In this section, a comparison of the machines is carried out for the machines in terms of the design and measured parameters.

A. Design Parameters

For the comparison purpose, reluctance machines were designed and built [19]. For the construction, IM 132 MA size frame was used and the stator windings were rewound to reach 10.5 kW machine. The laminations for the SynRM were designed and manufactured so that the machine's calculated nominal values were as in [20]. Then, the laminations were stacked and the SynRM's rotor was designed. The same procedure was applied for PMSynRM's rotor. Then, the ferrite PMs were added into the flux barriers as in Fig. 1. The designed rotors of the studied SynRM and PMSynRM are depicted in Fig. 4.

Table I presents the design parameters of the machines in terms of the electrical and mechanical specifications. Due to the same stator windings for the machines, the number of pole pairs and the rated power of the machines was the same. As a result of the same pole pairs, the rated speeds were equal for both machines. The usage of ferrite PMs and higher mass of the rotor resulted in a higher moment of inertia of the PMSynRM.

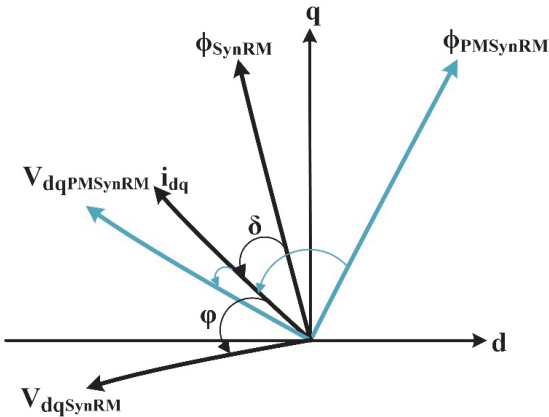


Fig. 3. The SynRM and PMSynRM vector diagram.



Fig. 4. The rotor structure of the designed SynRM (left side) and the PMSynRM (right side).

TABLE I. THE STUDIED MACHINES' DESIGN AND MEASURED PARAMETERS

Machine		
Parameter	SynRM	PMSynRM
Frame size	132 MA	132 MA
Rated Power (kW)	10.5	10.5
Number of poles	2	2
Rated Speed (rpm)	1500	1500
Moment of inertia (kgm ²)	0.02	0.04
R_s (Ω)	0.72	0.72
L_d (H)	0.08	0.09
L_q (H)	0.02	0.01
$\cos(\phi)$	0.6	0.8
Rated current (A)	25.3	18.9
Efficiency	85.2%	90.6%

B. Measured Parameters

In order to compare SynRM and PMSynRM, the machines' parameters were measured in the same condition. The stator resistance of the phases were measured by an ohmmeter, where the electrical resistance between the two phases was $R_{measured}$. This resistance had a relation with the phase resistance as below.

$$R_s = \frac{1}{2} R_{measured} \quad (10)$$

In order to measure the machines' inductances, the measurement circuit was designed as Fig. 5. To eliminate the effect of the flux linkage in the voltage of PMSynRM, the machine was locked. The measurement of L_d required the machines to be aligned with phase A and zero electrical degree. The $d-q$ equivalent circuit of the machines is utilized for measurements. Simplifying the equation (6), while the rotor was locked in zero electrical degree, the machines' current was calculated as:

$$i = \frac{V}{R_s} (1 - e^{-\frac{t}{\tau}}) \quad (11)$$

where $\tau = \frac{L}{R_s}$ is the circuit's time constant. Measuring the voltage and current, the total inductance of the machine was calculated. According to Fig. 5, the total inductance is equal to $L_s = \frac{3}{2} L_d$, while the machines were locked in phase A and

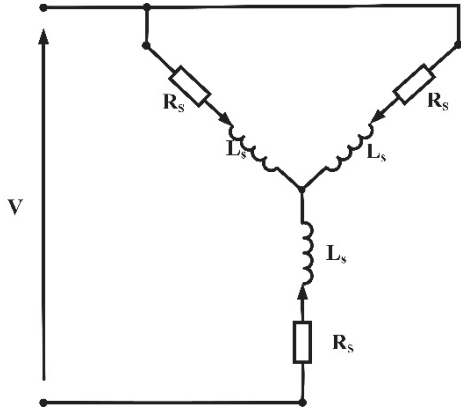


Fig. 5. Measurement circuit.

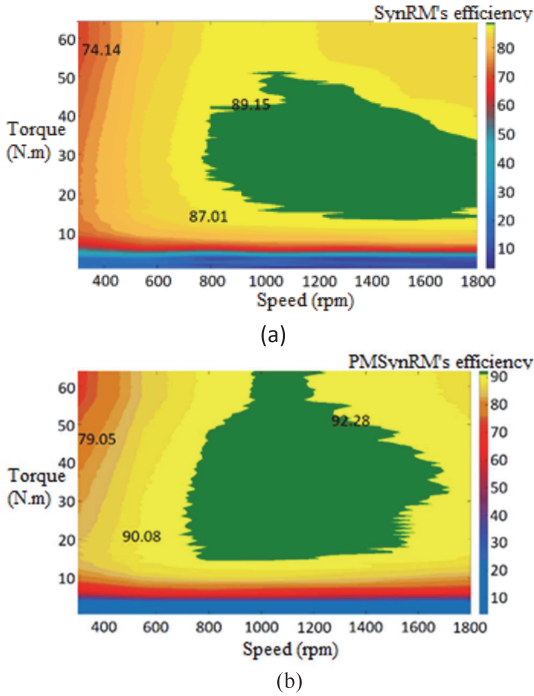


Fig. 6. Efficiency map of SynRM (a), and PMSynRM (b).

the zero electrical degree. Thus, the d -axis inductance of the machines was measured by this test. Likewise, the same test was done to measure L_q , while the machine was in the 90° electrical position. The nominal values are measured for the machines and presented in Table I. As can be seen from the table, the stator resistance of the machines was the same. The d -axis inductance was improved for 12.5% in PMSynRM, attributed to the PMs. Also, the measured values of the machines showed 50% decrement in L_q . Certainly, the saliency ratio of the PMSynRM was also increased. As a consequence, the power factor of PMSynRM was increased by 33.3%. Due to the higher power factor of the machine, the lower current flowed into the stator in PMSynRM. A remarkable decrease of 25% has occurred in PMSynRM's current. As a result, the copper losses in the stator were

reduced and the efficiency of the machines was measured, where the nominal efficiency of PMSynRM was improved against SynRM by 5%. With regard to the changes in the d , q -axis inductances, it can be concluded from equation (5) that the PMSynRM's maximum torque per ampere was also increased, which was assumed.

For a more detailed comparison of the studied machines' performances, the efficiency map of the machines was provided in a wide speed range. Fig. 6 shows the efficiency map of the machines. The method and the requirements of the test are described in detail in [20]. Both of the machines were tested in the steady-state condition. The efficiency maps of the machines show a notable change in the efficiency of the machines. It can be seen from the efficiency maps that, in the whole speed regions, the efficiency of the PMSynRM is improved.

IV. CONCLUSION

SynRM offers a reliable, cost-effective machine, which suffers from severe low power factor. To improve the performance characteristics of the SynRM, ferrite PMs were inserted into the rotor, which proposes PMSynRM. In this paper, the analysis of the effect of the PMs on the PMSynRM performance characteristics was reported. The study showed a considerable improvement in the PMSynRM inductances, which resulted in a higher saliency ratio. Higher saliency ratio resulted in higher torque and power factor improvement, which led to a remarkable decrement in the current of the machine in the same torque. Due to the lower current of PMSynRM, the losses in the machine decreased. Hence, the higher efficiency of PMSynRM in comparison with SynRM was measured and discussed. On the other hand, the ferrite PMs led to a fairly higher cost and harder manufacturing. In addition, the inertia of the machine was also increased in PMSynRM.

The $d-q$ equivalent circuit can be also applied for control purposes, which are in the scope of future research works.

REFERENCES

- [1] P. Subtitle, "High output synchronous reluctance motor and drive package - Optimized cost of ownership for pump and fan applications," *ABB, Press release*, 2012.
- [2] S. Taghavi, S. Member, and P. Pillay, "A Sizing Methodology of the Synchronous Reluctance Motor for Traction Applications," *IEEE J. Emerg. Sel. Top. Power Electron.*, vol. 2, no. 2, pp. 329–340, 2014.
- [3] E. Trancho *et al.*, "PM-Assisted Synchronous Reluctance Machine Flux Weakening Control for EV and HEV Applications," *IEEE Trans. Ind. Electron.*, 2018.
- [4] H. Heidari, A. Rassolkin, A. Kallaste, T. Vaimann, and A. Belachen, "Harmonics Distortion in Inverter-Fed Motor-Drive Systems: Case Study," in *2019 Electric Power Quality and Supply Reliability Conference (PQ) & 2019 Symposium on Electrical Engineering and Mechatronics (SEEM)*, 2019, pp. 1–4.
- [5] M. H. Holakoie, A. Taheri, and M. B. B. Sharifian, "MRAS based speed estimator for sensorless vector control of a linear induction motor with improved adaptation mechanisms," *J. Power Electron.*, vol. 15, no. 5, pp. 1274–1285, 2015.
- [6] H. Heidari *et al.*, "A Novel Vector Control Strategy for a Six-Phase Induction Motor with Low Torque Ripples and Harmonic Currents," *Energies*, vol. 12, no. 6, p. 1102, 2019.
- [7] G. Pellegrino, T. M. Jahns, N. Bianchi, W. Soong, and F. Cupertino, *The Rediscovery of Synchronous Reluctance and Ferrite Permanent Magnet Motors*. Cham: Springer International Publishing, 2016.
- [8] S. Orlova, V. Pugachov, A. Rassolkin, A. Kallaste, and T. Vaimann, "Design of Rotors for Synchronous Reluctance Motor: Analytical Treatment and Optimization Keywords Analytical Treatment of the

Rotor Designs,” in *Proceeding of EPE'19 ECCE Europe*, 2019, no. 1, pp. 1–9.

- [9] S. Orlova, A. Vezzini, and V. Pugachov, “Analysis of parameters for optimal design of synchronous Reluctance Motor,” in *2015 56th International Scientific Conference on Power and Electrical Engineering of Riga Technical University, RTUCON 2015*, 2015.
- [10] P. S. Ghahfarokhi, A. Belahcen, A. Kallaste, T. Vaimann, L. Gerokov, and A. Rassolkin, “Thermal analysis of a SynRM using a thermal network and a hybrid model,” in *Proceedings - 2018 23rd International Conference on Electrical Machines, ICEM 2018*, 2018, pp. 2682–2688.
- [11] B. Asad, T. Vaimann, A. Rassolkin, A. Kallaste, and A. Belahcen, “A Survey of Broken Rotor Bar Fault Diagnostic Methods of Induction Motor,” *Electr. Control Commun. Eng.*, vol. 14, no. 2, pp. 117–124, 2019.
- [12] S. Orlova, A. Rassolkin, A. Kallaste, T. Vaimann, and A. Belahcen, “Lifecycle Analysis of Different Motors from the Standpoint of Environmental Impact,” *Latv. J. Phys. Tech. Sci.*, vol. 53, no. 6, pp. 37–46, 2016.
- [13] A. T. De Almeida, F. J. T. E. Ferreira, and G. Baoming, “Beyond induction motors - Technology trends to move up efficiency,” *IEEE Trans. Ind. Appl.*, 2014.
- [14] Y. Wang, D. Ionel, D. G. Dorrell, and S. Stretz, “Establishing the Power Factor Limitations for Synchronous Reluctance Machines,” *IEEE Trans. Magn.*, vol. 51, no. 11, pp. 1–4, 2015.
- [15] N. Korn, T. Vaimann, A. Kallaste, and A. Belahcen, “Comparative study of slow-speed slotless synchronous generator using SmCo and NdFeB permanent magnets,” in *9th International: 2014 Electric Power Quality and Supply Reliability Conference, PQ 2014 - Proceedings*, 2014, pp. 247–250.
- [16] M. Barcaro, N. Bianchi, and F. Magnussen, “Permanent-magnet optimization in permanent-magnet-assisted synchronous reluctance motor for a wide constant-power speed range,” *IEEE Trans. Ind. Electron.*, 2012.
- [17] M. Ferrari, N. Bianchi, and E. Fornasiero, “Analysis of rotor saturation in synchronous reluctance and PM-assisted reluctance motors,” *IEEE Trans. Ind. Appl.*, 2015.
- [18] J. Pando-Acedo *et al.*, “Hybrid FEA-Simulink Modelling of Permanent Magnet Assisted Synchronous Reluctance Motor with Unbalanced Magnet Flux,” in *2019 IEEE 12th International Symposium on Diagnostics for Electrical Machines, Power Electronics and Drives (SDEMPED)*, 2019, pp. 174–180.
- [19] K. Janson, A. Belahcen, A. Kallaste, and T. Vaimann, “Permanent magnet reluctance motor (Patent),” P201400013, 2016.
- [20] A. Rassolkin, H. Heidari, A. Kallaste, J. P. Acedo, and E. Romero-cadaval, “Efficiency Map Comparison of Induction and Synchronous Reluctance Motors,” in *26th International Workshop on Electric Drives: Improvement in Efficiency of Electric Drives (IWED)*, 2019, pp. 4–7.

Paper IV

Heidari, H., Rassõlkin, A., Kallaste, A., Vaimann, T., Andriushchenko, E., A Comparison of the Vector Control of Synchronous Reluctance Motor and Permanent Magnet-Assisted Synchronous Reluctance Motor, 2021 XVIII International Scientific Technical Conference Alternating Current Electric Drives (ACED), 2021, pp. 1–6, doi: 10.1109/ACED50605.2021.9462265

A Comparison of the Vector Control of Synchronous Reluctance Motor and Permanent Magnet-Assisted Synchronous Reluctance Motor

Hamidreza Heidari, Anton Rassõlkin, Ants Kallaste, Toomas Vaimann, Ekaterina Andriushchenko, Anouar Belahcen
Department of Electrical Power Engineering and Mechatronics
Tallinn University of Technology
Tallinn, Estonia
haheid@taltech.ee

Arash Razzaghi
Department of Electrical Engineering
University of IAU
Mianeh, Iran
razzaghi.ieee@gmail.com

Abstract—Field-oriented control presents a high-performance control method that is applied for many motors. In this paper, the comparison of the field-oriented control of synchronous reluctance motor and permanent magnet-assisted synchronous reluctance motor is carried out. The highlighted features of the field-oriented control of the two motors are studied and the similarities and the differences are investigated. The motors are modeled and controlled in the Plescs simulation platform. The simulation results are verified by the experimental tests.

Keywords—Synchronous reluctance motor, permanent magnet-assisted synchronous reluctance motor, field-oriented control

I. INTRODUCTION

One of the severe obstacles against synchronous reluctance motor (SynRM) and permanent magnet-assisted synchronous reluctance motor (PMSynRM) development was the lack of the possibility of the grid-connected drive of these motors, as well all synchronous technology. Some line-start designs of these motors were proposed in the literature, which reduced the performance and the efficiency of the motors [1]. Thanks to the power electronic device advancements and the emergence of variable-speed drives (VSD), the inverter-fed drive has provided a convenient and more efficient, and high-performance control of SynRM and PMSynRM [2]. On the other hand, the application of VSDs causes some consequences such as injecting harmonics to the grid and the motors, as well [3]. Additionally, the VSDs can cause some losses themselves and decrease the efficiency of the total system in some operation conditions. Moreover, the VSD requirement of these motors for drive purposes is highly costly, which is auxiliary to the budget for the motor [4]. Having said this, the costs for implementation of SynRM can be covered in a short period [5]. Besides, VSD can double the efficiency of the SynRMs in the partial load, which makes the usage of motors more reasonable for pump and fan applications [6]. The environmental concerns can also be fulfilled with these motors, especially with inverted fed drives due to the lack of permanent magnets and less power consumption with comparable performance with the other well-developed technologies.

Considering the VSD requirement of the SynRM and PMSynRM drive, many research works are carried out recently on the control of these motors. Especially, these motors suffer from some drawbacks such as high torque

ripples, which in some applications is not desired and has attracted a considerable portion of attention in the control aspect [7]. Another interesting topic in control of SynRMs is to increase the efficiency of the whole drive system which makes these motors a promising competitive for the conventional motor types.

As a first approximation, in this study, field-oriented control (FOC) was selected because of the high performance of the control with low torque ripple and high efficiency. This is mostly due to the precise current control with proportional-integral (PI) controllers in the synchronous reference frame.

In the rest of the paper, the highlights of the FOC are presented in section II. Later, the models of the SynRM and PMSynRM are briefly discussed and compared in section III. The implementation of the FOC of the SynRM and PMSynRM is studied in section IV. Then, the simulation results are presented and compared in section V. The experimental results are discussed in section VI. A conclusion of the paper is presented in section VII.

II. THE HIGHLIGHTS OF FOC

FOC has the best steady-state performance among the control algorithms, and this method is prevalent for the applications where the efficiency of the system is important such as the mining and steel industry [8]. Also, the method is so convenient to apply to all the ac motors in diverse ranges of power with some modifications in the algorithm. Briefly, the advantages of FOC are listed as follows [9].

- High steady-state performance
- Precise current control
- Simple implementation of the method
- Simple compatibility with many ac motors
- Simple modulation system implementation
- Constant switching frequency

Concerning all the benefits of FOC, some severe drawbacks of this method convince the researchers to study other control methods. Firstly, the method is highly complicated in terms of the computation burden. Due to the usage of the PI controllers and PWM block, the execution time of the FOC algorithm in the processor is high [10]. This is one of the reasons that in many industrial applications, such as pump and fan, where the simplicity of the method and shorter execution time is required, some leading manufacturers have designed their VSDs based on other control methods [11]. Secondly, the dynamic of this method

The research has been supported by the Estonian Research Council under grant PSG453

is considerably low [12], [13]. The drawbacks of FOC are listed as follows.

- High computation burden for processor
- Low dynamic of the method
- Low robustness of the method due to the high dependency of the method to the motor's parameters (flux vector angle)

III. THE MODEL OF SYNRM AND PMSYNRM IN THE SYNCHRONOUS REFERENCE FRAME

The torque equation in the synchronous reference frame for the SynRM, and PMSynRM, which is independent of the rotor angle is as below.

$$T = \frac{3}{2}p(L_d - L_q)i_d i_q + \phi_m i_q \quad (1)$$

Where $L_{d,q}$ denote the inductances in d, and q-axes and $i_{d,q}$ denote the currents in d, and q-axes, respectively. ϕ_m denotes the flux linkage of the magnets in PMSynRM. Due to the lack of the magnets in SynRM, the flux linkage is zero in this machine, which shows that the torque for the SynRM is purely reluctance torque and is only produced due to the anisotropic structure of the rotor.

The voltages in the synchronous reference frame in SynRM and PMSynRM are as follows.

$$V_d = R_s i_d + \frac{d\phi_d}{dt} - \omega_e L_q i_q \quad (2)$$

$$V_q = R_s i_q + \frac{d\phi_q}{dt} + \omega_e L_d i_d + \omega_e \phi_m \quad (3)$$

Where V_{dq} and ϕ_{dq} denote the d, and q-axis voltages, and fluxes, respectively. R_s is the stator resistance of the machines, which is the same for the machines on account of the same stator application for both of the motors. ω_e denotes the electrical speed of the motor. The voltage vectors of the SynRM and PMSynRM have different q-axis values and the same d-axis values. This leads to different values for the motors' voltage and current angle (φ). This is shown in Fig.1. The decrement in φ and increment in power factor is projected as a result of inserting the magnets in the rotor.

The flux equations are defined for the machines as:

$$\phi_d = L_d i_d + \phi_m \quad (4)$$

$$\phi_q = L_q i_q \quad (5)$$

The fluxes have the same value in the q-axis and different values in the d-axis. This can be presented as the effect of the magnets, which affects the torque angle (δ). This difference of the motors is of paramount importance which should be accurately considered in the control of the motors.

IV. FOC OF THE SYNRM AND PMSYNRM

FOC provides the possibility of the control of three-phase SynRMs as a dc motor which makes the control more convenient and precise. This is done by transferring the equations of the motor from the three-dimensional stationary reference frame to the two-dimensional synchronous reference frame.

Fig. 2 shows the block diagram of FOC of the SynRM and PMSynRM. In principle, the three-dimensional currents of

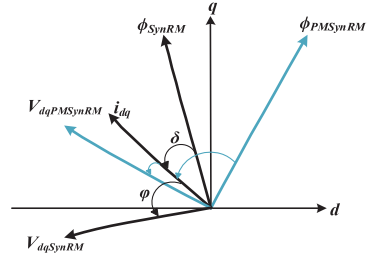


Fig. 1: The SynRM and PMSynRM vector diagram

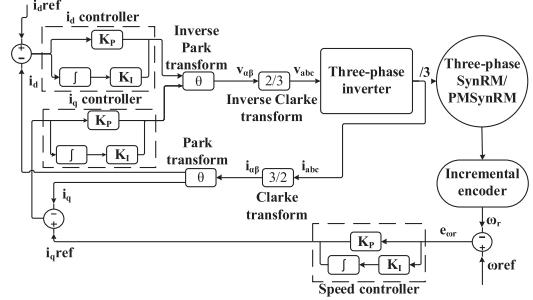


Fig. 2: FOC of SynRM and PMSynRM

the motors are measured and transformed into a two-dimensional stationary frame of $\alpha - \beta$ by means of Clarke transform. Thanks to the Park transform, the most sophisticated part of FOC is to transform the currents from the stationary reference frame to the synchronous reference frame. Then, the motor currents in the $d - q$ reference frame are compared with the reference values. The i_d corresponds to the flux in the FOC, which is correspondent to excitation current in dc motor, and the i_q represents the torque in FOC, which is correspondent to the armature current in the dc motor. In this sense, the feedback from rotor speed is compared with the required speed for the control, and the error is regulated through a PI controller. The output of this regulator is the reference value for the q-axis current, which is correspondent to the torque in the FOC loop. The d-axis current reference is also defined either with a constant value or a dynamic value, using the motors' model. Employing two PI regulators in the control loop, the errors of the d and q-axis currents are regulated. These controllers regulate the motor's currents in the synchronous reference frame. The regulated values of the d and q-axes currents generate the required voltages for the proper control of the motor. These values are in the synchronous reference frame, which through inverse Park transformer are transformed into the stationary reference frame. The two-dimensional voltages in the stationary reference frame are transformed into three-dimensional voltages by inverse Clark transform. Then, the modulation block of PWM is normally used in FOC to generate the voltages to the motor and drive the motor.

Apart from the similarities of the FOC of SynRM and PMSynRM with the conventional motors, some dissimilarities distinguish the FOC of synchronous, and salient motors (such as SynRM and PMSynRM) and the non-salient, and asynchronous symmetrical motors. The concept

is related to the different flux vector estimation and proportional and integral coefficients for the current controller. For non-salient motors, the coefficients for the PI controllers are the same. Conversely, this is not true for the SynRM and PMSynRM, where the operation of the motor is based on the saliency and the inductances of the motors are different in the different axes. For both the SynRM and PMSynRM, the coefficients for the d-axis and the q-axis should be different, compatible with the saliency of the motors. As the saliency of SynRM and PMSynRM are different, the coefficients of the PI controllers are different for each motor, as well. Another underlined feature of the FOC of SynRM and PMSynRM is the flux position information which is directly obtained from the rotor position information. This is due to the synchronized flux in these motors. Therefore, the method is highly sensitive to the flux position which requires precise information in the control loop. However, the absence of the slip in these motors has led to the simpler implementation of the FOC in these motors.

In the FOC of SynRM and PMSynRM, three points are crucial to pay attention to. These points are discussed in the rest of this section

A. PI regulators

There are some possible ways to determine the PI controllers' coefficients, which among them the Ziegler–Nichols method is a comprehensive method to name [14]. This method is widely used in many control applications with a simple PI tuning [15]. However, this method is designed for linear control systems, which in many cases with non-linearity the effectiveness of the method can not be guaranteed. In [16], a self-tuning PI controller is proposed for the control of electric motor drives. This method adjusts the PI controller gains and updates them online concerning the speed error. Although the method shows an acceptable parameter adjustment, it injects complexity into the control method, which leads to a high computation burden in FOC.

In this study, the PI gains are defined using the equations based on the natural frequencies of the motor. The speed regulator is dependent on the motor's moment of inertia and natural frequency of the speed closed-loop system, and the speed loop attenuation, which was determined through the poles of the closed-loop system transfer matrix. The proportional and integral gains of the speed PI regulator are calculated below.

$$K_p = 2 * \zeta * \omega_{0\omega} * J \quad (6)$$

$$K_I = \omega_0^2 * J \quad (7)$$

Where the $\omega_{0\omega}$ is the natural frequency of the speed controller loop and ζ is the attenuation of the loop.

Based on the current closed-loop system, the current PI controller gains were set with the application of the motor parameters. This is the basic reason to have different PI controller gains for each motor. This also affected the current controller closed-loop natural frequency. The PI controllers' gains were calculated through the equations below.

$$K_p = 2 * \zeta * \omega_0 * L - R \quad (8)$$

$$K_I = \omega_0^2 * L \quad (9)$$

TABLE I: THE SYNRM AND PMSYNRM PI CONTROLLER COEFFICIENTS

Motor	Speed controller		D-axis current controller		Q-axis current controller	
	P	I	P	I	P	I
SynRM	0.4	5	120	500	70	500
PMSynRM	0.5	5.5	150	500	50	500

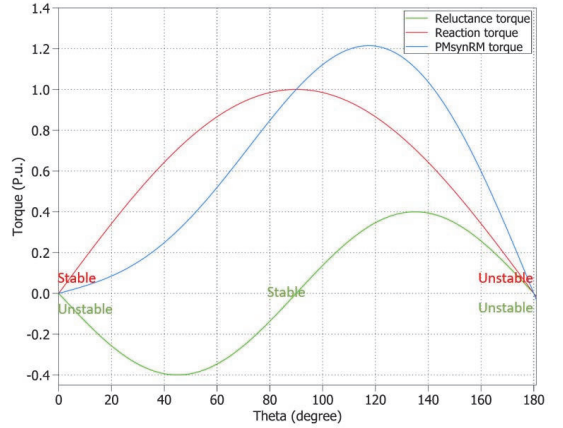


Fig. 3: The PMSynRM torque characteristics with respect to torque angle

Where ζ represents the current loop attenuation and ω_0 denotes the natural frequency of the current closed-loop system. Hence, the bandwidth of the current closed-loop system defines the PI gains. The PI gains are calculated based on the parameters of the motor presented in [17]. The gains are defined in Table I.

B. Flux position calculation

The information of flux position is vital for the FOC of SynRM and PMSynRM. The motors' control characteristics including torque in the shaft are extremely dependent on the accuracy of the flux position information. Especially, when the torque angle is high, a very small error in flux position calculation can lead to severe low performance of the control and even unstable control of the motor. Hence, it is crucial to obtain the flux position information before extracting the motor parameters.

For the sake of obtaining accurate flux position information, two factors are crucial to be considered. First, an accurate position sensor should be employed. The position sensors including encoders and resolvers offer different resolutions and obtain the position information with very high accuracy. However, an incremental encoder with a medium resolution can be accurate enough to provide the rotor position information in these motors' control applications. The second important factor that should be very precisely implemented is the alignment of the position sensor to the magnetic axis. The alignment can be carried out on the d or q-axis. However, if the alignment was carried out on the q-axis, it should be considered in the Park transform equations.

The torque characteristics in PMSynRM are presented in Fig. 3. This figure shows the different torques in PMSynRM with respect to the torque angle. As discussed, the total torque in PMSynRM includes the reluctance torque and magnetic

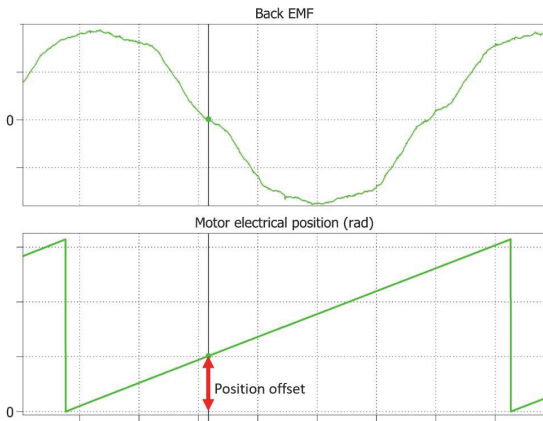


Fig. 4: The back EMF and the motor electrical position of the motors in the same time frame

torque. The reluctance torque is produced from the anisotropic structure of the rotor that allows the flux to pass through the lowest reluctance. This torque is represented by green color in Fig. 3. As the designed motors were identical in the stator and the rotor laminations, the reluctance torque in both motors were expected to be equal. When the magnetic poles are aligned with the magnets, there is zero torque production and the maximum magnetic torque is produced in 90° . The maximum reluctance torque is produced in 135° . In this study, the stator is with sinusoidally distributed windings and it had four poles. Therefore, the optimum angle between the rotor flux and the stator current is 45° .

To control the motors, it is vital to align the rotor with the flux. Commonly, there are three methods to align the position sensor to the motors' magnetic axis.

The first method can be implemented through a dc power supply. In this method, the magnetic poles were defined by locking the rotor in the d or q-axes and then marked. The details of defining the poles are described in [17] for the decay test. Then, the output of the encoder was monitored by the processor. In this test, the index pulse of the encoder was utilized and located in the aligned position with the magnet axis. If the encoder's index pulse position was aligned with the marked position of the magnet axis, for the manual rotation of the motor shaft, the position of the mechanical angle would differ from 0 to 2π . However, if the encoder index pulse was not aligned with the magnet axis, the counter would count up to some certain value and the index pulse would reset the counter. In this case, the position calculation output would differ from 0 to some value below 2π . Therefore, the differentiation of the maximum calculated value from 2π should be compensated in the software. This was done through an offset block to augment the offset position value to the position information. Afterward, in the control, if the rotor was not aligned with the magnet axis at the beginning of each test, the position information obtained by the encoder would give the rotor position estimation with offset until the rotor shafts pass by the index pulse position of the encoder, which is aligned with the magnetic axis. Then, the flux position is aligned with the rotor position and the position information is valid. However, this method is not accurate and manually alignment of the position of the

encoder's index pulse to the magnet axis might lead to some slight misalignments.

For more accurate alignment of the position sensor to the magnet axis, the second method offers the visualization of the back electromagnetic force (EMF) and the output of the encoder in the same graph. In this method, the back EMF of the motors was measured and illustrated in the same instant time frame with the encoders' position. In this way, the electrical position of the motor was monitored at the time that the negative zero crossings of the back EMF happened as shown in Fig. 4. The positive peak of the back EMF is the north magnet pole of the phase A magnet flux. The difference of the position of the negative zero crossings from zero was calculated and added as a position offset as it was described in the first method.

The third method was applied through an inverter. In this method, only a negative current was injected into the motor in d-axis. If the position sensor was aligned to the magnet axis, the negative current would lead to zero torque irrespective of the motor type. Any torque in the motor implied position offset. Then, the position offset was adjusted in the software until the torque in the motor was zero. The alignment of the position sensor with this method can lead to a wrong pole selection. Hence, it is important to identify the polarity of the magnets. This can be carried out by consideration of the saturation effect or observing the q-axis voltage when the d-axis current is injected.

C. The d-axis current reference

To benefit from the highest efficiency of the motor, in the speeds below the rated speed, the motor's flux is opted to have the highest torque with the current that flows in the stator. To apply maximum torque per ampere to the SynRM and PMSynRM, some differences should be considered. As it is clear from Fig. 1, the flux vector of the PMSynRM has a different angle from the flux vector of the SynRM. Therefore, the reference current in the d-axis should have a different value in the control of the motor. This is due to the magnetic flux in the rotor that results from the magnets. Hence, the produced i_d should have less value than then SynRM to produce the maximum torque concerning the current that flows in the stator. The difference in the i_d reference of the motors is very important from the point of view of the efficiency of the motors in the base speed range. At high speeds, injecting minus values to the d-axis currents provides the possibility of the field-weakening control.

V. SIMULATIONS

To investigate the performance of the vector control of the motors, the motors were initially modeled in the Plects platform. Then, the vector control of the motors was implemented with the considerations of the different PI controllers and i_d reference values. Fig. 5, and Fig. 6 show the performance of vector control for both motors. In these figures, from the top, the first figure depicts the stator phase voltages in three-phase. These voltages were desired voltages to apply to the motors and are known as command voltages. The scaled values of the phase voltages which were generated as duty cycles to apply to the PWM block are shown in the second figure. The third figure shows the stator phase currents. It can be seen that the current has the same

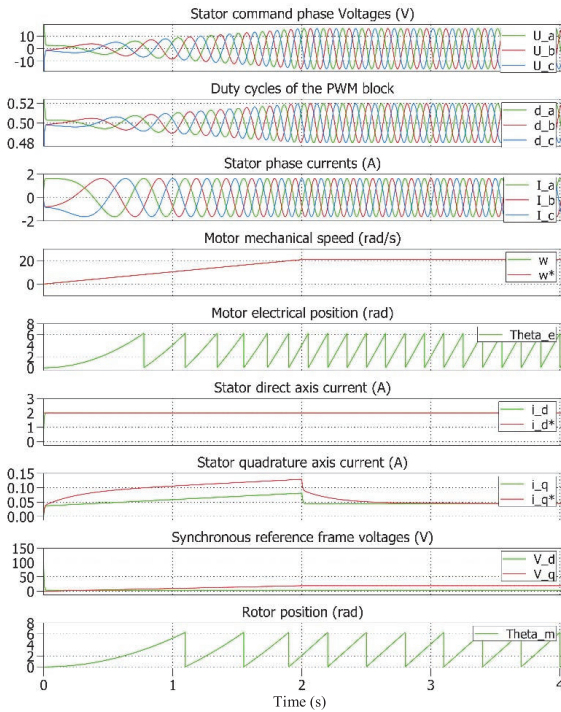


Fig. 5: The simulation results of FOC of SynRM

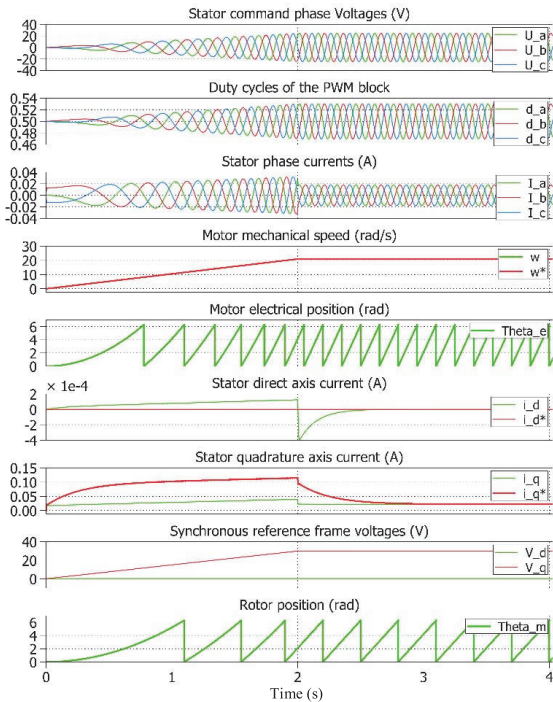


Fig. 6: The simulation results of PMSynRM

frequency as the voltages. The fourth figure demonstrate the reference values and the actual value of the speed of the

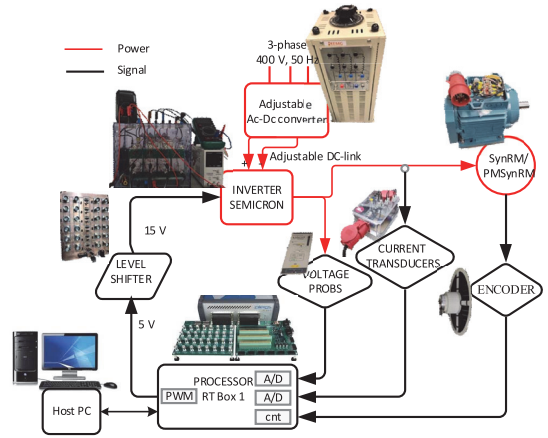


Fig. 7: The experimental setup block diagram

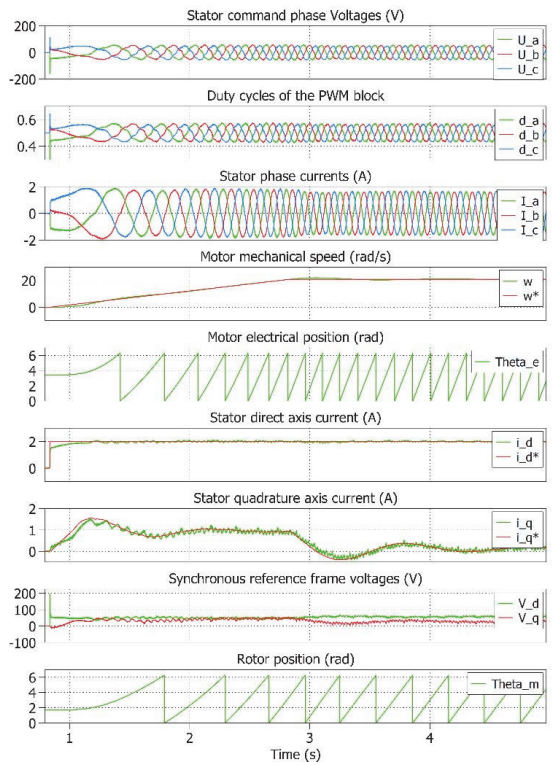


Fig. 8: The experimental results of FOC of SynRM

motors. It is shown that the vector control works properly, and the motors' model follows the commanded speed with very good dynamic. The fifth figure presents the motors' electrical position. It can be seen that in each period of the current waveforms, the flux rotates for one revolution which proves the correct performance of the control. In the sixth figure, the stator current and its reference in d-axis are demonstrated. The commanded current in SynRM had a positive value and in PMSynRM, no current is commanded

in d-axis. The motors' actual currents follow the reference with a very good accuracy which validates the performance of the control. The seventh figure shows the q-axis current which corresponds to the motor's torque. As there is no load injected, the q-axis current has a negligible value which is acceptable. The d and q-axes voltages in the synchronous reference frame are depicted in eight figure that was DC value as expected. Finally, the ninth figure shows the motor mechanical position. It is seen that for each mechanical rotation, there are two electrical revolutions for the motors that confirm that the control is properly performing.

VI. EXPERIMENTAL RESULTS

To validate the performance of the implemented vector control methods on the motors, an experimental setup was implemented. Fig. 7 shows the experimental setup block diagram. The motors were designed in the lab that is presented in [17]. The current feedback was measured by LA 55-P transducers in three phases. The motor's position and speed were measured by an incremental encoder of SICK with 2500 PPR. The voltages were measured by a differential voltage prob. An RT box 1 was used as the processor to implement the rapid control prototyping which was connecting to the PC with Ethernet cable via the cloud. The RT Box 1 was sending the PWM signals to the gates of the switches in the SMICRON three-phase inverter through a level shifter. An adjustable DC link was used to regulate the DC link.

Fig. 8 shows the experimental results for the SynRM. The figures are shown in the same sequence as the simulation results. The figures show that the motor speed follows the commanded speed very accurately, as well as the d-axis current. The currents show an acceptable range of values with a smooth variation.

VII. CONCLUSION

This paper was focused on the control of SynRM and PMSynRM by the FOC method. The performance of the control method was investigated. FOC of the motors presented a high performance in steady-state. It was concluded from the tests that the PMSynRM had an additional positive magnetomotive torque, which required less current in the d-axis in the control. Also, this research work showed that the motors had different parameters in each axis, which led to different parameters in the control method and different PI controllers. Similarly, the motors required different values in d-axis current due to the different rotor structures in terms of the presence of the ferrite magnets. The control challenges were the synchronous speed of the motors, which required more precise rotor flux angle feedback. However, the lack of slip provided less complex flux angle calculation in the control.

REFERENCES

- [1] A. T. De Almeida, F. J. T. E. Ferreira, and G. Baoming, "Beyond induction motors - Technology trends to move up efficiency," *IEEE Trans. Ind. Appl.*, vol. 50, no. 3, pp. 2103–2114, 2014, doi: 10.1109/TIA.2013.2288425.
- [2] M. H. Holakooie, A. Taheri, and M. B. B. Sharifian, "MRAS based speed estimator for sensorless vector control of a linear induction motor with improved adaptation mechanisms," *J. Power Electron.*, vol. 15, no. 5, pp. 1274–1285, 2015, doi: 10.6113/JPE.2015.15.5.1274.
- [3] H. Heidari, A. Rassolkin, A. Kallaste, T. Vaimann, and A. Belahcen, "Harmonics Distortion in Inverter-Fed Motor-Drive Systems: Case Study," in 2019 Electric Power Quality and Supply Reliability Conference (PQ) & 2019 Symposium on Electrical Engineering and Mechatronics (SEEM), Jun. 2019, pp. 1–4, doi: 10.1109/PQ.2019.8818230.
- [4] H. Heidari et al., "A parallel estimation system of stator resistance and rotor speed for active disturbance rejection control of six-phase induction motor," *Energies*, vol. 13, no. 5, 2020, doi: 10.3390/en13051121.
- [5] ABB, "Synchronous reluctance motor-drive package for machine builders. High performance for ultimate machine design." [Online]. Available: <http://search-ext.abb.com/library/Download.aspx?DocumentID=3AUA0000120962&LanguageCode=en&DocumentPartId=1&Action=Launch>.
- [6] P. Subtitle, "High output synchronous reluctance motor and drive package - Optimized cost of ownership for pump and fan applications," ABB, Press release, 2012.
- [7] N. Bianchi, S. Bolognani, D. Bon, and M. D. Pr e, "Rotor flux-barrier design for torque ripple reduction in synchronous reluctance and PM-assisted synchronous reluctance motors," *IEEE Trans. Ind. Appl.*, 2009, doi: 10.1109/TIA.2009.2018960.
- [8] T. Imen, K. Amor, S. Oussamal, C. Abdelkader, and B. Mohamed, "Performance analysis of FOC and DTC for Synchronous Reluctance Motor," in 2016 17th International Conference on Sciences and Techniques of Automatic Control and Computer Engineering, STA 2016 - Proceedings, Jun. 2017, pp. 260–264, doi: 10.1109/STA.2016.7952109.
- [9] I. Boldea, "Control Issues in Adjustable-Speed Drives," *IEEE Ind. Electron. Mag.*, no. September, pp. 32–50, 2008, doi: 10.1109/MIE.2008.928605.
- [10] S. Krim, S. Gdaim, A. Mtibaa, and M. F. Mimouni, "Hardware Implementation of a Predictive DTC-SVM with a Sliding Mode Observer of an Induction Motor on the FPGA *,"
- [11] ABB, "DTC: A motor control technique for all seasons." <https://new.abb.com/drives/dtc> (accessed Jan. 23, 2020).
- [12] H. Heidari et al., "A review of synchronous reluctance motor-drive advancements," *Sustain.*, vol. 13, no. 2, 2021, doi: 10.3390/su13020729.
- [13] H. Heidari et al., "A Novel Vector Control Strategy for a Six-Phase Induction Motor with Low Torque Ripples and Harmonic Currents," *Energies*, vol. 12, no. 6, p. 1102, 2019, doi: 10.3390/en12061102.
- [14] "Tuning of PID controller using Ziegler-Nichols method for speed control of DC motor - IEEE Conference Publication." <https://ieeexplore.ieee.org/abstract/document/6216102> (accessed Feb. 18, 2020).
- [15] Y. Q. Chen, T. Bhaskaran, and D. Xue, "Practical tuning rule development for fractional order proportional and integral controllers," *J. Comput. Nonlinear Dyn.*, vol. 3, no. 2, Apr. 2008, doi: 10.1115/1.2833934.
- [16] M. S. Zaky, "A self-tuning PI controller for the speed control of electrical motor drives," *Electr. Power Syst. Res.*, vol. 119, pp. 293–303, Feb. 2015, doi: 10.1016/j.epsr.2014.10.004.
- [17] H. Heidari, E. Andriushchenko, A. Rassolkin, A. Kallaste, T. Vaimann, and G. L. Demidova, "Comparison of Synchronous Reluctance Machine and Permanent Magnet-Assisted Synchronous Reluctance Machine Performance Characteristics," 2020 27th Int. Work. Electr. Drives MPEI Dep. Electr. Drives 90th Anniv. IWED 2020 - Proc., no. Im, pp. 9–13, 2020, doi: 10.1109/IWED48848.2020.9069583.

Paper V

Heidari, H., Rassõlkin, A., Kallaste, A., Vaimann, T., Andriushchenko, E., Belahcen, A. Design of a Research Laboratory Drive System for a Synchronous Reluctance Motor for Vector Control and Performance Analysis, *Inventions* 2021, 6(4), 64; <https://doi.org/10.3390/inventions6040064>



Article

Design of a Research Laboratory Drive System for a Synchronous Reluctance Motor for Vector Control and Performance Analysis

Hamidreza Heidari ^{1,*}, Anton Rassõlkin ^{1,2}, Ants Kallaste ¹, Toomas Vaimann ^{1,2}, Ekaterina Andriushchenko ¹ and Anouar Belahcen ^{1,3}

- ¹ Department of Electrical Power Engineering and Mechatronics, Tallinn University of Technology, Ehitajate tee 5, 19086 Tallinn, Estonia; anton.rassolkin@taltech.ee (A.R.); ants.kallaste@taltech.ee (A.K.); toomas.vaimann@taltech.ee (T.V.); ekandr@taltech.ee (E.A.); anouar.belahcen@taltech.ee (A.B.)
- ² Faculty of Control Systems and Robotics, ITMO University, 197101 Saint Petersburg, Russia
- ³ Department of Electrical Engineering and Automation, Aalto University, 02150 Espoo, Finland
- * Correspondence: haheid@taltech.ee; Tel.: +37-2561-39797

Abstract: Motor-drive systems have the most significant share in industrial energy consumption, which requires a deep study in every aspect of the field. This paper presents a synchronous reluctance motor (SynRM) drive system based on Plecs RT box 1. The system's design provides the opportunity for the open-loop and closed-loop control of the motor and a characteristic performance analysis of the motor. This paper focuses on the hardware implementation of a research laboratory setup and the precise vector control of the SynRM in real-time. The application of the digital controller and inverter to drive SynRM is examined. The voltage, current, and speed transducers were employed for monitoring the protective measures and to control the motor in the closed-loop. The design of the signal conditioning and the intermediary cards for isolation and data acquisition are described in detail. An algorithm is proposed to measure the whole system parameters, including motor, inverter, and cables. Thanks to the RT box 1, the principle of real-time simulation of control algorithms is investigated, and the rapid control prototyping of field-oriented control (FOC) of SynRM was implemented. The simulation of the system was carried out in the Plecs platform, and the results are presented. The experimental results of the implemented control algorithms validate the setup's performance and the control algorithm. Finally, as a study of the motor's performance, the efficiency map of the motor is drawn in different speed and torque ranges.

Keywords: motor-drive system; synchronous reluctance motor; parameter identification; rapid control prototyping; field-oriented control



Citation: Heidari, H.; Rassõlkin, A.; Kallaste, A.; Vaimann, T.; Andriushchenko, E.; Belahcen, A. Design of a Research Laboratory Drive System for a Synchronous Reluctance Motor for Vector Control and Performance Analysis. *Inventions* **2021**, *6*, 64. <https://doi.org/10.3390/inventions6040064>

Academic Editor: Shouu-Jinn Chang

Received: 31 August 2021

Accepted: 29 September 2021

Published: 4 October 2021

Publisher's Note: MDPI stays neutral with regard to jurisdictional claims in published maps and institutional affiliations.



Copyright: © 2021 by the authors. Licensee MDPI, Basel, Switzerland. This article is an open access article distributed under the terms and conditions of the Creative Commons Attribution (CC BY) license (<https://creativecommons.org/licenses/by/4.0/>).

1. Introduction

Nowadays, variable speed drives (VSDs) have been applied in many industries for the efficient, high-performance, robust, and precise control of electrical motors [1,2]. VSDs add up to the price of the motor-drive system. Meanwhile, to reach high efficiency of the systems, the application of VSDs is inevitable [3,4]. Besides, the differences between the prices of the drive systems in the same rated power can be compensated by the lower energy cost. As electric motors consume a significant share of energy in the industry, a lower energy consumption is needed to address the energy crisis in the industry [5]. Besides, the influence of synchronous machines on the distribution of grid stability is a factor that requires more detail in relation to these systems [6]. Therefore, system analysis methods were studied in this study, which aims to develop a more sustainable motor-drive system.

Recent studies, innovations, and the need for a higher efficiency and a better performance support the prospect of the widespread development of motor-drive systems in the industry in the future [7]. These parameters require more study in different areas that can be categorized as follows:

- Optimal design of motors;
- Optimal design of converters;
- Optimal design of controllers.

In recent studies in the literature, researchers have conducted numerous studies to increase the efficiency of motors [8]. Artificial intelligence has offered many popular optimization methods for motor designs. To name a few, genetic algorithms, neural networks, and Taguchi methods have been studied in [9–11]. Additive manufacturing motors are one of the novel developing technologies in this field [12]. Among different motor structures, SynRM represents a superior technology that has lately met the requirements of the IE5 standard [13]. This motor has proved to be a robust structure with a somewhat comparable performance to a well-developed permanent magnet synchronous motor and is potentially as cheap and affordable as an induction motor that lacks the rare-earth magnets in the rotor [8,14].

The control unit of the electric drive system plays a crucial role in system performance. A control system technology with a high performance ensures an efficient and reliable energy conversion. In general, a control unit contains the following:

- Output modules, i.e., a pulse-width modulation (PWM) module which continuously provides switching sequences;
- Peripheral modules for programming and data exchange;
- Main processor for executing and processing control algorithms.

The control algorithms characterize the behavior of the electric drive systems. Hence, to provide a high-performance drive system for motors, a proper control strategy should first be devised [15,16]. The usage of frequency converters controlled by microprocessors provides researchers with the potential to use flexible methods to achieve a better performance. On the other hand, VSDs inject some high-frequency currents into the system [17]. Consequently, some unexpected losses occur, requiring a more precise control algorithm on the drive [3].

There are numerous studies in the literature where the motor-drive systems' simulation or implementation have been discussed. In [18], the authors studied the interaction of the numerical analysis in Magnet with Matlab, which provides an interaction of Magnet and Plects. This study focused on the simulation of the motor-drive system, where our research work is based on the experimental setup. Besides, our study focuses on the precise implementation of the vector control based on Plects where the parameters of the whole motor-drive system are measured using the controller and the inverter in the experiments. Moreover, our paper studies the performance of the motor in a wide range of speeds and torques. Regarding the performance analysis of the motor, the authors of [19] have proposed a methodology to study the performance of the motor in the operation phase with proposer control implementation. Our study offers a comprehensive study of the vector control and the performance analysis of the motor.

This paper deals with the design of a research laboratory test bench for the control purpose of SynRM. Firstly, the hardware and the design of the devices in line with the safety tests for the validation of the performance of each device is described separately. Section 2 describes the simulation of the field-oriented control (FOC) of SynRM, which provides information on the modeling of the motor, the inverter and the control system. Then, the interconnection of the devices is investigated. This section describes the rapid control prototyping of the vector control of the SynRM for the sake of real-time simulation. Then a parameter identification algorithm is proposed, which will be employed in the experimental implementation of the control algorithm. The real-time implementation of the control and the results are demonstrated in Section 3. This section employs the implemented setup to analyze the performance characteristics of the motor. Section 5 discusses the results and the outcomes of the study. Finally, a comprehensive conclusion of the study is presented in Section 5.

2. Materials and Methods

2.1. The Hardware Implementation

Motor control systems are known as sandboxes of various engineering disciplines. This is because many engineering concepts should be applied for an efficient and high-performance drive of the motor. To name a few: power electronics, analog devices, data, digital devices and data, software design, digital signal processing, digital filters, dynamics, mechanics, thermal mechanics, and heat transfer are the main disciplines that should be considered in every motor control setup [20,21]. The complexity of these systems requires a comprehensive scheme for the setup design, where every device is examined accurately in isolated systems and applied in the integrated system along with all other devices. Thus, the setup is divided into three parts of the control unit, the inverter, and the motor. In this section, the design of each piece of hardware and the proper connection is described. Then, an appropriate test is designed for each device to validate the performance with safety consideration, and their proper application in the setup is defined.

2.1.1. The Control Unit

The control unit is the main core of the drive system, which simply runs the motor by applying appropriate signals to the gate drivers of the switches in the inverter. In the closed-loop control systems, the control unit collects the feedback from the motor and, based on the current status of the motor, executes the control processes and implements the control algorithms to generate the signal for the application of the command voltages through the inverter. In this paper, the control unit is categorized into three classifications as follows.

The processor

In the control unit, the processor is the intelligent part where all the other devices are employed to send/receive data to/from other devices in the whole drive system. The algorithms were implemented in the processor, which executed the control process. The PLECS RT box 1 “Plexim GmbH, Zurich Switzerland” was utilized in this setup, which benefitted from the Xilinx Zynq processor of Z-7030. The CPU core of this processor is 2×1 GHz, which denotes that it has two cores, each of which has a clock that beats 1 billion times per second. Regarding the resolution of 16 bits, the RT box 1 can manipulate 16 numbers of the bits in each clock bit. Therefore, in each clock bit, the processor provides a possibility of one billion manipulations for each core in all 16 bits. Furthermore, this device provides 2 mega samples per second, which denotes a high sample update rate. For most motor control applications, a sampling rate of 10 kHz is adequate. Therefore, this device offers a strong processor that perfectly meets the motor control applications’ requirements.

The RT box 1 provided the opportunity for rapid control prototyping where the control algorithm was designed in the real-time simulation Plects platform, and the device was employed as a controller. Furthermore, the high sampling rate and high-fidelity PWM signals, along with the FPGA embedded CPU of RT box 1 offered a versatile processing unit that facilitated the research into control systems for any type of algorithm implementation. Furthermore, thanks to the Xilinx Zynq system-on-chip that benefits from FPGA and CPU cores, the RT box 1 provided a low data transmission latency. In this way, one of the cores was used for communication with the user, and the other core was employed for real-time simulation.

The digital inputs and outputs

The device offered 32 digital inputs and outputs with the logic of 3.3 V and 5 V. The digital breakout board made all digital inputs and outputs accessible via terminal blocks and pin headers. Figure 1 shows a capture of the PWM signals designed with a 10 kHz carrier frequency for two sinusoidal signals. In addition, the signals were designed with 1 μ s dead-time, meaning that for each fall and rise of the first signals, the inverted signal had a delay of 1 μ s for rising or falling, respectively. This concept secured the operation of the IGBTs in each leg of the inverter. Therefore, with this concept, there were no longer two

turned-on switches at the same time in one leg, and any short circuit in the inverter’s legs was avoided.

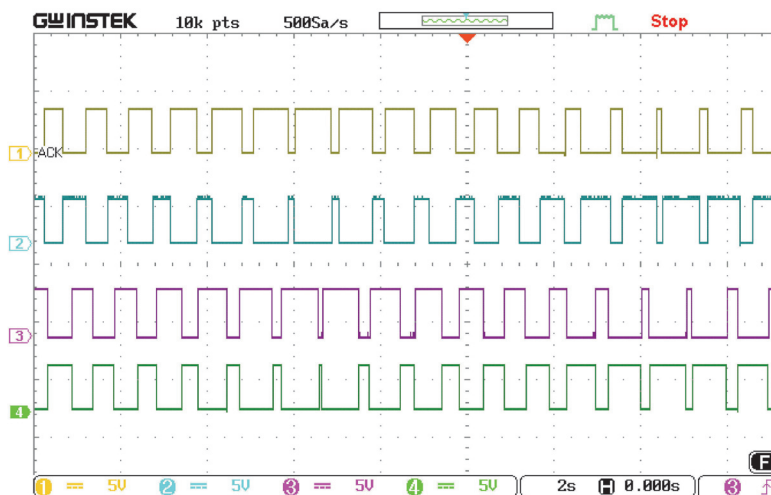


Figure 1. PWM outputs for two sinusoidal signals with 1 Hz frequency and a 120 degree shift with 1 μ s dead-time: (Cha-1, 3) a and b signals, (Cha-2, 3) inverted correspondent of a and b.

The level shifter

The RT box 1 generated the PWM signals for the inverter with the logic of 3.3 V or 5 V, while the inverter (which will be discussed further) in this setup required 15 V of logic for the gate drivers. This being said, a level translator was required to amplify the PWM signals’ level to the gate driver’s level. Hence, a board was designed for dual low-side MOSFET drivers. In this board, the MOSFET driver MIC4127YME “Microchip Technology Inc. West Chandler Blvd, Chandler, Arizona, USA” was utilized. The MIC4127YME translated TTL or CMOS input logic levels to output voltage levels that swung within 25 mV of the positive supply or ground, whereas comparable bipolar devices are capable of swinging only to within 1 V of the supply. Therefore, a desirable output of the board was achieved with this board to have the maximum accuracy of the PWM signals. The PCB design was carried out in ALTIUM, the board was printed in double layers, and the components were assembled in the lab. In this design, the IC-Dual MOSFET Driver required ± 15 V for operation. To supply the driver, a positive voltage regulator of L7805CV was supplied by a 2.5 mm power jack that was connected to the grid by a low voltage power supply adaptor with the voltage level of 9 V. The regulated positive voltage output of the voltage regulator was fed to a DC-DC converter of MAU209. The DC-DC converter provided an accurate ± 15 V for the current driver. The printed board is illustrated in Figures 2 and 3 presents the board’s output for a 5 V level PWM signal.

The speed transducer

As the RT box 1 digital inputs work with the TTL logic, all the digital inputs must be compatible with this logic. Hence, to measure the speed and position status of the motor, an incremental encoder of SICK “Myllynkivenkuja 1, Vantaa, Finland” with TTL/RS-422 was employed in the setup. This encoder generates 2500 pulses per revolution to acquire precise information of the motor shaft position and velocity. The device was supplied with 5 V DC to generate a 5 V output of the transducer. This encoder generates 3 pairs of signals. The pairs of A and B were signals with 90 degree shifts that generated 2500 line pairs in each revolution. The sequence of these pairs indicates the direction of the rotation. Thus, one can define the positive or negative direction of the rotation based on the sequence of the pulses. The pairs of Z provided the index pulse that generated one pulse per rotation.

This signal is mainly used in applications where the motor’s position is highly critical, and in case of missed pulses for A and B channels, this signal will reset the counter in each revolution. Besides, in some applications, certain positions are of importance. Hence, in these applications (SynRM control), that particular position (the north pole of phase A in SynRM control) was aligned with the index pulse. In this way, regardless of the initial position of the encoder (as well as SynRM), the encoder output would reset by the first index pulse, and afterward, the zero position of the encoder output would be aligned with the defined position.

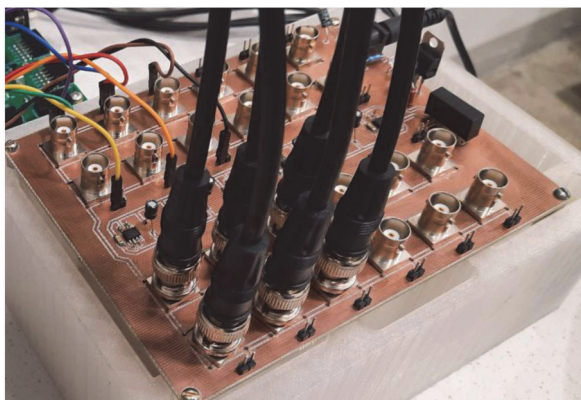


Figure 2. The two-layered level shifter board.

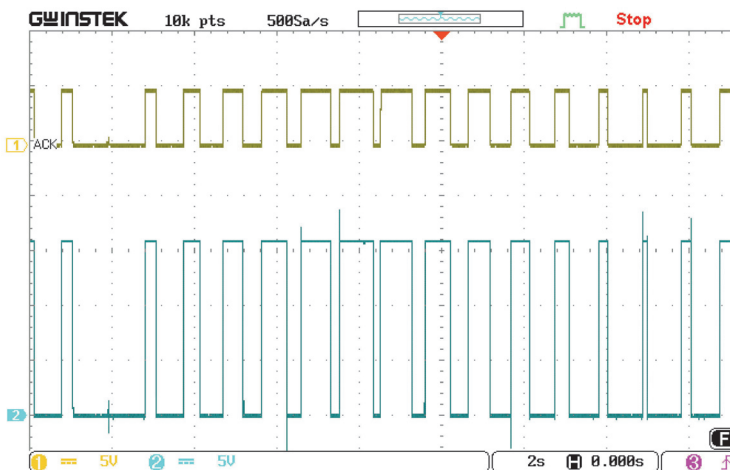


Figure 3. (Cha-1) The PWM digital output, and (Cha-2) the translated signal by the level shifter board.

To mount the encoder on the motor, a 3D printed coupling was designed in the SOLIDWORKS “2020, Wyman Street, Waltham, MA, USA” platform and a frame was used to hold the encoder on the motor. The coupling and the holder were printed in the lab. Then, the encoder was coupled to the motor by the coupling and held by the holder, as shown in Figure 4.



Figure 4. The 3D printed holder and coupling for mounting the encoder on the motor.

To test the encoder, it was first supplied by 5 V DC and the outputs of A, B, and an oscilloscope profiled z . Then, the motor was run at a certain speed, and the outputs were displayed. The A and B outputs had the same pulse width and frequency with a 90 degree shift.

To employ the encoder in the real-time setup, the output of the encoder was properly wired to the pin header connection and connected to the RT Box 1 through the digital breakout board. The QEP block of the Plecs simulation setup was employed to count the input pulses of the encoder and to measure the rotor position and speed. The counter of the QEP block was set to $(2500 \times 4)-1$ since all the rising and falling edges were set to count. Then the counted pulses were divided by $360/10,000$ to calculate the shaft's position in the dimension of degrees. To convert this value to the radian, it was multiplied by $2\pi/360$. To validate the results, the motor shaft was rotated for one revolution. In this test, the output of the position calculation block counted up to 2π and dropped to zero. To validate the outputs, a more sophisticated test was completed by rotating the motor with the loading motor at a certain speed. Later, the speed and position information were employed in the closed-loop control of the motor, and the results are displayed in the next section.

The analog inputs and outputs

The RT box 1 offered 16 analog input and output channels with -10 – 10 V and -5 – 5 V voltage ranges. The analog input impedance was adjustable to 1 M Ω and 1 Ω with a capacity of 24 pF. The Analogue Breakout Board made the analog inputs and outputs individually accessible via BNC sockets. The breakout board provided the opportunity of reading the single-ended or differential inputs. In this study, the channels were set to -10 to 10 V and 1 k Ω impedance of inputs read in single-ended mode.

The analog transducers

For data exchange, the intermediary devices were designed and exploited in the setup to obtain feedback from the power unit and provide reliable information about the system's status in terms of voltage and current. Hence, the transducers offered a safe connection between the control unit and the system's power unit. The applied transducers in this setup were as follows.

The current transducers

For most of the drive applications, the high accuracy of the current feedback was of paramount importance. In this setup, the hall effect LEM "LEM, Bern, Switzerland" current sensors were applied to obtain the current feedback from the motor. As the working point of the system reached up to 30 A, the current transducer of LA 55-P was opted for, which provided the opportunity of measuring up to ± 70 A of AC with a supply of ± 15 V while keeping the accuracy of $\pm 0.65\%$. A two-layer board was designed in Altium to assemble

on a printed circuit board. In this design, the current transducer required a ± 15 V supply for operation. For this purpose, a positive voltage regulator of L7805CV was supplied by a 2.5 mm power jack connected to the grid by a low voltage power supply adaptor with the voltage level of 9 V. The regulated positive voltage output of the voltage regulator was fed to a DC-DC Converter of MAU209. The DC-DC converter provided an accurate ± 15 V for the current transducer. The current signal output of L.A. 55-P was connected to the ground of the circuit with a 100 Ohm resistance to generate a precise sensor voltage output. BNC outputs obtained this output. The board was printed in the lab, and the components were assembled. The board was tested, and FLUKE current clamps verified the performance of the board in the lab. To provide a handy device for three-phase connections, the board was placed in a box with 3-phase inputs and outputs, and the supply socket and the BNC outputs were also accessible. Figure 5 shows the designed current transducers board and the Fluke current clamp to validate the outputs.

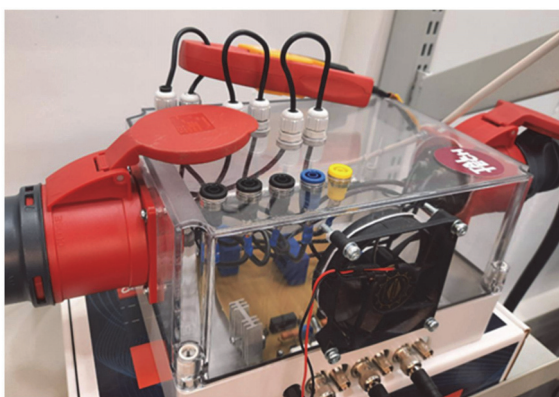


Figure 5. The current LEM current transducers PCB and FLUKE current clamp meter.

To test the current transducers, a three-phase voltage input was applied to a three-phase resistance. Figure 6 shows the setup for the validation of the current transducers box. The oscilloscope profiled the three-phase currents of the lines. The outputs of the transducers are illustrated in Figure 7. The sensors correctly measured the three-phase currents, where they showed the same magnitude and frequency with a 120 degree phase shift. To validate the results, the Fluke current clamp was placed in phase a. It can be seen that the current in phase a, which was measured by Fluke, was nearly identical to the current that LEM measured. However, the LEM sensor had a higher accuracy and a bigger bandwidth (200 kHz). Hence, more harmonics were measured by this sensor. One can notice that the scale of the LEM sensors was 10 times bigger than Fluke, which showed that it generated a 10 times bigger output to the same measured current amplitude. It is worth mentioning that using the LEM sensor made the measurement of the DC possible, which was not possible with the Fluke current sensor. Measuring the DC currents is critical for the drive applications. For instance, for the standstill parameter identification test, the measurement of the DC currents is required.

The voltage transducers

The voltage transducer of LTS 25-np “LEM, Bern, Switzerland” was chosen to measure the voltages of the DC link and the line voltages of the motor. The PCB design was designed and prepared in Altium. This board is under work to print and assemble. A differential voltage probe of Pico was utilized in the setup, temporarily.

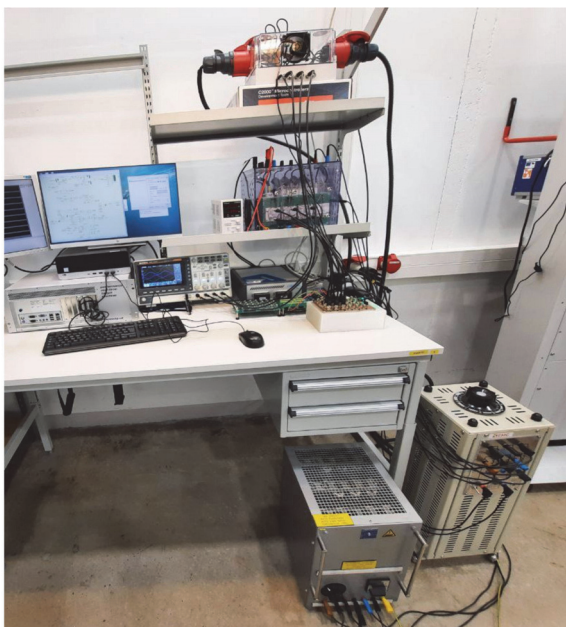


Figure 6. The setup for the current transducers box and the loading test of the inverter.

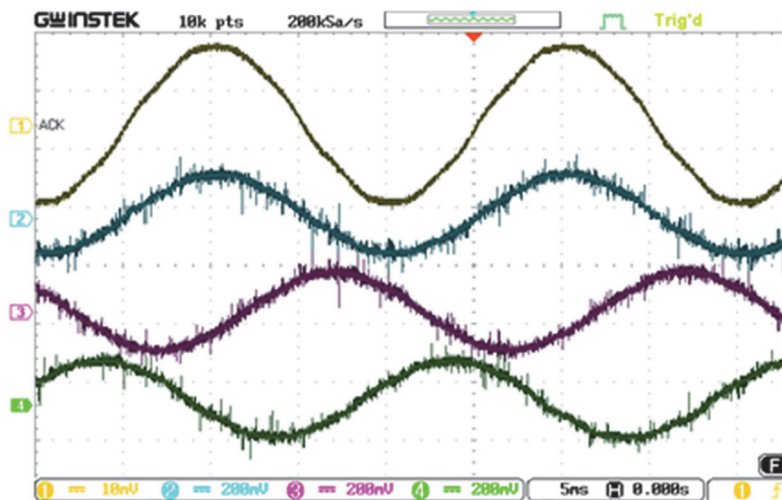


Figure 7. The outputs of the current transducers after applying a three-phase voltage to a three-phase resistance, (Cha-1) FLUKE current sensor on the first phase, (Cha-2, 3, 4) LEM current sensors to phase a, b, and c, respectively.

2.1.2. Inverter

In this setup, the SEMITACH model of SEMICRON inverters was utilized to produce a desirable set of voltages. To provide a safe operation of the inverter, several tests were designed with this inverter. The inverter worked with the nominal current of 30 A and DC-link of 750 V. The three-phase power inputs and outputs were connected with 4 mm banana connectors. To drive the gate drivers through the level-shifter, 15 V BNC connectors were used. In this inverter, the DC link allowed for the application of a desirable DC voltage.

The snubber capacitors were placed as close to the IGBT module as possible to minimize the inductance between the switches and the capacitor. The reverse bias safe operating area of a switching IGBT is square, which means that there is no need to pull the voltage down to zero before reapplying the current or reverse voltage. This means that the IGBT can be switched at full current and full voltage. As far as the switching characteristics of the IGBT alone are concerned, there is theoretically no need for a snubber unless there is a drastic need to reduce the switching losses. However, a snubber is required to deal with short-circuits and the parasitic inductances of the complete switching loop. External elements forced us to use a snubber, and the snubber will be designed according to the converter's mechanical design. The capacitor snubber was only used for reducing the over vs. the IGBTs turn off by applying zero voltage to the gate drivers. A comprehensive description of the commutation is presented below.

Turn-on: $0 \dots t_1$ (blocked transistor): Gate current will be triggered by applying a control voltage. Up to the charge quantity, the current solely charges the gate capacitance. The gate voltage rises. As the gate voltage is still below the threshold voltage, no gate current will flow during this period.

Turn-on: $t_1 \dots t_2$ (rise of gate current): As soon as the gate voltage has reached the gate voltage threshold, the transistor is turned on, first passing the active region. Gate current rises to load current level (ideal free-wheeling diode) or even exceeds load current pattern for a real free-wheeling diode. Similarly, gate voltage, which is connected to the collector current in the active region by the transconductance, will increase. Since the free-wheeling diode can block the current only at t_2 , the collector-emitter voltage will not drop considerably up to t_2 . At $t = t_2$ the charge gate signal will flow into the gate.

Turn-on: switching interval $t_2 \dots t_3$ (transistor during turn-on): When the free-wheeling diode is turned off, the collector-emitter voltage will drop almost to the on-state value by time t_3 . Between t_2 and t_3 , the drain current and gate-source voltage will still be coupled by transconductance; therefore, the collector-emitter voltage remains constant. While the collector-emitter voltage is decreasing, the Miller capacitance is recharged by the gate current with the charge quantity. By $t = t_3$ charge will flow into the gate.

Turn-on: $t_3 \dots t_4$ (saturation region): At t_3 the transistor is turned on and its curve will have passed the pinch-off area to enter the ohmic area. The gate voltage and collector current are no longer coupled. The charge conducted to the gate at this point affects a further increase in gate voltage up to the gate control voltage. Since the collector-emitter on-resistance depends on the collector current and the gate voltage, the on-state voltage may be adjusted to the physical minimum by the total charge quantity conducted to the gate. The higher the collector-emitter voltage (or commutation voltage), the bigger the charge required to reach a certain gate-emitter voltage.

Turn-off: During turn-off, the described processes will run in the reverse direction; the charge has to be conducted out of the gate by the control current.

Two tests were designed to safely analyze the performance of the inverter as follows. Gate drivers test

In this test, a DC supply was initially used to supply the gate drivers of the inverter. Then, a DC power supply was utilized to supply the DC link with a limited current range. Then, a function generator was applied to generate PWM signals to the input of the gate drivers. Finally, the outputs of the phase voltages were profiled using a scope to validate the setup's performance. This test showed that the gate drivers were working with the 15 V logic of the PWM. To avoid any in-rush current, a resistor was connected in series with the DC link. Figure 8 shows the test bench for this test.

Loading test for the inverter

To assure the performance of the inverter in loading conditions, the outputs of the inverter were connected in a star connection to a three-phase resistor. Then the switching was carried out on the gate drivers, and the voltages were applied to the resistors. The inverter showed a desirable output which validated the performance. Figure 6 shows the setup for this test. In this test, loading was carried out using a set of pulses commanded

by three sinusoidal voltages applied to a three-phase resistance. The test was carried out through the Plecs RT box 1 to generate the PWM pulses. However, a function generator could be sufficient to generate the three-phase pulses. Therefore, in this test, to apply the dead-time and to avoid any risk of damage to the inverter, the RT box 1 was utilized.

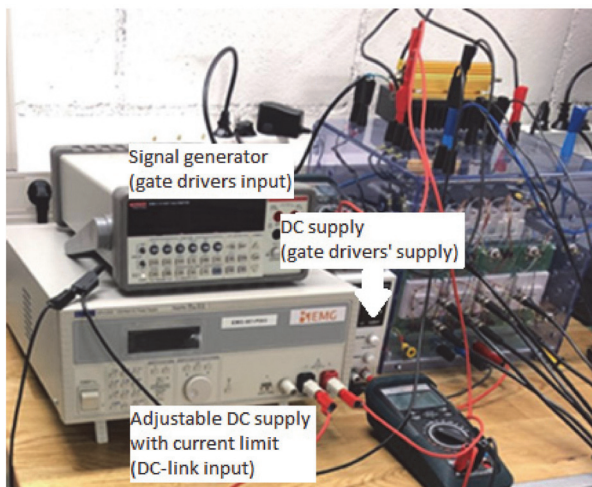


Figure 8. The inverters gate drivers test.

Figure 9 shows the results of the inverter loading test. The figure shows the currents of the three-phase resistances sensed by LEM sensors and the phase a current measured by Fluke current clamp. The figure shows that the results were compatible for each phase with a 120 degree shift, and the LEM transducers were capable of measuring higher harmonics and a higher preciseness of the current. Thus, the test validated the performance of all the gate drivers and the power switches, and the inverter could be used in the loop.

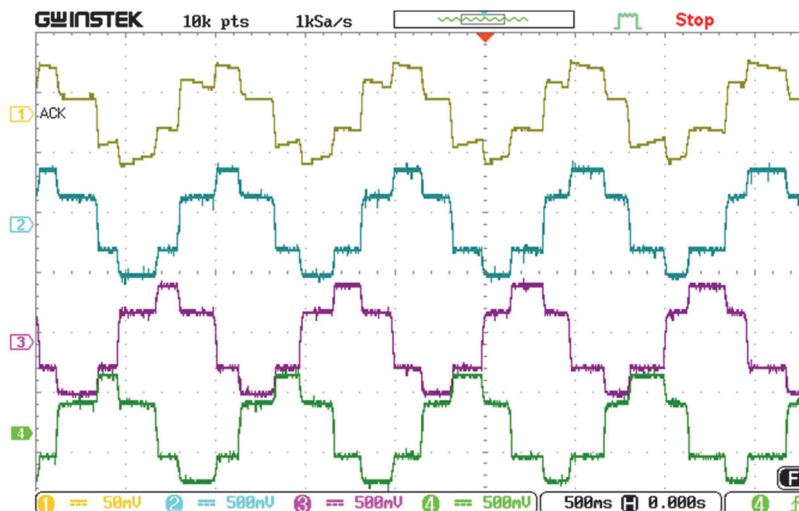


Figure 9. The inverter output currents for a three-phase resistance load, (Cha-1) phase a measurements with the Fluke current clamp meter, (Cha-2,3,4) phases a, b, c with LEM current transducers, respectively.

2.2. Simulation of FOC of SynRM

In this section, the simulation of the FOC of the SynRM is studied. For the sake of vector control of the motor, the d-q model of the motor was studied in [22]. This model of the motor was simulated in the PLECS platform. The parameters of the motor were measured by the DC decay test and utilized in the simulation. After modeling the motor, the FOC of the motor was implemented in the simulation, as illustrated in Figure 10. For this purpose, the output of the speed and the current inputs of the motor were utilized in the control process as feedback. With the flux position information from the motor's model and the three-phase current feedback, it was feasible to transform the three-phase currents in the stationary reference frame to the synchronous reference frame using Park's transform. By this, the motor was replicated as a DC motor with the correspondence of d-axis current to the flux in the motor and the q-axis current to the motor's torque as the armature and field currents act in the DC motor.

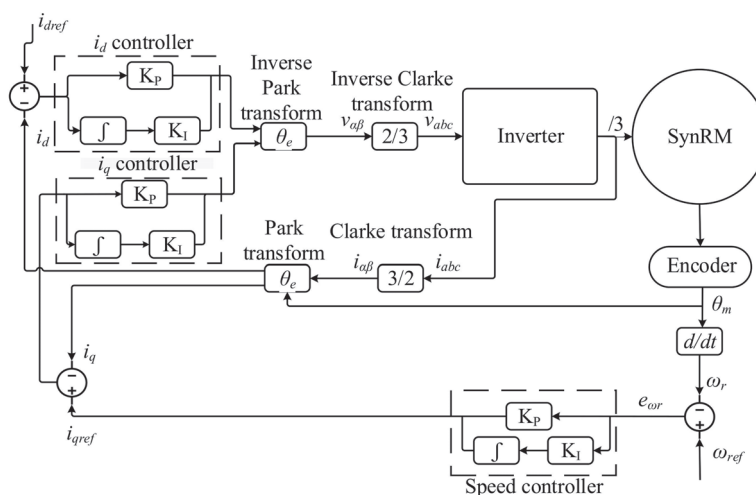


Figure 10. FOC of SynRM.

Where, $i_{d,q}$ are the currents in the d and q axes, respectively and $i_{d,qref}$ indicate the reference currents in these axes. v_{abc} represents the phase voltages and $v_{\alpha,\beta}$ and $v_{d,q}$ are the voltages in the stationary and synchronous reference frame, respectively. θ indicates the position of the motor, which was synchronized with the flux position in this motor. In this simulation, the current reference of the d-axis was a constant value. Using a proportional-integral (PI) controller, the q-axis current was generated by regulating the speed error between the reference speed with the instantaneous speed utilizing a proportional-integral (PI) controller. After generating the errors of the d and q-axes currents by comparing the reference values to the actual values, two PI controllers were employed to regulate the errors and amplify them to generate the d and q-axes' voltages in the synchronous reference frame. Then, the generated voltages were transformed to the three-phase stationary reference frame using the inverse Park transform. Finally, the generated voltages were applied as PWM signals to a model of a three-phase inverter, and the command voltages were applied to the motor's model. In this way, the control was carried out in simulation. Figure 11 shows the results of the simulation of the FOC of SynRM.

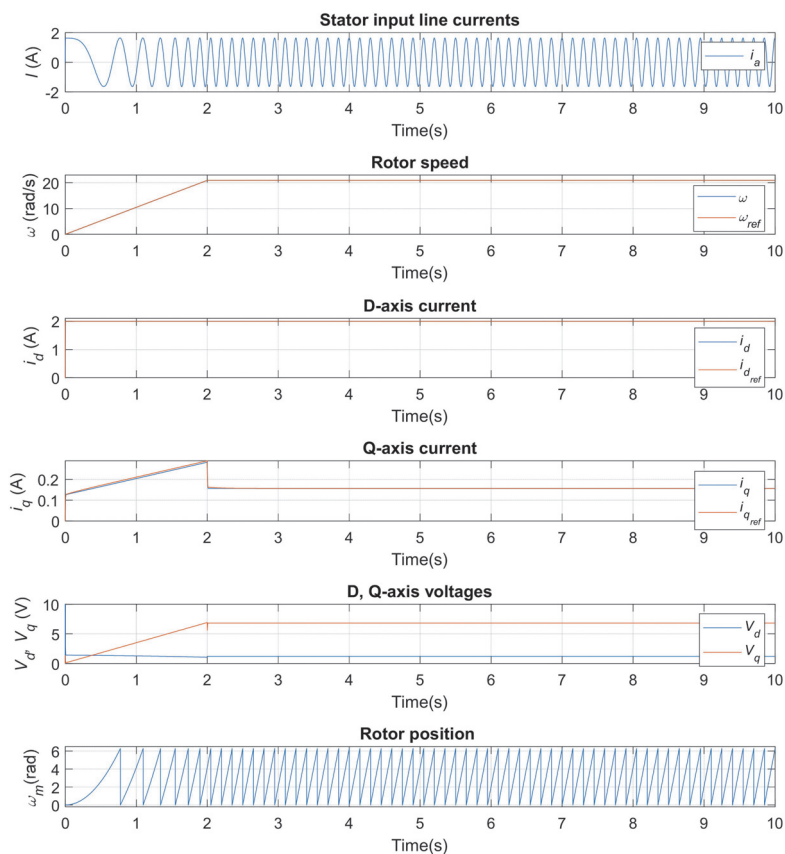


Figure 11. Simulation results of the startup ramp response of FOC of SynRM; I_a : the measured phase a current, ω : the measures speed (ω) and the reference speed (ω_{ref}), i_d : the direct axis current (i_d) and the direct axis current reference (i_{dref}), i_q : the quadrature axis current (i_q) and the quadrature axis current reference (i_{qref}), V_{dq} : the direct and quadrature axis voltages, θ_m : the mechanical angle of the rotor.

2.3. The Integration of the Hardware

The proper integration of the devices is a substantial subject that requires a comprehensive understanding of the devices. The connection of the devices, starting from the appropriate connectors to the type of data that each device can send/receive, are critical considerations to take into account. For instance, the secure connectors and wires to connect the inverter to the motor were employed to handle 30 A of a nominal current. For low-voltage analog signals, BNC connectors were utilized. Figure 12 shows the block diagram of the scheme of the setup. The figure illustrates the connection of the power and the signal parts of the system and the integration of all the devices.

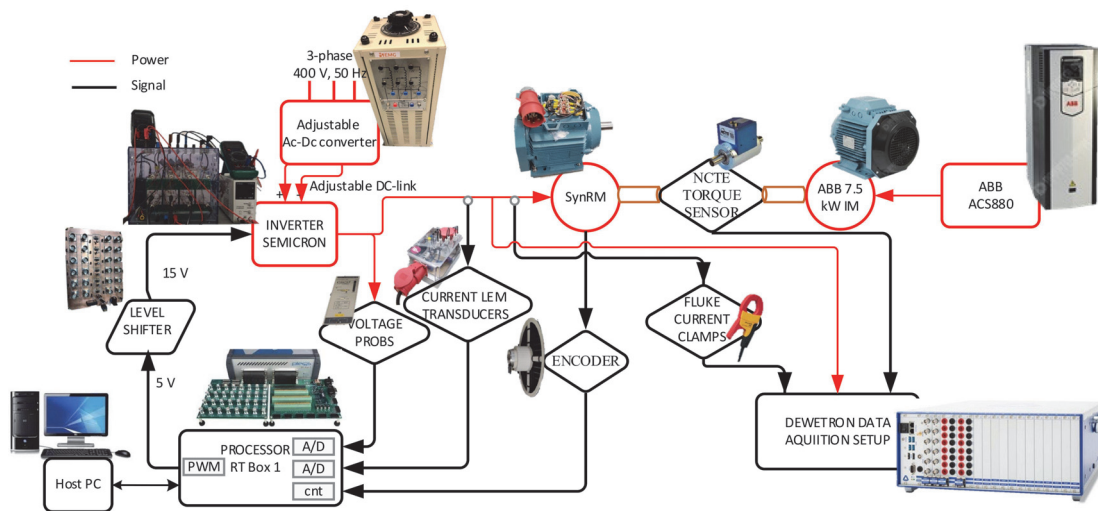


Figure 12. The integrated research laboratory setup block diagram.

2.4. Rapid Control Prototyping of FOC of SynRM

In this section, the real-time implementation of the FOC of SynRM is discussed. Using the rapid control prototyping of Plecs RT box 1, the closed-loop control of the motor was carried out in real-time, and the vector control of the SynRM was implemented. The FOC of SynRM is described in the next section. First, this cascade control was applied on the motor using an outer controller on the speed with a relatively low sampling frequency because of the low dynamic of the mechanical speed. Then, the inner control was carried out on the currents in a synchronous reference frame with a fairly high sampling frequency due to the high dynamic of the current.

In this method, the motor’s current was transformed from the stationary reference frame to the synchronous reference frame using Park’s transform. This required precise information of the flux angle, which was obtained by the incremental encoder. Then, an error-driven control concept was applied to compare the reference values of the currents in the d and q-axes. The reference values of the currents in the synchronous reference frame were chosen as constant values for the d-axis, and the q-axis current was generated using a PI controller upon the error value of the commanded and the measured values of speed. Then, the errors of the current were regulated through two PI controllers to generate voltage commands. Using the inverse Park transform, the generated voltages in the synchronous reference frame were transformed to the stationary reference frame. Next, the generated voltages were applied to a PWM module as duty cycles compared with a sawtooth waveform. Finally, the generated signals were applied to the gate drivers of the inverter’s switches to apply the commanded voltages to the motor.

2.5. Parameter Identification

For the precise vector control of the SynRM, one should consider measuring all the parameters of the motor-drive system. A DC decay test was proposed in our recent study in [22]. In this test, a DC power supply was used to test and measure the motor parameters in an isolated test. This test was initially conducted to simulate the motor’s model. However, apart from the measurement approximations and the inaccurate measurement approach of the test, this method only considered the motor parameters’ identification, and the inverter and the cables were neglected. To cover this shortcoming, in this study, an algorithm is proposed to calculate the motor parameters and the inverter switches, and the cables in the system. Besides, to tune the encoder information, this method proposes a novel approach to remove the encoder offset using the processor and injecting a

certain set of voltages to the motor. Figure 13 shows the block diagram of the parameter identification method.

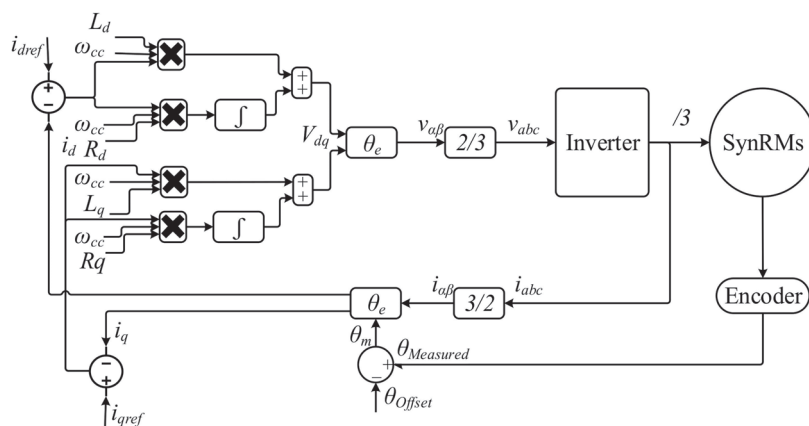


Figure 13. Block diagram of the parameter identification algorithm.

Where, $L_{d,q}$ and $R_{d,q}$ are the inductances and resistances in the d, and q axes, respectively. ω_{cc} is the current regulator bandwidth. In this method, to remove the encoder offset, a non-zero current was commanded to reference the motor in the d-axis. The error between the instantaneous d-axis current and the reference value was regulated using a proportional regulator. In this test, the q-axis current was a zero value. The d and q-axes voltage commands were generated in the synchronous reference frame. These voltages were then transferred to the stationary reference frame using Park transform. Then, the command voltages were applied to the motor using the inverter. As discussed earlier, the d-axis current corresponded to the flux, and the q-axis current corresponded to the torque in the motor. Hence, the applied voltages were anticipated not to generate any torque in the motor unless the flux angle information was incorrect. This could be seen from the q-axis current in the control and a slight rotation in the motor shaft. The test was designed so that a block with a constant value was added to the flux angle information obtained from the encoder. This block was considered as the encoder offset. The current injection was carried out in the d-axis to the motor, and the q-axis current was profiled. If the q-axis current was non-zero, this indicated the wrong flux angle information. The flux angle information was corrected by adding values to the encoder offset block, and the injection of current in the d-axis would not result in current in the q-axis and the shaft movements. It should be noted that the encoder index pulse was considered to indicate the north pole of phase a. In this way, the initial position of the motor was unknown until it reached the position of the index pulse, and the motor position was corrected.

3. Results

The experimental setup was integrated, and all the hardware was prepared to implement the closed-loop control in experiments. Figure 14 shows the experimental setup of the designed motor-drive system. In this section, some tests are discussed that were conducted to validate the performance of the real-time control of SynRM. Firstly, a startup ramp will be discussed that aimed to prove the performance of the control in no load. Then the loading condition of the motor will be studied, and then the motor's response to a step reference will be studied at different speeds.

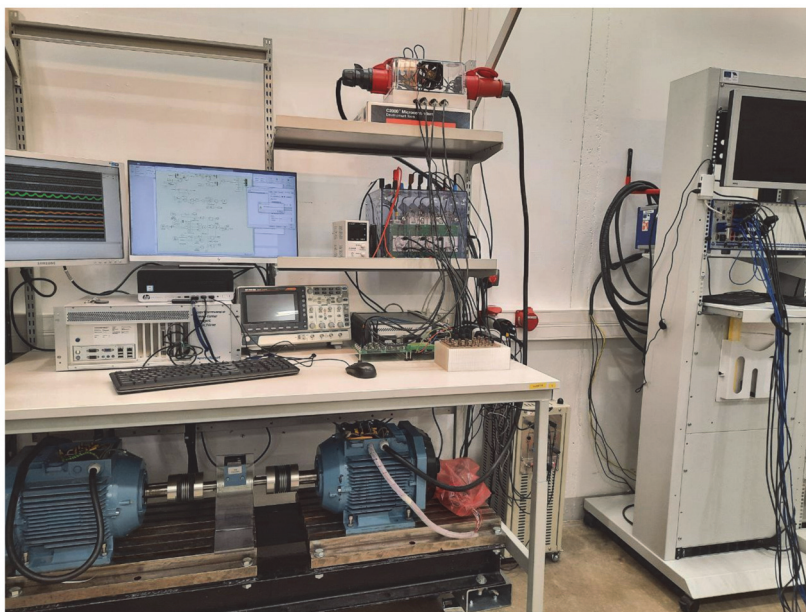


Figure 14. The experimental setup of the research laboratory drive system.

3.1. Startup Ramp Response

In this test, a ramp speed reference was applied to the motor to analyze the performance of the control. The motor parameters are presented in [22]. In these tests, the reference speed increased up to 200 rpm and then remained constant in that speed. A constant value of 2 A was applied in the d-axis, and the instantaneous value followed the reference value. Figure 15 shows the results of the test. The motor's phase current was sinusoidal, proving the proper control of the motor currents in terms of suppressing the slotting harmonics in the motor compared to the grid-fed control. In the q-axis, the reference was generated by the output of the speed error regulator, which increased to roughly 1.5 A and dropped to nearly zero ampere due to the no-load condition of the motor control. The d and q-axes' voltages were generated and applied to the motor with a slight variation in the steady-state. The motor position information matched with the speed results as well as the current frequency. It is worth mentioning that the experimental results had a slight difference with the simulation due to the approximations in parameter identifications and the motor's modeling. Apart from that, the noises in the environment in the lab resulted in some pulsations, which should be covered in a future study. It should be noted that the frequency of the current matched the speed of the motor, considering the number of poles of the motor. This was true for the mechanical position of the motor's shaft, which was two times bigger than the electrical position of the motor.

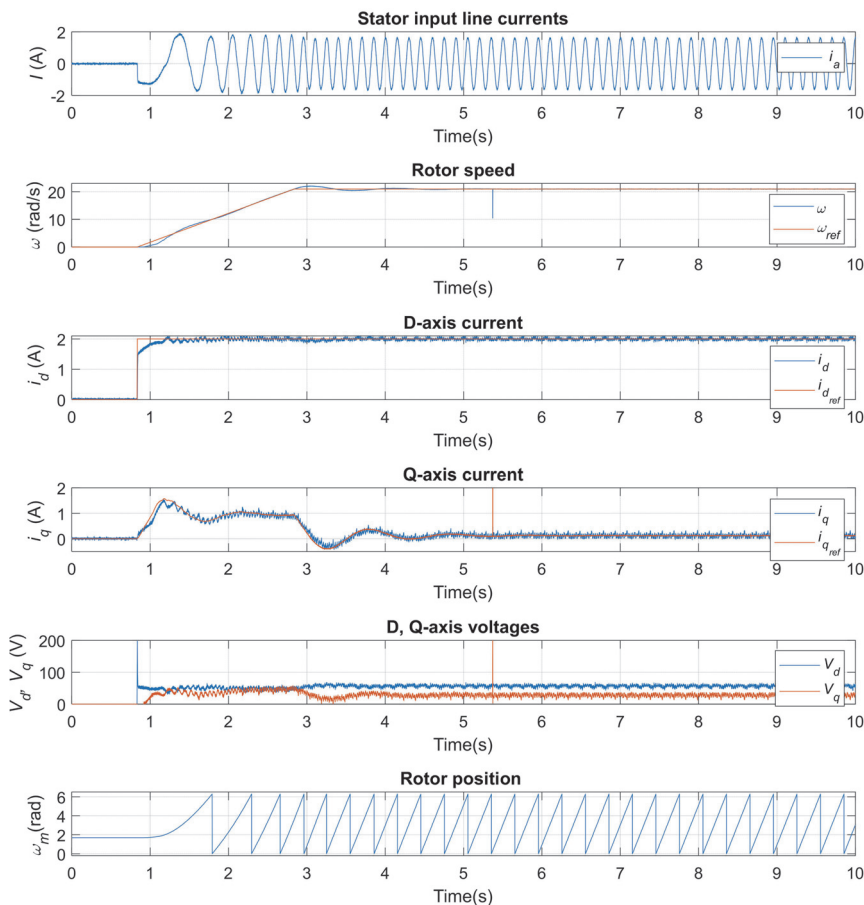


Figure 15. Startup ramp response of FOC of SynRM; i_a : the measured phase a current, ω : the measures speed (ω) and the reference speed (ω_{ref}), i_d : the direct axis current (i_d) and the direct axis current reference (i_{dref}), i_q : the quadrature axis current (i_q) and the quadrature axis current reference (i_{qref}), V_{dq} : the direct and quadrature axis voltages, θ_m : the mechanical angle of the rotor.

3.2. Loading Test

The second test that was projected to analyze the performance of the control imposed a step load to the motor and removed the load after reaching the steady-state. For this purpose, the loading motor was coupled to the motor under test. An industrial frequency converter drove the loading motor in the opposite direction. It should be noted that the loading motor was controlled in torque control mode to just inject the reference torque regardless of the output speed. In this way, the loading motor was driven in generator mode since the load and the speed were in opposite directions. By starting the loading motor, a step load of 10% of the nominal torque of the motor was imposed on the motor. To avoid the motor running in the generator mode, a safety algorithm was devised to monitor the DC link of the inverter and the speed and current of the motor. This algorithm was devised to switch off the PWM block in case limits that were defined were passed. After imposing the load with the loading motor, the motor speed was anticipated to drop for a short while and reach the reference value in the steady-state. In the phase of removing the load, the motor speed was projected to have an overshoot for a short while and follow the reference speed in the steady-state. Figure 16 shows the results of the experimental test. The results show that the motor current increased under load to increase the input

power of the motor to dominate the load on the motor shaft. As can be seen, the d-axis current, which corresponded to the flux, remained nearly constant, and the increase in the current was due to an increase in the q-axis current, which corresponded to the torque. As a consequence, the motor generated more torque on the shaft in the opposite direction with the loading motor. Thus, the speed recovered after a small portion of time and followed the reference speed. The voltage in q-axis increased in the loading condition, and the d-axis current dropped negligibly. As can be seen, all the parameters settled down to their initial values after the load was removed.

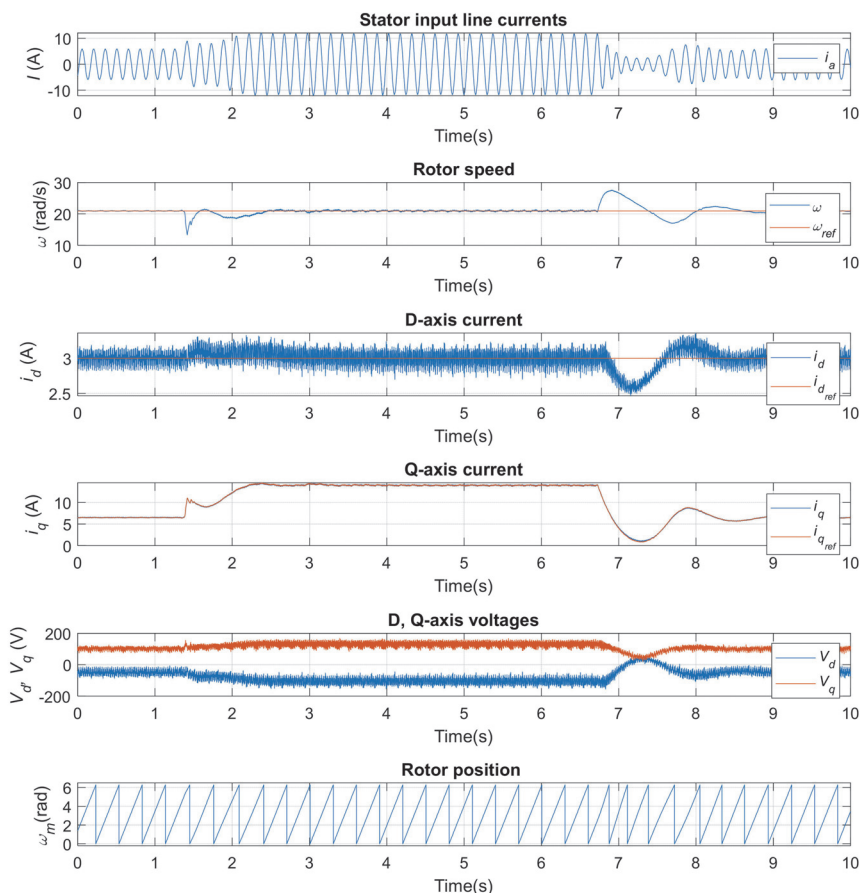


Figure 16. Step-load imposing and unloading; i_a : the measured phase a current, ω : the measures speed (ω) and the reference speed (ω_{ref}), i_d : the direct axis current (i_d) and the direct axis current reference (i_{dref}), i_q : the quadrature axis current (i_q) and the quadrature axis current reference (i_{qref}), V_{dq} : the direct and quadrature axis voltages, θ_m : the mechanical angle of the rotor.

3.3. Speed Step Response

To validate the dynamic of the control, a more intensive test was carried out at different speeds of the motor. In this test, step commands were applied to the motor speed reference, and the motor’s outputs and inputs, including the speed, were examined. Figure 17 represents the results for the step speed response in different speeds in experiments. The results show that the motor presented an acceptable dynamic, and the motor accelerated to the reference speed in a short time and, with a small overshoot, reached the reference speed without any underdamped settled down on the reference speed, and the steady-state was reached in a short portion of time. This motor dynamic was examined with a step

reference, and the motor showed nearly the same behavior, and the control was carried out. It can be seen from the figure that the motor speeded up to the reference speed in upward increments with an acceptable dynamic as well as the downward step speed responses. The current results show that the controller injected a high current to the motor using the inverter in the step times. This was due to the increment of the speed error because of the sudden increment in the reference and consequently the increment of the differential between instantaneous and reference speed. Hence, as shown in Figure 10, the output of the outer speed controller, which generated the q-axis current reference, saw a sudden increment. Thus, the q-axis current rapidly increased to a high value. Considering the constant d-axis current reference, the increment in the q-axis current resulted in the increment of the current in the motor. The current figure shows that the current amplitude roughly dropped to the initial value in the steady-state due to the same loading condition, which was only the fan and the friction of the motors. The q-axis current and the voltages show that the final values in the steady-state in all the speeds were nearly equal. It is worth mentioning that the voltages saw a dramatic change in the imposing step reference phase, where the step resulted in a very high voltage in both the upward and downward speed change scenarios. It should be noted that the frequency of the current was compatible with the speed and position information of the motor shaft, and the results validate the performance of the control.

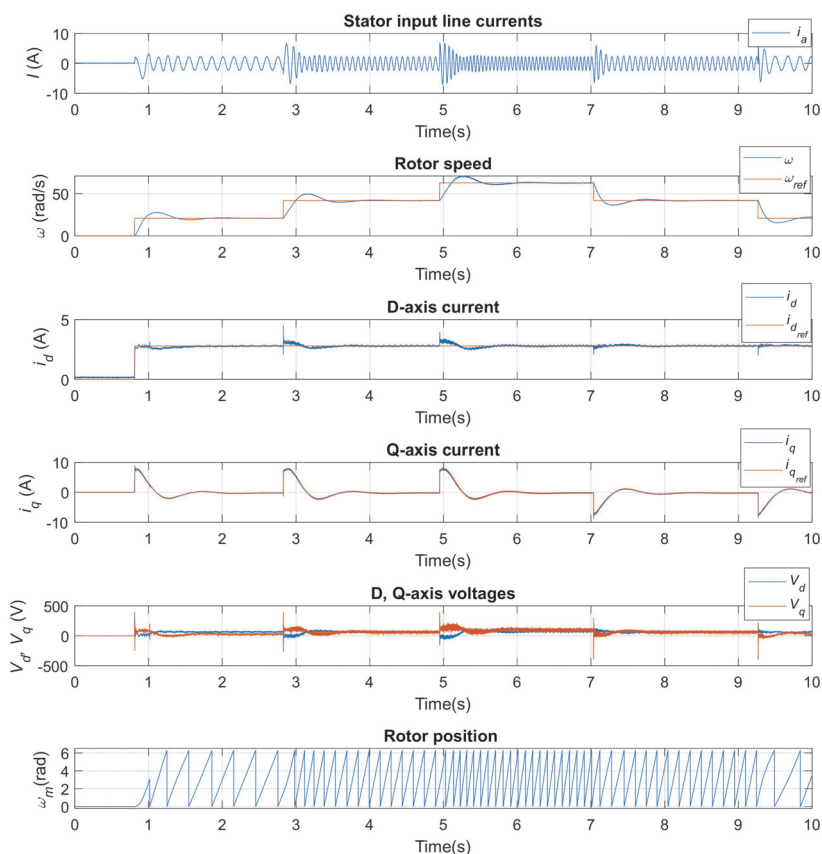


Figure 17. Speed step response in different speeds; I_a : the measured phase a current, ω : the measures speed (ω) and the reference speed (ω_{ref}), i_d : the direct axis current (i_d) and the direct axis current reference (i_{dref}), i_q : the quadrature axis current (i_q) and the quadrature axis current reference (i_{qref}), V_{dq} : the direct and quadrature axis voltages, θ_m : the mechanical angle of the rotor.

3.4. Motor Performance Analysis

One of the objectives of this study was to analyze the designed motor’s performance characteristics. The motor efficiency at different speeds and under different load conditions was studied. The test was designed to run the motor at different speeds with the step of 200 rpm up to 1800 rpm, which was over the nominal speed of the motor. Then, a ramp load was designed using the industrial frequency converter to ramp up to the nominal torque and impose on the motor. Fluke current clamp meters and Dewetron data acquisition setup measured the motor’s input currents and voltages. As well as the inputs, the motor’s outputs were sensed using a NCTE torque transducer and registered by the Dewetron data acquisition setup. The power analyzer in Oxygen software was employed to calculate the input power of the motor as well as the output power. Finally, the efficiency of the motor was calculated at different speeds and torques. Figure 18 shows the efficiency map of the motor. The figure shows that the motor presented a big range of high efficiency of around 90% in the nominal speed range and the middle of the nominal torque. A vast region of a nearly high efficiency of 80% was registered in the speeds higher than 500 rpm and torques higher than 15 Nm. This shows that the motor can work in a wide range of speeds and torques with high efficiency. As it was expected for most of the motors, when it came to low speeds, the motor’s efficiency dropped to a low value. This was true for the low torques, which required the engineers to opt for the motors regarding the applications in the right power range.

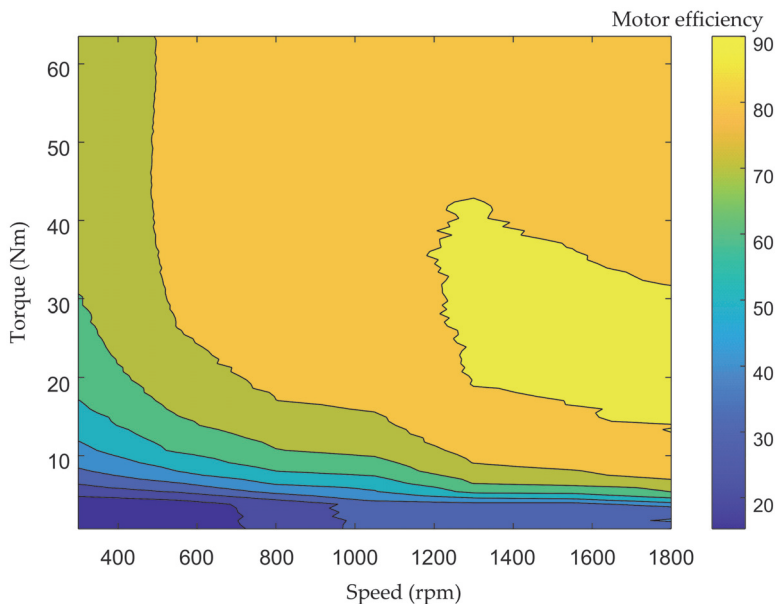


Figure 18. Efficiency map of SynRM.

4. Discussions

The results of the tests from the controller, inverter, and the inputs and outputs showed that the experimental setup was properly designed and the devices were tuned in the system. The performance of each device was tested in the open-loop with safe tests where the results confirmed them.

The simulations of the motor-drive system were successfully carried out and the results were convincing.

The parameter identification algorithm was properly proposed and tested in experiments. The experimental results validated the performance of the vector control which

certified the preciseness of the measured parameters. The experimental results were in acceptable agreement with the simulation results which validated the correctness of the simulations. The motor was loaded in the experiment that confirmed the high-performance control of the motor with the vector control algorithm. Besides, the dynamic and stability of the control were tested by the step speed reference. The motor showed a desirable dynamic in different speed regions and the transition was smooth where the motor followed the reference speed in a short period.

The performance of the motor was widely tested regarding the efficiency where the motor showed a desirable efficiency with a wide range of high efficiency in the high output power range.

5. Conclusions

This paper provides comprehensive guidelines in relation to a case study of the SynRM drive system. The paper dealt with hardware implementation of the device in the setup and integrating all the components. The devices were designed and tested in independent tests. The performance of each device was validated in a safe test, and each device was prepared for implementation in the setup. Moreover, the whole system was integrated to implement the vector control of SynRM. The simulation of the whole motor-drive system was carried out on the PLECS platform. For the sake of precise control, a parameter identification method was proposed to measure the system parameters and obtain the precise angle of the flux using the incremental encoder. The FOC of SynRM was implemented in real-time using rapid control prototyping. The experimental results validated the simulation results, and the performance of the systems was examined in practice. Finally, the efficiency map of the motor was drawn under experimental tests. A future study will involve improving the efficiency of the motor opting for an optimal torque angle.

Author Contributions: Conceptualization, methodology, validation, formal analysis, writing—original draft preparation, H.H.; writing—review and editing, resources, funding acquisition, A.R.; project administration, T.V.; investigation, A.K. and E.A.; supervision, A.B. All authors have read and agreed to the published version of the manuscript.

Funding: The research has been supported by the Estonian Research Council under grant PSG453 “Digital twin for propulsion drive of autonomous electric vehicle”.

Conflicts of Interest: The authors declare no conflict of interest.

References

1. ABB. DTC: A Motor Control Technique for All Seasons. Available online: <https://new.abb.com/drives/dtc> (accessed on 23 January 2020).
2. Holakooie, M.H.; Iwanski, G. An Adaptive Identification of Rotor Time Constant for Speed-sensorless Induction Motor Drives: A Case Study for Six-phase Induction Machine. *IEEE J. Emerg. Sel. Top. Power Electron.* **2020**, *9*, 5452–5464. [\[CrossRef\]](#)
3. Taheri, A.; Ren, H.-P.; Holakooie, M.H. Sensorless Loss Model Control of the Six-Phase Induction Motor in All Speed Range by Extended Kalman Filter. *IEEE Access* **2020**, *8*, 118741–118750. [\[CrossRef\]](#)
4. Glac, A.; Šmidl, V.; Peroutka, Z.; Hackl, C.M. Dependence of IPMSM Motor Efficiency on Parameter Estimates. *Sustainability* **2021**, *13*, 9299. [\[CrossRef\]](#)
5. Javied, T.; Rackow, T.; Stankalla, R.; Sterk, C.; Franke, J. A Study on Electric Energy Consumption of Manufacturing Companies in the German Industry with the Focus on Electric Drives. *Procedia CIRP* **2016**, *41*, 318–322. [\[CrossRef\]](#)
6. Petrik, T.; Daneček, M.; Uhlíř, I.; Poulek, V.; Libra, M. Distribution Grid Stability—Influence of Inertia Moment of Synchronous Machines. *Appl. Sci.* **2020**, *10*, 9075. [\[CrossRef\]](#)
7. De Almeida, A.T.; Ferreira, F.J.T.E.; Baoming, G. Beyond Induction Motors—Technology Trends to Move Up Efficiency. *IEEE Trans. Ind. Appl.* **2013**, *50*, 2103–2114. [\[CrossRef\]](#)
8. Heidari, H.; Rassölkin, A.; Kallaste, A.; Vaimann, T.; Andriushchenko, E.; Belahcen, A.; Lukichev, D. A Review of Synchronous Reluctance Motor-Drive Advancements. *Sustainability* **2021**, *13*, 729. [\[CrossRef\]](#)
9. Andriushchenko, E.; Kallaste, A.; Belahcen, A.; Vaimann, T.; Rassölkin, A.; Heidari, H.; Tiismus, H. Optimization of a 3D-Printed Permanent Magnet Coupling Using Genetic Algorithm and Taguchi Method. *Electronics* **2021**, *10*, 494. [\[CrossRef\]](#)
10. Andriushchenko, E.; Kaska, J.; Kallaste, A.; Belahcen, A.; Vaimann, T.; Rassölkin, A. Design Optimization of Permanent Magnet Clutch with Ārtap Framework. *Period. Polytech. Electr. Eng. Comput. Sci.* **2021**, *65*, 106–112. [\[CrossRef\]](#)

11. Panek, D.; Orosz, T.; Karban, P. Artap: Robust Design Optimization Framework for Engineering Applications. In Proceedings of the 2019 Third International Conference on Intelligent Computing in Data Sciences (ICDS), Marrakech, Morocco, 28–30 October 2019; pp. 1–6.
12. Tiismus, H.; Kallaste, A.; Belahcen, A.; Rassõlkin, A.; Vaimann, T. Challenges of Additive Manufacturing of Electrical Machines. In Proceedings of the 2019 IEEE 12th International Symposium on Diagnostics for Electrical Machines, Power Electronics and Drives (SDEMPED), Toulouse, France, 27–30 August 2019; pp. 44–48.
13. ABB IE5 SynRM Motors Deliver Ultra-Premium Energy Efficiency. Available online: <https://new.abb.com/news/detail/58874/abb-ie5-synrm-motors-deliver-ultra-premium-energy-efficiency> (accessed on 27 May 2020).
14. Mohammadi, M.H.; Lowther, D.A. A Computational Study of Efficiency Map Calculation for Synchronous AC Motor Drives Including Cross-Coupling and Saturation Effects. *IEEE Trans. Magn.* **2017**, *53*, 1–4. [[CrossRef](#)]
15. Heidari, H.; Rassõlkin, A.; Holakooie, M.H.; Vaimann, T.; Kallaste, A.; Belahcen, A.; Lukichev, D.V. A Parallel Estimation System of Stator Resistance and Rotor Speed for Active Disturbance Rejection Control of Six-Phase Induction Motor. *Energies* **2020**, *13*, 1121. [[CrossRef](#)]
16. Heidari, H.; Rassõlkin, A.; Vaimann, T.; Kallaste, A.; Taheri, A.; Holakooie, M.H.; Belahcen, A. A Novel Vector Control Strategy for a Six-Phase Induction Motor with Low Torque Ripples and Harmonic Currents. *Energies* **2019**, *12*, 1102. [[CrossRef](#)]
17. Heidari, H.; Rassõlkin, A.; Kallaste, A.; Vaimann, T.; Belahcen, A. Harmonics distortion in inverter-fed motor-drive systems: Case study. In Proceedings of the 2019 Electric Power Quality and Supply Reliability Conference (PQ) and 2019 Symposium on Electrical Engineering and Mechatronics (SEEM), Kärđla, Estonia, 12–15 June 2019; pp. 1–4.
18. Varvolik, V.; Prystupa, D.; Buticchi, G.; Peresada, S.; Galea, M.; Bozhko, S. Co-Simulation Analysis for Performance Prediction of Synchronous Reluctance Drives. *Electronics* **2021**, *10*, 2154. [[CrossRef](#)]
19. Tawfiq, K.B.; Ibrahim, M.N.; El-Kholy, E.E.; Sergeant, P. Performance Analysis of a Five-phase Synchronous Reluctance Motor Connected to Matrix Converter. In Proceedings of the 2021 IEEE International Electric Machines & Drives Conference (IEMDC), Hartford, CT, USA, 17–20 May 2021; pp. 1–6.
20. Ghahfarokhi, P.S.; Belahcen, A.; Kallaste, A.; Vaimann, T.; Gerokov, L.; Rassõlkin, A. Thermal analysis of a SynRM using a thermal network and a hybrid model. In Proceedings of the 2018 XIII International Conference on Electrical Machines (ICEM), Alexandroupoli, Greece, 3–6 September 2018; pp. 2682–2688.
21. Asad, B.; Vaimann, T.; Belahcen, A.; Kallaste, A.; Rassõlkin, A.; Heidari, H. The Low Voltage Start-up Test of Induction Motor for the Detection of Broken Bars. In Proceedings of the 2020 International Conference on Electrical Machines (ICEM), Gothenburg, Sweden, 23–26 August 2020; Volume 1.
22. Heidari, H.; Andriushchenko, E.; Rassõlkin, A.; Demidova, G.L. Comparison of synchronous reluctance machine and permanent magnet-assisted synchronous reluctance machine performance characteristics. In Proceedings of the 2020 27th International Workshop on Electric Drives: MPEI Department of Electric Drives 90th Anniversary (IWED), Moscow, Russia, 27–30 January 2020; pp. 9–13.

Paper VI

Heidari H, Rassölkin A, Holakooie MH, Vaimann T, Kallaste A, Belahcen A, Lukichev DV. A Parallel Estimation System of Stator Resistance and Rotor Speed for Active Disturbance Rejection Control of Six-Phase Induction Motor. *Energies*. 2020; 13(5):1121. <https://doi.org/10.3390/en13051121>

Article

A Parallel Estimation System of Stator Resistance and Rotor Speed for Active Disturbance Rejection Control of Six-Phase Induction Motor

Hamidreza Heidari ^{1,*} , Anton Rassölkin ¹ , Mohammad Hosein Holakooie ² ,
Toomas Vaimann ¹ , Ants Kallaste ¹ , Anouar Belahcen ^{1,3} , and Dmitry V. Lukichev ⁴ 

¹ Department of Electrical Power Engineering and Mechatronics, Tallinn University of Technology, 19086 Tallinn, Estonia; anton.rassolkin@taltech.ee (A.R.); toomas.vaimann@taltech.ee (T.V.); ants.kallaste@taltech.ee (A.K.); anouar.belahcen@aalto.fi (A.B.)

² Department of Electrical Engineering, University of Zanjan, Zanjan 45371-38791, Iran; hosein.holakooie@znu.ac.ir

³ Department of Electrical Engineering, Aalto University, 11000 Aalto, Finland

⁴ Faculty of Control Systems and Robotics, ITMO University, 197101 St. Petersburg, Russia; lukichev@itmo.ru

* Correspondence: haheid@taltech.ee

Received: 03 February 2020; Accepted: 24 February 2020; Published: 2 March 2020



Abstract: In this paper, a parallel estimation system of the stator resistance and the rotor speed is proposed in speed sensorless six-phase induction motor (6PIM) drive. First, a full-order observer is presented to provide the stator current and the rotor flux. Then, an adaptive control law is designed using the Lyapunov stability theorem to estimate the rotor speed. In parallel, a stator resistance identification scheme is proposed using more degrees of freedom of the 6PIM, which is also based on the Lyapunov stability theorem. The main advantage of the proposed method is that the stator resistance adaptation is completely decoupled from the rotor speed estimation algorithm. To increase the robustness of the drive system against external disturbances, noises, and parameter uncertainties, an active disturbance rejection controller (ADRC) is introduced in direct torque control (DTC) of the 6PIM. The experimental results clarify the effectiveness of the proposed approaches.

Keywords: active disturbance rejection controller (ADRC); direct torque control (DTC); full-order observer; sensorless; six-phase induction motor (6PIM); stator resistance estimator

1. Introduction

Three-phase induction motor drives have become a mature technology in the last years, but investigations into concepts of multiphase induction motor drives are still taking place. Multiphase drive systems have a nearly 40-year history of research and study due to their promising advantages against the conventional three-phase systems. The phase redundancy of the multiphase drives provides extra merits such as fault-tolerant operation, series-connected multimotor drive systems, asymmetry and braking systems. Six-phase induction motors (6PIMs) are known for its fault-tolerant capability, low rate of inverter switches, and low DC-link voltage utilization

compared with its three-phase one [1–3]. On the other hand, the modular three-phase structure of the 6PIM allows the use of well-known three-phase technologies. The 6PIM is successfully used in special applications, such as electric ships, electric aircrafts, electric vehicles, and melt pumps, where the high reliability and continuity of the operation are critical factors for the system [4]. The phase redundancy of the 6PIM provides the ability of the open-phase fault-tolerant operation without any extra electronic components [5,6].

Among different structures of the 6PIM [4], the asymmetrical 6PIM with double isolated neutral points, which consists of two sets of three-phase windings spatially shifted by 30 electrical degrees, has attracted the interest of many researchers [7–10]. The traditional three-phase control strategies, including switching table-based direct torque control (ST-DTC) [7], modulation-based DTC [8], the field-oriented control (FOC) [9], and finite control set-model predictive control (FCS-MPC) [10], can be extended to 6PIM (or other multi-phase machines) with some modifications to use more freedom degrees that exist in multi-phase machines. DTC is a well-accepted technique due to its simplicity, quick dynamics, and robustness [11]. The modulation-based DTC strategy offers better phase current, torque, and flux response. On the contrary, this method has more complexity against conventional ST-DTC. The ST-DTC approach has straightforward and simple structure, but it is completely overshadowed by low-order harmonics due to unused voltage vectors in the losses subspaces. To overcome this restriction, the idea of duty cycle control is introduced by several researchers [12,13].

The rapid development of intelligent and high-performance control technologies has also brought about changes in the adjustable speed drive system for different industrial applications [14,15]. To operate safely and reliably under different conditions, there is a lot of debate nowadays about the main control strategy of the system [16,17]. Among different high-performance control strategies of drive systems, the DTC strategy has a straightforward algorithm. The DTC technique is inherently speed sensorless. Nevertheless, if an outer speed loop is added to the DTC, the speed value is also necessary. Sensorless three/multi-phase induction machine drives are widely addressed in the technical literature due to multiple shortcomings of shaft encoders [18–23]. To investigate the instability problem of the traditional rotor flux-based model reference adaptive system (MRAS) speed estimators in the regenerating-mode low-speed operation, a stator current-based and back electromotive force-based MRASs are addressed in [19] and [20], respectively. In [21], two modified adaptation mechanisms are proposed to replace the classical proportional-integral (PI) regulator. The full-order Luenberger and Kalman filter observers are discussed in [22] and [23], respectively. Providing a DTC drive system with parallel identification of the rotor speed and the stator resistance is a challenging task because the operation of the DTC scheme is severely dependent on the stator resistance. This problem is sporadically reported for three-phase induction machines (3PIMs) [24,25], where the rotor speed and the stator resistance estimators encounter an overlap due to limited freedom degrees of 3PIM. In this paper, the problem of parallel estimation is investigated using more freedom degrees of 6PIM.

The outer speed control loop of the DTC scheme conventionally contains the PI regulator to obtain torque command from speed error. In general, the control law of a PID regulator is a linear combination of proportional-integral-derivative terms, which is suitable for linear systems. For nonlinear systems, such as the 6PIM drive system, the PI regulator has been given a lot of attention due to its simplicity. However, it suffers from multiple problems including: (1) tuning of its parameters; (2) high sensitivity against noise and external disturbances; and (3) loss of efficiency due to oversimplified control law [26,27]. One promising technique to relatively get rid of the drawbacks of PI regulator is active disturbance rejection controller (ADRC) [26,28]. The ADRC is a nonlinear control scheme, which provides a robust control against noises, external disturbances, and parameter uncertainties. For these reasons, the ADRC technique has recently attracted more attention for electric drive systems. To address this issue, a modified FOC scheme based on first-order ADRCs for current and speed control loops is proposed in [29]. A combined active disturbance rejection and sliding-mode controller for an induction motor is presented to achieve total robustness [30].

The aim of this paper is to present an ADRC-based DTC scheme for sensorless 6PIM drives. The speed estimator is based on adaptive full-order observer, and its control law is designed using Lyapunov stability theorem. Besides the speed estimation system, a stator resistance estimator is proposed using additional degrees of freedom of the 6PIM to enhance the robustness of the sensorless DTC strategy against stator resistance uncertainties. The adaptation law for the stator resistance estimator is derived using the Lyapunov stability theorem to ensure its overall convergence.

The rest of this paper is organized as follows. Section 2 introduces the mathematical model of the 6PIM. Section 3 presents the design procedure of the adaptive full-order observer, the speed estimator, and the stator resistance estimator. The DTC scheme of the 6PIM is discussed in Section 4, which includes the ST-DTC scheme, and ADRC in DTC. The experimental results are presented in Section 5. Finally, Section 6 summarizes the findings and concludes the paper.

2. Dynamic Model of 6PIM

There are two popular approaches for modeling of the multi-phase machines: (1) multiple d–q approach [9]; (2) vector space decomposition (VSD) approach [31]. The first method is exclusively used for modular three-phase structures-based multi-phase machines such as six-phase and nine-phase machines. However, the second method can be used for all types of multi-phase machines. In this research, the VSD approach is used, where a 6PIM with distributed windings is modeled in the three orthogonal subspaces, i.e., the $\alpha - \beta$, $z_1 - z_2$ and $o_1 - o_2$. Among them, only the $\alpha - \beta$ variables are in relation with electromechanical energy conversion, while $z_1 - z_2$ and $o_1 - o_2$ variables do not actively contribute to the torque production.

The schematic diagram of a six-phase voltage source inverter (VSI)-fed an 6PIM with two isolated neutral points is shown in Figure 1. The transfer between the normal $a - x - b - y - c - z$ variables and $\alpha - \beta - z_1 - z_2 - o_1 - o_2$ variables is performed by T_6 transformation matrix as follows [31]:

$$T_6 = \frac{1}{3} \begin{bmatrix} 1 & \frac{\sqrt{3}}{2} & -\frac{1}{2} & -\frac{\sqrt{3}}{2} & -\frac{1}{2} & 0 \\ 0 & \frac{1}{2} & \frac{\sqrt{3}}{2} & \frac{1}{2} & -\frac{\sqrt{3}}{2} & -1 \\ 1 & -\frac{\sqrt{3}}{2} & -\frac{1}{2} & \frac{\sqrt{3}}{2} & -\frac{1}{2} & 0 \\ 0 & \frac{1}{2} & -\frac{\sqrt{3}}{2} & \frac{1}{2} & \frac{\sqrt{3}}{2} & -1 \\ 1 & 0 & 1 & 0 & 1 & 0 \\ 0 & 1 & 0 & 1 & 0 & 1 \end{bmatrix} \quad (1)$$

By applying T_6 matrix to the voltage equations in the original six-dimensional system, the 6PIM model can be represented in the three orthogonal submodels, identified as $\alpha - \beta$, $z_1 - z_2$, and $o_1 - o_2$. The voltage space vector equations of the 6PIM in the $\alpha - \beta$ subspace are written as follows:

$$v_s = R_s i_s + p \Psi_s \quad (2)$$

$$0 = R_r i_r + p \Psi_r - j\omega_r \Psi_r \quad (3)$$

The flux linkages are

$$\Psi_s = L_s i_s + L_m i_r \quad (4)$$

$$\Psi_r = L_m i_s + L_r i_r \quad (5)$$

where v , i , Ψ , R , and L represent voltage, current, flux linkage, resistance, and inductance, respectively, for stator (s subscript) and rotor (r subscript) quantities, and p denotes derivative operator. The electromagnetic torque produced by the 6PIM is expressed as

$$T_e = 3P \Psi_s \otimes i_s \quad (6)$$

where P is pole pairs and \otimes denotes the cross product.

The 6PIM voltage equations in the $z_1 - z_2$ subspace are the same as a passive R-L circuit as follows:

$$v_{sz1} = R_s i_{sz1} + L_{ls} p i_{sz1} \quad (7)$$

$$v_{sz2} = R_s i_{sz2} + L_{ls} p i_{sz2} \quad (8)$$

where L_{ls} is stator leakage inductance.

On the presumption that the stator mutual leakage inductances can be neglected, the 6PIM model in the $o_1 - o_2$ subspace has the same form of the $z_1 - z_2$ subspace. However, the applied 6PIM with two isolated neutral points avoids zero-sequence currents because it contains two sets of balanced three-phase windings.

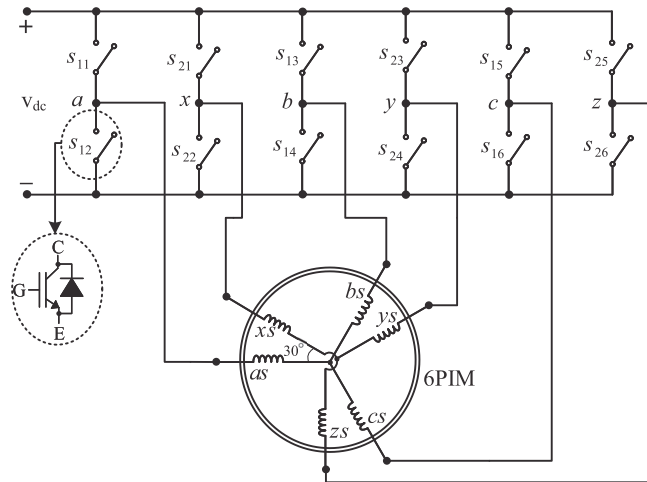


Figure 1. Six-phase two-level VSI-fed 6PIM.

3. Adaptive Full-Order Observer

The block diagram of the proposed R_s and ω_r estimators based on the adaptive state observer is shown in Figure 2. It contains the stator current and rotor flux observers, the stator resistance identifier, and the rotor speed estimator, which are discussed below.

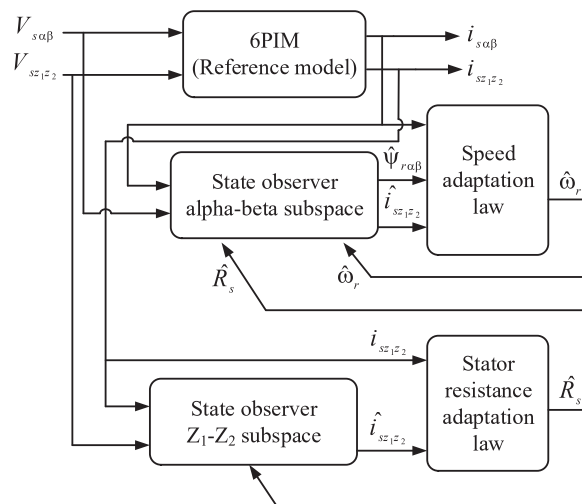


Figure 2. The block diagram of the proposed parallel estimation system of the stator resistance and the rotor speed based on an adaptive full-order observer.

3.1. Stator Current and Rotor Flux Observers

The general form of state-space model of the 6PIM in the $\alpha - \beta$ subspace is

$$\begin{cases} \dot{x}_1 = A_1 x_1 + B_1 u_1 \\ y_1 = C_1 x + D_1 u_1 \end{cases} \quad (9)$$

Assuming stator current and rotor flux as state variables and using Equations (2) and (3), the elements of state-space representation in $\alpha - \beta$ subspace will be

$$x_1 = [i_{s\alpha} \quad i_{s\beta} \quad \psi_{r\alpha} \quad \psi_{r\beta}]^T \quad (10)$$

$$A_1 = \begin{bmatrix} (-\frac{R_s}{\sigma L_s} - \frac{1-\sigma}{\sigma T_r})I & \frac{L_m}{\sigma L_s L_r} (\frac{1}{T_r} I - \omega_r J) \\ \frac{L_m}{T_r} I & -\frac{1}{T_r} I + \omega_r J \end{bmatrix} \quad (11)$$

$$B_1 = \begin{bmatrix} \frac{1}{\sigma L_s} I & O \end{bmatrix}^T \quad (12)$$

$$u_1 = [v_{s\alpha} \quad v_{s\beta}]^T \quad (13)$$

$$y_1 = [i_{s\alpha} \quad i_{s\beta}]^T \quad (14)$$

$$C_1 = [I \quad O] \quad (15)$$

with

$$I = \begin{bmatrix} 1 & 0 \\ 0 & 1 \end{bmatrix}, J = \begin{bmatrix} 0 & -1 \\ 1 & 0 \end{bmatrix}, O = \begin{bmatrix} 0 & 0 \\ 0 & 0 \end{bmatrix} \quad (16)$$

where $T_r = L_r/R_r$ is rotor time constant and $\sigma = 1 - L_m^2/L_s L_r$ is leakage coefficient.

The state observer of the 6PIM has a similar form of state-space representation except that an additional compensation term based on error of measurable states and observer gain matrix is added to it. The state observer can be written as

$$\begin{cases} \dot{\hat{x}}_1 = \hat{A}_1 \hat{x}_1 + B_1 u_1 + G_1 (\hat{i}_s - \hat{i}_s) \\ \hat{y}_1 = C_1 \hat{x}_1 \end{cases} \quad (17)$$

where the marker $\hat{}$ indicates the estimated values, and G_1 is the observer gain matrix. The matrix A_1 contains unknown parameters of the 6PIM such as the rotor speed and the stator resistance. These parameters can be estimated by the designing of a suitable adaptation control law with a nonlinear theorem such as a Lyapunov stability theorem. It is worth mentioning here that the matrix A_1 also contains the rotor time constant. However, simultaneous estimation of the rotor speed, the rotor time constant, and the stator resistance is challenging because of persistency of excitation conditions problem [32]. Some techniques have recently been developed based on signal injection to provide persistent excitation [33], which suffer from steady-state torque and speed ripples. In this paper, the stator resistance is estimated from additional degrees of freedom of the 6PIM, while the rotor speed is provided using the 6PIM equations in $\alpha - \beta$ subspace. This procedure provides the stator resistance independent from the rotor speed.

The observer gain matrix G_1 must be designed to ensure stability and good dynamic response of the observer at a wide range of the speeds. Using pole-placement method, the elements of matrix G_1 is provided as [22,34]

$$G_1 = \begin{bmatrix} g_1 & g_2 & g_3 & g_4 \\ -g_2 & g_1 & -g_4 & g_3 \end{bmatrix}^T \quad (18)$$

where

$$\begin{cases} g_1 = (1 - K_{po})(R_s L_r^2 + R_r L_m^2) / \sigma L_s L_r^2 \\ g_2 = (K_{po} - 1) \hat{\omega}_r \\ g_3 = (K_{po} - 1)(R_s L_s - K_{po} R_s L_r) / L_m \\ g_4 = (1 - K_{po}) \hat{\omega}_r \sigma L_s L_r / L_m \end{cases} \quad (19)$$

where $K_{po} > 0$ is observer constant gain.

3.2. Stator Resistance Identification

In this paper, a stator resistance adaptation system is proposed using the machine model in the $z_1 - z_2$ subspace. This method can be utilized for any multi-phase machines. It is completely decoupled from the rotor speed and the rotor time constant, whereas most of the conventional stator resistance estimators, developed for three-phase machines, are related to these parameters. The proposed R_s estimator only depends on the stator leakage inductance L_{ls} , which can be approximately assumed to be constant.

The state-space model of 6PIM in the $z_1 - z_2$ subspace, with consideration of i_{sz1} and i_{sz2} as the state variables, can be derived from Equations (7) and (8) as follows:

$$\begin{aligned} \begin{bmatrix} \dot{i}_{sz1} \\ \dot{i}_{sz2} \end{bmatrix} &= \begin{bmatrix} -\frac{R_s}{L_{ls}} & 0 \\ 0 & -\frac{R_s}{L_{ls}} \end{bmatrix} \begin{bmatrix} i_{sz1} \\ i_{sz2} \end{bmatrix} + \frac{1}{L_{ls}} \begin{bmatrix} v_{sz1} \\ v_{sz2} \end{bmatrix} \\ \begin{bmatrix} i_{sz1} \\ i_{sz2} \end{bmatrix} &= \begin{bmatrix} 1 & 0 \\ 0 & 1 \end{bmatrix} \begin{bmatrix} i_{sz1} \\ i_{sz2} \end{bmatrix} \end{aligned} \quad (20)$$

In this case, the proposed states observer is given by

$$\begin{cases} \dot{\hat{x}}_2 = \hat{A}_2 \hat{x}_2 + B_2 u_2 \\ \hat{y}_2 = C_2 \hat{x}_2 \end{cases} \quad (21)$$

It should be noted that a correction term $G_2(x_2 - \hat{x}_2)$ is neglected in Equation (21) due to the inherent stability of the observer.

The proposed adaptation law for the stator resistance estimation is

$$\hat{R}_s = K_{pr} \epsilon_{R_s} + K_{ir} \int \epsilon_{R_s} dt \quad (22)$$

where K_{ir} and K_{pr} are the integral and proportional gains, respectively, and ϵ_{R_s} is the stator resistance error signal

$$\epsilon_{R_s} = \hat{i}_{sz1}(i_{sz1} - \hat{i}_{sz1}) + \hat{i}_{sz2}(i_{sz2} - \hat{i}_{sz2}) \quad (23)$$

The proof for the stator resistance adaptation law is presented in Appendix A.

3.3. Rotor Speed Estimation

In order to design the speed adaptation law, it is considered as an unknown parameter. First, an appropriate positive definite function is chosen as the Lyapunov candidate. Then, the adaptation law is obtained using the Lyapunov criterion to ensure asymptotic stability of the system. The speed adaptation law is

$$\hat{\omega}_r = K_{p\omega} \epsilon_\omega + K_{i\omega} \int \epsilon_\omega dt \quad (24)$$

where $K_{p\omega}$ and $K_{i\omega}$ are proportional and integral gains, respectively, and ϵ_ω is the speed error signal as follows:

$$\epsilon_\omega = (i_{s\alpha} - \hat{i}_{s\alpha}) \hat{\psi}_{r\beta} - (i_{s\beta} - \hat{i}_{s\beta}) \hat{\psi}_{r\alpha} \quad (25)$$

The proof for the speed adaptation law is presented in Appendix B.

4. DTC of 6PIM

4.1. ST-DTC Scheme

A six-phase VSI contains overall $2^6 = 64$ different voltage space vectors, 60 active, and four zero vectors, where the active voltage vectors are distributed in four non-zero levels depicted in Figure 3. The electrical angle of each sectors is 30° . The 6PIM phase-to-neutral voltages can be calculated as

$$\begin{bmatrix} V_a \\ V_b \\ V_c \\ V_x \\ V_y \\ V_z \end{bmatrix} = \frac{V_{dc}}{3} \begin{bmatrix} 2 & -1 & -1 & 0 & 0 & 0 \\ -1 & 2 & -1 & 0 & 0 & 0 \\ -1 & -1 & 2 & 0 & 0 & 0 \\ 0 & 0 & 0 & 2 & -1 & -1 \\ 0 & 0 & 0 & -1 & 2 & -1 \\ 0 & 0 & 0 & -1 & -1 & 2 \end{bmatrix} \begin{bmatrix} S_a \\ S_b \\ S_c \\ S_x \\ S_y \\ S_z \end{bmatrix} \quad (26)$$

where $S_i = \{0, 1\}$, $i = \{a, x, b, y, c, z\}$ is the switching state. When $S_i = 1$ ($S_i = 0$), the corresponding stator terminal is connected to positive (negative) DC-link rail. The voltage space vectors are given by

$$v_s = \frac{1}{3} [V_a + aV_x + a^4V_b + a^5V_y + a^8V_c + a^9V_z] \quad (27)$$

$$v_z = \frac{1}{3} [V_a + a^5V_x + a^8V_b + aV_y + a^4V_c + a^9V_z] \quad (28)$$

where $v_z = v_{sz1} + jv_{sz2}$ and $a = e^{j\pi/6}$.

The flux estimator is obtained from

$$\psi_{s\alpha} = \int (v_{s\alpha} - \hat{R}_s i_{s\alpha}) dt \quad (29)$$

$$\psi_{s\beta} = \int (v_{s\beta} - \hat{R}_s i_{s\beta}) dt \quad (30)$$

and the torque estimator is obtained from (6). In the traditional ST-DTC, the torque and stator flux errors are applied to hysteresis regulators to provide the sign of torque (ϵ_T) and stator flux (ϵ_ψ). According to gained signals and also the position of stator flux, a proper large voltage vector is selected based on Table 1 during each sampling period. From Figure 3, the corresponding voltage vectors in the $z_1 - z_2$ subspace will produce large current harmonics, when only large voltage vectors are used to control the torque and flux. Hence, it can alleviate the current harmonics through reduction of the $z_1 - z_2$ components by applying a combined voltage vector during each sampling period. This technique is referred to as duty cycle control, where a virtual vector (synthesized by large and medium voltage space vectors) is applied to the inverter in each sampling period because the large and medium voltage vectors are in the opposite direction in the $z_1 - z_2$ subspace (see Figure 3). The duration of the applied vectors is calculated in order to reduce the average volt-seconds in the $z_1 - z_2$ subspace [4]. The block diagram of the proposed sensorless DTC strategy with the adaptive full-order observer is shown in Figure 4a. In this figure, the speed control loop is based on the ADRC strategy, which will be discussed in the next subsection.

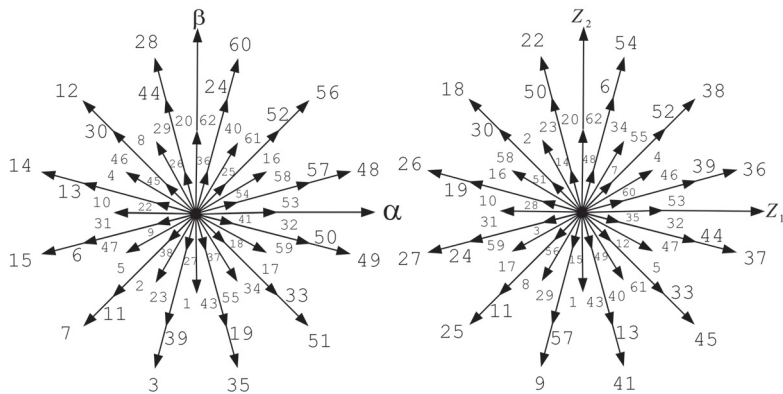


Figure 3. The $\alpha - \beta$ (top side) and the $z_1 - z_2$ (down side) vector subspaces for a six-phase VSI.

Table 1. Switching table of DTC strategy

ϵ_T	ϵ_ψ	Selected Voltage *
1	1	V_{m+1}
1	0	V_{m+4}
0	1	V_0
0	0	V_0
-1	1	V_{m-2}
-1	0	V_{m-5}

* m is sector number.

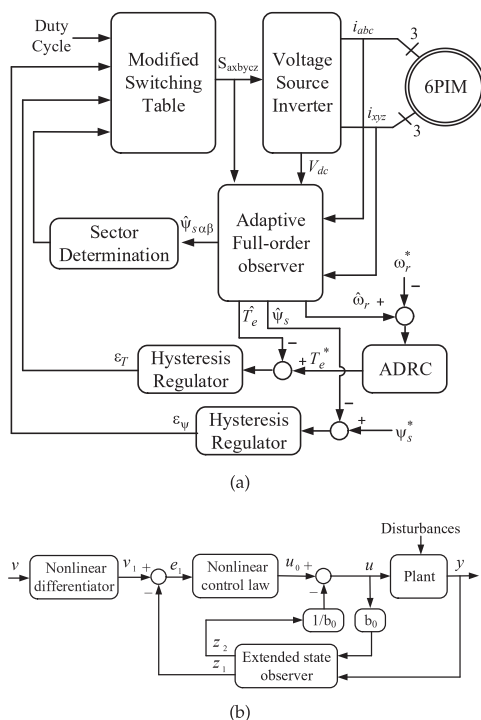


Figure 4. Block diagram of (a) the proposed sensorless DTC strategy; (b) ADRC.

4.2. ADRC in DTC

To enhance the robustness of the DTC technique against external disturbances and measurement noises, the ADRC is proposed to replace with the conventional PI regulator in the outer speed control loop. The block diagram of ADRC is shown in Figure 4b. It consists of three main elements: (1) nonlinear differentiator; (2) extended state observer; (3) nonlinear control law.

In some industrial applications, the command values are changed as step function, which is not suitable for the control system because of a sudden jump of output and control signals. To solve this problem, the nonlinear differentiator is used, which makes a reasonable transient profile from command signals for tracking [26]. The nonlinear differentiator can be expressed by

$$\begin{cases} v_1(k+1) = v_1(k) + hv_2(k) \\ v_2(k+1) = v_2(k) + hf_1(v_1(k) - v(k), v_2(k), r_0, h_0) \end{cases} \tag{31}$$

where f_1 is a nonlinear function as

$$f_1(v_1(k), v_2(k), r_0, h_0) = - \begin{cases} a(k)/h_0 & |a(k)| \leq r_0h_0 \\ r_0\text{sign}(a(k)) & |a(k)| > r_0h_0 \end{cases} \tag{32}$$

with

$$\begin{aligned} a(k) &= \begin{cases} v_2(k) + y_0(k)/h_0 & |a(k)| \leq r_0h_0^2 \\ v_2(k) + (a_0(k) - r_0h_0)/2 & |a(k)| > r_0h_0^2 \end{cases} \\ y_0(k) &= v_1(k) + h_0v_2(k) \\ a_0(k) &= \sqrt{(r_0h_0)^2 + 8r_0|y_0(k)|} \end{aligned}$$

where r_0 and h_0 are the parameters of the nonlinear differentiator, and h is sampling period.

The extended state observer is an enhanced version of feedback linearization method to compensate the total disturbances of the system. Using this observer, the state feedback term can be estimated online; hence, it is an adaptive robust observer against model uncertainties and external disturbances. The extended state observer is represented as follows:

$$\begin{cases} z_1(k+1) = z_1(k) + h[z_2(k) - \beta_1 f_2(e(k), \alpha_1, \delta_1) + b_0 u(k)] \\ z_2(k+1) = z_2(k) - h\beta_2 f_2(e(k), \alpha_1, \delta_1) \\ e(k) = z_1(k) - y(k) \end{cases} \quad (33)$$

where the nonlinear function f_2 is defined as

$$f_2(e(k), \alpha, \delta) = \begin{cases} e(k)/\delta^{1-\alpha} & |e(k)| \leq \delta \\ |e(k)|^\alpha \text{sign}(e(k)) & |e(k)| > \delta \end{cases} \quad (34)$$

where α_1 , δ_1 , β_1 , β_2 , and b_0 are the parameters of the extended state observer.

The conventional PI controller is based on the linear combination of proportional and integral terms of error, which may degrade the performance of the DTC scheme. Different nonlinear combination of error can be presented to overcome this problem. In this paper, the following nonlinear control law is used:

$$\begin{cases} e_1(k) = v_1(k) - z_1(k) \\ u_0(k) = \beta_3 f_2(e_1(k), \alpha_2, \delta_2) \\ u(k) = u_0(k) - z_2(k)/b_0 \end{cases} \quad (35)$$

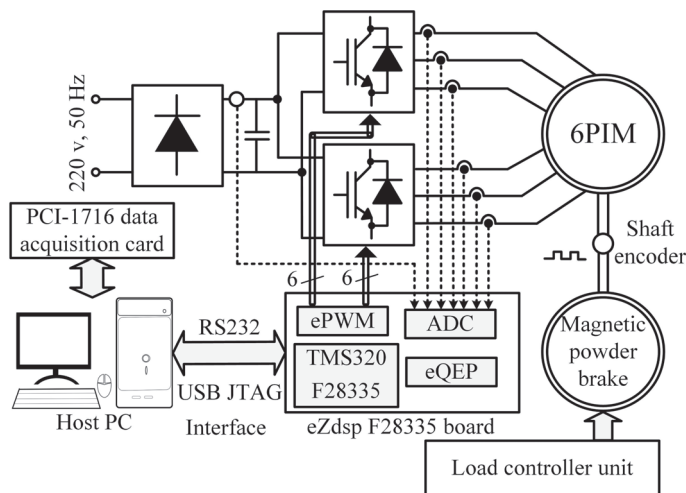
where α_2 , β_3 , and δ_2 are the parameters of nonlinear control law.

5. Experimental Validation

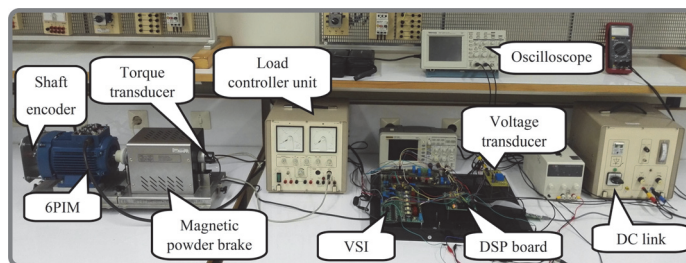
5.1. Description of Experimental Setup

The schematic and photograph of the experimental setup are shown in Figure 5a,b, respectively. The principal elements are

- a TMS320F28335-based digital signal processor (DSP) board.
- two custom-made two-level three-phase VSIs based on BUP 314D IGBTs and LEM LTS 6-NP current transducers.
- an LEM LV25-P voltage transducer.
- an Autonics incremental shaft encoder.
- a magnetic powder brake mechanically coupled to the 6PIM.
- a bridge rectifier.
- a 1-hp three-phase induction motor, which has been rewound to provide an asymmetrical 6PIM. The specifications of the 6PIM are shown in Table 2.



(a)



(b)

Figure 5. Experimental setup (a) schematic (b) photograph.

Table 2. The parameters of 6PIM.

Symbol	Quantity	Value
T_n	Nominal torque	2 Nm
P	Pole pairs	1
R_s	Stator resistance	4.08 Ω
R_r	Rotor resistance	3.73 Ω
L_s	Stator inductance	443.6 mH
L_r	Rotor inductance	443.6 mH
L_m	Magnetizing inductance	429.8 mH
J	Moment of inertia	0.000718 kg·m ²

5.2. Experimental Results

The performance of the proposed sensorless DTC strategy has been experimentally surveyed using DSP platform, programmed through Code Composer Studio (CCS v.3.3) and MATLAB. The IQmath and digital motor control (DMC) libraries have been used to provide optimized code. A 10 kHz sampling frequency with a 2 μ s dead-band has been adopted. The experimental results have been captured using an Advantech PCI-1716 data acquisition card (DAQ) and serial port with LABVIEW and MATLAB, respectively. The serial communications interface (SCI) module has been employed to provide a serial connection between host PC and DSP. An incremental shaft encoder has been used to verify the performance of the speed estimation algorithm. All of the experiments have been carried

out in sensorless mode as well as closed-loop adaptation of the stator resistance under various test scenarios, emphasizing on the low-speed region.

The experimental results of the proposed parallel estimation system of stator resistance and rotor speed under 50% initial stator resistance mismatch are shown in Figure 6. The speed command is 7% rated speed under rated load torque. In this test, the electric drive is allowed to start with a wrong stator resistance. This causes an error in estimated electromagnetic torque and actual speed. However, the estimated speed and the stator flux follow their reference values because of the controller action. It can be seen that the estimation error of the speed and the electromagnetic torque due to detuned stator resistance are removed within short seconds after activation of the stator resistance estimator at $t = 5$ s.

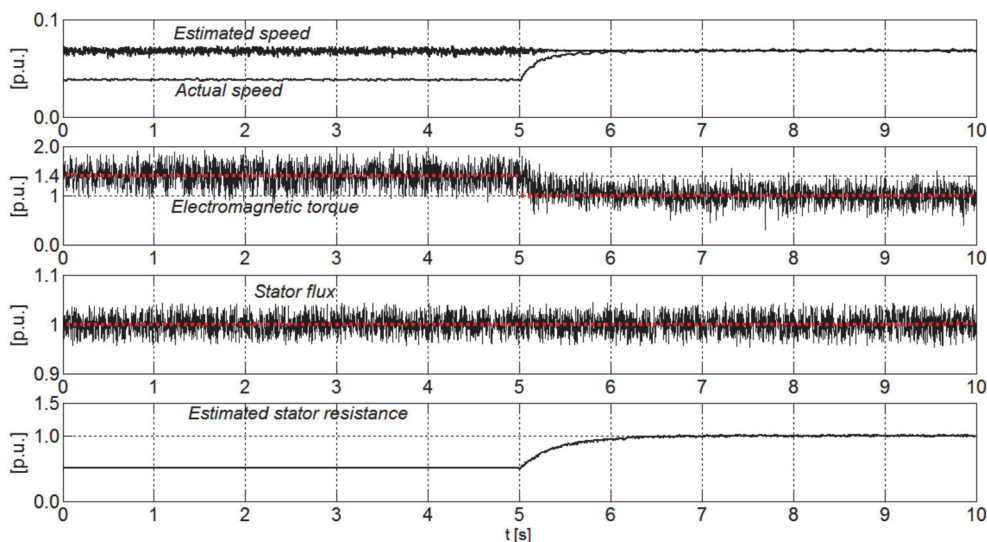


Figure 6. Experimental results of the proposed parallel estimation system under initial mismatch of stator resistance.

As already mentioned, the proposed parallel estimation system has the merit of avoiding overlap between stator resistance and rotor speed estimators, whereby the stator resistance is independently estimated from rotor speed using additional freedom degrees of 6PIM. The experimental results of estimated stator resistance under speed changes and load change are shown in Figure 7a,b, respectively. In Figure 7a, the speed command is changed as a step function from a very low speed to 17% rated speed, and, in Figure 7b, a load torque is suddenly applied to the motor at $t = 2$ s. It can be clearly adjudged that the adaptation process of stator resistance is independent of speed and load torque changes.

Disturbance-free operation of the ADRC-based speed controller is evaluated through a comparative study of its performance and the conventional PI regulator. The experimental results for the estimated speed under sudden load torque changes at 7% rated speed when the conventional PI and introduced ADRC are utilized as speed controllers are shown in Figure 8. As can be seen, applying the external load torque to the 6PIM leads to a larger overshoot (undershoot), when the conventional PI regulator is employed. The ADRC properly improves the disturbance rejecting capability, which in turn provides a robust performance against load torque changes.

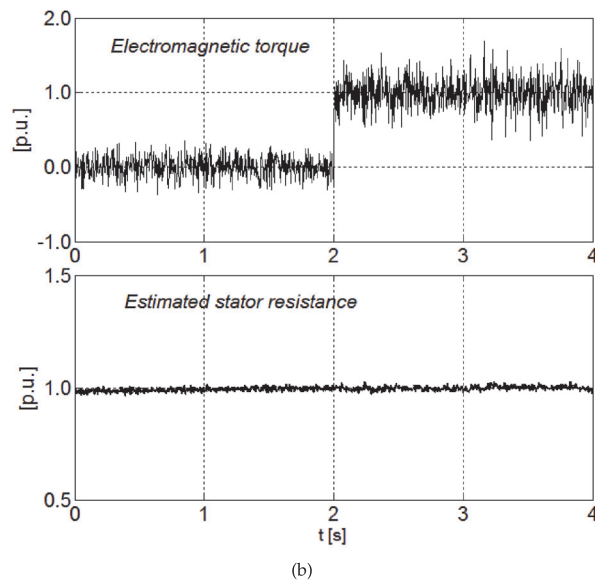
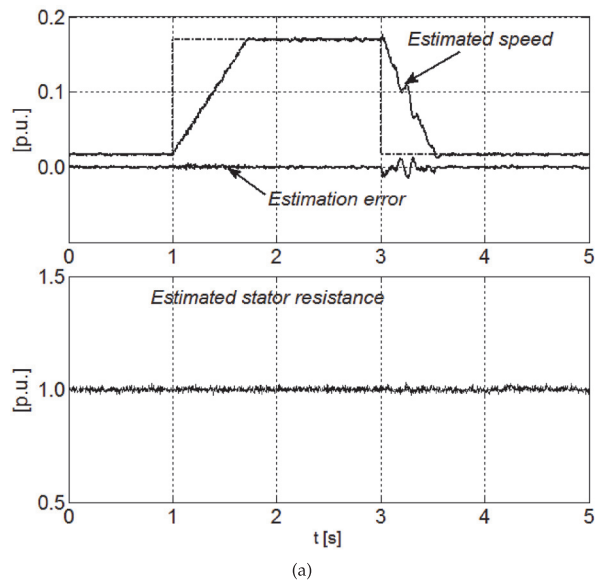


Figure 7. Experimental results of the estimated stator resistance under (a) speed changes (b) load torque change.

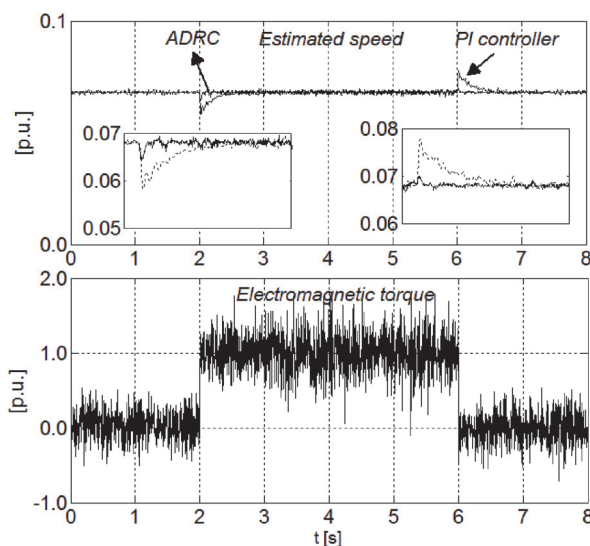


Figure 8. Experimental results of the estimated speed with PI and ADRC-based speed controllers under load changes.

6. Conclusions

Multiphase electrical machines and drives have different advantages over their traditional three phase counterparts. In recent years, multiple research works have been published to explore the specific advantages of multiphase machines and drives. In this regard, a parallel estimation system of the stator resistance and the rotor speed for direct torque-controlled 6PIM was proposed in this paper. The speed estimator is based on an adaptive full-order observer, which estimates the speed signal using the 6PIM model in the $\alpha - \beta$ subspace, while the stator resistance estimator employs the 6PIM model in the $z_1 - z_2$ subspace. Hence, the stator resistance is identified independently of the rotor speed. The rotor speed- and the stator resistance-adaptation laws were derived using the Lyapunov stability theorem. The performance of the proposed sensorless DTC was experimentally investigated, where the obtained results confirmed its capabilities in terms of accuracy as well as no overlap between the stator resistance and the rotor speed estimators. In order to provide a robust performance for the DTC technique against external load torques, the PI regulator was replaced by an ADRC, as a well-known disturbance-free controller. The better performance of the DTC scheme based on ADRC was verified through a comparative study with the conventional PI regulator.

Author Contributions: Conceptualization, methodology, validation, formal analysis, writing—original draft preparation, H.H., M.H.H.; writing - review and editing, resources, A.R.; project administration, T.V.; investigation, A.K.; funding acquisition, D.V.L.; supervision, A.B. All authors have read and agreed to the published version of the manuscript.

Funding: The research has been supported by the Estonian Research Council under grant PSG453 “Digital twin for propulsion drive of autonomous electric vehicle” and was financially supported by Government of Russian Federation (Grant 08-08).

Conflicts of Interest: The authors declare no conflict of interest.

Appendix A The Design of Adaption Law for Stator Resistance Estimation

The quadratic Lyapunov function for asymptotic stability of the proposed stator resistance estimation system is defined as

$$V_r = e_r^T e_r + \frac{\Delta R_s^2}{\lambda_r} \quad (\text{A1})$$

where λ_r is a positive constant, $\Delta R_s = \hat{R}_s - R_s$, \hat{R}_s is the estimated stator resistance, R_s is the real stator resistance, and e_r is the error matrix of the state variables in the $z_1 - z_2$ subspace as

$$e_r = x_2 - \hat{x}_2 = \begin{bmatrix} i_{sz1} - \hat{i}_{sz1} & i_{sz2} - \hat{i}_{sz2} \end{bmatrix}^T \tag{A2}$$

The asymptotic stability of the stator resistance estimator is assured when the Lyapunov candidate function V_r is positive definite as well as its time derivative pV_r is negative definite. The time derivative of the Lyapunov candidate function is calculated as

$$pV_r = e_r^T p e_r + p e_r^T e_r + \frac{2}{\lambda_r} \Delta R_s p \hat{R}_s \tag{A3}$$

With some mathematical manipulation, Equation (A3) can be written as

$$pV_r = e_r^T (A_2 + A_2^T) e_r - [e_r^T \Delta A_2 \hat{x} + \hat{x}_2^T \Delta A_2^T e_r] + \frac{2}{\lambda_r} \Delta R_s p \hat{R}_s \tag{A4}$$

The first term of Equation (A4) is inherently negative definite. The stability of the system is eventually assured, when the sum of the last two terms of Equation (A4) is zero as

$$\frac{2}{\lambda_r} \Delta R_s p \hat{R}_s - [e_r^T \Delta A_2 \hat{x}_2 + \hat{x}_2^T \Delta A_2^T e_r] = 0 \tag{A5}$$

which leads to

$$\hat{R}_s = -\frac{\lambda_r}{2} \int \epsilon_{R_s} dt \tag{A6}$$

where the tuning signal ϵ_{R_s} is

$$\epsilon_{R_s} = \hat{i}_{sz1}(i_{sz1} - \hat{i}_{sz1}) + \hat{i}_{sz2}(i_{sz2} - \hat{i}_{sz2}) \tag{A7}$$

A PI regulator is employed to enhance the dynamic behaviour of the proposed estimator, instead of Equation (A6) as

$$\hat{R}_s = K_{pr} \epsilon_{R_s} + K_{ir} \int \epsilon_{R_s} dt \tag{A8}$$

where K_{ir} and K_{pr} are the integral and proportional constants.

Appendix B The Design of Adaption Law for Speed Estimation

The Lyapunov candidate function for asymptotic stability of the speed estimation system is

$$V_\omega = e_\omega^T e_\omega + \frac{\Delta \omega_r^2}{\lambda_\omega} \tag{A9}$$

where λ_ω is a positive constant, $\Delta \omega_r = \hat{\omega}_r - \omega_r$, and e_ω is the error matrix of the estimated and real values in $\alpha - \beta$ subspace as

$$e_\omega = x_1 - \hat{x}_1 = \begin{bmatrix} i_{s\alpha} - \hat{i}_{s\alpha} & i_{s\beta} - \hat{i}_{s\beta} & \psi_{r\alpha} - \hat{\psi}_{r\alpha} & \psi_{r\beta} - \hat{\psi}_{r\beta} \end{bmatrix}^T \tag{A10}$$

In this case, the first-order time derivative of Lyapunov function can be deduced as

$$pV_{\omega} = e_{\omega}^T[(A_1 - G_1C_1) + (A_1 - G_1C_1)^T]e_{\omega} + (e_{\omega}\Delta A_2\hat{x}_2 + \hat{x}_2\Delta A^Te_{\omega}) + \frac{2}{\lambda_{\omega}}\Delta\omega_r p\hat{\omega}_r \quad (\text{A11})$$

The first term of Equation (A11) is guaranteed to be negative definite by suitable adopting of observer gain matrix G_1 . The Lyapunov stability criterion is satisfied, if the sum of second and third terms of Equation (A11) is zero. With some calculations, the adaptation law for speed estimator is acquired as

$$\hat{\omega}_r = K_{p\omega}\epsilon_{\omega} + K_{i\omega} \int \epsilon_{\omega} dt \quad (\text{A12})$$

where the tuning signal ϵ_{ω} is

$$\epsilon_{\omega} = (i_{s\alpha} - \hat{i}_{s\alpha})\hat{\psi}_{r\beta} - (i_{s\beta} - \hat{i}_{s\beta})\hat{\psi}_{r\alpha} \quad (\text{A13})$$

References

1. Levi, E.; Bojoi, R.; Profumo, F.; Toliyat, H.A.; Williamson, S. Multiphase induction motor drives—A technology status review. *IET Electr. Power Appl.* **2007**, *1*, 489–516.
2. Heidari, H.; Rassölkin, A.; Vaimann, T.; Kallaste, A.; Taheri, A.; Holakooie, M.H.; Belahcen, A. A novel vector control strategy for a six-phase induction motor with low torque ripples and harmonic currents. *Energies* **2019**, *12*, 1102.
3. Levi, E. Multiphase Electric Machines for Variable-Speed Applications. *IEEE Trans. Ind. Electron.* **2008**, *55*, 1893–1909.
4. Holakooie, M.H.; Ojaghi, M.; Taheri, A. Direct Torque Control of Six-Phase Induction Motor With a Novel MRAS-Based Stator Resistance Estimator. *IEEE Trans. Ind. Electron.* **2018**, *65*, 7685–7696.
5. Che, H.S.; Duran, M.J.; Levi, E.; Jones, M.; Hew, W.P.; Rahim, N.A. Postfault Operation of an Asymmetrical Six-Phase Induction Machine With Single and Two Isolated Neutral Points. *IEEE Trans. Power Electron.* **2014**, *29*, 5406–5416.
6. Lu, H.; Li, J.; Qu, R.; Ye, D. Fault-tolerant predictive current control with two-vector modulation for six-phase permanent magnet synchronous machine drives. *IET Electr. Power Appl.* **2018**, *12*, 169–178.
7. Holakooie, M.H.; Ojaghi, M.; Taheri, A. Modified DTC of a Six-Phase Induction Motor With a Second-Order Sliding-Mode MRAS-Based Speed Estimator. *IEEE Trans. Power Electron.* **2019**, *34*, 600–611.
8. Bojoi, R.; Farina, F.; Griva, G.; Profumo, F.; Tenconi, A. Direct torque control for dual three-phase induction motor drives. *IEEE Trans. Ind. Appl.* **2005**, *41*, 1627–1636.
9. Singh, G.K.; Nam, K.; Lim, S.K. A simple indirect field-oriented control scheme for multiphase induction machine. *IEEE Trans. Ind. Electron.* **2005**, *52*, 1177–1184.
10. Gregor, R.; Barrero, F.; Toral, S.L.; Duran, M.J.; Arahal, M.R.; Prieto, J.; Mora, J.L. Predictive-space vector PWM current control method for asymmetrical dual three-phase induction motor drives. *IET Electr. Power Appl.* **2010**, *4*, 26–34.
11. Zaid, S.A.; Mahgoub, O.A.; El-Metwally, K.A. Implementation of a new fast direct torque control algorithm for induction motor drives. *IET Electr. Power Appl.* **2010**, *4*, 305–313.
12. Hoang, K.D.; Ren, Y.; Zhu, Z.Q.; Foster, M. Modified switching-table strategy for reduction of current harmonics in direct torque controlled dual-three-phase permanent magnet synchronous machine drives. *IET Electr. Power Appl.* **2015**, *9*, 10–19.
13. Tatte, Y.N.; Aware, M.V. Torque Ripple and Harmonic Current Reduction in a Three-Level Inverter-Fed Direct-Torque-Controlled Five-Phase Induction Motor. *IEEE Trans. Ind. Electron.* **2017**, *64*, 5265–5275.
14. Rassölkin, A.; Vaimann, T.; Kallaste, A.; Kuts, V. Digital twin for propulsion drive of autonomous electric vehicle. In Proceedings of the 2019 IEEE 60th International Scientific Conference on Power and Electrical Engineering of Riga Technical University (RTUCON), Riga, Latvia, 7–9 October 2019; pp. 1–4.
15. Kuts, V.; Tahemaa, T.; Otto, T.; Sarkans, M.; Lend, H. Robot manipulator usage for measurement in production areas. *J. Mach. Eng.* **2016**, *16*, 57–67.

16. Sell, R.; Leier, M.; Rassölkin, A.; Ernits, J.P. Self-driving car ISEAUTO for research and education. In Proceedings of the 2018 19th International Conference on Research and Education in Mechatronics (REM), Delft, The Netherlands, 7–8 June 2018; pp. 111–116.
17. Rassölkin, A.; Sell, R.; Leier, M. Development case study of the first estonian self-driving car, iseauto. *Electr. Control Commun. Eng.* **2018**, *14*, 81–88.
18. Kumar, R.; Das, S.; Syam, P.; Chattopadhyay, A.K. Review on model reference adaptive system for sensorless vector control of induction motor drives. *IET Electr. Power Appl.* **2015**, *9*, 496–511.
19. Gadoue, S.M.; Giaouris, D.; Finch, J.W. Stator current model reference adaptive systems speed estimator for regenerating-mode low-speed operation of sensorless induction motor drives. *IET Electr. Power Appl.* **2013**, *7*, 597–606.
20. Rashed, M.; Stronach, A.F. A stable back-EMF MRAS-based sensorless low-speed induction motor drive insensitive to stator resistance variation. *IEE Proc. Electr. Power Appl.* **2004**, *151*, 685–693.
21. Holakooie, M.H.; Taheri, A.; Sharifian, M.B. MRAS Based Speed Estimator for Sensorless Vector Control of a Linear Induction Motor with Improved Adaptation Mechanisms. *J. Power Electron.* **2015**, *15*, 1274–1285.
22. Holakooie, M.H.; Ojaghi, M.; Taheri, A. Full-order Luenberger observer based on fuzzy-logic control for sensorless field-oriented control of a single-sided linear induction motor. *ISA Trans.* **2016**, *60*, 96–108.
23. Habibullah, M.; Lu, D.D.C. A Speed-Sensorless FS-PTC of Induction Motors Using Extended Kalman Filters. *IEEE Trans. Ind. Electron.* **2015**, *62*, 6765–6778.
24. Lee, K.B.; Blaabjerg, F. Sensorless DTC-SVM for Induction Motor Driven by a Matrix Converter Using a Parameter Estimation Strategy. *IEEE Trans. Ind. Electron.* **2008**, *55*, 512–521.
25. Lascu, C.; Boldea, I.; Blaabjerg, F. Direct torque control of sensorless induction motor drives: a sliding-mode approach. *IEEE Trans. Ind. Appl.* **2004**, *40*, 582–590.
26. Han, J. From PID to Active Disturbance Rejection Control. *IEEE Trans. Ind. Electron.* **2009**, *56*, 900–906.
27. Mahmudizad, M.; Ahangar, R.A. Improving load frequency control of multi-area power system by considering uncertainty by using optimized type 2 fuzzy pid controller with the harmony search algorithm. *World Acad. Sci. Eng. Technol.* **2016**, *10*, 1051–1061.
28. Wang, G.; Wang, B.; Li, C.; Xu, D. Weight-transducerless control strategy based on active disturbance rejection theory for gearless elevator drives. *IET Electr. Power Appl.* **2017**, *11*, 289–299.
29. Li, J.; Ren, H.P.; Zhong, Y.R. Robust Speed Control of Induction Motor Drives Using First-Order Auto-Disturbance Rejection Controllers. *IEEE Trans. Ind. Appl.* **2015**, *51*, 712–720.
30. Alonge, F.; Cirrincione, M.; D'ippolito, F.; Pucci, M.; Sferlazza, A. Robust Active Disturbance Rejection Control of Induction Motor Systems Based on Additional Sliding-Mode Component. *IEEE Trans. Ind. Electron.* **2017**, *64*, 5608–5621.
31. Zhao, Y.; Lipo, T.A. Space vector PWM control of dual three-phase induction machine using vector space decomposition. *IEEE Trans. Ind. Appl.* **1995**, *31*, 1100–1109.
32. Kubota, H.; Matsuse, K. Speed sensorless field-oriented control of induction motor with rotor resistance adaptation. *IEEE Trans. Ind. Appl.* **1994**, *30*, 1219–1224.
33. Wang, K.; Chen, B.; Shen, G.; Yao, W.; Lee, K.; Lu, Z. Online updating of rotor time constant based on combined voltage and current mode flux observer for speed-sensorless AC drives. *IEEE Trans. Ind. Electron.* **2014**, *61*, 4583–4593.
34. Yin, Z.; Zhang, Y.; Du, C.; Liu, J.; Sun, X.; Zhong, Y. Research on Anti-Error Performance of Speed and Flux Estimation for Induction Motors Based on Robust Adaptive State Observer. *IEEE Trans. Ind. Electron.* **2016**, *63*, 3499–3510.



Paper VII

Heidari, H., Rassõlkin, A., Kallaste, A., Vaimann, T., & Andriushchenko, E. Vector Control of Synchronous Reluctance Motor with Reduced Torque Ripples, 2020 XI International Conference on Electrical Power Drive Systems (ICEPDS), 2020, pp. 1–5, doi: 10.1109/ICEPDS47235.2020.9249309

Vector Control Of Synchronous Reluctance Motor With Reduced Torque Ripples

Hamidreza Heidari, Anton Rassölkin, Ants Kallaste, Toomas Vaimann, Ekaterina Andriushchenko
Department of Electrical Power Engineering and Mechatronics
Tallinn University of Technology
Tallinn, Estonia
haheid@taltech

Abstract— High torque ripples associated with direct torque control (DTC) of synchronous reluctance motor (SynRM) have become a severe challenge in high-performance applications. This paper proposes a modified method to suppress the torque ripple for a vector controlled SynRM drive system. The switching-table based DTC is opted to control the motor. The method exploits the decoupled currents in the synchronous reference frame in order to generate a more accurate set of inputs for the switching table. In addition, the active voltage application time is regulated to avoid high torque ripples. The method reduced the high torque ripples of the SynRM by simply using hysteresis controllers and switching table with different inputs. Moreover, the pulse-width modulation algorithm is avoided, resulting in less computation burden of the control. The simulation results are carried out and the performance of the method is validated.

Keywords—synchronous reluctance motor, direct torque control, field-oriented control, torque ripples

I. INTRODUCTION

The interest in synchronous reluctance motor (SynRM) in the industry is growing due to the intrinsic high efficiency of the motor [1]. With the simple structure of the rotor, SynRM can offer high reliability, high overloadability, high dynamic, and high power density [2], [3]. In fact, the variable speed drives have provided the efficient application of this motor type, which has convinced the leading manufacturers to introduce their SynRM motor-drive package to the market [4]. On the other hand, the high torque ripples of SynRM has become a challenge for the researchers to overcome [5]. Many research works are carried out on the design of SynRM to cover this drawback such as in [6]. Moreover, suppressing the torque ripple is viable with a proper control method in the variable speed drives [7], [8].

The field-oriented control (FOC) strategy offers an interesting choice for researchers in terms of the control of SynRM with low torque ripple. This is due to the decoupled control of the currents in the synchronous reference frame, which proposes a high-performance control in the steady-state. However, its low dynamic and high computation burden direct some research work to the other control methods [9], [10].

Direct torque control (DTC) is one of the alternatives for control of SynRM [11]. The direct control of the torque and flux in the stationary reference frame with the hysteresis controllers and the application of the command voltages by a simple lookup-table provides a high dynamic and straightforward control strategy. Though, the high torque ripple and the variable switching frequency of DTC are the undeniable shortcomings of this method [12], [13]. To take SynRM's high torque ripples into account, conventional DTC of these motors causes sever torque ripples in the motor. Lack

of current controller in DTC's block diagram leads to high torque ripples. Multilevel inverters have recently been a proper solution for torque ripples, which are studied for DTC in [14]. Another solution that amends the shortcoming of the high torque ripple of DTC is the overmodulation scheme for DTC of SynRM, presented by Zhang et al. in [7]. This method keeps the simplicity of DTC, and in the meanwhile, decreases the torque ripples and provides constant switching frequency. One more viable approach is the duty ratio regulation-based DTC, which is also known as dead-beat DTC [15]. Basically, the method tries to apply the active voltages not for the whole sampling period, as so the motors' torque and similarly the flux does not considerably pass the hysteresis limit. This results in a notable reduction in torque ripple with the cost of a little bit of imposing a complexity to the method, beside a notably higher switching frequency. A more sophisticated and more robust version of this method is applied by Foo et al. in [16] for the DTC of SynRM.

In this paper, a combination of DTC and FOC techniques is used in such a way that the decoupled currents of the d and q-axes are applied to the switching table to obtain more precise inputs and select the more precise voltage vectors in each sampling period. Moreover, the active voltages are no longer applied for the whole sampling period and the null voltage vector is applied for a ratio of the period. This leads the motor's torque to not increase/decrease so higher than the hysteresis band and the torque ripples dramatically decrease. The duty ratio is selected according to a simple optimization function to reduce the current errors.

In the rest of this paper, the proposed method is investigated in section II. Section III presents the simulation results for DTC and the proposed method for the SynRM control. A conclusion of the study is presented in section IV.

II. THE PROPOSED METHOD FOR TORQUE RIPPLE REDUCTION IN DTC OF SYNRM

A. The Origin Of High Torque Ripple In DTC Of SYNRM

Basically, the DTC strategy aims to directly control the stator flux magnitude and position by means of imposing the active voltage vectors regarding the position of stator flux as well as the sign of flux and torque. The torque and stator flux are controlled by radial and tangential components of stator flux. The block diagram of the classical DTC is shown in Fig. 1. In principle, the stator flux vector magnitude and position as well as the electromagnetic torque are estimated using measured DC-link voltage and phase currents. Then, the estimated values are compared by the stator flux vector reference, given as a command value, and the torque reference, which is provided by the outer speed control loop. The torque reference is obtained by the proportional-integral (PI) control of the speed error signal between the command value and the instant value of the speed. In the SynRM, the stator flux vector is aligned with the rotor position.

The research has been supported by the Estonian Research Council under grant PSG453 "Digital twin for propulsion drive of an autonomous electric vehicle.

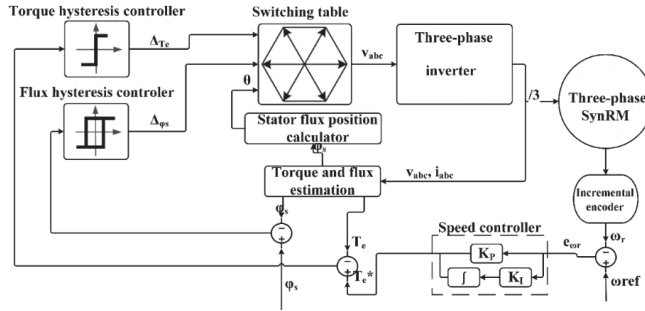


Fig. 1: DTC of SynRM

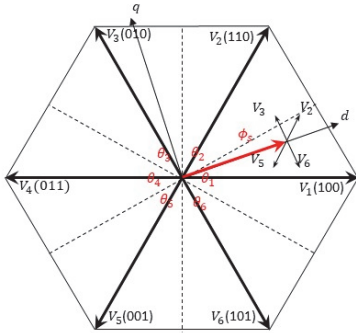


Fig. 2: The voltage vectors- active voltages ($V_{1..6}$) and the zero voltages ($V_7(000), V_8(111)$)

TABLE I. SWITCHING TABLE OF CONVENTIONAL DTC

e_λ, e_T	θ	θ_1	θ_2	θ_3	θ_4	θ_5	θ_6
$e_\lambda = 1$	$e_T = 1$	V_2	V_3	V_4	V_5	V_6	V_1
	$e_T = 0$	V_7	V_8	V_7	V_8	V_7	V_8
	$e_T = -1$	V_6	V_1	V_2	V_3	V_4	V_5
$e_\lambda = 0$	$e_T = 1$	V_3	V_4	V_5	V_6	V_1	V_2
	$e_T = 0$	V_8	V_7	V_8	V_7	V_8	V_7
	$e_T = -1$	V_5	V_6	V_1	V_2	V_3	V_4

In line with the flux and torque error signals, the stator flux position is used as the inputs of a lookup table in order to generate the command voltages to the motor. This lookup table is known as the switching table, as it generates the command switching states. The switching table is presented in Table I. The generated switching states are applied to the motor by means of a model of a three-phase voltage source inverter. The active voltages are depicted in Fig. 2, which denote the states of the inverter's legs. The states of the upper switch in each leg denote the state of the leg. In this figure, the stator flux vector is also illustrated, which is aligned with the d-axis. Also, the flux vector's sectors are defined as $\theta_{1..6}$, which provides information about the position of the flux vector for the switching table.

The high torque ripple of DTC originates from two substantial reasons, which are related to parameter regulation and the voltage application method. Inherently, the hysteresis controllers provide the sign of error signals, which require the

active voltage usage for the whole sampling period, regardless of the error signals' amplitude. In addition, the switching table is defined based on the error signals, which makes the voltage selection more dependent on the regulators. Moreover, the active voltages are applied to the motor for all sampling periods, which can inevitably cause the flux vector to pass the hysteresis bands.

B. The Alternative Inputs For The Switching Table

The simple voltage application to the motor through the DTC has altered the conventional PWM method. However, this simplification leads to a variable switching frequency in the method. In addition, the conventional DTC sacrifices the precise control of the stator currents, which leads to high torque ripples in the motor. The high torque ripple is avoided in FOC by precise control of the motor. A combination of FOC and DTC can provide precise control of the currents, while can keep the simplicity of the method. The decoupled currents of the SynRM are correspondent to the torque and flux of the motor. Bearing in mind the FOC concept, the traditional inputs of the torque and flux errors are replaced by the d and q-axes currents' error in the synchronous reference frame, respectively. This concept is represented as follows:

$$\begin{cases} T_e \propto i_q \\ \lambda_s \propto i_d \end{cases} \quad (1)$$

In this method, the currents in d, and q-axes are compared to the reference values and the error signals are applied as inputs of the hysteresis controller to produce the corresponding signs for the switching table. The reference values are generated by means of the PI regulator. The d-axis reference is produced by the regulation of the error between estimated flux and the reference flux. The q-axis reference is produced through a comparison of the estimated torque and the reference torque, which is generated from the regulation of the speed error signal. The method's block diagram is illustrated in Fig. 3. In this figure, Δi_q and Δi_d denote to the error signals' sign of i_q and i_d in the method. In this method, in case of demand for increasing i_q , the error signals' sign is defined as $\Delta i_q = 1$. $\Delta i_q = 0$ implies to no i_q requirement. Similarly, with the demand for decrement of i_q , $\Delta i_q = -1$ is defined, and the $\Delta i_d = 1$ denotes to the required i_d increment, and for no change in i_d , the indication is defined as $\Delta i_d = 0$. The error signals' sign and the demand for the change in the d -axes are obtained as:

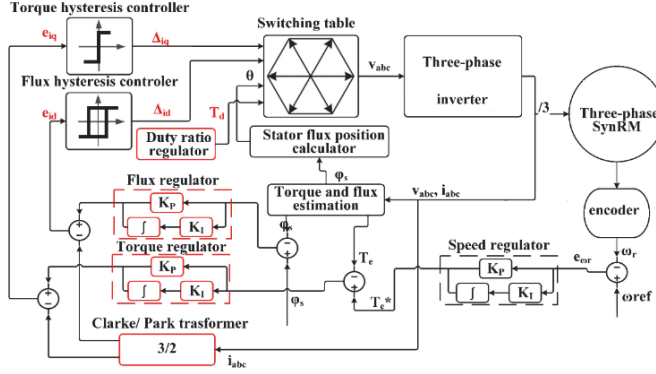


Fig. 3: A proposed method for SynRM control

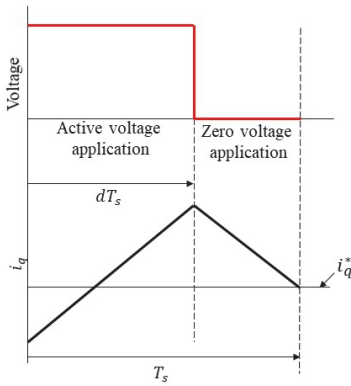


Fig. 4: The demonstration of the duty ratio regulation of the q-axis current

TABLE II. SWITCHING TABLE OF THE PROPOSED METHOD FOR DTC OF SYNRM

e_{i_d}, e_{i_q}	θ	θ_1	θ_2	θ_3	θ_4	θ_5	θ_6
$e_{i_d} = 1$	$e_{i_q} = 1$	V_2	V_3	V_4	V_5	V_6	V_1
	$e_{i_q} = 0$	V_7	V_8	V_7	V_8	V_7	V_8
	$e_{i_q} = -1$	V_6	V_1	V_2	V_3	V_4	V_5
$e_{i_d} = 0$	$e_{i_q} = 1$	V_3	V_4	V_5	V_6	V_1	V_2
	$e_{i_q} = 0$	V_8	V_7	V_8	V_7	V_8	V_7
	$e_{i_q} = -1$	V_5	V_6	V_1	V_2	V_3	V_4

$$\begin{aligned} \Delta i_q &= 1 \quad \text{if } i_q \leq i_q^* - |\text{hysteresis band}| \\ \Delta i_q &= 0 \quad \text{if } i_q = i_q^* \\ \Delta i_q &= -1 \quad \text{if } i_q \geq i_q^* + |\text{hysteresis band}| \end{aligned} \quad (2)$$

With a similar definition, Δi_d is described as:

$$\begin{aligned} \Delta i_d &= 1 \quad \text{if } i_d \leq i_d^* - |\text{hysteresis band}| \\ \Delta i_d &= 0 \quad \text{if } i_d \geq i_d^* + |\text{hysteresis band}| \end{aligned} \quad (3)$$

and the position of the stator flux vector. For instance, if the flux vector is in the first sector, and the increment of the d and

q-axes currents is required, V_2 is selected by the switching table to apply to the motor.

Table II defines the switching table for the proposed method. According to this table, the active and zero voltages are opted considering the signs of d, and q-axes currents' error

C. The Duty Ratio Regulation Method

In classical DTC, the optimal active voltages are opted through the switching table to apply to the motor. Whereas, the application of the active voltages for the whole sampling period causes the motor torque to increase/decrease to a higher/lower value than the demanded torque. This is due to the lack of control on the active voltage during one sampling period. In this paper, the active and null vectors are employed in the proposed method to significantly decrease the torque ripples in SynRM. This decreases the torque ripple of the proposed method for a lower value. Fig. 4 demonstrates the concept of the duty ratio regulation, which on the top figure the active and zero voltage applications are depicted and at the bottom, the i_q response is illustrated as an example. In this figure, it is seen that the i_q , as well as torque, can be adjusted by altering the time duration of the voltage vector's application. Assuming the increment requirement for the i_q , the active voltage is applied for a shorter duration of time than sampling time. Certainly, the applied voltage increases the i_q value of the motor. Particularly, if the defined sampling frequency for the method is not high enough, the applied voltage will cause the motor's i_q , as well as torque, increase for higher value than the desired value. The duty ratio regulation method prevents the i_q to increase/decrease for whole of the sampling time, which causes the i_q to settle to the desired value at the end of the sampling time. In order to have torque ripple-suppressed control of the SynRM, the proposed method is improved by regulating the duty ratio of the active voltage's application time. The ratio of the active voltage application is calculated as follows:

$$d = \left| \frac{E_{i_q}}{c_{i_q}} \right| + \left| \frac{E_{i_d}}{c_{i_d}} \right| = \left| \frac{i_q^* - i_{q0}}{c_{i_q}} \right| + \left| \frac{i_d^* - i_{d0}}{c_{i_d}} \right| \quad (4)$$

Where d is the duty of the active voltage application, i_q^* is the q-axis current reference value and i_d^* is the d-axis current reference value; i_{q0} , and i_{d0} are the instant values of the q and d-axes currents at the beginning of the sampling time,

respectively; and C_{i_q} , and C_{i_d} are the two constant values used to determine the duty ratio of active voltage application. To tune these constants, we made a tradeoff between dynamic and steady-state responses. The larger the constant values are, the less torque ripple will appear in the proposed method with duty ratio regulation with the cost of the degraded dynamic performance of the method.

III. SIMULATION RESULTS

The SynRM's model was simulated in MATLAB/SIMULINK according to the parameters of the motor that are presented in [17]. The proposed method is implemented in simulation to control the SynRM in line with the simulation of the DTC method. The performance of the method is compared with the conventional DTC. First, the comparison is carried out by applying two different step loads with no change in the speed command. The motor starts with partial load and at $t=1$ s, a higher step load is applied. Second, the performance of the proposed method is compared with conventional DTC by changing the direction of the rotation speed under no-load condition. In this test, SynRM is driven at the beginning with the nominal speed. Then, at $t=1$ s, the speed command changes to the negative direction with the same value. The proposed method is tuned in order to have a similar speed response as the classic DTC.

Figures 5-7 present the simulation results of DTC and the proposed method for the first test. Fig. 5 shows the speed response of the SynRM for the classical DTC and the proposed method. The speed responses are similar, and the SynRM tracks the speed in an acceptable dynamic with stable responses in load changes. Fig. 6 shows that the torque response of the proposed method can follow the loads in steady-state and the SynRM stabilizes in a short period of time with an acceptable peak in the transient mode. The superiority of the proposed method against the classical DTC is clear in terms of torque ripples reduction. It is worth mentioning that for DTC of SynRM, the higher the load is, the higher the torque ripple appears in the motor's torque. This issue is addressed by the proposed method, where the torque ripples fairly remain low in higher loads, as well. Also, the phase a current is illustrated in Fig. 7. This figure shows that the proposed method slightly avoids the current ripples. Hence, it presents a better current response than classical DTC. In the loading condition, the proposed method has roughly higher current in the transient mode.

Figures 8-10 present the simulation results for the speed direction change of SynRM controlled by DTC and the proposed method. In this test, the speed command of the motor is the positive nominal speed and at the time of $t=1$ s, the speed command changes to the negative nominal speed. Fig. 8 shows the speed response of the model. In this figure, the proposed method tracks the command speed. The proposed method shows a desirable dynamic and the speed of the motor has a comparable performance with DTC in the transient mode. In the speed direction change, the proposed method shows a high dynamic, which is comparable with fast dynamic DTC method. In the steady-state, the speed of the SynRM stabilizes in the command speed in both directions. In Fig. 9, the torque response of the SynRM is presented. The figure shows that at the beginning of the test, the proposed method has comparable value to DTC in transient mode with the lower ripples. This shows the superiority of the proposed

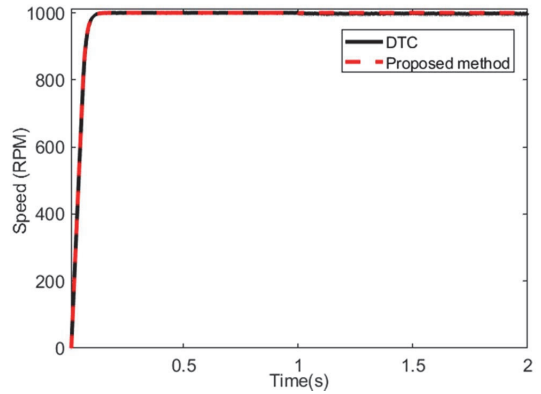


Fig. 5: The speed response of the SynRM for DTC and the proposed method for applied loads

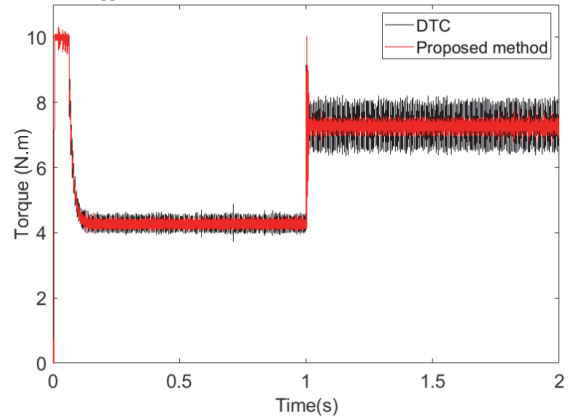


Fig. 6: The torque response of the SynRM for DTC and the proposed method for applied loads

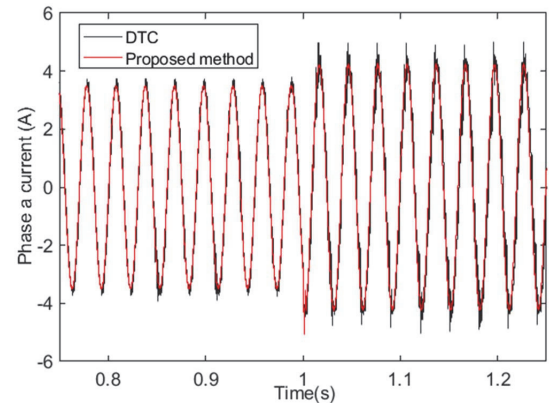


Fig. 7: The phase a current response of the SynRM for DTC and the proposed method for applied loads

method against the conventional DTC method. The results show by far lower torque ripples in the speed direction condition and better performance is achieved by the proposed method. Also, in the steady-state, the torque ripples are lower with the proposed method. Fig. 10 shows the phase-a current response of the simulations. This figure shows less current ripple in steady-state with the proposed method. In the speed

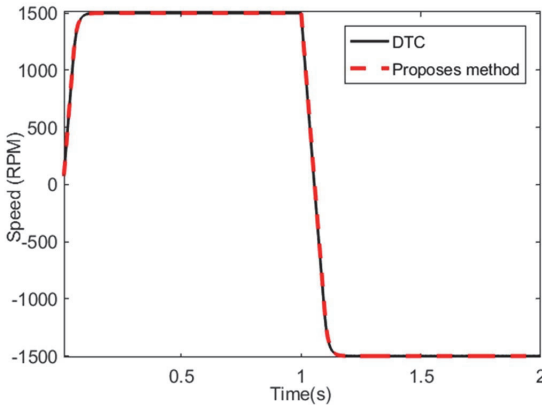


Fig. 8: The speed response of the SynRM for DTC and the proposed method for speed direction change

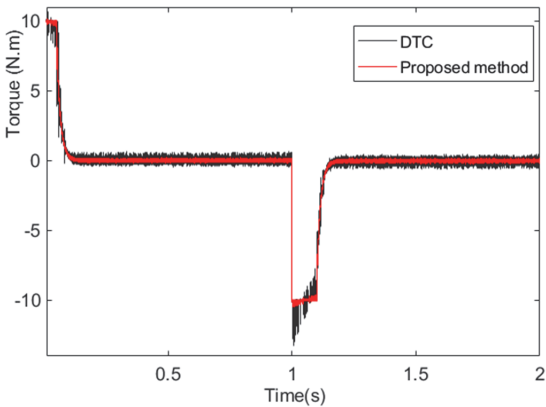


Fig. 9: The torque response of the SynRM for DTC and the proposed method for speed direction change

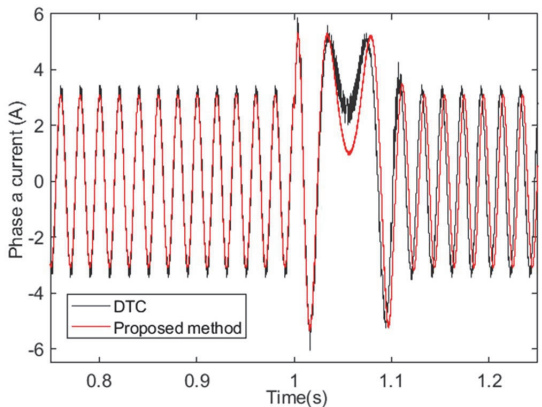


Fig. 10: The phase a current response of the SynRM for DTC and the proposed method for speed direction change

direction test, the proposed method shows better performance with lower ripples in the currents.

IV. CONCLUSION

The concept of decoupled control of d and q-axes currents in FOC was applied to DTC to obtain more precise inputs for the switching table. In addition, a duty ratio regulation

method was implemented to dedicate a certain period to the active voltages to apply to SynRM's model. Imposing suitable null voltage to the motor prevented the motor's torque from passing the hysteresis bands in one sampling period. Application of both methods to the SynRM decreased the torque ripples, significantly. The proposed method maintained the fast dynamic of the DTC. The simulation results verified the performance of the method. The method will be implemented in a real-time test bench and will be evaluated in terms of torque ripples, switching frequency, and execution time in the future.

V. REFERENCES

- [1] A. Rassölkin et al., "Life cycle analysis of electrical motor-drive system based on electrical machine type," *Proc. Est. Acad. Sci.*, vol. 69, no. 2, p. 162, 2020.
- [2] A. T. De Almeida, et al., "Beyond induction motors - Technology trends to move up efficiency," *IEEE Trans. Ind. Appl.*, 2014.
- [3] H. Heidari et al. "Harmonics Distortion in Inverter-Fed Motor-Drive Systems: Case Study," in 2019 Electric Power Quality and Supply Reliability Conference (PQ) & 2019 Symposium on Electrical Engineering and Mechatronics (SEEM), 2019, pp. 1–4.
- [4] "ABB IE5 SynRM motors deliver ultra-premium energy efficiency." Available: <https://new.abb.com/news/detail/58874/abb-ie5-synrm-motors-deliver-ultra-premium-energy-efficiency>.
- [5] H. Liu, I. Kim, Y. J. Oh, and S. Go, "Design of Permanent Magnet-Assisted Synchronous Reluctance Motor for Maximized Back-EMF and Torque Ripple Reduction," *IEEE Trans. Magn.*, vol. 53, no. 6, pp. 1–4, 2017.
- [6] M. N. F. Ibrahim, P. Sergeant, and E. Rashad, "Simple design approach for low torque ripple and high output torque synchronous reluctance motors," *Energies*, vol. 9, no. 11, 2016.
- [7] X. Zhang and G. H. B. Foo, "Overmodulation of Constant-Switching-Frequency-Based DTC for Reluctance Synchronous Motors Incorporating Field-Weakening Operation," *IEEE Trans. Ind. Electron.*, 2019.
- [8] M. H. Holakooie, et al., "MRAS based speed estimator for sensorless vector control of a linear induction motor with improved adaptation mechanisms," *J. Power Electron.*, vol. 15, no. 5, pp. 1274–1285, 2015.
- [9] H. Heidari et al., "A Novel Vector Control Strategy for a Six-Phase Induction Motor with Low Torque Ripples and Harmonic Currents," *Energies*, vol. 12, no. 6, p. 1102, 2019.
- [10] A. Taheri, et al. "Sensorless Loss Model Control of the Six-phase Induction Motor in all Speed range by Extended Kalman Filter," *IEEE Access*, pp. 1–1, Jan. 2020.
- [11] S. Bolognani, L. Peretti, and M. Zigliotto, "Online MTPA Control Strategy for DTC Synchronous-Reluctance-Motor Drives," vol. 26, no. 1, pp. 20–28, 2011.
- [12] H. Heidari et al., "A parallel estimation system of stator resistance and rotor speed for active disturbance rejection control of six-phase induction motor," *Energies*, vol. 13, no. 5, 2020.
- [13] M. H. Holakooie et al., "Modified DTC of a Six-Phase Induction Motor with a Second-Order Sliding-Mode MRAS-Based Speed Estimator," *IEEE Trans. Power Electron.*, vol. 34, no. 1, pp. 600–611, 2018.
- [14] D. Mohan et al., "Generalized DTC Strategy for Multilevel Inverter Fed IPMSMs with Constant Inverter Switching Frequency and Reduced Torque Ripples," *IEEE Trans. Energy Convers.*, vol. 32, no. 3, pp. 1031–1041, 2017.
- [15] G. H. B. Foo and X. Zhang, "Robust Direct Torque Control of Synchronous Reluctance Motor Drives in the Field-Weakening Region," *IEEE Trans. Power Electron.*, vol. 32, no. 2, pp. 1289–1298, 2017.
- [16] G. H. Foo and X. Zhang, "Robust Direct Torque Control of Synchronous Reluctance Motor Drives in the Field-Weakening Region," *IEEE Trans. Power Electron.*, vol. 32, no. 2, pp. 1289–1298, 2017.
- [17] H. Heidari et al., "Comparison of Synchronous Reluctance Machine and Permanent Magnet-Assisted Synchronous Reluctance Machine Performance Characteristics," *Proceeding 27th Int. Work. Electr. Drives*, no. 1m, pp. 9–13, 2020.

Paper VIII

Heidari H, Rassölkin A, Vaimann T, Kallaste A, Taheri A, Holakooie MH, Belahcen A. A Novel Vector Control Strategy for a Six-Phase Induction Motor with Low Torque Ripples and Harmonic Currents. *Energies*. 2019; 12(6):1102. <https://doi.org/10.3390/en12061102>

Article

A Novel Vector Control Strategy for a Six-Phase Induction Motor with Low Torque Ripples and Harmonic Currents

Hamidreza Heidari ^{1,*}, Anton Rassölkin ¹, Toomas Vaimann ¹, Ants Kallaste ¹,
Asghar Taheri ², Mohammad Hosein Holakooie ² and Anouar Belahcen ^{1,3}

¹ Department of Electrical Power Engineering and Mechatronics, Tallinn University of Technology, 19086 Tallinn, Estonia; anton.rassolkin@taltech.ee (A.R.); toomas.vaimann@taltech.ee (T.V.); ants.kallaste@taltech.ee (A.K.); anouar.belahcen@aalto.fi (A.B.)

² Department of Electrical Engineering, University of Zanjan, Zanjan 45371-38791, Iran; taheri@znu.ac.ir (A.T.); hosein.holakooie@znu.ac.ir (M.H.H.)

³ Department of Electrical Engineering, Aalto University, 11000 Aalto, Finland

* Correspondence: haheid@taltech.ee; Tel.: +372-5613-9797

Received: 25 January 2019; Accepted: 19 March 2019; Published: 21 March 2019



Abstract: In this paper, a new vector control strategy is proposed to reduce torque ripples and harmonic currents represented in switching table-based direct torque control (ST-DTC) of a six-phase induction motor (6PIM). For this purpose, a new set of inputs is provided for the switching table (ST). These inputs are based on the decoupled current components in the synchronous reference frame. Indeed, using both field-oriented control (FOC) and direct torque control (DTC) concepts, precise inputs are applied to the ST in order to achieve better steady-state torque response. By applying the duty cycle control strategy, the loss subspace components are eliminated through a suitable selection of virtual voltage vectors. Each virtual voltage vector is based on a combination of a large and a medium vector to make the average volt-seconds in loss subspace near to zero. Therefore, the proposed strategy not only notably reduces the torque ripples, but also suppresses the low frequency current harmonics, simultaneously. Simulation and experimental results clarify the high performance of the proposed scheme.

Keywords: direct torque control; duty cycle control; harmonic currents; six-phase induction motor; torque ripple

1. Introduction

With the emergence of power electronic devices and adjustable-speed drives, multiphase machines have attracted wide attention for special applications in the naval, automotive, and aerospace industries [1,2]. The key features of these machines are high reliability, fault tolerant operation, low rate of power switches, low torque pulsation and low dc-link voltage [3–7]. Among multiphase motors, multiple three-phase winding motors have received more interest due to their advantage of compatibility with conventional three-phase technology. Considering this benefit, the asymmetrical 6PIM, which is composed of two sets of three-phase windings spatially shifted by 30 electrical degrees, seems desirable for many applications.

Direct Torque Control (DTC) is a simple and powerful scheme for variable speed 6PIM drives that provides high-performance torque and stator flux control [8]. However, it suffers from some serious drawbacks, including high torque ripples and low-frequency current harmonics, which can strikingly degrade the performance of the drive system [9,10]. A great deal of effort has been invested

in alleviating DTC high torque ripples, which mostly includes the modification of the hysteresis controller [11,12], amending the switching table (ST) [13,14], or replacing hysteresis controllers with other control strategies to provide Pulse Width Modulation (PWM)-based DTC [15]. A global minimum torque ripple using modified switching pattern has been proposed in [16]. In [17], the torque ripples have been reduced by applying active and zero voltage vectors in each sampling period using a predictive DTC. With regard to a large number of voltage vectors in six-phase voltage source inverter (VSI), elimination of loss subspace components seems possible through the vector space decomposition (VSD) model. Aiming to reduce harmonic currents, elimination of $z_1 - z_2$ (loss subspace) components using the duty cycle concept in DTC is proposed in [9,12] for a five-phase induction motor, and a six-phase permanent magnet motor, respectively. Moreover, harmonic currents have been reduced by adding an inductance filter to the 6PIM drive system [18]. On the other hand, structure reconfiguration of 6PIM to minimize both harmonic currents and torque ripples has been done in [4]. On the other hand, field-oriented control (FOC) can be easily applied to many types of electrical machines [19].

The main focus of this paper is on the parallel torque ripple and harmonic current reduction in vector control of a 6PIM. To achieve these goals, a new vector control scheme is proposed, using a combination of DTC FOC concepts to moderate steady-state torque ripples. To reduce harmonic currents, twelve virtual voltage vectors are introduced by combination of large and single medium voltage vectors (e.g., 48 and 57 in Figure 1a, respectively). The duration of each voltage vector is determined such that the average volt-seconds in the $z_1 - z_2$ subspace becomes near to zero. Consequently, low-frequency current harmonics experience a considerable reduction, current will be much smoother, and the efficiency of the drive system will be increased.

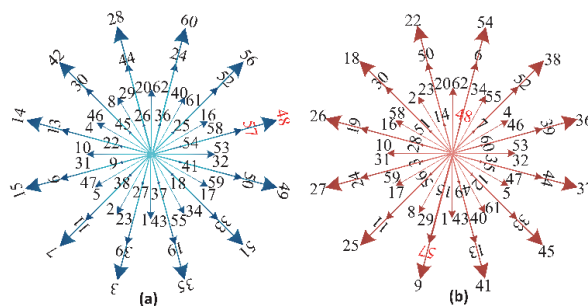


Figure 1. 6PIM model in (a) $\alpha - \beta$, (b) $z_1 - z_2$ bspace.

The rest of this paper is organized as follows: in Section 2, 6PIM modeling is presented. The conventional DTC and its drawbacks such as torque ripples and harmonic currents are discussed in Section 3. The proposed method to reduce torque ripples and harmonic currents is presented in Section 4.

2. 6PIM Modelling

There are two common methods for modelling of 6PIMs: double $d - q$ [20] and VSD [21]. According to the VSD approach, the machine's parameters are mapped into active and loss subspaces, which makes the control strategy more convenient and efficient. Moreover, the VSD method can easily be extended to other types of motors. In this study, the 6PIM modelling is based on the VSD strategy. According to this modelling technique, a 6PIM with near-sinusoidal distributed windings is modelled in three orthogonal subspaces, which are commonly named as the $\alpha - \beta$, $z_1 - z_2$, and $o_1 - o_2$ subspaces. The produced voltage space vectors by switching states of a two-level six-phase voltage source inverter in the $\alpha - \beta$, $z_1 - z_2$ subspaces are shown in Figure 1. Among these subspaces, only the $\alpha - \beta$ components share useful electromechanical energy conversion, while $z_1 - z_2$ and $o_1 - o_2$ components do not generate any electromechanical energy in the air-gap and just produce losses.

The fundamental components and also harmonics of the order $12n \pm 1$ ($n = 1, 2, 3, \dots$) are mapped into the $\alpha - \beta$ subspace. The losses of 6PIM are mapped into the $z_1 - z_2$ and $o_1 - o_2$ subspaces which include harmonics by the order of $6n \pm 1$ ($n = 1, 3, 5, \dots$) and $3n$ ($n = 1, 2, 3, \dots$), respectively. By the assumption that the stator mutual leakage inductance is ignored, the components of $z_1 - z_2$ and $o_1 - o_2$ subspaces have the same form [21]. Since the active and loss components are investigated separately, it is clear that the control of 6PIM will be more efficient by using VSD. Additionally, isolation of the neutral points of two three-phase windings, makes the $o_1 - o_2$ subspace losses become zero [21].

2.1. 6PIM Model in $\alpha - \beta$ Subspace

As already mentioned, only the $\alpha - \beta$ subspace components contribute to the electrical energy conversion. Using the VSD strategy, the normal six-dimensional electrical components of the 6PIM are mapped into the $\alpha - \beta$, $z_1 - z_2$, and $o_1 - o_2$ subspaces by an appropriate matrix named T_6 , which is presented in Appendix A. The $\alpha - \beta$ voltage equations in the stationary reference frame are as follows:

$$\begin{cases} \bar{V}_s = R_s \bar{I}_s + \rho \bar{\Psi}_s \\ 0 = R_r \bar{I}_r + \rho \bar{\Psi}_r - j\omega_r \bar{\Psi}_r \end{cases} \quad (1)$$

where, $\bar{V}_s = v_{s\alpha} + jv_{s\beta}$, $\bar{I}_s = i_{s\alpha} + ji_{s\beta}$, $\bar{I}_r = i_{r\alpha} + ji_{r\beta}$, $\bar{\Psi}_s = \psi_{s\alpha} + j\psi_{s\beta}$, $\bar{\Psi}_r = \psi_{r\alpha} + j\psi_{r\beta}$, R_s is the stator resistance, R_r is the rotor resistance, ω_r is the angular speed, and ρ is the derivative operator. The stator flux linkage ($\bar{\Psi}_s$) and rotor flux linkage ($\bar{\Psi}_r$) can be expressed as:

$$\begin{bmatrix} \bar{\Psi}_s \\ \bar{\Psi}_r \end{bmatrix} = \begin{bmatrix} L_s & M \\ M & L_r \end{bmatrix} \begin{bmatrix} \bar{I}_s \\ \bar{I}_r \end{bmatrix} \quad (2)$$

where, L_s , L_r , and M are the stator, rotor and magnetizing inductances, respectively.

2.2. 6PIM Model in $z_1 - z_2$ Subspace

The 6PIM model in the $z_1 - z_2$ subspace behaves as a passive resistor-inductor ($R-L$) circuit as:

$$\begin{bmatrix} V_{sz_1} \\ V_{sz_2} \end{bmatrix} = \begin{bmatrix} R_s + \rho L_{ls} & 0 \\ 0 & R_s + \rho L_{ls} \end{bmatrix} \begin{bmatrix} I_{sz_1} \\ I_{sz_2} \end{bmatrix} \quad (3)$$

where, L_{ls} is the stator leakage inductance. In this paper, 6PIM is applied with two isolated neutral points, with which this structure prevents the zero sequence currents. Hence, the $o_1 - o_2$ components can be neglected.

3. Conventional DTC of 6PIM

In a six-phase voltage source inverter (VSI), there are $2^6 = 64$ switching states. Each state produces a voltage space vector (defined as V_k) in the $\alpha - \beta$ or $z_1 - z_2$ subspaces, shown in Figure 1. As can be seen, there are 12 large (e.g., 48), 12 single medium (e.g., 57), 24 double medium (e.g., 53), 12 small (e.g., 54), and 4 null voltage vectors. The block diagram of conventional DTC is shown in Figure 2.

The stator flux in this approach is obtained as:

$$\bar{\Psi}_s = \int (\bar{V}_s - R_s \bar{I}_s) dt \quad (4)$$

The electromagnetic torque can be calculated using the stator flux and current as:

$$T_e = 1.5 P (\bar{\Psi}_s \cdot \bar{I}_s^*) \quad (5)$$

where, P is the number of pole pairs. The reference values of the stator flux and electromagnetic torque are compared with the estimated ones, and the errors are applied to the hysteresis controller.

The outputs of the hysteresis regulators denote the signs of torque and flux change. In order to minimize the errors, the optimum vector is selected through ST, which is tabulated in Table 1.

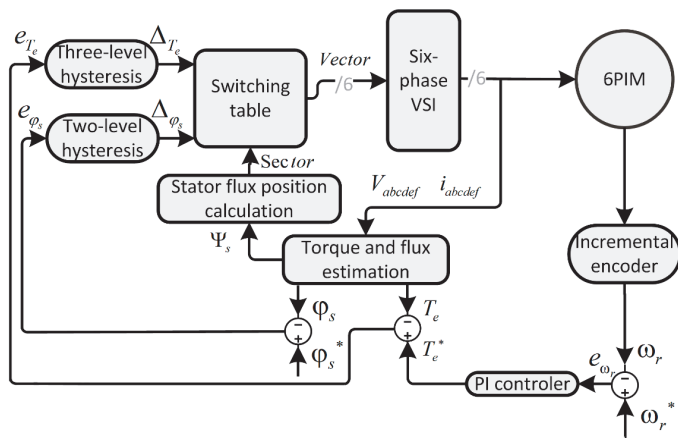


Figure 2. Conventional DTC block diagram.

In this table, k is the number of the sector. V_k is the applied voltage vector to the inverter, which is defined as binary numbers in switching states of VSI as in Table 2.

Table 1. ST of conventional DTC.

$\Psi_s/\text{sector } k$	$\Delta T_e=1$	$\Delta T_e=0$	$\Delta T_e=-1$
$\Delta\phi_s = 1$	V_{k+1}	V_0	V_{k+10}
$\Delta\phi_s = -1$	V_{k+4}	V_0	V_{k+7}

Table 2. Selected vectors in ST of conventional DTC.

V_0	V_1	V_2	V_3	V_4	V_5	V_6	V_7	V_8	V_9	V_{10}	V_{11}	V_{12}
0, 21, 42, 63	48	56	60	28	12	14	15	7	3	35	57	49

In the conventional DTC, only the large voltage vectors in the $\alpha - \beta$ subspace are applied to the 6PIM to maximize the utilization of the dc-link. From Equation (4), it can be seen that the stator flux variations and the applied voltage vectors have the same direction. Hence, the changes in the stator flux depend on the applied voltage vectors. Compared to the stator time constant, the rotor time constant is very large. Therefore, the rotor flux linkage changes are negligible and it can be assumed constant during short transients [22]. By the application of the active voltage vectors, stator flux linkage vector will be moved away from rotor flux linkage vector and the angle between them will be greater. This leads to changes in torque according to Equation (5).

4. Harmonic Currents Reduction by Duty Cycle Control Strategy

From Figure 1, it can be seen that each voltage vector in the $\alpha - \beta$ subspace has a corresponding vector in the $z_1 - z_2$ subspace with different position and magnitude. It is recommended to make the average volt-second outcome in the $z_1 - z_2$ subspace near to zero. Accordingly, two voltage vectors have been applied to the inverter in each sampling period. Active voltage vectors should be in a same direction (in order to have high effect on torque) and their correspondents in $z_1 - z_2$ subspace should be in an opposite direction (in order to have less losses). Therefore, the selected vectors will produce high outcome in $\alpha - \beta$ subspace and low outcome in the $z_1 - z_2$ subspace.

The applied voltage vectors in the $\alpha - \beta$ subspace are expressed as:

$$\begin{cases} V_{M_{\alpha-\beta}} = \frac{\sqrt{2}}{3} V_{dc} \\ V_{L_{\alpha-\beta}} = \frac{\sqrt{6+\sqrt{2}}}{6} V_{dc} \end{cases} \quad (6)$$

where, $V_{M_{\alpha-\beta}}$ and $V_{L_{\alpha-\beta}}$ are single-medium and large voltage vectors in the $\alpha - \beta$ subspace. A suitable duty ratio is calculated as:

$$\begin{cases} |V_{M_{\alpha-\beta}} T_{M_{\alpha-\beta}}| = |V_{L_{\alpha-\beta}} T_{L_{\alpha-\beta}}| \\ T_{M_{\alpha-\beta}} + T_{L_{\alpha-\beta}} = T_s \end{cases} \Rightarrow \begin{cases} T_{L_{\alpha-\beta}} = 0.73 T_s \\ T_{M_{\alpha-\beta}} = 0.27 T_s \end{cases} \quad (7)$$

where, $T_{L_{\alpha-\beta}}$ and $T_{M_{\alpha-\beta}}$ are the duration of the large and single-medium voltage vectors application in the $\alpha - \beta$ subspace, and T_s is the sampling period. In this way, the losses in the $z_1 - z_2$ subspace are reduced strikingly, while the reduction in the electromagnetic components is subtle. For instance, vectors number 48 and 57 have the same direction in the $\alpha - \beta$ subspace and the opposite direction in the $z_1 - z_2$ subspace. These voltage vectors are applied to the motor as illustrated in Figure 3, where g_n is the number of legs in six-phase VSI, and K_v is the duty ratio defined as:

$$K_v = 1 - \frac{|V_{M_{\alpha-\beta}}|}{|V_{L_{\alpha-\beta}}|} = 0.27 \quad (8)$$

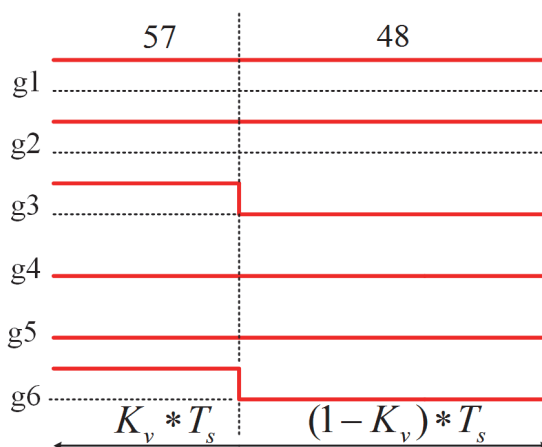


Figure 3. Switching pattern.

If $g_n = 1$ the upper switch is on and the lower switch is off. On the contrary, when $g_n = 0$, the lower switch becomes on and the upper switch turns off. The compound of these vectors in each sampling period is named virtual vector, shown in Figure 4.

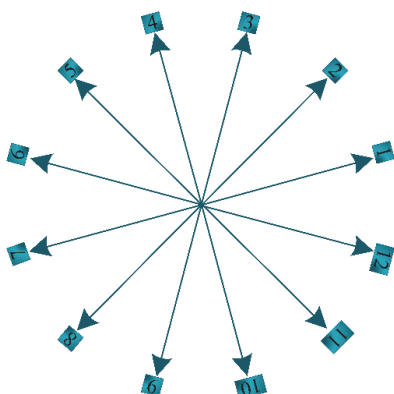


Figure 4. Virtual vectors in α - β subspace.

Figure 3 shows that in two legs (among the six legs) of the inverter, the switches' status has been changed. Therefore, by this method has more switching frequency against DTC. This increase in switching frequency is less than twice. The vectors in the $\alpha - \beta$ subspace are replaced by virtual vectors in ST shown in Table 2.

5. Proposed Control Algorithm for the 6PIM Drive

Using FOC framework [23], 6PIM's mathematical equations are transformed to the synchronous reference frame ($d - q$), which creates possibility of decoupled control of the torque and flux as a permanent-magnet separated-excitation dc motor. In this reference frame, the stator flux vector is located on d -axis which is shown in Figure 5.

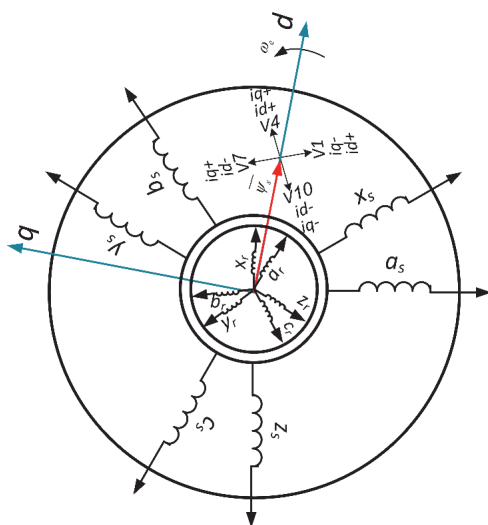


Figure 5. 6PIM structure and stator flux vector in 3rd sector and applied inverter voltage vectors.

Orthogonal currents of the 6PIM are mapped into the synchronous reference frame using Park transformation based on the flux vector position, which is achieved by field orientation process. For the

6PIM control, i_q is a torque -and i_d is a flux- producing components. Hence, the equations of the torque and flux are related to stator currents in the $d - q$ frame as follows:

$$\begin{cases} T_e \propto i_q \\ \lambda_s \propto i_d \end{cases} \tag{9}$$

In order to decrease the torque ripples in the 6PIM, a new approach is employed by modifying the ST’s inputs. Since the inputs of the ST in the classical ST-DTC are the errors between command and actual values of the electromagnetic torque and the stator flux, it seems effective to use the errors between the set and actual values of the i_q, i_d , instead. In order to redesign the ST-DTC method to use these inputs, the inputs of ST in the conventional DTC are used as inputs for PI regulators. The outputs of PI regulators are the command values of the currents in the $d - q$ axis. Replacing $\Delta T_e, \Delta \phi_s$ by $\Delta i_q, \Delta i_d$ in ST-DTC, respectively, the proposed method provides better inputs to the same ST presented in Table 1 which leads to a better performance in 6PIM. Table 3 shows that through defining virtual vectors, the ST is the same with conventional DTC with different inputs.

Table 3. The switching table of the proposed scheme.

$\Psi_s/\text{Sector } k$	$\Delta i_q=1$	$\Delta i_q=0$	$\Delta i_q=-1$
$\Delta i_d = 1$	V_{k+1}	V_0	V_{k+10}
$\Delta i_d = -1$	V_{k+4}	V_0	V_{k+7}

Δi_q and Δi_d imply that changing the signs of the i_q and i_d is required. If i_q needs to be increased, then $\Delta i_q = 1$. If there is no i_q requirement, then $\Delta i_q = 0$. Also, $\Delta i_q = -1$ denotes the decrease of i_q . All the states are defined as the same for the notation of Δi_d . These digital output signals of the hysteresis controllers are described as:

$$\begin{aligned} \Delta i_q &= 1 \quad \text{if } i_q \leq i_q^* - |\text{hysteresis band}| \\ \Delta i_q &= 0 \quad \text{if } i_q = i_q^* \\ \Delta i_q &= -1 \quad \text{if } i_q \geq i_q^* + |\text{hysteresis band}| \end{aligned} \tag{10}$$

Similarly, for the changes required for the d-axis of the stator current, Δi_d is described as:

$$\begin{aligned} \Delta i_d &= 1 \quad \text{if } i_d \leq i_d^* - |\text{hysteresis band}| \\ \Delta i_d &= 0 \quad \text{if } i_d \geq i_d^* + |\text{hysteresis band}| \end{aligned} \tag{11}$$

The block diagram of the proposed control strategy is shown in Figure 6. To concurrently achieve low Total Harmonics Distortion (THD) (of the motor currents and low torque ripples, the proposed vector control scheme is synthesized with the duty cycle control strategy. The ST applies two voltage vectors in each sampling period in order to eliminate $z_1 - z_2$ subspace components. In comparison with the conventional DTC, the switching frequency of the proposed scheme is increased (less than twice according to Figure 3.) because two voltage vectors are applied in each sampling period. In contrary, both harmonic currents and torque ripples are reduced. Moreover, the proposed scheme has fast dynamic response, similar to the conventional DTC, and does not need any PWM modulator that creates complexity and time delay.

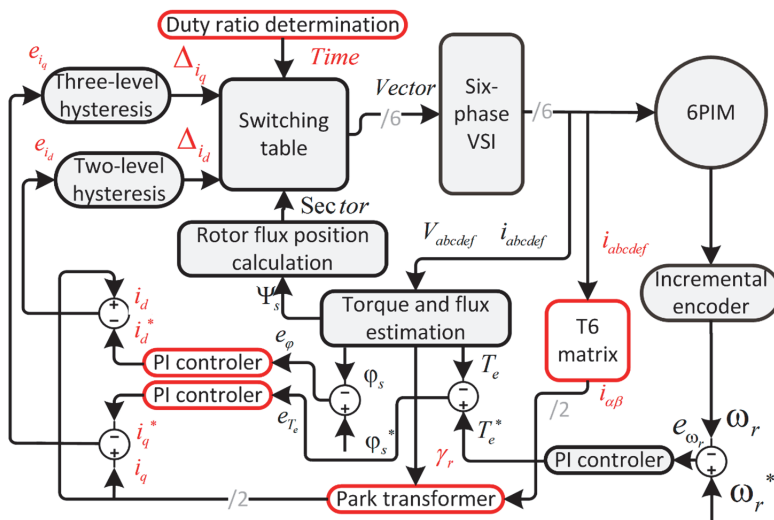


Figure 6. Block diagram of the proposed control scheme for 6PIM.

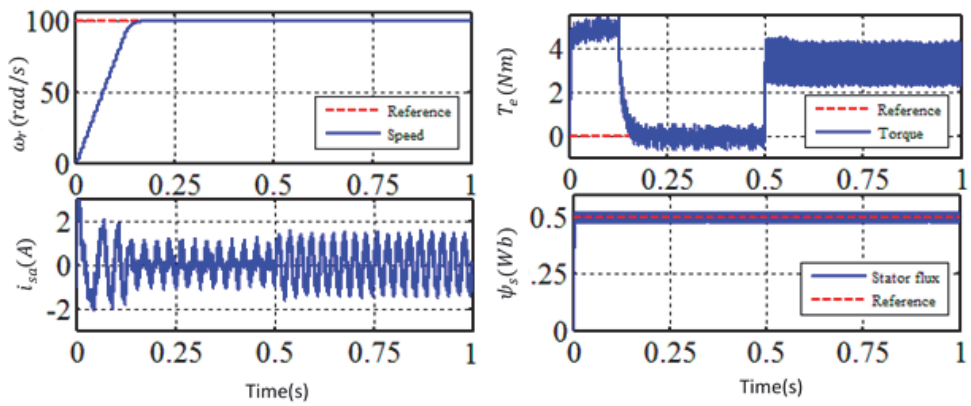
6. Simulation Results

The proposed and duty cycle control methods are simulated in MATLAB/Simulink. The sampling period of both methods are set to 100 μs. All the parameters are assumed to be constant, although each of them can be changed under the thermal effect, which is not within the scope of this essay. The simulations are carried out based on real specifications for 6PIM. The 6PIM parameters are specified in Table 4.

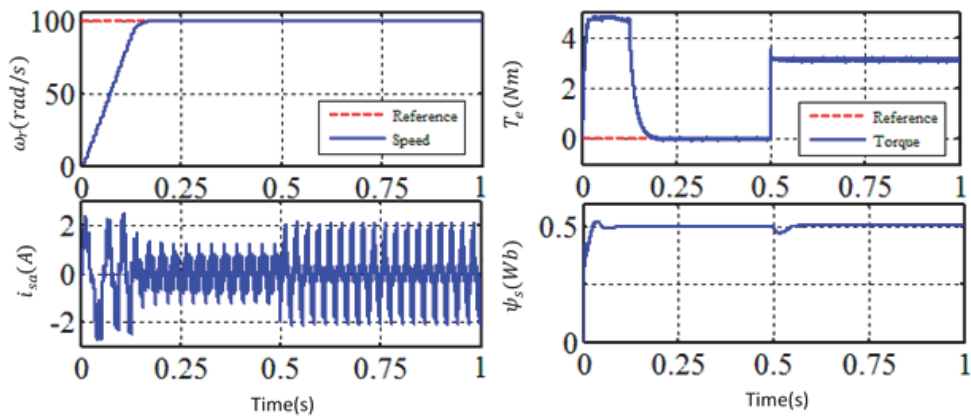
Table 4. 6PIM parameters.

Parameter, Unit	Value	Parameter, Unit	Value
Rated power, W	700	$L_{m,r}$, mH	588
Rated voltage, V	200	$L_{s,r}$, mH	603.3
Rated current, A	2	$L_{r,r}$, mH	604.4
Rated speed, rpm	1400	$R_{s,r}$, Ω	15.0
Frequency, Hz	50	$R_{r,r}$, Ω	7.91

The simulation results for the duty cycle and the proposed DTC strategies under load change from 0 to about 3.5 Nm at $t = 0.5$ s, speed command of 100 rad/s, and flux command of 0.5 Wb are shown in Figures 7 and 8, a speed torque and stator flux reference signals are shown with red dashed lines.

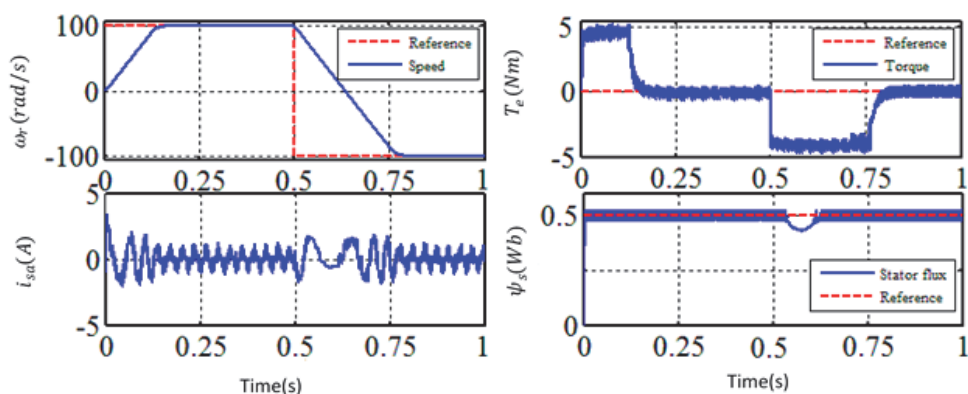


(a)

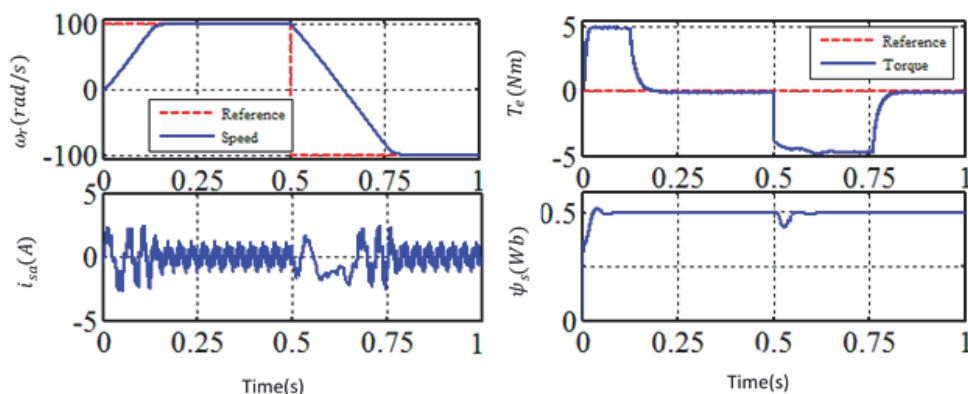


(b)

Figure 7. Load change condition of the 6PIM controlled by the duty cycle control strategy (a) and proposed method (b).



(a)



(b)

Figure 8. Speed direction change condition of the 6PIM controlled by the duty cycle control strategy (a) and proposed method (b).

As it can be seen from the both simulations (Figures 7 and 8), the torque ripples and stator flux fluctuations of proposed method is lower in compared to duty cycle control strategy. However, due to additional PI controller is used for stator flux, Equation (4), running time is higher.

7. Experimental Setup

In addition to the simulations, the performance of the proposed method is validated experimentally. Figure 9 shows the experimental setup, which contains the 6PIM and its coupled load, the main processor, two three-phase VSIs, current and voltage transducers, shaft encoder, and single-phase bridge rectifier.

The applied processor used in the driver is an eZDSP F28335 based on the floating point TMS320F28335 chip. The motor speed is measured by an Autronics incremental shaft encoder (Autronics, Busan, South Korea) mechanically coupled to the 6PIM with resolution of 2500 P/R. LEM LTS6np current transducers are implemented to measure all the phases' currents in order to be used in the estimation and the control processes. The DC-link voltage is also measured using LV 25 - p voltage transducer. A DC generator is applied as load machine and a PCI-1716 data acquisition card (DAQ, Advantech, Milpitas, CA, USA) as an A/D converter. A 700-W, 24-stator slots three-phase squirrel-cage

induction motor, which has been rewound to construct a 4-pole asymmetrical 6PIM is also tested for the proposed method performance. The MATLAB/Embedded Coder is used to generate usable code for the code composer studio development environment. The digital motor control and *IQmath* libraries along with *IQ17* data type are employed. The sampling period is set to $T_s = 100 \mu s$ with a dead-time of $2 \mu s$.

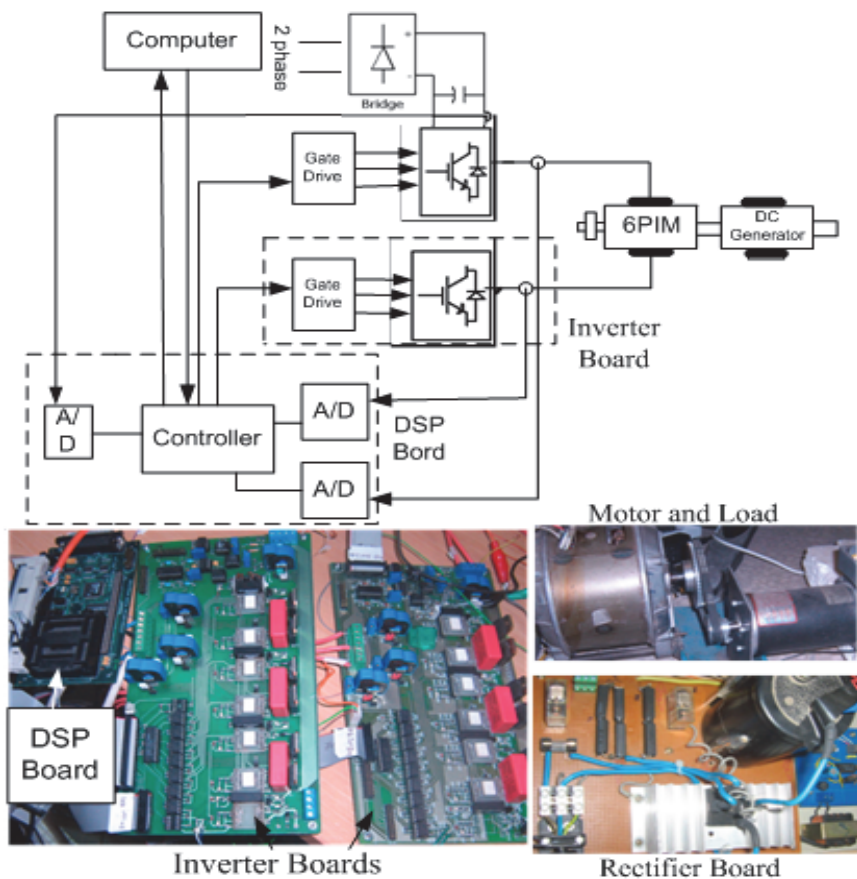


Figure 9. Experimental setup.

To demonstrate the torque ripples reduction precisely, the torque figures are shown within a short time frame in Figure 10.

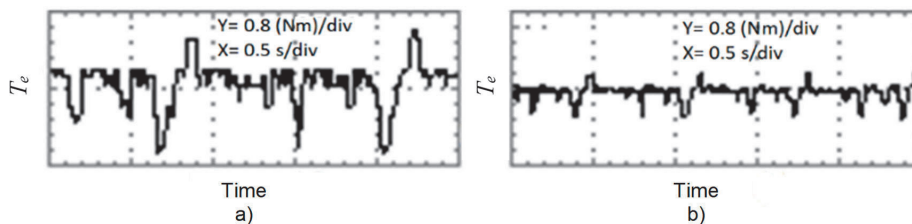


Figure 10. The torque response of the 6PIM in steady state with 4 Nm load, derived by (a) duty cycle control strategy; (b) proposed method.

The experimental results of the duty cycle control strategy and the proposed method under the load changing from 0 to about 3.5 N/m are shown in Figure 11. In this test, the speed and flux commands are 100 rad/s and 0.5 Wb, respectively. The provided tests illustrate the alleviation of torque ripples in the proposed method compared with the duty cycle control strategy.

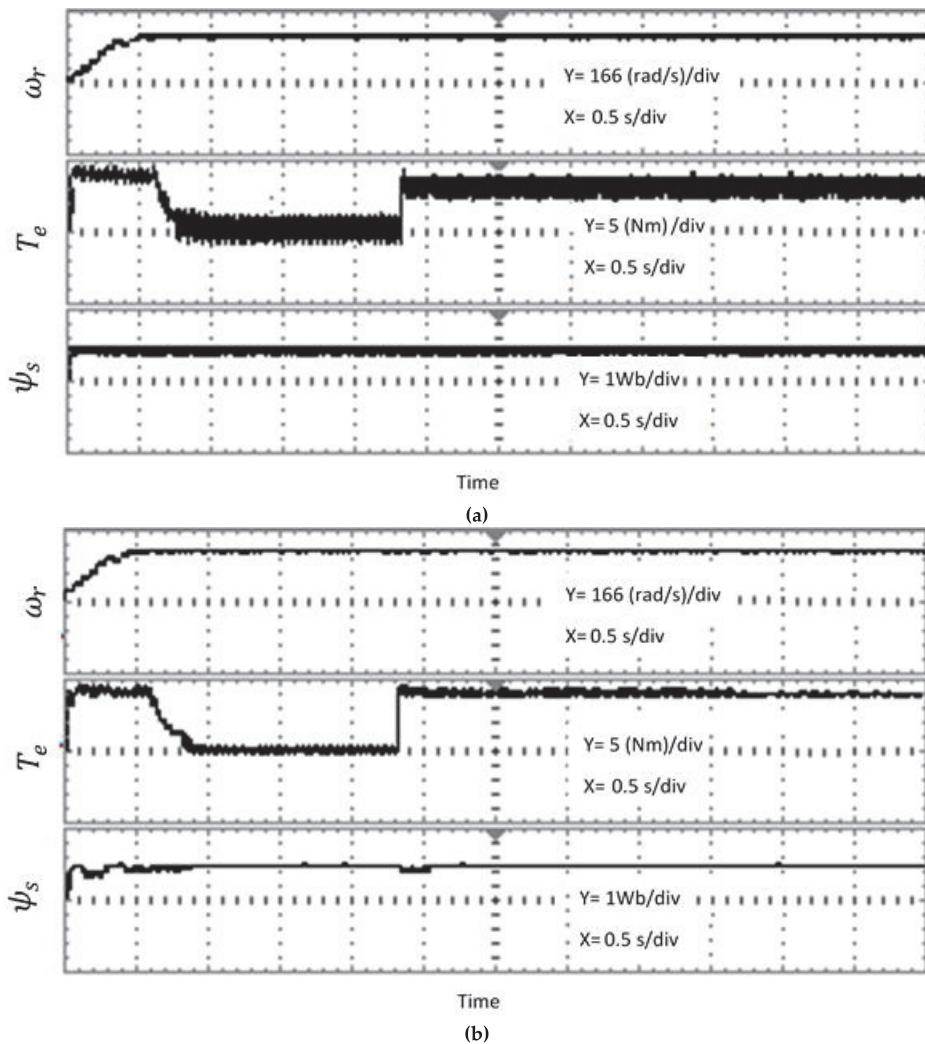
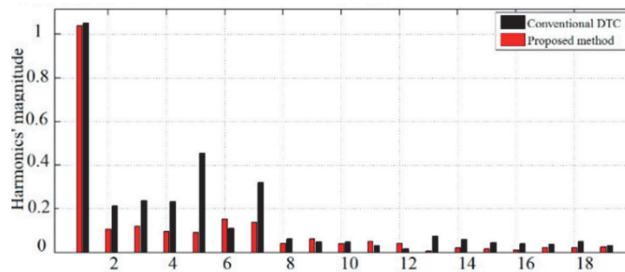


Figure 11. Load injection experiment of 6PIM, controlled by duty cycle control strategy (a) and proposed method (b).

In Table 5, the torque ripples in the no load condition are investigated to show the differences between the proposed method and the conventional DTC and the duty cycle control-based DTC strategies. It is clear that the torque ripples for the 6PIM is effectively decreased for the proposed method in comparison with other two methods. Furthermore, as it is seen from current THD in Figure 12, the low order harmonics of the stator currents, especially the fifth and seventh harmonics, are considerably reduced for the proposed control method.

Table 5. Torque ripples in three different conditions of 6PIM driving by three different methods.

Method	No-Load	Rated Load	50% Load
Conventional DTC	%45	%49	%47
Duty cycle control	%41	%37	%39
Proposed method	%9	%12	%10

**Figure 12.** Current THD of the conventional DTC and proposed method.

8. Conclusions

In this paper the performance of the 6PIM was improved by a new vector control strategy. Using a new set of inputs for the ST in DTC method and applying the duty cycle control strategy leads to decrease in both torque ripples and harmonic currents. From a complexity viewpoint, the proposed technique falls between the DTC and FOC. This method is more simple compared with FOC strategy due to the absence of PWM algorithm, and has a fast dynamic similar to DTC strategy. The main limitation of the proposed technique is variable switching frequency compared with FOC. The effectiveness of the proposed control strategy was confirmed using both simulation and experimental tests.

Author Contributions: Methodology, validation and formal analysis, H.H.; writing—original draft H.H., A.T., M.H.H.; writing—review & editing, A.R., T.V. and A.K.; supervision, A.B.

Funding: This work was supported by the Estonian Research Council under Grants PUT1260.

Conflicts of Interest: The authors declare no conflict of interest.

Appendix A

$$T = \frac{1}{\sqrt{3}} \begin{bmatrix} 1 & \cos(4\gamma) & \cos(8\gamma) & \cos(\gamma) & \cos(5\gamma) & \cos(9\gamma) \\ 1 & \sin(4\gamma) & \sin(8\gamma) & \sin(\gamma) & \sin(5\gamma) & \sin(9\gamma) \\ 1 & \cos(8\gamma) & \cos(4\gamma) & \cos(5\gamma) & \cos(\gamma) & \cos(9\gamma) \\ 1 & \sin(8\gamma) & \sin(4\gamma) & \sin(5\gamma) & \sin(\gamma) & \sin(9\gamma) \\ 1 & 1 & 1 & 0 & 0 & 0 \\ 0 & 0 & 0 & 1 & 1 & 1 \end{bmatrix}$$

where, $\gamma = \alpha = \frac{\pi}{6}$

References

- Levi, E. Multiphase electric machines for variable-speed applications. *IEEE Trans. Ind. Electron.* **2008**, *55*, 1893–1909. [[CrossRef](#)]
- Holakoio, M.H.; Ojaghi, M.; Taheri, A. Direct Torque Control of Six-Phase Induction Motor with a Novel MRAS-Based Stator Resistance Estimator. *IEEE Trans. Ind. Electron.* **2018**, *65*, 7685–7696. [[CrossRef](#)]

3. Che, H.S.; Duran, M.J.; Levi, E.; Jones, M.; Hew, W.P.; Rahim, N.A. Postfault operation of an asymmetrical six-phase induction machine with single and two isolated neutral points. *IEEE Trans. Power Electron.* **2014**, *29*, 5406–5416. [[CrossRef](#)]
4. Jahns, T.M. Improved reliability in solid-state drives for large asynchronous ac machines by means of multiple independent phase-drive units. *IEEE Trans. Ind. Appl.* **1980**, *IA-16*, 321–331. [[CrossRef](#)]
5. Fnaiech, M.A.; Betin, F.; Capolino, G.A.; Fnaiech, F. Fuzzy logic and sliding-mode controls applied to six-phase induction machine with open phases. *IEEE Trans. Ind. Electron.* **2010**, *57*, 354–364. [[CrossRef](#)]
6. Parsa, L.; Toliyat, H.A.; Goodarzi, A. Five-phase interior permanent-magnet motors with low torque pulsation. *IEEE Trans. Ind. Appl.* **2007**, *43*, 40–46. [[CrossRef](#)]
7. Marouani, K.; Baghli, L.; Hadiouche, D.; Kheloui, A.; Rezzoug, A. A new PWM strategy based on a 24-sector vector space decomposition for a six-phase VSI-Fed dual stator induction motor. *IEEE Trans. Ind. Electron.* **2008**, *55*, 1910–1920. [[CrossRef](#)]
8. Pandit, J.K.; Aware, M.V.; Nemade, R.V.; Levi, E. Direct Torque Control Scheme for a Six-Phase Induction Motor with Reduced Torque Ripple. *IEEE Trans. Power Electron.* **2017**, *32*, 7118–7129. [[CrossRef](#)]
9. Zheng, L.; Fletcher, J.E.; Williams, B.W.; He, X. A novel direct torque control scheme for a sensorless five-phase induction motor drive. *IEEE Trans. Ind. Electron.* **2011**, *58*, 503–513. [[CrossRef](#)]
10. Lokriti, A.; Salhi, I.; Doubabi, S. IM Direct Torque Control with no flux distortion and no static torque error. *ISA Trans.* **2015**, *59*, 256–267. [[CrossRef](#)]
11. Ambrozic, A.; Buja, G.S.; Menis, R. Band-Constrained Technique for Direct Torque Control of Induction Motor. *IEEE Trans. Ind. Electron.* **2004**, *51*, 776–784. [[CrossRef](#)]
12. Ren, Y.; Zhu, Z.Q. Enhancement of steady-state performance in direct-torque-controlled dual three-phase permanent-magnet synchronous machine drives with modified switching table. *IEEE Trans. Ind. Electron.* **2015**, *62*, 3338–3350. [[CrossRef](#)]
13. Taheri, A.; Rahmati, A.; Kaboli, S. Comparison of efficiency for different switching tables in six-phase induction motor DTC drive. *J. Power Electron.* **2012**, *12*, 128–135. [[CrossRef](#)]
14. Singh, B.; Jain, S.; Dwivedi, S. Torque ripple reduction technique with improved flux response for a direct torque control induction motor drive. *IET Power Electron.* **2013**, *6*, 326–342. [[CrossRef](#)]
15. Lai, Y.S.; Chen, J.H. A new approach to direct torque control of induction motor drives for constant inverter switching frequency and torque ripple reduction. *IEEE Trans. Energy Convers.* **2001**, *16*, 220–227.
16. Shyu, K.K.; Lin, J.K.; Pham, V.T.; Yang, M.J.; Wang, T.W. Global minimum torque ripple design for direct torque control of induction motor drives. *IEEE Trans. Ind. Electron.* **2010**, *57*, 3148–3156. [[CrossRef](#)]
17. Abad, G.; Rodriguez, M.A.; Poza, J. Two-Level VSC Based Predictive Direct Torque Control of the Doubly Fed Induction Machine with Reduced Torque and Flux Ripples at Low Constant Switching Frequency. *IEEE Trans. Power Electron.* **2008**, *23*, 1050–1061. [[CrossRef](#)]
18. Wang, T.; Fang, F.; Wu, X.; Jiang, X. Novel filter for stator harmonic currents reduction in six-step converter fed multiphase induction motor drives. *IEEE Trans. Power Electron.* **2013**, *28*, 498–506. [[CrossRef](#)]
19. Autou, S.; Saroka, V.; Karpovich, D.; Rassolkina, A.; Gevorkov, L.; Vaimann, T.; Kallaste, A.; Belahcen, A. Comparative study of field-oriented control model in application for induction and synchronous reluctance motors for life-cycle analysis. In Proceedings of the 2018 25th International Workshop on Electric Drives: Optimization in Control of Electric Drives (IWED), Moscow, Russia, 31 January–2 February 2018.
20. Nelson, R.H.; Krause, P.C. Induction machine analysis for arbitrary displacement between multiple winding sets. *IEEE Trans. Power Appar. Syst.* **1974**, *PAS-93*, 841–848. [[CrossRef](#)]
21. Zhao, Y.; Lipo, T.A. Space Vector PWM Control of Dual Three-phase Induction Machine Using Vector Space Decomposition. *IEEE Trans. Ind. Appl.* **1995**, *31*, 1100–1109. [[CrossRef](#)]
22. Binder, A.; Muetze, A. Scaling effects of inverter-induced bearing currents in AC machines. *IEEE Trans. Ind. Appl.* **2008**, *44*, 769–776. [[CrossRef](#)]
23. Holakooie, M.H.; Taheri, A.; Sharifian, M.B.B. MRAS based speed estimator for sensorless vector control of a linear induction motor with improved adaptation mechanisms. *J. Power Electron.* **2015**, *15*, 1274–1285. [[CrossRef](#)]



Curriculum vitae

Personal data

Name: Hamidreza Heidari
Date of birth: 5.04.1989
Place of birth: Islamic Republic of Iran
Citizenship: Iranian

Contact data

E-mail: hamidrezaheidari1989@gmail.com

Education

2018–2022 PhD, Tallinn University of Technology (Electrical Power Engineering and Mechatronics)
2015–2017 MSC, Zanjani ülikool (Electrical and Computer Engineering)
2013–2015 BSC, Zanjani ülikool (Digital Electronics)

Language competence

Persian Native
English Fluent
Estonian Beginner

Field of research (CERCS - classifier)

T190 Electrical Engineering
T170 Electronics
T455 Motors and propulsion systems

Grants and projects

PUT1260 “Lifecycle Influenced Optimization Methodology for Electrical Motor-Drives” (1.01.2016–31.12.2019); Principal Investigator: Anouar Belahcen; Tallinn University of Technology
PSG453 “Digital twin for propulsion drive of autonomous electric vehicle” (1.01.2020–31.12.2023); Principal Investigator: Anton Rassõlkin; Tallinn University of Technology

Elulookirjeldus

Isikuandmed

Nimi: Hamidreza Heidari
Sünniaeg: 5.04.1989
Sünnikoht: Iraani Islamivabariik
Kodakondsus: iraanlane

Kontaktandmed

E-post: hamidrezaheidari1989@gmail.com

Hariduskäik

2018–2022 PhD, Tallinna Tehnikaülikool (Elektroenergeetika ja mehhatroonika)
2015–2017 MSC, Zanjani ülikool (Elektro- ja arvutitehnika)
2013–2015 BSC, Zanjani ülikool (Digitaalne elektroonika)

Keelteoskus

Pärsia keel emakeel
Inglise keel kõrgtase
Eesti keel algtase

Teadustöö põhisuunad

T190 Elektrotehnika
T170 Elektroonika
T455 Mootorid ja ajamid

Jooksvad projektid

PUT1260 “Elutsüklit arvestav elektrimootorajamite optimeerimismetodoloogia”
(1.01.2016–31.12.2019); Vastutav täitja: Anouar Belahcen; Tallinna
Tehnikaülikool
PSG453 “Isejuhtiva elektrisõiduki veoajami digitaalne kaksik”
(1.01.2020–31.12.2023); Vastutav täitja: Anton Rassõlkin; Tallinna
Tehnikaülikool

ISSN 2585-6901 (PDF)
ISBN 978-9949-83-799-1 (PDF)